

MICROSCOPIC VIEW OF CHARGE INJECTION IN A
MODEL ORGANIC SEMICONDUCTOR

A Dissertation

Presented to the Faculty of the Graduate School

of Cornell University

in Partial Fulfillment of the Requirements for the Degree of

Doctor of Philosophy

by

William Richard Silveira

August 2005

MICROSCOPIC VIEW OF CHARGE INJECTION IN A
MODEL ORGANIC SEMICONDUCTOR

William Richard Silveira, Ph.D.

Cornell University 2005

The lack of a microscopic understanding of charge injection from a metal into a π -conjugated organic system currently limits progress toward commercial organic electronic devices. This thesis describes the use of high-sensitivity electric force microscopy to evaluate predominant models of charge injection and a new source of energetic disorder in one of the most well understood organic materials, the molecularly doped polymer system.

The motivation for this critical examination of a model organic semiconductor is outlined and recent studies of organic materials by electric force microscopy and complementary techniques are discussed. A detailed description of the development of a custom-built variable temperature electric force microscope is given. The current understanding of charge transport and injection in the molecularly doped polymer system is then reviewed, followed by two significant investigations: (1) The microscopic observation of the transition from Ohmic conduction to space-charge limited conduction, from which we determine charge injection energetics at the metal/organic interface and (2) the observation of a surprisingly large variation of the surface potential of topographically uniform molecularly doped polymer films under a number of chemical and physical conditions.

TABLE OF CONTENTS

| | | |
|----------|---|-----------|
| 1 | Introduction | 1 |
| 1.1 | π -conjugated organic materials for electronics | 1 |
| 1.2 | Classes of organic electronic materials | 4 |
| 1.3 | Characterization of organic electronic materials | 7 |
| 1.4 | Significant findings presented in this thesis | 12 |
| | Chapter 1 references | 14 |
| 2 | Scanned probe microscopy of organic materials | 18 |
| 2.1 | Scanning tunneling and atomic force microscopies | 18 |
| 2.2 | Quantitative high-sensitivity electric force microscopy | 19 |
| 2.3 | Imaging variations of the surface potential: Film morphology and electronic properties | 21 |
| 2.4 | Noncontact electric force microscopy of π -conjugated organic device structures | 22 |
| 2.4.1 | The field-effect transistor | 22 |
| 2.4.2 | Measuring the local potential in an organic device | 23 |
| 2.4.3 | Testing microscopic theories of charge injection | 24 |
| 2.5 | Related characterization techniques | 27 |
| 2.5.1 | Conducting probe atomic force microscopy | 27 |
| 2.5.2 | Scanning tunneling microscopy of organic polymers | 29 |
| 2.5.3 | Kelvin probe and photoelectron spectroscopies | 29 |
| 2.6 | Summary and conclusions | 31 |
| | Chapter 2 references | 33 |
| 3 | High-sensitivity electric force microscopy | 36 |
| 3.1 | Detection of the force sensor | 38 |
| 3.1.1 | Overview of detection methods | 38 |
| 3.1.2 | The fiber-optic interferometer | 40 |
| 3.2 | A variable temperature coarse positioning mechanism | 43 |
| 3.2.1 | Engineering the coarse positioning mechanism | 45 |
| 3.2.2 | Final design of the coarse positioning mechanism | 61 |
| 3.2.3 | Thermal stability | 66 |
| 3.3 | Sample positioning | 71 |
| 3.3.1 | Cryogenic bimorph piezo-based scanning stage | 72 |
| 3.3.2 | Coarse positioning mechanism | 73 |
| 3.4 | Mechanical design, vacuum, and vibration isolation | 76 |
| 3.4.1 | Operation at cryogenic temperatures | 77 |
| 3.5 | Measuring forces and force gradients, microscopically | 78 |
| 3.5.1 | The force-distance curve | 78 |
| 3.5.2 | Amplitude modulation near a surface | 79 |

| | | |
|--|--|------------|
| 3.5.3 | Imaging topographical features | 81 |
| 3.5.4 | Electrostatic forces and force gradients | 83 |
| 3.5.5 | Force sensitivity | 88 |
| 3.5.6 | Overview of experimental procedures | 90 |
| Chapter 3 references | | 93 |
| 4 Charge transport and injection in a model organic semiconductor | | 97 |
| 4.1 | Overview of the molecularly doped polymer system | 97 |
| 4.2 | Chemical nature of the triarylamine | 98 |
| 4.3 | Charge transport in molecularly doped polymers | 102 |
| 4.3.1 | Time of flight technique | 103 |
| 4.3.2 | Hopping transport and the Gaussian disorder model | 104 |
| 4.3.3 | \sqrt{E} , dipoles, and the correlated disorder model | 112 |
| 4.4 | Space-charge limited conduction | 115 |
| 4.5 | Models of charge injection | 123 |
| 4.5.1 | The Mott-Gurney interface | 123 |
| 4.5.2 | The Schottky interface | 125 |
| 4.5.3 | Emtage and O'Dwyer's model for diffusion-limited thermionic emission into an insulator | 133 |
| 4.6 | Conclusions | 134 |
| Chapter 4 references | | 135 |
| 5 Microscopic view of charge injection in a model organic semiconductor | | 138 |
| 5.1 | Introduction | 139 |
| 5.2 | Experimental | 141 |
| 5.3 | A microscopic view of space-charge limited conduction | 144 |
| 5.4 | Evaluating models of charge injection | 150 |
| 5.4.1 | Thermionic emission theory | 151 |
| 5.4.2 | The Schottky model for diffusion-limited thermionic emission into a semiconductor | 153 |
| 5.4.3 | Emtage and O'Dwyer's model for diffusion-limited thermionic emission into an insulator | 158 |
| 5.5 | Effects of film degradation | 162 |
| 5.6 | Conclusions | 166 |
| 5.7 | Future directions | 166 |
| Chapter 5 references | | 168 |

| | |
|--|------------|
| 6 Variation of the surface potential in a model organic semiconductor | 171 |
| 6.1 Introduction | 171 |
| 6.2 Possible causes of the surface potential variation | 173 |
| 6.3 Experimental procedures | 176 |
| 6.3.1 Preparation of the substrate | 176 |
| 6.3.2 Preparation of the molecularly doped polymer films | 177 |
| 6.3.3 Electric force microscopy and image interpretation | 177 |
| 6.4 Varying the chemical and physical environment of TPD | 182 |
| 6.4.1 Molecularly doped polymer films on gold | 182 |
| 6.4.2 Varying the interface energetics | 189 |
| 6.4.3 Surface charges on low mobility organic films | 196 |
| 6.4.4 Varying the degree of energetic disorder | 202 |
| 6.4.5 The potential variation at low temperatures | 207 |
| 6.4.6 Thickness dependence of the potential variation | 209 |
| 6.5 Summary of chemical and physical perturbations | 210 |
| 6.6 Interaction between the cantilever and sample | 213 |
| 6.7 The density of background charge carriers | 217 |
| 6.7.1 Electrical characterization | 219 |
| 6.7.2 Expected density of charge carriers | 220 |
| 6.8 Theoretical modeling | 223 |
| 6.8.1 Modeling random surface and bulk dipoles | 224 |
| 6.8.2 Potential from charges dispersed in a dielectric film | 224 |
| 6.9 Conclusions | 237 |
| 6.10 Future directions | 240 |
| Chapter 6 references | 241 |
| A Harmonic oscillator measurements | 243 |
| A.1 Thermal energy and the harmonic oscillator | 243 |
| A.1.1 The discrete power spectral density | 245 |
| A.1.2 Analysis of a force-distance curve | 245 |
| A.1.3 Induced cantilever excitation | 247 |
| A.2 Origin of the contact potential difference | 248 |
| A.3 Energy stored in a capacitor | 252 |
| A.4 The capacitive force | 253 |
| Appendix A references | 256 |
| B Space-charge limited conduction | 257 |
| B.1 Space-charge limited conduction | 257 |
| B.2 Simplified argument for the current in the space-charge limit | 260 |
| Appendix B references | 262 |

| | |
|---|------------|
| C Probe design | 263 |
| C.1 Cryogenic vacuum space | 263 |
| C.1.1 Probe height adjustment | 264 |
| C.1.2 Fiber-optic and electrical feedthroughs | 271 |
| C.2 Modular design of the microscope head | 271 |
| C.3 Cryogenic sample scanner | 275 |
| C.4 Vibration Isolation | 280 |
| Appendix C references | 288 |
| D Circuit diagrams | 289 |
| D.1 Feedback circuitry for tip-height control | 289 |
| D.2 Positive feedback circuitry | 291 |
| Appendix D references | 294 |

LIST OF TABLES

| | | |
|-----|---|-----|
| 1.1 | Comparison of microscopic characterization methods | 9 |
| 3.1 | Thermal compensation of the coarse positioning mechanism | 69 |
| 3.2 | Force and force gradient sensitivities | 89 |
| 4.1 | Typical SCLC parameters for a molecularly doped polymer device | 117 |
| 5.1 | Emtage and O'Dwyer's model for the Au/TPD-PS interface | 160 |
| 5.2 | Effects of TPD crystallization | 165 |
| 6.1 | Summary of the potential variation under various conditions | 211 |
| 6.2 | Expected density of intrinsic charge carriers | 222 |
| 6.3 | Concentration dependence of the calculated potential variation . | 235 |
| A.1 | Cantilever parameters from the power spectral density | 245 |

LIST OF FIGURES

| | | |
|------|---|-----|
| 1.1 | Conjugated organic molecules | 3 |
| 1.2 | Electric force microscopy of organic materials | 4 |
| 1.3 | Examples of organic electronic materials | 5 |
| 1.4 | Classes of organic electronic materials | 5 |
| 1.5 | Morphology of pentacene and polythiophene thin films | 7 |
| 2.1 | The field-effect transistor | 23 |
| 3.1 | High-sensitivity electric force microscope | 37 |
| 3.2 | Fiber-optic interferometer | 40 |
| 3.3 | Temperature tuning of the interferometer | 43 |
| 3.4 | Initial horizontal coarse positioning mechanism | 47 |
| 3.5 | Fastening down the first generation positioning mechanism | 48 |
| 3.6 | Second generation coarse positioning mechanism | 50 |
| 3.7 | Vertically operational coarse positioning mechanism | 51 |
| 3.8 | Cycloid waveform for driving the coarse positioner | 52 |
| 3.9 | Long-range travel of the coarse positioning mechanism | 53 |
| 3.10 | Coarse positioning mechanism driven by the cycloid waveform | 55 |
| 3.11 | Dynamic motion of the coarse positioning mechanism | 57 |
| 3.12 | Characterization at low temperatures | 60 |
| 3.13 | Final design of the coarse positioning mechanism | 62 |
| 3.14 | Step sizes at variable temperatures | 65 |
| 3.15 | Uniform steps of the coarse positioning mechanism | 67 |
| 3.16 | First generation atomic force microscope | 68 |
| 3.17 | Thermal compensation of the coarse positioning mechanism | 70 |
| 3.18 | Cryogenic sample scanner | 74 |
| 3.19 | Coarse sample positioning mechanism | 75 |
| 3.20 | Coarse positioning of a calibration grating | 76 |
| 3.21 | Force-distance curve on NaCl | 79 |
| 3.22 | Cantilever response to a coherent driving force | 80 |
| 3.23 | Amplitude modulation near a silicon surface | 82 |
| 3.24 | Demonstration of contact mode imaging | 83 |
| 3.25 | Topography of HOPG | 84 |
| 3.26 | Cantilever resonance frequency shift | 85 |
| 3.27 | Quadratic response of the cantilever resonance frequency | 87 |
| 3.28 | Energy of a cantilever when part of a capacitor | 87 |
| 3.29 | Power spectral density of a cantilever – Brownian motion | 88 |
| 4.1 | Chemical structure of the triarylamine, TPD | 97 |
| 4.2 | Chemical structure of polystyrene and polycarbonate | 98 |
| 4.3 | Chemical moieties of the triarylamine, TPD | 99 |
| 4.4 | Calculated dipoles of the triarylamine, TPD | 102 |
| 4.5 | Time of flight experiment | 103 |

| | | |
|------|--|-----|
| 4.6 | Hopping transport | 105 |
| 4.7 | Gaussian distribution of localized states | 106 |
| 4.8 | Hopping transport and energy considerations | 107 |
| 4.9 | Energy and intersite distance dependence of hopping transport . . | 108 |
| 4.10 | Dilute charge carrier energies | 110 |
| 4.11 | Energy barrier lowering - Gaussian disorder model | 112 |
| 4.12 | Noncorrelated and correlated energy levels | 114 |
| 4.13 | Parallel plate device | 116 |
| 4.14 | Potential, electric field and charge density in the space-charge limit | 118 |
| 4.15 | Electric field altered by space-charge | 119 |
| 4.16 | Ohmic and space-charge limited currents | 121 |
| 4.17 | The Mott-Gurney interface | 124 |
| 4.18 | Mott-Gurney parameters for a typical Au/TPD-PS interface . . . | 126 |
| 4.19 | Schottky interface for electrons | 127 |
| 4.20 | Energy barrier lowering for electron injection | 129 |
| 5.1 | Transition: Ohmic conduction to space-charge limited conduction . | 140 |
| 5.2 | Potential and capacitance derivative | 146 |
| 5.3 | Electric field and degree of space-charge limited conduction . . . | 147 |
| 5.4 | Comparison to Mott-Gurney potential and electric field | 148 |
| 5.5 | Qualitative picture of space-charge limited conduction | 149 |
| 5.6 | Comparison to thermionic emission theory | 152 |
| 5.7 | Charge density at the metal/organic interface | 153 |
| 5.8 | Testing the Schottky model of charge injection | 155 |
| 5.9 | Calculating the chemical potential of TPD | 156 |
| 5.10 | Energy level diagram for Au/TPD-PS | 158 |
| 5.11 | Testing Emtage and O'Dwyer's model of charge injection | 159 |
| 5.12 | Current-voltage curve and potential profiles of an aged device . . | 162 |
| 5.13 | Crystallization of a TPD-PS film | 163 |
| 5.14 | Potential and electric field profiles of an aged device | 164 |
| 6.1 | Structures of TPD, polystyrene and polycarbonate | 172 |
| 6.2 | Variation of the surface potential | 174 |
| 6.3 | Likely causes of the potential variation | 175 |
| 6.4 | Experimental arrangement of the cantilever and sample | 178 |
| 6.5 | Potential variation – 50% TPD-PC on polycrystalline gold . . . | 180 |
| 6.6 | Potential variation – Polycrystalline gold film | 184 |
| 6.7 | Potential variation – Epitaxially grown gold film | 186 |
| 6.8 | Potential variation – 50% TPD-PC on epitaxially grown gold . | 188 |
| 6.9 | Interface dipole and Mott-Gurney accumulation region | 190 |
| 6.10 | Potential variation – Polycrystalline aluminum film | 191 |
| 6.11 | Potential variation – 50% TPD-PC on aluminum | 193 |
| 6.12 | Potential variation – 50% TPD-PC on SiO ₂ | 195 |
| 6.13 | Charge deposition on 5% TPD-PS | 198 |

| | | |
|------|--|-----|
| 6.14 | Charge deposition on polycarbonate films | 201 |
| 6.15 | Dipole doping TPD-PC films | 203 |
| 6.16 | Structure of butyl sulfone | 204 |
| 6.17 | Potential variation – 50% TPD-PS on epitaxially grown gold | 205 |
| 6.18 | Potential variation at 77 K – 50% TPD-PS polycrystalline gold | 208 |
| 6.19 | Height dependence of the potential and capacitance derivative | 214 |
| 6.20 | Height dependence of the potential over a TPD-PC film | 216 |
| 6.21 | Height dependence of the potential variation | 218 |
| 6.22 | Determining the density of background charge carriers | 219 |
| 6.23 | Modeling random charges in a dielectric film | 226 |
| 6.24 | Simulated image of the potential from a single charge | 227 |
| 6.25 | Tip-surface distance and charge-depth dependence of the potential | 228 |
| 6.26 | Broadening of the potential | 229 |
| 6.27 | Charge-depth dependence of the potential | 229 |
| 6.28 | Comparison of experimental and simulated images | 230 |
| 6.29 | Dependence of the potential on the dielectric film thickness | 232 |
| 6.30 | Tip-surface distance dependence of the potential variation | 233 |
| 6.31 | Concentration dependence of the calculated potential variation | 234 |
| 6.32 | Concentration dependence of the calculated potential variation | 236 |
| A.1 | Power spectral density of a cantilever | 244 |
| A.2 | Analysis of a force-distance curve | 246 |
| A.3 | Piezo stage for cantilever excitation | 247 |
| A.4 | Piezo excitation of the cantilever | 249 |
| A.5 | Contact potential difference | 250 |
| A.6 | Energy stored in a capacitor | 252 |
| A.7 | Electric force microscopy of a simple device structure | 255 |
| B.1 | Parallel plate device for space-charge limited conduction | 257 |
| C.1 | High vacuum cryogenic vacuum space | 265 |
| C.2 | Vacuum space component 1 | 266 |
| C.3 | Vacuum space component 2 | 267 |
| C.4 | Vacuum space component 3 | 268 |
| C.5 | Vacuum space component 4 | 269 |
| C.6 | Dewar seal and probe height adjustment mechanism | 270 |
| C.7 | Early prototype of the electric force microscope | 273 |
| C.8 | Design of mounting plates | 274 |
| C.9 | Entire microscope head | 276 |
| C.10 | Cryogenic sample scanner | 277 |
| C.11 | Design of the cryogenic sample scanner top outer scan stage | 278 |
| C.12 | Design of the cryogenic sample scanner center scan stage | 279 |
| C.13 | Design of the cryogenic sample scanner bottom base | 280 |
| C.14 | Assembly of the cryogenic sample scanner | 281 |

| | | |
|------|---|-----|
| C.15 | Vibration isolation frame - top view | 284 |
| C.16 | Vibration isolation frame and top plate - side view | 285 |
| C.17 | Vibration isolation - top view of 2000 pound plate | 286 |
| C.18 | Mounting plate for the cryogenic dewar | 287 |
| D.1 | Proportional/Integral feedback control electronics | 290 |
| D.2 | Front panel of the feedback circuit box | 291 |
| D.3 | Testing the feedback circuitry | 292 |
| D.4 | Basic principle of the positive feedback circuitry | 293 |

CHAPTER 1

INTRODUCTION

The focus of this thesis is a microscopic investigation of charge injection in a model π -conjugated organic system, molecularly doped polymers, using high-sensitivity electric force microscopy (EFM). In this chapter, we introduce the motivation for this work, followed by a brief review of the methods available to the experimentalist to gain an understanding of the electronic properties of organic materials. Finally, we will discuss the unique ability of high-sensitivity electric force microscopy to elucidate mechanisms of charge injection and transport in organic materials.

1.1 π -conjugated organic materials for electronics

Conducting and semiconducting organic materials have long been known [1]. The delocalization of p_z electrons creates a system capable of conducting charge along a carbon backbone, illustrated by the bonding within the simple molecules 1,3-butadiene and benzene, shown in Figure 1.1. This type of bonding is present in all classes of semiconducting organic materials, which range from small molecules to polymers. The conductive properties of π -conjugated organic materials make them extremely well suited for constructing high-efficiency solar cells [2,3], light emitting diodes [4, 5], chemical sensors [6, 7], and solution-processed thin film transistors [8, 9].

The electronic properties of organic materials, coupled with the endless possibilities for new organic molecules and polymers, have created a lively field with much to learn. Great excitement generated by the electronic properties of π -conjugated organic molecules and polymers has led to investigations of charge transport and

charge injection in organic materials. Fascinating investigations ranging from single crystal charge transport measurements [10] to a device constructed from a single organic molecule, have been achieved [11–13].

While it is unlikely that the performance of organic materials will ever rival that of silicon technology, organic materials distinguish themselves by their inherent physical flexibility, which enables a variety of innovative technologies and fabrication techniques. Advances in synthetic chemistry [14–16] have recently addressed the long standing promise of mass produced, inexpensive organic electronic devices by increasing solubility and improving fabrication techniques. Finally, since the physical, electronic and optical properties of organic materials can be modified by chemical synthesis and because they can be processed and patterned under ambient conditions, organic materials are ideal for electronics that can be fabricated inexpensively on large area substrates.

In recent years, steps have been taken to improve the charge transport in the bulk organic and charge injection at the metal/organic interface [17]. Success of the organic field-effect transistor (OFET), a switching device, is critical to the use of organic materials for electronic applications. Steady progress has taken place to increase the OFET’s performance [18–21].

Despite significant advances, several issues remain to be solved in the field of organic electronics. While charge transport has received considerable experimental and theoretical attention, a microscopic view of the process will allow us to put our current understanding [22,23] to the test and will inevitably lead to new questions, ideas, and a more complete picture. More importantly, the lack of a satisfying microscopic description of charge injection has limited progress toward developing widely-applicable organic electronic structures [24]. The development of organic

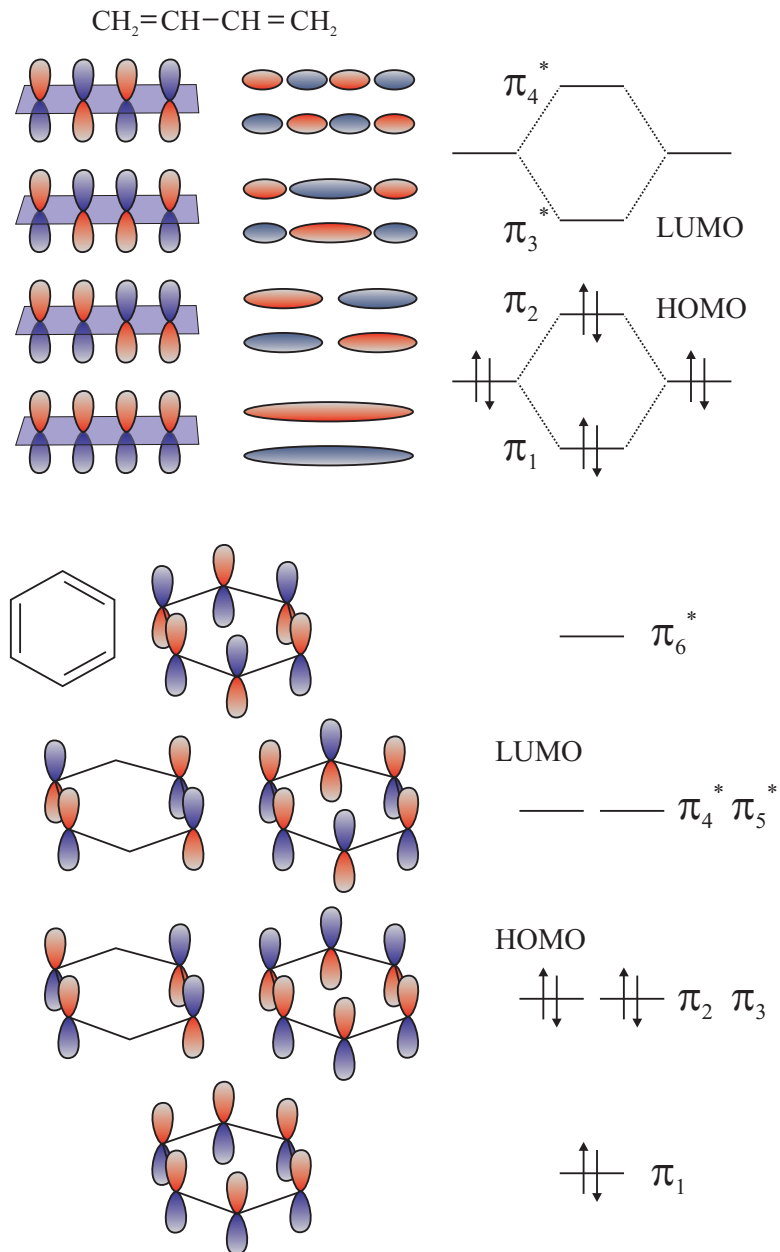


Figure 1.1: These simple molecules demonstrate the delocalization of p_z electrons along the carbon backbone. (a) The atomic and molecular orbitals of 1,3-butadiene. (b) The atomic orbitals of benzene. The energy levels, including that of the highest occupied molecular orbital (HOMO) and lowest unoccupied molecular (LUMO) are shown on the right.

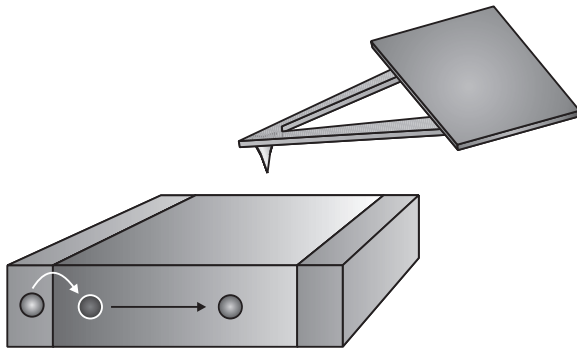


Figure 1.2: Electric force microscopy for detection of charge injection and transport processes. The electrostatic forces between the micromachined cantilever and charge in the sample are mapped for a microscopic view of the electronic properties of organic materials.

electronic devices today proceeds largely by trial and error because of the lack of a fundamental understanding of this process. Our understanding of charge injection from a metal to an organic, an area of elevated debate, will benefit greatly from a microscopic approach (Figure 1.2).

1.2 Classes of organic electronic materials

The diversity of organic materials makes them both interesting and useful for electronic applications, yet significantly increases the difficulty in explaining their unique electronic properties. The composition of these π -conjugated, van der Waals bonded organic solids range from small, crystalline polyacenes, such as pentacene [25], to thiophene oligomers [26] and semicrystalline polymers [27], as illustrated in Figure 1.3.

Semiconducting organic polymers, represented by Figure 1.4(a), are π -conjugated and conduct along the polymer backbone or between adjacent polymer chains. Molecular solids (Figure 1.4(b)), are composed of small, closely spaced π -conjugated

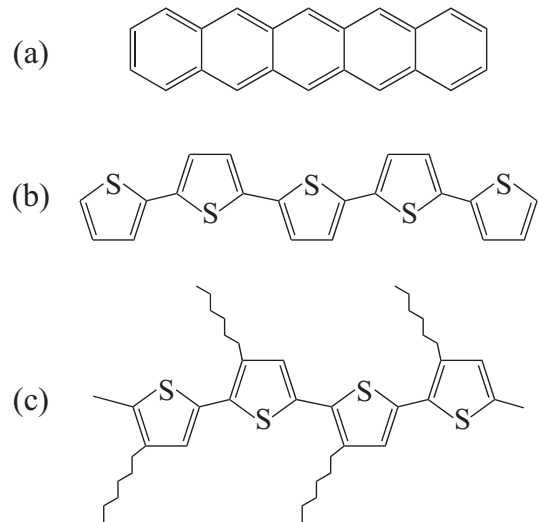


Figure 1.3: Examples of organic electronic materials: (a) Pentacene. (b) Thiophene oligomer. (c) Poly(3-hexylthiophene).

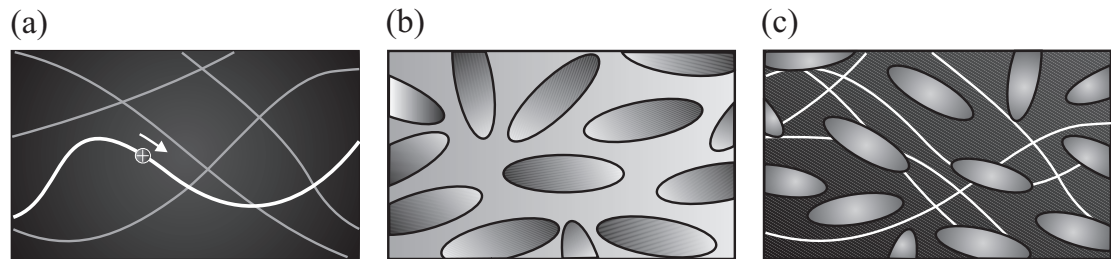


Figure 1.4: Classes of organic electronic materials. (a) Semiconducting polymers. (b) Molecular solids. (c) Molecularily doped polymers.

organic molecules. Molecularly doped polymers (Figure 1.4(c)), are also composed of small π -conjugated organic molecules. However, the conductive molecules are dispersed in a nonconductive host polymer. Each class exhibits different degrees of order and disorder, which is evident from the variety of morphologies encountered with organic thin films (Figure 1.5). Semiconducting organic polymers are often solution cast or electrochemically deposited as films that have ordered domains separated by amorphous disordered regions. Molecular solids can be amorphous or crystalline, depending whether the film was solution cast or thermally evaporated, respectively. Molecularly doped polymers form extremely uniform, amorphous films.

Considering the large number of organic materials available for study, one is faced with the difficult task of choosing a system. This thesis describes the use of high-sensitivity electric force microscopy to obtain a microscopic understanding of charge injection in a molecularly doped polymer system. Molecularly doped polymers have found considerable success as transport layers in xerography and are the basis for successful theoretical descriptions of charge transport [22]. This system is often considered a “model” organic semiconductor. They are also utilized as charge transport layers in a variety of organic device structures [4,5]. Molecularly doped polymers are now proving crucial to the development of charge injection theories for organic materials. For these reasons, this system is an ideal testing ground for a critical look at charge injection with high-sensitivity electric force microscopy.

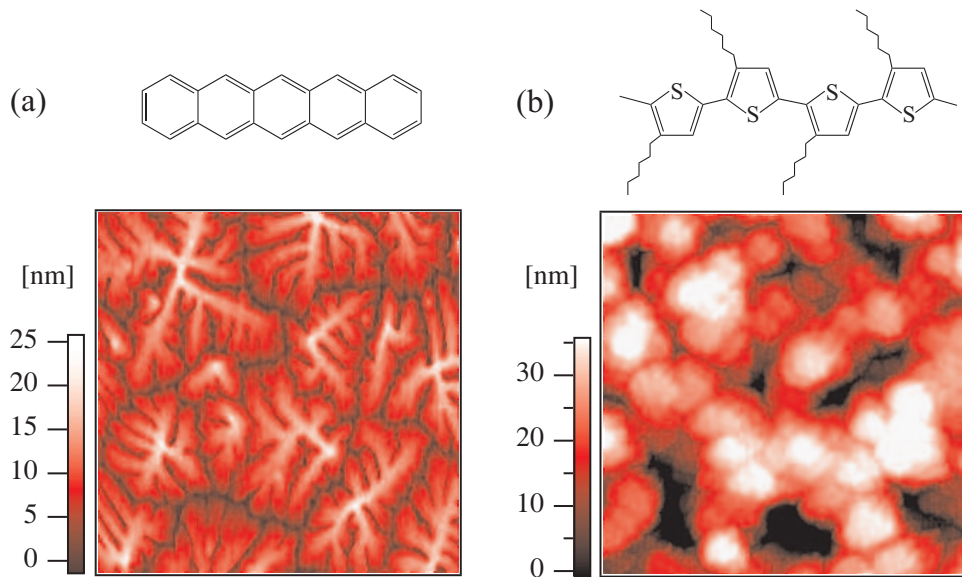


Figure 1.5: (a) $5 \mu\text{m} \times 5 \mu\text{m}$ topographical image of a thermally evaporated pentacene film on SiO_2 . (b) $2 \mu\text{m} \times 2 \mu\text{m}$ topographical image of a solution cast poly(3-hexylthiophene) film on SiO_2 .

1.3 Characterization of organic electronic materials

The photophysics and mechanisms of charge conduction in heavily-doped disordered bulk polymers such as polyacetylene and polyaniline has been well studied [28]. Disordered molecularly doped polymers, in which charge motion occurs via hopping transport, are also quite well studied [1, 22], although the origin of the universally observed field-dependent mobility in these materials was only recently explained [29–35].

The present microscopic picture of the organic/metal interface, charge injection, transport, and trapping has been developed primarily via photoelectron spectroscopy [36–38], hole and electron time of flight [22, 39], and charge transport measurements [17, 24, 40, 41] – generally all bulk measurements. This picture is far from complete, however, in part because of the limitations of these bulk charac-

terization techniques. For example, photoelectron spectroscopy cannot be easily applied to polymer and polymer-molecule solid solutions, particularly in working devices. Metal/organic interfaces prepared in ultrahigh vacuum typically exhibit large interface dipoles, yet devices prepared under realistic manufacturing conditions are usually found to have a negligible interface dipole [17]. The role of the interface dipole in devices prepared under ambient conditions remains to be clarified. Electron and hole time of flight measurements become challenging in samples with high mobility, because of the short time scales involved, and the technique can only be applied to a test device having a blocking contact. Interpreting charge transport measurements requires a careful disentangling of bulk and contact effects by modeling the transport through devices of different length [40]. Only “bad” contacts, which contribute significantly to the total device resistance, can be studied by transport measurements. In a device with a “good” contact, the device current is space-charge limited and independent of the contact resistance altogether. Given these limitations, it is important to ask what new information might be obtained from methods with higher spatial resolution.

Table 1.1 lists microscopies that have been, or could be, used to study charge injection, transport, and trapping in device-grade organic electronic materials. Before high-sensitivity (vacuum) electric force microscopy (EFM) was employed to study organic electronic materials, CP-AFM, NSOM, STM, and EFM in air had shown that these materials’ properties are heterogeneous at the 10-100 nm length-scale.

Frisbie *et al.* have investigated iodine-doped monolayer sexithiophene crystals [42] by conducting probe atomic force microscopy (CP-AFM) [43–45]. They have investigated charge transport across a single grain boundary, the role of contacts,

| Technique | Subsurface | Disordered | Charge |
|--|------------|------------|--------|
| transmission electron microscopy | N | N | N |
| scanning tunneling microscopy | N | Y | N |
| atomic force microscopy | N | Y | N |
| near field scanning optical microscopy | Y | Y | N |
| conducting probe atomic force microscopy | N | Y | Y |
| scanning capacitance microscopy | Y | Y | Y |
| scanning single electron transistor | Y | Y | Y |
| electric force microscopy | Y | Y | Y |

Table 1.1: Microscopies for studying organic films and devices. We briefly evaluate each technique according to its ability to probe subsurface features and to observe charge directly in organic systems.

Acronyms: transmission electron microscopy (TEM), scanning tunneling microscopy (STM), atomic force microscopy (AFM), near field scanning optical microscopy (NSOM), conducting probe atomic force microscopy (CP-AFM), scanning capacitance microscopy (SCM), scanning single electron transistor (S-SET), and electric force microscopy (EFM).

the temperature dependence of the mobility, and the dependence of the conduction on crystal thickness [42, 46–48].

Those thin-film organic materials that fluoresce are amenable to study by near-field scanning optical microscopy (NSOM) [49], as has been recently reviewed by Buratto [50] and Barbara [51]. Vanden Bout *et al.* [52] have used polarization-resolved NSOM to show that even in cases where a spin-coated thin film of poly(*p*-pyridylvinylene) appears atomically flat, the polymer exhibits 200 nm domains of molecular orientation. The Buratto group has shown that photoluminescence, photoconductivity, and photooxidation depend dramatically on variations in morphology at the 100-500 nm length scale in, for example, poly(*p*-phenylene) [53–55].

Atomic force microscopy (AFM) and electric force microscopy (EFM) have been used by Semenikhin *et al.* to probe local structural inhomogeneity and a nonuniform dopant distribution in conducting polythiophenes [56–58] and by Hassenkam *et al.* [59] to view potential drops across individual grains in doped polythiophene. Scanning tunneling spectroscopy has been used to measure the exciton binding energy in conjugated polymers and to explore local variations in the single-particle bandgap [60, 61].

These microscopic studies clearly demonstrate that doping, conductivity, molecular orientation, and energy level splittings are heterogeneous in a wide variety of π -conjugated systems. By enabling the detection of charge and potential directly in organic materials by a non-contact measurement, we will show that high-sensitivity electric force microscopy extends this picture considerably.

Electric force microscopy [62, 63] has a number of advantages over techniques previously used to study organic electronic materials. EFM measures local capacitance and potential, which are directly relevant to device operation. Trapped

charge can be followed as well, via the resulting shift in the surface potential. Because electrostatic forces are long range, EFM can be used to probe charge trapped below a surface [64, 65]. It has a much higher charge sensitivity than scanning capacitance microscopy. The single electron transistor has comparable sensitivity, but only operates at cryogenic temperatures.

A potential disadvantage of EFM is that it requires planar samples, which would seem to preclude studying directly sandwich structures such as organic light emitting diodes. EFM's spatial resolution depends on tip shape and distance from the sample. Its typical resolution of 100 nm is much worse than for STM, but more than adequate to disentangle bulk and contact resistances in a working thin-film device. If meaningful EFM data are to be collected, care must be taken with low mobility samples to prevent triboelectric charging during topographic scanning. Achieving the highest possible sensitivity demands using a microscope operating in vacuum.

Nevertheless, EFM is extremely powerful. Potential drops can be observed across individual grains [59, 64] and at contacts [66–69], allowing one to estimate both the contact resistance and the true mobility in the organic film. The electric force microscope furthermore gives local information that is not revealed by any other method. Differentiating the potential measured in a device gives the local lateral electric field. This electric field can be combined with measured current density to give, in samples with well characterized mobility, information about local charge density. The evolution of this charge density with local electric field gives information about orbital lineups at the organic/inorganic interface [70]. In gated samples the locally induced charge density can be estimated from measured local potential, in which case current and local electric field information can be

combined to give the local mobility [67, 71].

EFM is a non-contact technique; this is important when studying fragile polymer films. It is well suited for variable-temperature work, which enables the elucidation of charge conduction mechanisms and rigorous testing of theories of charge injection and trapping. Finally, EFM is extremely sensitive – single charge sensitivity has been reported in vacuum at room temperature [72–75].

1.4 Significant findings presented in this thesis

This thesis presents:

- The development of a high-sensitivity electric force microscope [76]. This microscope demonstrates the unique capability of high-sensitivity electric force microscopy for the investigation of charge injection and transport in organic materials.
- The measurement of the local charge density, ρ , at the organic/metal interface as a function of electric field in a model organic semiconductor, the molecularly doped polymer system. These studies suggest that charge injection is not completely described by the widely assumed diffusion-limited thermionic emission theories [70].
- A surprisingly large variation of the surface potential in molecularly doped polymer films under a number of chemical and physical conditions. This spatial variation is a source of long range energetic disorder, which is currently unaccounted for in charge transport and injection theories [77].

We show that imaging the local potential and capacitance in organic device structures and films using high-sensitivity electric force microscopy is a powerful

and general way to address the present lack of understanding of fundamental processes in organic electronic materials. The results of recent microscopic studies presented in this thesis and by others (Chapter 2), have been dramatic and surprising, calling into question widely-accepted theories of charge injection and bring attention to unexpected microscopic observations in some of the most widely-used organic electronic materials.

Chapter 1 references

- [1] M. Pope and C. E. Swenberg, *Electronic Processes in Organic Crystals, Monographs on the Physics and Chemistry of Materials*, Oxford University Press, New York, 1982.
- [2] P. Peumans, A. Yakimov, and S. R. Forrest, *Journal of Applied Physics* **93**, 3693 (2003).
- [3] P. Strohriegl and J. V. Grazulevicius, *Advanced Materials* **14**, 1439 (2002).
- [4] R. H. Friend *et al.*, *Nature* **397**, 121 (1999).
- [5] U. Mitschke and P. Bauerle, *Journal of Materials Chemistry* **10**, 1471 (2000).
- [6] D. T. McQuade, A. E. Pullen, and T. M. Swager, *Chemical Reviews* **100**, 2537 (2000).
- [7] J. Janata and M. Josowicz, *Nature Materials* **2**, 19 (2002).
- [8] H. Klauk and T. N. Jackson, *Solid State Technology* **43**, 63 (2000).
- [9] C. D. Dimitrakopoulos and D. J. Mascaro, *IBM Journal of Research and Development* **45**, 11 (2001).
- [10] R. W. I. de Boer, M. E. Gershenson, A. F. Morpurgo, and V. Podzorov, *Physica Status Solidi (A)* **201**, 1302 (2004).
- [11] L. A. Bumm *et al.*, *Science* **271**, 1705 (1996).
- [12] X. D. Cui *et al.*, *Science* **294**, 571 (2001).
- [13] J. Park *et al.*, *Thin Solid Films* **438-439**, 457 (2003).
- [14] R. D. McCullough *et al.*, *Synthetic Metals* **55**, 1198 (1993).
- [15] H. S. O. Chan and S. C. Ng, *Progress in Polymer Science* **23**, 1167 (1998).
- [16] A. Pron and P. Rannou, *Progress in Polymer Science* **27**, 135 (2002).
- [17] Y. Shen, A. Hosseini, M. H. Wong, and G. G. Malliaras, *ChemPhysChem* **5**, 16 (2004).
- [18] H. E. Katz and Z. Bao, *Journal of Physical Chemistry B* **104**, 671 (2000).
- [19] H. E. Katz, *Chemistry of Materials* **16**, 4748 (2004).
- [20] C. D. Dimitrakopoulos and P. R. L. Malenfant, *Advanced Materials* **14**, 99 (2002).

- [21] Y. Sun, Y. Liu, and D. Zhu, *Journal of Materials Chemistry* **15**, 53 (2004).
- [22] P. M. Borsenberger and D. S. Weiss, *Organic Photoreceptors for Xerography*, Marcel Dekker, Inc., New York, 1998.
- [23] D. Braun, *Journal of Polymer Science* **41**, 2622 (2003).
- [24] J. Campbell Scott, *Journal of Vacuum Science and Technology A* **21**, 521 (2003).
- [25] Y. Lin, D. I. Gundlach, S. F. Nelson, and T. N. Jackson, *IEEE Transactions on Electron Devices* **44**, 1325 (1997).
- [26] G. Horowitz, *Advanced Materials* **10**, 365 (1999).
- [27] F. Garnier and G. Horowitz, *Synthetic Metals* **18**, 693 (1987).
- [28] T. A. Skotheim, R. L. Elsenbaumer, and J. R. Renolds, editors, *Handbook of Conducting Polymers*, Marcel Dekker, Inc., New York, second edition, 1998.
- [29] S. V. Novikov and A. V. Vannikov, *Journal of Physical Chemistry* **99**, 14573 (1995).
- [30] Y. N. Gartstein and E. M. Conwell, *Chemical Physics Letters* **245**, 351 (1995).
- [31] D. H. Dunlap, P. E. Parris, and V. M. Kenkre, *Physical Review Letters* **77**, 542 (1996).
- [32] S. V. Novikov, D. H. Dunlap, V. M. Kenkre, P. E. Parris, and A. V. Vannikov, *Physical Review Letters* **81**, 4472 (1998).
- [33] P. E. Parris, D. H. Dunlap, and V. M. Kenkre, *Physica Status Solidi (B)* **218**, 47 (2000).
- [34] S. V. Novikov and A. V. Vannikov, *Mol. Cryst. Liquid Cryst.* **361**, 89 (2001).
- [35] R. E. Parris, V. M. Kenkre, and D. H. Dunlap, *Physical Review Letters* **87**, 126601 (2001).
- [36] H. Ishii, K. Sugiyama, E. Ito, and K. Seki, *Advanced Materials* **11**, 605 (1999).
- [37] D. Cahen and A. Kahn, *Advanced Materials* **15**, 271 (2003).
- [38] A. Kahn, N. Koch, and W. Y. Gao, *Journal of polymer science. Part B, Polymer physics* **41**, 2529 (2003).
- [39] M. Abkowitz, J. S. Facci, and J. Rehm, *Journal of Applied Physics* **83**, 2670 (1998).
- [40] B. H. Hamadani and D. Natelson, *Applied Physics Letters* **84**, 443 (2004).

- [41] R. J. Chesterfield *et al.*, Journal of Applied Physics **95**, 6396 (2004).
- [42] M. J. Loiacono, E. L. Granstrom, and C. D. Frisbie, Journal of Physical Chemistry B **102**, 1679 (1998).
- [43] C. Shafai, D. J. Thomson, M. Simard-Normandin, G. Mattiussi, and P. J. Scanlon, Applied Physics Letters **64**, 342 (1994).
- [44] B. Alperson, S. Cohen, I. Rubinstein, and G. Hodes, Physical Review B **52**, R17017 (1995).
- [45] H. Dai, E. W. Wong, and C. M. Lieber, Science **272**, 523 (1996).
- [46] T. W. Kelley, E. L. Granstrom, and C. D. Frisbie, Advanced Materials **11**, 261 (1999).
- [47] T. W. Kelley and C. D. Frisbie, Journal of Vacuum Science and Technology B (Microelectronics and Nanometer Structures) **18**, 632 (2000).
- [48] A. B. Chwang and C. D. Frisbie, Journal of Physical Chemistry B **104**, 12202 (2000).
- [49] E. Betzig, J. K. Trautman, T. D. Harris, J. S. Weiner, and R. L. Kostelak, Science **251**, 1468 (1991).
- [50] S. K. Buratto, Current Opinion in Solid State and Material Science **1**, 485 (1996).
- [51] P. F. Barbara, D. M. Adams, and D. B. O'Connor, Annual Review of Material Science **29**, 433 (1999).
- [52] D. A. Vanden Bout, J. Kerimo, D. A. Higgens, and P. F. Barbara, Accounts of Chemical Research **30**, 204 (1997).
- [53] J. A. DeAro, K. D. Weston, S. K. Buratto, and U. Lemmer, Chemical Physics Letters **277**, 532 (1997).
- [54] J. A. DeAro, D. Moses, and S. K. Buratto, Applied Physics Letters **75**, 3814 (1999).
- [55] G. M. Credo *et al.*, Journal of Chemical Physics **112**, 7864 (2000).
- [56] O. Semenikhin, L. Jiang, T. Iyoda, K. Hashimoto, and A. Fujishima, The Journal of Physical Chemistry **100**, 18603 (1996).
- [57] O. A. Semenikhin, L. Jiang, T. Iyoda, K. Hashimoto, and A. Fujishima, Eletrochemica ACTA **42**, 3321 (1997).
- [58] O. A. Semenikhin, L. Jiang, K. Hashimoto, and A. Fujishima, Synthetic Metals **110**, 115 (2000).

- [59] T. Hassenkam, D. R. Greve, and T. Bjornholm, Advanced Materials **13**, 631 (2001).
- [60] S. F. Alvarado, P. F. Seidler, D. G. Lidzey, and D. D. C. Bradley, Physical Review Letters **81**, 1082 (1998).
- [61] S. F. Alvarado *et al.*, Advanced Functional Materials **12**, 117 (2002).
- [62] Y. Martin, D. W. Abraham, and H. K. Wickramasinghe, Applied Physics Letters **52**, 1103 (1988).
- [63] M. Nonnenmacher, M. P. O'Boyle, and H. K. Wickramasinghe, Applied Physics Letters **58**, 2921 (1991).
- [64] L. Bürgi, T. Richards, M. Chiesa, R. H. Friend, and H. Sirringhaus, Synthetic Metals **146**, 297 (2004).
- [65] E. M. Muller and J. A. Marohn, Advanced Materials (in press) (2005).
- [66] J. A. Nichols, D. J. Gundlach, and T. N. Jackson, Applied Physics Letters **83**, 2366 (2003).
- [67] L. Bürgi, T. J. Richards, R. H. Friend, and H. Sirringhaus, Journal of Applied Physics **94**, 6129 (2003).
- [68] K. P. Puntambekar, P. V. Pesavento, and C. D. Frisbie, Applied Physics Letters **83**, 5539 (2003).
- [69] O. Tal, W. Gao, C. K. Chan, A. Kahn, and Y. Rosenwaks, Applied Physics Letters **85**, 4148 (2004).
- [70] W. R. Silveira and J. A. Marohn, Physical Review Letters **93**, 116104 (2004).
- [71] L. Bürgi, H. Sirringhaus, and R. H. Friend, Applied Physics Letters **80**, 2913 (2002).
- [72] C. Schönenberg and S. F. Alvarado, Physical Review Letters **65**, 3162 (1990).
- [73] T. D. Krauss and L. E. Brus, Physical Review Letters **83**, 4840 (1999).
- [74] T. D. Krauss, S. O'Brien, and L. E. Brus, Journal of Physical Chemistry B **105**, 1725 (2001).
- [75] R. Ludeke and E. Cartier, Applied Physics Letters **78**, 3998 (2001).
- [76] W. R. Silveira and J. A. Marohn, Review of Scientific Instruments **74**, 267 (2003).
- [77] W. R. Silveira and J. A. Marohn, *in preparation* (2005).

CHAPTER 2

SCANNED PROBE MICROSCOPY OF ORGANIC MATERIALS

This chapter gives a brief history of scanned probe microscopy, reviewing the development of experimental techniques and theoretical work which served as a foundation for increasing our knowledge of organic materials. The ability to measure forces microscopically enabled the imaging of electrostatic forces, known as electric force microscopy (EFM). Efforts to quantify the method and increase sensitivity to sub-electron detection dramatically increased the usefulness EFM, which has been used to correlate the morphology and electronic structure of thin organic films and disentangle charge injection from bulk charge transport in an organic device structure. We take particular notice of the results of recent microscopic studies that have sought to explain charge injection in some of the most widely-used organic electronic materials. Finally, we discuss other methods to probe the metal/organic interface, including bulk Kelvin probe and photoelectron spectroscopies.

2.1 Scanning tunneling and atomic force microscopies

The first scanning tunneling microscope (STM), based on quantum mechanical tunneling between a sharp tip and a conductive surface, was developed in the 1980s by a research team led by Gerd Binnig and Heinrich Rohrer of IBM's Zurich Research Laboratory. They were awarded the Nobel prize for Physics in 1986 for the invention of the STM [1–3]. The first STM demonstrated unprecedented spatial resolution and potential for visualizing surface science at the atomic scale. Shortly after, the atomic force microscope (AFM) was developed by the same group [4], marking the emergence of microscopic force measurements as a powerful

tool to advance surface science on both insulating and conducting materials. Little time was required to improve the new technique. Atomic resolution by AFM was achieved on graphite and other nonconducting surfaces [5].

The earliest AFM experiments involved making contact between a sharp, micromachined cantilever tip and a surface. Scanning either the sample or the tip while measuring the deflection of the cantilever generated a topographical image. This technique is known as contact mode AFM and while useful, it inevitably leads to surface and cantilever damage. Still used today at ambient pressure, a breakthrough noncontact imaging technique based on a vibrating cantilever was developed [6]. This mode of imaging involves vibrating a cantilever near its resonance frequency approximately 2-20 nm above the surface. As the force gradient experienced by the cantilever changes, the amplitude response is shifted, and this is the quantity used to keep the tip-surface separation constant via feedback control electronics.

2.2 Quantitative high-sensitivity electric force microscopy

Quantitative high-sensitive electric force microscopy includes scanned probe microscopy measurements that reduce interaction between the cantilever tip and sample plane into quantities that reflect changes in the dielectric constant, the potential and Coulombic interactions. There are several experimental schemes employed to achieve signal separation, depending on the nature of the sample and experimental conditions.

Initial studies demonstrated changes in the force due to a change in capacitance over an organic film of photoresist on silicon [7]. In addition, the authors observed the change in the force across a pn-junction, which marked the first microscopic

investigation of a working device by scanned probe microscopy [7]. A more elegant experiment was performed by modulating the applied voltage near the cantilever resonance frequency and nulling the electric field between the cantilever and the surface by varying the potential applied at zero frequency (DC) [8].

Surface charge was the first phenomenon studied on organic thin films lacking π -conjugation. Charging properties of insulating materials are of great interest for several industrial applications [9, 10]. The deposition of positive and negative charge on a 1 mm film of polymethylmethacrylate (PMMA) on a metal electrode was investigated by recording contours of constant force gradient [11]. Triboelectric charging, commonly known as static, was also investigated during the early days of EFM by electrostatic force gradient imaging [12]. The authors claim, rather dramatically, the mechanism of triboelectric charge transfer has remained a mystery since the times of the ancient Greeks!

Single charge recombination events were first observed on a film of Si_3N_4 [13]. Quantitative electric force microscopy also enabled the study of single charges in CdSe nanocrystals [14–16], modeling the interaction between the cantilever and the sample surface as a combination of capacitive and Coulombic forces [12]. High-sensitivity force gradient imaging uncovered individual defect sites in a thin layer (1.8 nm) of SiO_2 on silicon and at the SiO_2 -Si interface [17]. Single charge events were studied in a carbon nanotube by perturbing the system with the electric field from the sharp cantilever, known as scanning gate microscopy, at low temperatures. This difficult experiment demonstrated how a quantum system interacts with a mechanical oscillator [18].

2.3 Imaging variations of the surface potential:

Film morphology and electronic properties

The electronic properties of a π -conjugated organic film are highly dependent on morphology. For this reason, atomic force microscopy and electric force microscopy are an excellent approach to investigate the correlation between the topography and electronic structure of organic materials. Depending on the chemical nature of the system, the deposition technique, and the substrate, the film may be crystalline, amorphous, or anything in between. Pentacene is deposited by thermal evaporation in high vacuum, forming a highly crystalline film with a dendritic-like morphology. At the other end of the spectrum, molecularly doped polymers, which are spin-cast at ambient temperatures, are amorphous and have extremely flat surfaces. Between these two extremes are polymers such as polythiophene and polyaniline, which can be spin-cast or electrochemically deposited. They show ordered crystalline structure combined with a disordered amorphous phase [19].

The correlation of morphology with the surface potential of a doped π -conjugated organic film allows for the spatial determination of doping density. Semenikhin *et al.* [20] have found that thin films of polybithiophene are naturally doped more heavily within the bulk of a grain, whereas electrochemical doping of the same film results in a more heavily doped grain boundary. Further studies have shown that electrochemically undoping the polybithiophene film did not return the polymer to its original state [21]. A correlation between morphology and doping levels was uncovered for electrochemically deposited poly-3-methylthiophene by the same group [22].

In a similar investigation, electrochemically deposited polypyrrole was found

to have a larger dopant concentration at the grain boundaries, as inferred from the lower surface potential in these areas [23]. Polyaniline films, prepared by solution casting, were found to have a slightly smaller variation of the work function compared to polypyrrole [24]. The same study demonstrated the photovoltaic properties of polythiophene films.

2.4 Noncontact electric force microscopy of π -conjugated organic device structures

Scanned probe microscopy is extremely useful for determining the relationship between morphology and surface potential of thin π -conjugated organic films, discussed in Section 2.3. Measuring the potential in a device, a powerful extension of the work on thin films, is just beginning to illuminate mechanisms of charge transport and injection. The investigations into organic field-effect transistors by the group of R. H. Friend *et al.* [25, 26] are an excellent example of the utility of electric force microscopy to study organic electronics and are worth reviewing in some detail.

2.4.1 The field-effect transistor

First let us review the basic operation of the organic field-effect transistor (OFET), illustrated in Figure 2.1. The gate electrode and the organic layer are separated by a nonconductive oxide, forming a capacitor. The potential applied to the gate, V_g , modulates the charge density at the interface of the organic and the oxide. Most organic materials are p-type. Therefore, the application of a negative V_g leads to an accumulation of holes at the organic/oxide interface, which conduct

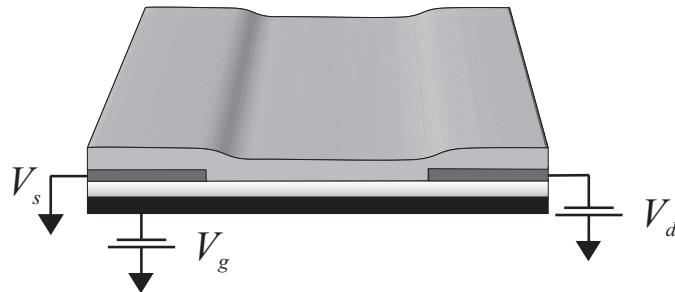


Figure 2.1: The field-effect transistor: The gate electrode (black), oxide layer (light grey), and organic film (grey) form a capacitor. Application of a potential V_g to the gate electrode results in the accumulation of charges at the organic/oxide interface that travel between the source and drain electrodes (dark grey).

between the source and drain electrodes.

2.4.2 Measuring the local potential in an organic device

In the first scanned probe study of a working organic field-effect transistor [25], Bürgi *et al.* demonstrate how the gate electrode potential, V_g , induces the formation of an accumulation region. The experiments are performed at temperatures ranging from 50–298 K. The polymeric material in this study is regioregular head-to-tail coupled poly(3-hexylthiophene) (P3HT), which is spin-cast on a bottom-contact transistor substrate. The most interesting result here is the detection of buried charge at an interface. The accumulation region is thought to form at the interface between the polymer and the insulator. In order to test the assertion that an interfacial charge density is being measured, the insulating oxide between the source and the drain electrodes was patterned with hexamethyldisilazane (HMDS), which is known to increase the mobility. Moving across the OFET channel from the hole-injecting electrode to the hole-extracting electrode, the potential drop is

noticeably steeper in the region where HMDS is not present, and the measured mobility is ~ 20 higher with the HMDS treatment. This evidence supports the claim that the measured potential is due to the accumulation layer.

Combining the current and the potential, $V(x)$, the authors calculate the local field-effect mobility. This is a major breakthrough because it allows for the separation of poor contacts from bulk transport. They use the following expression for the current at the drain electrode: $I_d = W en(x) \mu E(x)$, where $en(x)$ is the charge density induced at the interface, given by $C_i V'_g$. V'_g is difference between the potentials at the accumulation layer and the gate electrode, $V(x) - V_g$ and C_i is the capacitance of the accumulation layer and the gate electrode. Since they measure the potential, $V(x)$, they can compute the electric field, $E(x)$, and the potential between the accumulation layer and the gate, V'_g . Using the measured drain current, I_d , they can obtain the field-effect mobility, μ , spatially, to get $\mu(x)$. This is an exciting local measurement! They find the mobility has an activation energy of ~ 100 mV and see a small field enhancement of the mobility. They also present the gate bias dependence of the mobility, which increases with increasing V_g . At lower temperatures, the mobility is more dependent on the gate bias. Without measuring the drop in potential at the source and drain electrodes, this work shows that correctly calculating the field-effect mobility, μ , in an organic transistor is clearly not possible without major assumptions.

2.4.3 Testing microscopic theories of charge injection

This section summarizes the findings of the only critical microscopic examination of charge injection by EFM to date [26], besides our own [27], which is presented in Chapter 5. The reason for this detailed evaluation and comparison

stems from the general lack of interpretation of EFM studies. Notably missing from most experiments is an analysis that attempts to test charge injection theory.

A more thorough examination of charge injection followed the initial study [25] described in Section 2.4. The quantitative study discussed here [26] investigated bottom-contact transistors composed of poly(3-hexylthiophene) (P3HT) and poly-9,9' dioctyl-fluorine-co-bithiophene (F8T2) thin films.

The authors vary the work function of the electrodes, the ionization potential of the polymer, and temperature, which lowers the mobility and allows for the determination of activation energies of the contact resistance and mobility. The activation energy of the source contact was found to be \sim 60-140 mV, surprisingly smaller than the activation energy of the mobility and the expected Schottky barrier. The authors point out that most experimental investigations conclude the commonly assumed diffusion-limited thermionic emission is the “dominant” process for charge injection. Their primary conclusion is the diffusion-limited thermionic emission model, assumed to be the dominant charge injection mechanism, is inadequate.

For large injection barriers, the resistance of the injecting interface dominates the total resistance. Applying diffusion-limited thermionic emission theory leads to a total activation energy of $\Delta_R = \Delta_\mu + \phi_b - \Delta\phi$ [26], the sum of the activation energy of the mobility, the injection barrier, and the barrier lowering, respectively. However, this study finds that Δ_R is less than ϕ_b and Δ_μ . It is unlikely that the barrier lowering can account for this large difference, leading the authors to conclude that the diffusion-limited thermionic emission theory is not the dominant mechanism for charge-injection, and that thermally assisted tunneling and injection into the energetically disordered material is likely to contribute. They proceed to propose a simple model for charge injection and extraction that is consistent with

their results.

A simple charge injection model is proposed, where the resistance of the entire device is no longer given by $R_s + R_{ch} + R_d$, the sum of the resistance of the source metal/organic interface, the accumulation layer in the polymer channel, and the organic/drain metal interface. Rather, the resistance is $R_i + R_b + R_{ch} + R_b$, where R_i is the resistance at the source metal/organic interface R_b is a resistance from a depletion region near the interfaces of the source and drain. The resistance, R_b , from the depletion layer, is present at both electrodes, explaining the voltage drop observed at the extracting electrode. At low barrier heights, R_b dominates, but with large barriers, R_i dominates and leads to the observed asymmetry from larger voltage drop at the injecting electrode.

Similar investigations

Other groups have investigated π -conjugated organic devices made from interesting samples such as DNA [28] and pentacene [29, 30]. Nichols *et al.* have found that with pentacene field-effect transistors, the potential drops primarily at the injecting electrode for these small, vacuum deposited molecules [29]. Hassenkamp *et al.* were able to resolve potential drops between 100-200 nm polymer domains [31]. Trapped charge in an organic field-effect transistor has been followed as well, via the resulting shift in the surface potential [32, 33], illuminating the spatial distribution of charge traps at the subsurface accumulation layer.

The devices discussed so far have been bottom contact structures where the organic film is deposited on top of the metal electrodes. However, it is also possible to evaporate the electrode directly onto the organic. Puntambekar *et al.* [30] have used surface potential profiling to study the difference between top and bottom

contact pentacene field-effect transistors.

One disadvantage to scanned probe microscopy of organic structures is the limitation of the planar device geometry. It is likely that several technologically useful organic devices will be made from a parallel plate geometry. Planar electrodes, with the electric field between the sharp edges of the metal can lead to different behavior from parallel plate electrodes, in which the electric field is uniform. The electric field is expected to increase at the edge of the planar electrode [34, 35]. However, recent experiments have attempted to minimize this drawback. Tal *et al.* developed a sandwich structure based on evaporating the first electrode on a doped gallium arsenide crystal, followed by the organic layer and the second electrode [36]. In a nitrogen environment, the sandwich structure is cleaved and the newly exposed face is studied by electric force microscopy. They observed the interface dipole between gold and an organic film of Alq₃, tris(8-hydroxy-quinoline) aluminum. They also modeled, by finite element analysis, the expected potential profile from a 1 V step in potential and found such a change, which one might find at an electrode, is broadened by up to 300 nm.

2.5 Related characterization techniques

In this section, we discuss conducting probe atomic force microscopy, scanning tunneling microscopy, and Kelvin probe/photocurrent spectroscopy of organic materials.

2.5.1 Conducting probe atomic force microscopy

Conducting probe atomic force microscopy (CP-AFM) is a technique used heavily by the research group of C. D. Frisbie to investigate π -conjugated organic ma-

terials [37]. CP-AFM involves contacting a thin organic film with a metal-coated AFM cantilever tip and applying a controlled, constant force while measuring the current-voltage characteristics between the cantilever, the film, and another electrode on the sample. It is possible to image the device by conventional AFM techniques and choose interesting morphological structures to investigate one point at time.

Kelley *et al.* have measured the resistance from a single grain boundary in sexithiophene films, demonstrated how the grain boundary is a considerable bottleneck for charge conduction in π -conjugated organic films [37,38]. Sexithiophene is an oligomer containing 6 thiophene rings. The molecule is oriented perpendicular to the substrate, so it is possible to measure the resistance of just one or two monolayers. Inducing charge in the organic layer with a gate electrode, the resistance of a single grain boundary was found to have a gate bias dependence and the activation energy of the grain was estimated to be 100 mV [39]. Using CP-AFM to study a transistor made from sexithiophene with a source-drain gap length of only 400 nm, Seshadri *et al.* were able to measure the potential at discrete points, showing a large contact resistance between charge injecting electrode (gold) and the oligimer [40].

Although very useful information has been obtained from CP-AFM, especially concerning the resistance at a grain boundary, the technique is very time consuming and it is problematic to map resistance over large areas and structures with complicated morphology. It is also unclear if damage is done to the sample surface and the cantilever during the measurement. However, the Frisbie group has been careful to monitor changes via topographical imaging.

2.5.2 Scanning tunneling microscopy of organic polymers

Electric force microscopy at room temperatures and ambient pressure is a very common scanned probe technique for characterization of the electronic properties of π -conjugated organic materials. Although more rare, in part because it is experimentally more difficult, scanning tunneling microscopy (STM) is advantageous for the accurate measurement of small currents and high spatial resolution. The technique is limited to soft, thin organic films and is rather destructive considering it can involve penetrating the organic layer with the tip.

The injection barriers and exciton binding energies of various conjugated polymers have been studied by Alvarado *et al.* using STM [41]. By modifying the custom STM to include optical collection, they have monitored the radiative decay of an exciton created by the tip [42]. Finally, the distance-voltage relationship has been related to the potential distribution in the tip/organic/substrate device [43].

2.5.3 Kelvin probe and photoelectron spectroscopies

The energy level alignment between the orbitals of a π -conjugated organic molecule and those of a metal determine how efficiently charge can be injected by setting the height of energetic barriers for hole or electron injection. Energy level alignment at the organic/metal interface has been studied in great detail using the macroscopic Kelvin probe method (KPM) [44]. Although this method is limited to molecular films and cannot probe the electrical properties of polymers, it allows for the determination of interfacial energetics of a very ideal, “clean” system. This approach is a great way to unravel the complicated nature of the interface and is usually corroborated by ultraviolet photoelectron spectroscopy (UPS) studies [45], which allows one to determine shifts in the vacuum level defined just outside of

the material. The UPS experiment is similar to the KPM work in that a clean material is deposited as the interface is monitored. These powerful techniques have uncovered the presence of an interface dipole, appearing as a shift in the work function and vacuum level, at most molecular organic/metal interfaces.

An interface dipole has been observed for films of N,N'-diphenyl-N-N'-bis(3-methylphenyl)-(1,1'-biphenyl)-4,4'-diamine, or simply TPD, which is the organic molecule of interest in this thesis. The magnitude of the interface dipole is -1.15 eV on a clean gold surface [46]. The interface dipole is smaller for metals with a lower work function. Band bending was not observed at the TPD/Au interface, leading the authors to question whether the Fermi levels of the TPD and metal film equilibrate at such high purity, which causes a very limited number of free carriers available at the interface. Possible physical origins of the interface dipole include charge transfer, an image force between the molecular orbital and image charge generated in the metal, modification of the inherent dipole at the bare metal, and orientation of the molecular dipole at the metal surface [47].

The study of organic/metal interfaces using UPS and X-ray photoemission spectroscopy (XPS) has been reviewed by Knupfer and Peisert [48]. Their work used XPS to discover that with TPD films on indium-tin oxide, the cationic form of TPD, TPD^+ , is present at quite high concentrations within the first monolayer. In another review of UPS, XPS, and Kelvin probe studies of the organic/metal interface, the investigations of Kahn *et al.* also support the formation of an interface dipole between nearly all molecular organic films and metals they have investigated [49].

It is clear from the studies discussed up to this point that molecular films of TPD form an interface dipole with a variety of substrates under clean conditions.

The interface dipole is of critical importance because it increases the barrier for hole injection to well over 1 eV under these conditions. Decreased barrier heights have been achieved by doping, which brings the Fermi level down in hole transport (p-type) materials, facilitating charge transfer at the interface and causing strong band bending [50]. The interface dipole remains, but its effect is significantly diminished due to the new energetic alignment at the interface and increased tunneling rates through the thin depletion region. Polymer electrodes have also been shown to have a much smaller injection barrier. Koch *et al.* [51] propose that the interface dipole arises from modification of the surface dipole already present on the bare metal as electrons tail into space.

The investigations of interface energetics by UPS, XPS, and bulk KPM have significantly increased our understanding of the organic/metal interface. Although these tools are used to investigate ideal samples, the interface dipole and band bending are most likely serious issues in real devices made under much less favorable conditions. Of course, these ‘real’ devices have even more problems to take into account, but the studies described here have given the field an important piece of the puzzle.

2.6 Summary and conclusions

In this chapter we discussed the emergence of scanned probe microscopy, namely STM and AFM. The noncontact imaging approach opened the door for more exotic microscopies such as magnetic and electric force microscopy. Quantitative EFM enabled several analytical investigations of surface charge, down to single electron detection in a number of unique experiments. EFM has also proved very useful for comparing film morphology and the surface potential to help under-

stand the electronic structure and how it is related to various methods of sample preparation. Most importantly, we discussed the use of EFM to investigate the operation of organic device structures, which enables the microscopic disentanglement of charge injection and bulk transport phenomena. Finally, we summarized the important contributions of other microscopic techniques, including CP-AFM, STM, and Kelvin probe and photoelectron spectroscopies. From the work presented in this chapter, it is clear that most π -conjugated organic materials are heterogeneous at sub-micron length scales and that EFM is a powerful technique for studying charge in organic materials and device structures to better understand charge injection and transport.

Noticeably lacking from the experiments discussed here is the investigation of a π -conjugated organic system from which far reaching implications can be obtained. The sheer number of organic materials precludes us from studying every possible material. The approach taken in the experiments presented in this work essentially seeks to find what we can learn about charge injection and transport from a new view of one of the most well understood organic systems to date.

Chapter 2 references

- [1] G. Binnig, H. Rohrer, C. Gerber, and E. Weibel, Physical Review Letters **49**, 57 (1982).
- [2] G. Binnig and H. Rohrer, Scientific American **253**, 40 (1985).
- [3] G. Binnig and H. Rohrer, IBM Journal of Research and Development **30**, 355 (1986).
- [4] G. Binnig, C. F. Quate, and C. Gerber, Physical Review Letters **56**, 930 (1986).
- [5] T. R. Albrecht and C. F. Quate, Journal of Applied Physics **7**, 2599 (1987).
- [6] Y. Martin, C. C. Williams, and H. K. Wickramasinghe, Journal of Applied Physics **61**, 4723 (1987).
- [7] Y. Martin, D. W. Abraham, and H. K. Wickramasinghe, Applied Physics Letters **52**, 1103 (1988).
- [8] M. Nonnenmacher, M. P. O'Boyle, and H. K. Wickramasinghe, Applied Physics Letters **58**, 2921 (1991).
- [9] J. F. Hughes, *Electrostatic Particle Charging*, Research Studies Press Ltd., 1997.
- [10] N. Jonassen, *Electrostatics*, Kluwer Academic Publishers, Massachusetts, 2002.
- [11] J. E. Stern, B. D. Terris, H. J. Mamin, and D. Rugar, Applied Physics Letters **53**, 2717 (1988).
- [12] B. D. Terris, J. E. Stern, D. Rugar, and H. J. Mamin, Physical Review Letters **63**, 2669 (1989).
- [13] C. Schönenberger and S. F. Alvarado, Physical Review Letters **65**, 3162 (1990).
- [14] T. D. Krauss and L. E. Brus, Physical Review Letters **83**, 4840 (1999).
- [15] T. D. Krauss, S. O'Brien, and L. E. Brus, Journal of Physical Chemistry B **105**, 1725 (2001).
- [16] O. Cherniavskaya, L. Chen, V. Weng, L. Yuditsky, and L. E. Brus, Journal of Physical Chemistry B **107**, 1525 (2003).
- [17] R. Ludeke and E. Cartier, Applied Physics Letters **78**, 3998 (2001).
- [18] M. T. Woodside and P. L. McEuen, Science **296**, 1098 (2002).

- [19] H. Sirringhaus *et al.*, *Nature* **401**, 685 (1999).
- [20] O. A. Semenikhin, L. Jiang, T. Iyoda, K. Hashimoto, and A. Fujishima, *The Journal of Physical Chemistry* **100**, 18603 (1996).
- [21] O. A. Semenikhin, L. Jiang, T. Iyoda, K. Hashimoto, and A. Fujishima, *Electrochimica Acta* **42**, 3321 (1997).
- [22] O. A. Semenikhin, L. Jiang, K. Hashimoto, and A. Fujishima, *Synthetic Metals* **110**, 115 (2000).
- [23] J. N. Barisci, R. Stella, G. M. Spinks, and G. G. Wallace, *Electrochimica Acta* **46**, 519 (2000).
- [24] J. N. Barisci, R. Stella, G. M. Spinks, and G. G. Wallace, *Synthetic Metals* **124**, 407 (2001).
- [25] L. Bürgi, H. Sirringhaus, and R. H. Friend, *Applied Physics Letters* **80**, 2913 (2002).
- [26] L. Bürgi, T. J. Richards, R. H. Friend, and H. Sirringhaus, *Journal of Applied Physics* **94**, 6129 (2003).
- [27] W. R. Silveira and J. A. Marohn, *Physical Review Letters* **93**, 116104 (2004).
- [28] C. H. Lei, A. Das, M. Elliott, and J. E. Macdonald, *Applied Physics Letters* **83**, 482 (2003).
- [29] J. A. Nichols, D. J. Gundlach, and T. N. Jackson, *Applied Physics Letters* **83**, 2366 (2003).
- [30] K. P. Puntambekar, P. V. Pesavento, and C. D. Frisbie, *Applied Physics Letters* **83**, 5539 (2003).
- [31] T. Hassenkam, D. R. Greve, and T. Bjornholm, *Advanced Materials* **13**, 631 (2001).
- [32] L. Bürgi, T. Richards, M. Chiesa, R. H. Friend, and H. Sirringhaus, *Synthetic Metals* **146**, 297 (2004).
- [33] E. M. Muller and J. A. Marohn, *Advanced Materials* **17**, 1410 (2005).
- [34] K. J. Donovan, N. E. Fisher, and E. G. Wilson, *Synthetic Metals* **28**, D557 (1989).
- [35] N. E. Fisher, *Journal of Physics - Condensed Matter* **6**, 2047 (1994).
- [36] O. Tal, W. Gao, C. K. Chan, A. Kahn, and Y. Rosenwaks, *Applied Physics Letters* **85**, 4148 (2004).

- [37] T. W. Kelley, E. L. Granstrom, and C. D. Frisbie, *Advanced Materials* **11**, 261 (1999).
- [38] T. W. Kelley and C. D. Frisbie, *Journal of Vacuum Science and Technology B (Microelectronics and Nanometer Structures)* **18**, 632 (2000).
- [39] T. W. Kelley and C. D. Frisbie, *Journal of Physical Chemistry B* **105**, 4538 (2001).
- [40] K. Seshadri and C. D. Frisbie, *Applied Physics Letters* **78**, 993 (2001).
- [41] S. F. Alvarado, P. F. Seidler, D. G. Lidzey, and D. D. C. Bradley, *Physical Review Letters* **81**, 1082 (1998).
- [42] S. F. Alvarado, L. Rossi, P. Müller, P. F. Seidler, and W. Riess, *IBM Journal of Research and Development* **45**, 89 (2001).
- [43] M. Kemerink *et al.*, *Physical Review Letters* **88**, 096803 (2002).
- [44] H. Ishii *et al.*, *Physica Status Solidi* **201**, 1075 (2004).
- [45] H. Ishii, K. Sugiyama, E. Ito, and K. Seki, *Advanced Materials* **11**, 605 (1999).
- [46] N. Hayashi, E. Ito, H. Ishii, Y. Ouchi, and K. Seki, *Synthetic Metals* **121**, 1717 (2001).
- [47] K. Seki *et al.*, *Synthetic Metals* **119**, 19 (2001).
- [48] M. Knupfer and H. Peisert, *Physica Status Solidi* **201**, 1055 (2004).
- [49] A. Kahn, N. Koch, and W. Gao, *Journal of Polymer Science: Part B: Polymer Physics* **41**, 2529 (2003).
- [50] W. Gao and A. Kahn, *Journal of Applied Physics* **94**, 359 (2003).
- [51] N. Koch *et al.*, *Applied Physics Letters* **82**, 70 (2003).

CHAPTER 3

HIGH-SENSITIVITY ELECTRIC FORCE MICROSCOPY

This chapter describes the variable temperature high-sensitivity electric force microscope, shown in Figure 3.1, developed to investigate charge injection in organic materials at variable temperatures. The goal of creating a versatile scanned probe microscope that operates from 4.2–340 K in high vacuum with large scan range at cryogenic temperatures and *in situ* coarse sample positioning was realized. By building our own microscope we gained the following unique combination of abilities:

- Operating over a large temperature range, from 4.2–340 K. This is crucial because essentially all fundamental processes – charge injection, transport, and trapping – are thermally activated in organic electronic materials.
- Operating in high vacuum. This eliminates degradation concerns associated with our materials reacting with oxygen and water, and increases cantilever sensitivity by 10-20 fold by reducing viscous damping due to air.
- Using a fiber-optic interferometer. This allows us to quantitatively measure cantilever oscillations as small as 10×10^{-3} Å (in a 1 Hertz measurement bandwidth) which in turn lets us monitor cantilever frequency shifts as small as 5 parts in 10^7 .
- A large-range piezoelectric scanner. This enables imaging of entire working organic devices, even at low temperature. A scan range of 5 μm is obtained at 4.2 K. A coarse positioning mechanism allows locating device structures on a large substrate *in situ*.

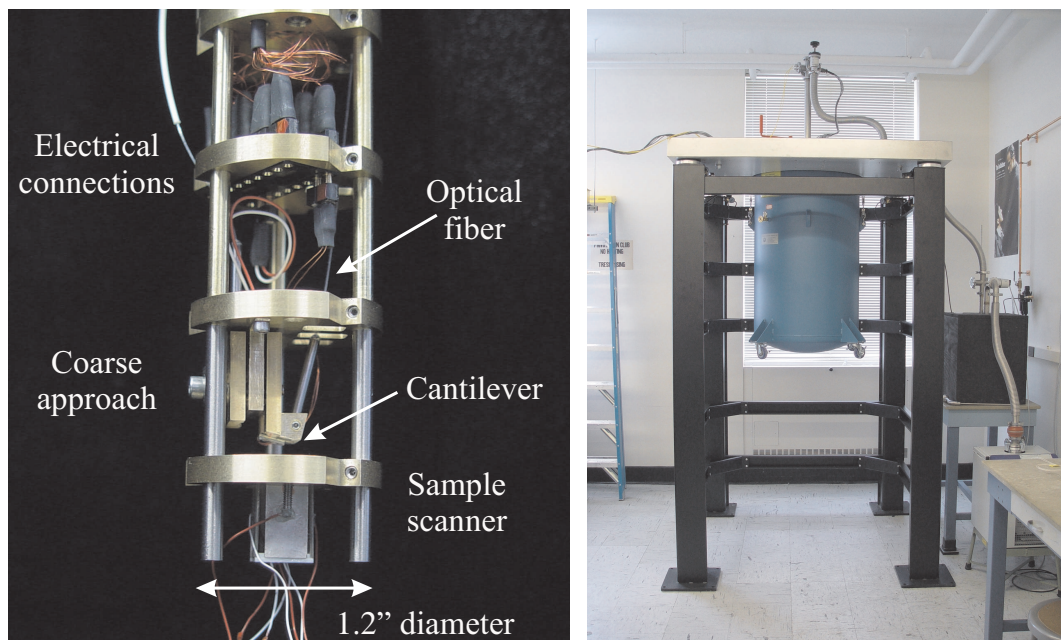


Figure 3.1: High-sensitivity electric force microscope. This custom built microscope (left) fits inside a long vacuum chamber inside of a dewar, all of which rests on a large vibration isolation platform (right).

- A novel mechanism for bringing a cantilever into close proximity with a surface in nanometer-sized controllable steps, very reliably, at temperatures ranging from 4.2 K to 340 K [1].

We now discuss development of the main components and operating modes of the microscope.

3.1 Detection of the force sensor

Detecting motion of the force sensor is a critical component of high-sensitivity electric force microscopy. Our requirements also include overall simplicity and compact design, an easily quantifiable output signal, and compatibility with cryogenic temperatures and high vacuum.

3.1.1 Overview of detection methods

The first low-temperature atomic force microscope resolved atomic scale surface features of 2H-MoS₂ at room temperature and immersed in liquid helium at 4.2 K in contact mode [2]. Amazingly, this instrument used a tunneling tip to detect cantilever motion. Alignment with tunneling detection can be a severe problem at low temperatures, as the tunneling tip must be located within a nanometer of the cantilever. However, this method contributes a very small amount of energy into the system, which is an advantage when working at cryogenic temperatures.

Piezoresistive cantilevers, which do not suffer from misalignment issues, have been implemented in several instruments [3–9]. The disadvantages of piezo-based cantilevers include a limited range of force constants and resonance frequencies [10]. Energy dissipation can also be quite high [5]. A related design uses piezoresistive

tuning forks for tip-sample control [11].

At room temperature, laser beam deflection is quite common, especially in commercial instruments. Few groups have made use of this detection system at low temperatures [12,13]. Cooling of the deflection system causes severe misalignment, and therefore only the sample is cooled to minimize misalignment. This creates a thermal gradient in the microscope, and temperatures below 100 K have not been achieved.

Albrecht *et al.* designed the first atomic force microscope using a fiber-optic interferometer detection system [14]. Alignment of the optical fiber with the cantilever is much more forgiving than the tunneling sensor. Also, it does not require electronics inside the cryogenic microscope head and achieves very high-sensitivity. The laser reflects off the cantilever and does not affect the sample below, which can be a problem with beam deflection detection. Many groups have successfully implemented the fiber-optic interferometer into their low temperature scanned probe microscopes [10,15–25]. Sensitivity at the thermodynamic limit is the fundamental noise set by the thermal motion of cantilever at a given temperature. At the time we designed our microscope, only three groups reported sensitivity at the thermodynamic limit [10, 24, 26–29]. Atomic resolution in non-contact mode at low temperatures is equally rare [23, 30–32].

Our microscope employs a fiber-optic interferometer [33–35]. By using radio frequency current injection [36] to eliminate mode-hopping instabilities in the interferometer’s diode laser, the interferometer’s noise floor (minimum detectable displacement) can be as good as $\sim 10 \text{ m}\text{\AA}/\sqrt{\text{Hz}}$ at a typical fiber-separation of 50–100 μm . The basic operation of the interferometer is described in Section 3.1.2. A detailed description of the 1310 nm interferometer used in the Marohn laboratory

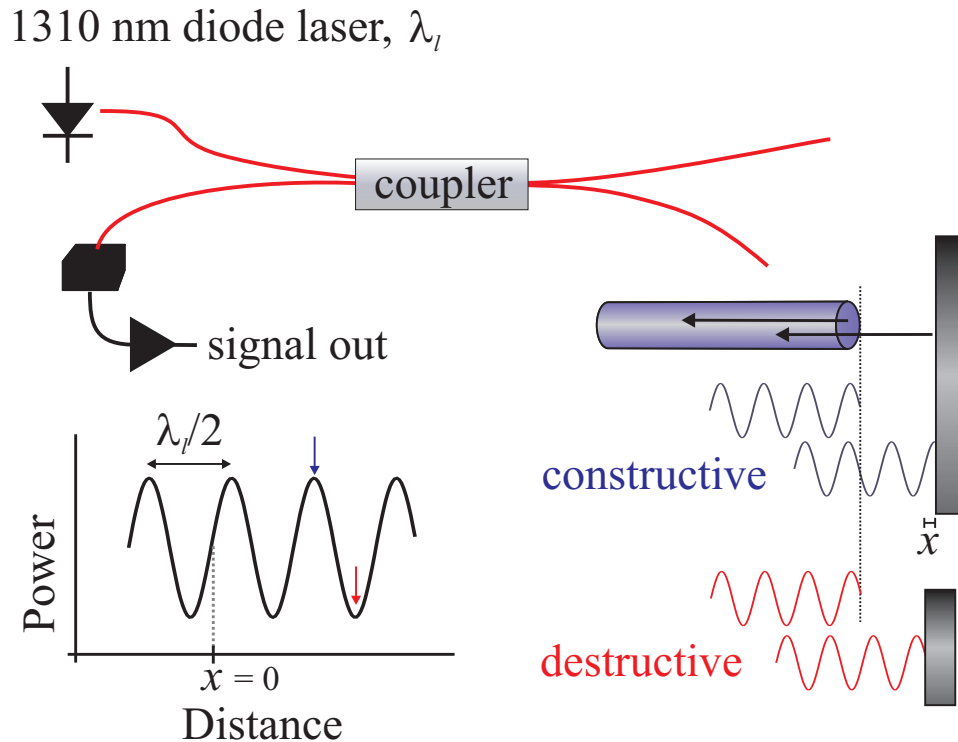


Figure 3.2: Fiber-optic interferometer for detection of cantilever motion.

is given in the Ph.D. thesis of E. M. Muller [37].

3.1.2 The fiber-optic interferometer

The fiber-optic interferometer is an extremely convenient detection method. It eliminates the need for complicated electronics near the cantilever and is compatible with operation in high vacuum [38] and cryogenic temperatures. Most importantly, the interferometer allows for quantitative force microscopy. The basic principle of the fiber-optic interferometer is illustrated in Figure 3.2. A laser diode passes light into a flexible optical fiber. Next, the light passes through a fiber-optic coupler. The coupler allows a fraction of the light into the adjacent optical fiber and we will now focus only on the outcome of the light in the adjacent fiber. The light travels to the cleaved end of the optical fiber, where $\sim 4\%$ of the

initial power is reflected from the surface of the cleaved edge and remains in the optical fiber, but travels in the opposite direction. $\sim 96\%$ of the power exits the fiber and is reflected off the object of interest, which may be a cantilever or a polished surface. This light re-enters the fiber and interferes with the fraction of light initially reflected at the cleaved end of the optical fiber, eventually reaching the photodiode where it is transduced into a voltage. An interference pattern is created by moving the object in front of an optical fiber.

Depending on the path length between the edge of the optical fiber and the object, constructive or destructive interference will be observed. Constructive and destructive interference, caused by the in-phase and out-of-phase combination of the light reflected from the cleaved edge of the fiber and the light reflected off the object, is shown on the right of Figure 3.2. The change in path length, Δl , for a given change in distance, x , is $\Delta l = 2x$. If the object is moved by a distance of $\lambda_l/2$, where λ_l is the wavelength of the laser, the total change in the path length will be $\Delta l = \lambda_l$ and we will have passed through one period of the interference pattern. Therefore, one cycle of the interference pattern is equivalent to a displacement of $\lambda_l/2$. Counting interference fringes is an extremely useful method for characterizing the motion of various scanning stages. However, for detecting small displacements of a cantilever, we need to calibrate the output signal.

For a given displacement, the most sensitive change in output signal is midway between a peak and valley on the roughly sinusoidal interference pattern. We have labeled this point $x = 0$ on the interference pattern in Figure 3.2. As the distance between the fiber and the object increases, the total power decreases. Therefore, the interference pattern is not a pure sinusoid, but there is an envelope to the signal. However, let us approximate it as a sinusoid, such that the output voltage

is given by

$$V(x) = V_0 + A \sin \frac{2\pi x}{\lambda_l/2}, \quad (3.1)$$

where A is the amplitude of the sinusoid. Expanding Equation 3.1 about $x = 0$ gives the slope, S , of the interference pattern,

$$S = A \frac{2\pi}{\lambda_l/2} = \frac{A4\pi}{\lambda_l} = \frac{V_{\text{pk-pk}} 2\pi}{\lambda_l}, \quad (3.2)$$

using the fact that the peak-to-peak output voltage of the interference pattern, which we measure in the laboratory, is simply twice the amplitude, $V_{\text{pk-pk}} = 2A$. Note the units of S are [V]/[nm]. This enables us to quantify small displacements about the $x = 0$ point on an interference pattern.

In order to measure displacements at $x = 0$, we can adjust the distance between the optical fiber and the object. This requires a positioning mechanism of some sort. Fortunately, by varying the temperature of the laser, we can change the wavelength by a small amount. The variation of λ_l causes a phase shift between the reflected light at the end of the optical fiber and the light reflected off the object. Using this technique, often referred to as ‘temperature tuning’ [35], we have another way to generate an interference pattern and thus tune to the most sensitive slope of the output signal. Figure 3.3 shows the generation of an interference pattern from changing the fiber-object distance (left) and by varying the temperature of the laser (right). A simple digital feedback loop, with an update rate of 1 Hz, is used to adjust the temperature of the laser in order to remain at the most sensitive slope, defined here as $x = 0$, of the interference pattern. Note that this is also a convenient method to obtain $V_{\text{pk-pk}}$, for calibration purposes. Another way to obtain $V_{\text{pk-pk}}$ is to drive the cantilever at an amplitude large enough to reach constructive and destructive points on the interference pattern and observe the maximum and minimum output signal on the oscilloscope.

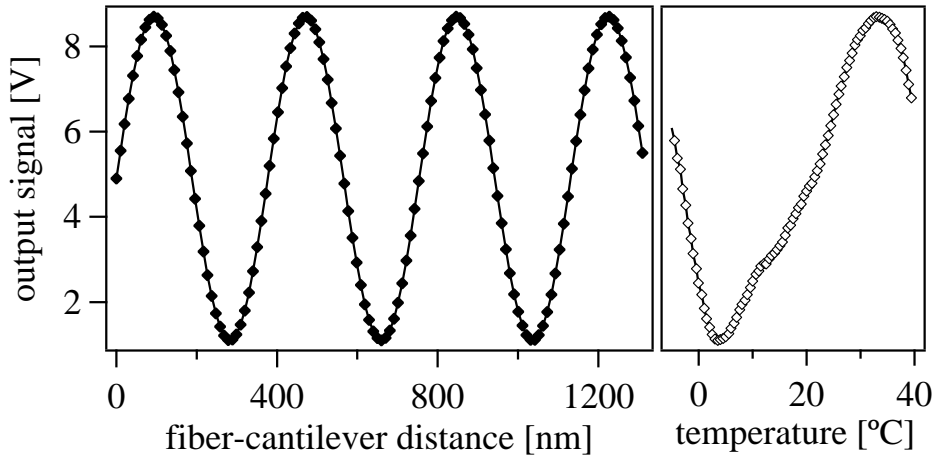


Figure 3.3: Temperature tuning of the fiber-optic interferometer. $\lambda_l = 780$ nm.

3.2 A variable temperature coarse positioning mechanism

Variable temperature scanned probe microscopy requires a reliable, compact, yet functional coarse positioning mechanism for bringing the cantilever and the sample surface to close proximity, usually 10 to 50 nm. Often, this is the most difficult engineering aspect of the microscope. A successful design must be able to travel over a few millimeters and take steps less than the fine positioning range, which is typically a few hundred nanometers. This is critical in order to avoid destructive, experiment-ending cantilever probe crashes into the surface. Our requirements for the mechanism to operate reliably in a wide temperature range (4.2–340 K) and high magnetic fields (up to 9 T) only complicates things further. Despite a large number of published designs, we have developed our own inertial coarse positioning mechanism to create a highly modular scanned probe microscope, which we have shown to be well suited for high-sensitivity electric force microscopy (EFM) and easily modified for more exotic forms of microscopy,

including dissipation force microscopy and magnetic resonance force microscopy (MRFM).

The most common positioning mechanism used in scanning tunneling microscopy (STM) is based on the design by Besocke [39]. While this extremely stable mechanism, which combines the tip-sample positioning, tip scanning and sample positioning, is very successful due to its rigid, thermally compensated design, our requirements for a large scan range, up to 5 μm at 4.2 K, would require an unreasonably large peizo tube.

Pan developed a mechanism called the ‘piezoelectric motor’ [40], which has also become very popular in variable temperature scanning microscopy experiments. This mechanism uses 6 shear piezos to translate a sapphire prism forward and backward. A similar mechanism based on a piezotube with the electrode arrangement allowing the tube to move in 6 different directions and crawl through a cavity, has also been developed [41]. Although these designs have achieved excellent results, they are bulky, very complicated, and quite unreliable at times.

Pohl was the first to apply the principle of inertial sliding to a horizontally operating sub-micron positioning mechanism [42]. We chose to pursue this type of mechanism because inertial coarse positioning mechanisms do not require mechanical attachments outside the instrument, which is a great advantage for work done in high vacuum, and can be quite compact, resulting in a microscope with high resonance frequencies and is therefore much less susceptible to room vibrations. Translation mechanisms based on inertial sliding were later developed by Niedermann *et al.* [43] and Lyding *et al.* [44]. Their mechanisms were able to operate at inclines up to 7° and 10°, respectively. A vertically operational coarse positioning mechanism based on parallel sapphire rods was developed by Renner *et al.* [45]

and similar designs followed [46–49].

Building a variable temperature electric force microscope has led us to design a versatile inertial coarse positioning mechanism that controls fine positioning of the cantilever height with the same piezoelectric stack that drives the coarse steps. Our design is most similar to that of Renner *et al.*, yet does not require the complication of parallel sapphire rails. It is reliable, mechanically simple and easy to control. The inertial positioning mechanism operates horizontally and vertically in high vacuum from 4.2 to 340 K. This compact, rigid design is both nonmagnetic and glueless, which is beneficial for work in strong magnetic fields while holding up under the demanding stresses of temperature cycling, respectively. We have successfully incorporated this positioning mechanism into a variable temperature atomic force microscope (AFM) [1] and a magnetic resonance force microscope (MRFM) [50, 51]. We now describe prototype translation mechanisms which led to the final design presented in Section 3.2.2.

3.2.1 Engineering the coarse positioning mechanism

The first coarse positioning mechanism was designed to operate horizontally and served an important purpose in what was our very empty laboratory for proof-of-concept testing with piezoelectric materials, experience with inertial positioning, and precision machining of small, intricate parts made of brass, aluminum, and stainless steel. A diagram and photograph of the horizontal model is shown in Figure 3.4. Here, the light outer body is 0.200" in height, machined from standard aluminum stock and rides on three sapphire spheres with a diameter of 1/16" (Small Parts, Inc.), two of which are situated in a brass V-shaped track machined into the surface underlying the mechanism that aids in the alignment of the ap-

proach. The mechanism is very compact – just 0.600” by 0.550” and easily fits into a 1” space, the probe diameter available in our first microscope. The aluminum body weighs 1.29 g and is connected to a heavier brass mass of 3.48 g through a piezoelectric stack (Thorlabs, Inc., part number AE0203D04). The sapphire spheres are glued to small 0.020” depressions machined into the aluminum piece with a pilot drill. The stack is glued with Krazy Glue on both ends. In general, we found that cyanoacrylate glues such as Krazy Glue hold piezoelectric materials to metal surfaces quite well at room temperatures. It also holds the sapphire spheres to metal surfaces reliably.

Although the track helps, it is not absolutely necessary for operation. We initially placed the translation mechanism in a track defined by two glass slides spaced approximately 0.05” apart. We also discovered that with the brass V-shaped groove, the depth of the groove must be shallow enough so that the sapphire spheres ride in on the edges of the groove. Riding on the face of the groove leads to a large frictional force. Unfortunately, the wires on the stack provided by the manufacturer are quite bulky and can cause erratic behavior by exerting large forces on the mechanism, causing unwanted lateral motion. Small, lightweight 36-gauge copper wire was found to significantly decrease this effect.

All characterization of the translation mechanism in Figure 3.4 was done by eye or with the aid of a microscope. An asymmetric analog sawtooth waveform with a frequency 3 kHz and a 5-10 V amplitude created from a Wavetek waveform generator was found to easily drive the inertial positioning mechanism at room temperature. The steep part of this sawtooth waveform falls off in approximately 20 μ s. During the slow ramp, the sapphire spheres remain in place. The fast ramp causes the spheres to slip as they are pushed against the inertia of the

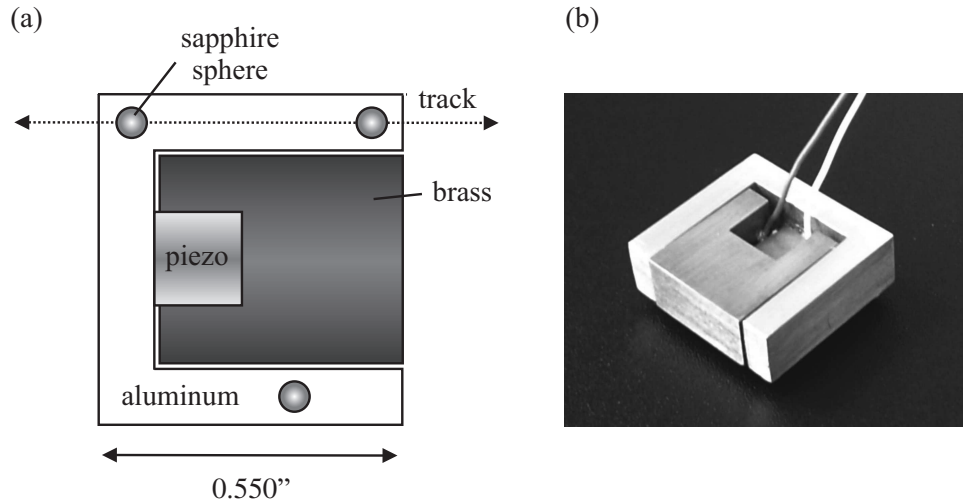


Figure 3.4: The first horizontally operational inertial coarse positioning mechanism in the Marohn laboratory. (a) The underside of the positioning mechanism with the aluminum body, sapphire spheres, piezo, and brass counterweight. (b) Photograph of the coarse positioning mechanism.

heavier brass part, resulting in net displacement over the cycle of one sawtooth waveform. The direction of the translation mechanism can be changed by reversing the symmetry of the asymmetric sawtooth waveform. The mechanism was able to carry up to 7.5 g placed on the brass center part and still travel very efficiently. Continuously pulsing the piezoelectric stack yielded a maximum speed of 0.3 mm/s with a 3 kHz, 10 V amplitude sawtooth waveform. The step size was 300 nm per waveform, estimated by sending a finite number of pulses (3000) and measuring the distance traveled. This suggests a maximum speed of 0.9 mm/s, greater than the observed rate. The dynamics created by a continuous train of sawtooth waveforms may cause a loss of efficiency in each step if some recovery is required by either the piezoelectric material or the inertial positioning mechanism itself. The piezo is known to heat significantly with an AC drive (see Thorlabs Document 0846-S01 Rev C 10/30/98) and this most likely decreases the ability of the piezo to

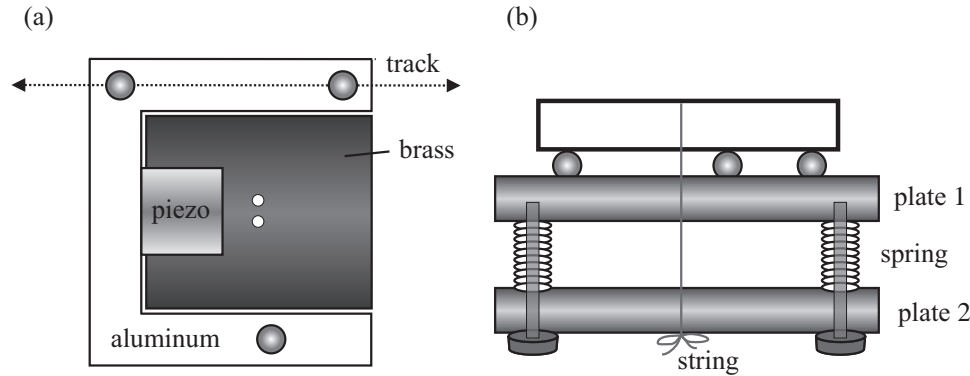


Figure 3.5: Springing down the first generation inertial positioning mechanism. (a) The top view of the spring fastened mechanism. (b) The side view and the arrangement of springs and plates.

expand for a given electric field. Excessive heating can also lead to de-poling of the piezoelectric material, which decreases the ability of the material to expand in an electric field.

Although the mechanism depicted in Figure 3.4 worked very well horizontally, our requirements for a vertically operating approach mechanism led us to spring down this model in a similar fashion to Smith *et al.* [52] shown in Figure 3.5. Two holes are drilled through the heavier brass mass as shown in Figure 3.5(a). A fine string (nonwaxed dental floss works very well, and mint flavored floss makes the probe smell great) is passed through the holes and through the baseplate on which the mechanism rides. Tension is achieved by tying the string to a second, spring-loaded plate, as shown in Figure 3.5(b). The small springs were purchased from Small Parts, Inc. (part number Y-CS-47), and placed on each corner of the plate. We expected this design to have limited travel considering that the plates cannot travel effectively in the horizontal direction and the tension will build in the string as the slider moves. In fact, the travel was much too limited, with a displacement of only 0.5 mm. Although downward travel was easily achieved, the mechanism

traveled upward unreliably. The tension in the string holding the mechanism to the plate was adjusted over 2-10g with no significant change in performance. Although we were successful in obtaining vertical motion, this design left much to be desired. The diagram of Figure 3.6 shows a second generation coarse positioning mechanism very similar to the design by Niedermann *et al.* [43], where shear deformation of a piezoelectric element was used to drive a mass on sapphire spheres along a track. Instead of using a shear piezoelectric element, we drive an aluminum part, which we call the ‘shaker’ with a sawtooth wave. The piezoelectric stack, which is the same component used in the previously described translation mechanism, is glued to the 0.100” thick aluminum shaker and a support stage, plate 1, as shown in Figure 3.6. Sapphire spheres of diameter 1/16”, again from Small Parts, Inc., were glued to small depressions machined into the aluminum shaker. The triangular arrangement of the sapphire spheres is shown in Figure 3.6(b). A 0.200” thick, 0.385” × 0.580” brass ‘mover’ sits on one side of the sapphire spheres. A 0.040” deep V-shaped groove is machined into the brass ‘mover’ for alignment with two of the sapphire spheres, illustrated in Figure 3.6(b). The brass mover is fastened down against the aluminum shaker and plate 1 with a tension-creating design identical to the previously described translation mechanism shown in Figure 3.5. The brass mover, as the name suggests, slides on the aluminum shaker during the fast part of the sawtooth waveform and remains in place during the slow ramp.

This design worked extremely well both horizontally and vertically at room temperature. The fact that the heavier brass mover was able to reliably travel against gravity was a significant step. Although the design worked well, it still suffered some serious drawbacks. First of all, the design is very large and bulky. It is also not trivial to assemble. The travel of the ‘mover’ is limited to less than 1 mm

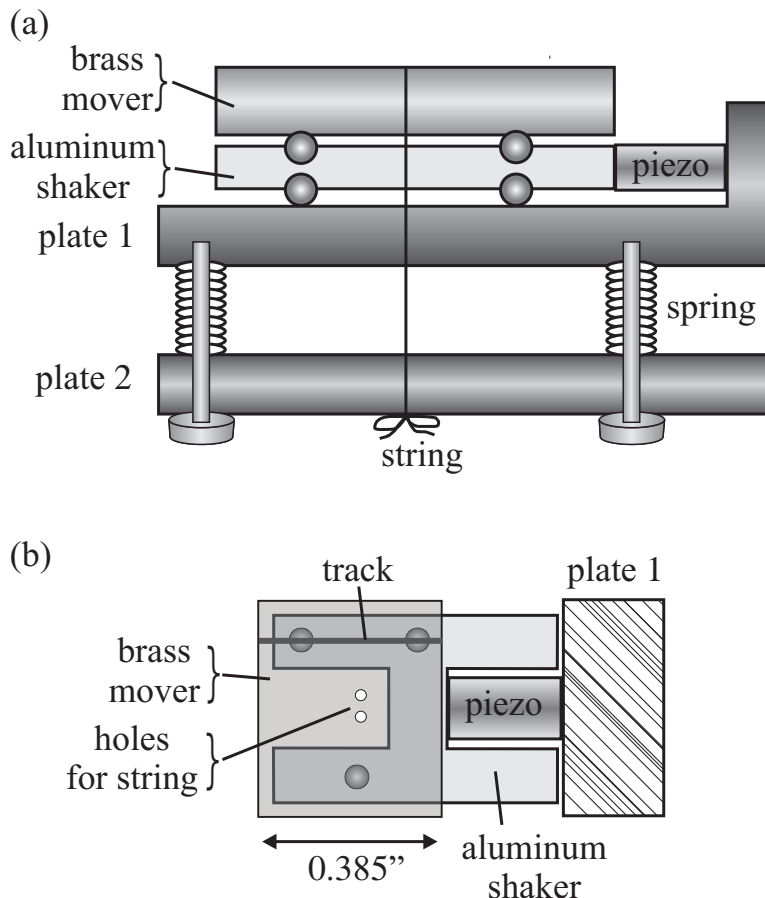


Figure 3.6: Second generation coarse positioning mechanism. (a) Diagram illustrating the basic design of a second generation coarse positioning mechanism. (b) Accurate diagram of the brass ‘mover’ (shown transparent) on top of the aluminum ‘shaker’ as viewed from above. Only part of plate 1 is shown and plate 2 is omitted for clarity.

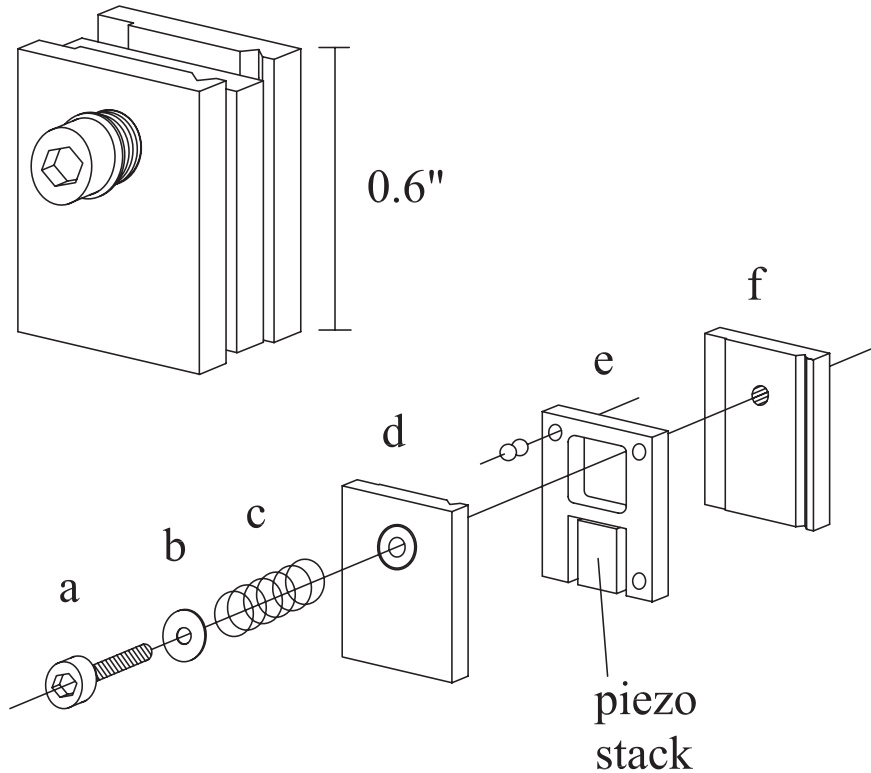


Figure 3.7: Exploded view of a vertically operational inertial positioning mechanism. (a) 2-56 screw to hold the plates together, (b) 2-56 washer, (c) BeCu spring, (d) Front brass slider plate with 2-56 clearance hole and V-groove, (e) Brass driver plate with piezoelectric stack and sapphire spheres, (f) Back brass slider plate, tapped 2-56 with a V-groove.

due to the fastening mechanism. However, the basic idea of a ‘mover’ riding along a ‘shaker’ was a critical step to reaching the next design, which is mechanically much simpler, more compact and travels over large distances. Reliable long-range vertical motion at room temperature was first achieved with the design shown in Figure 3.7. The design was the precursor to the glueless design described in detail in the next section. It is very simple and compact and extremely reliable at room temperature. Plates (d) and (f), shown in Figure 3.7, form a cart with tracks that slide along the $1/16"$ sapphire spheres on plate (e). Plates (d) and (f)

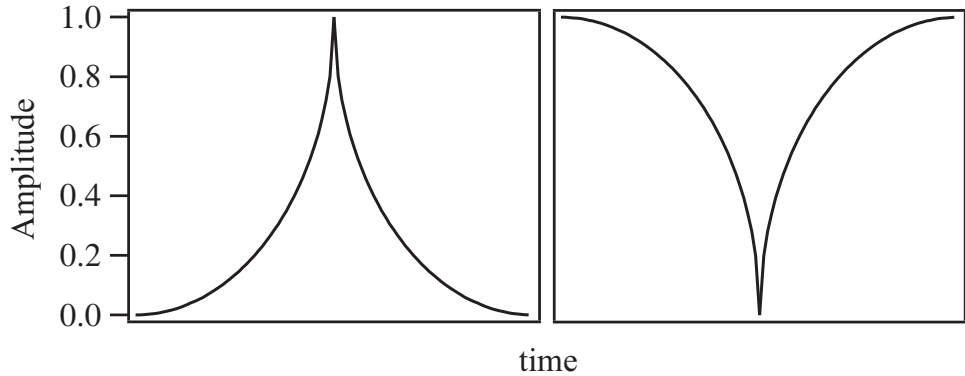


Figure 3.8: Cycloid waveforms for efficiently driving the coarse positioning mechanism.

are held together with a small CuBe spring and a 2-56 screw. The piezoelectric element drives plate (e) against a baseplate (not shown). We found that a 3.0 kHz digitally created asymmetric sawtooth waveform drives this mechanism very well. Individual step sizes, with the displacement measured by fiber-optic interferometry, ranged from 10 nm to 1 μm and were achieved with amplitudes of 5-100 V. For voltages larger than 10 V, we used a piezo amplifier purchased from Thorlabs, Inc. However, the cycloid waveform, which leads to a very large acceleration in one direction, has been found to drive inertial coarse positioning mechanisms much more efficiently [45] and we quickly moved to fully characterizing the performance of the translation mechanism while driven by the cycloid waveform. As suggested in the literature, we found the cycloid waveform much more efficient for driving the mechanism with and against gravity. We have used the mathematical description by Bordoni *et al.* [48], given below in Equation 3.4 to digitally create a cycloid

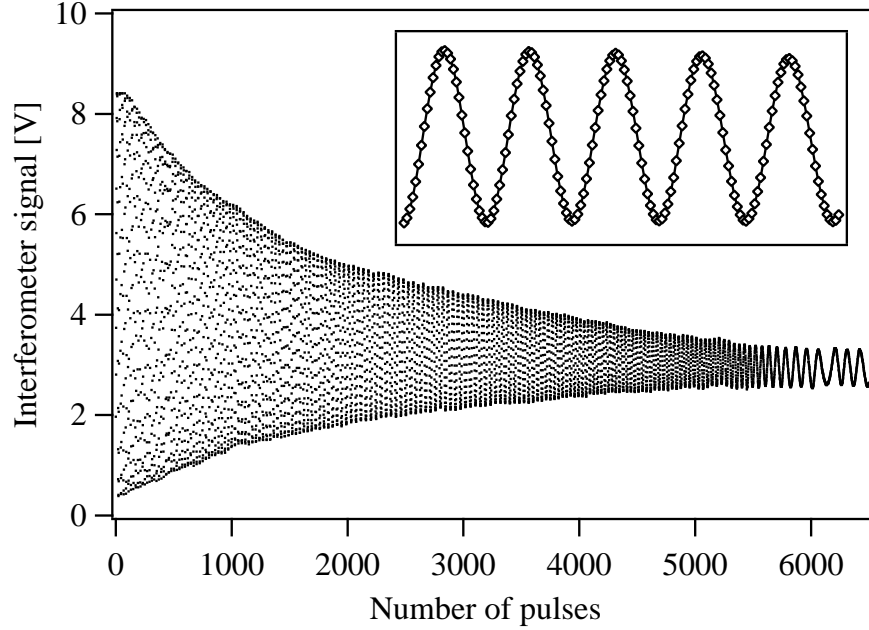


Figure 3.9: Monitoring the coarse positioning mechanism with a fiber optic interferometer. As the distance between the coarse positioning mechanism and the fiber increases, the reflected light diminishes and the envelope of the signal decreases. The inset shows the interference pattern for several uniform steps (each point) taken from the larger data set.

waveform for driving the piezo.

$$\begin{aligned}
 y &= A[1 - 2(x_1(1 - x_1)^{\frac{1}{2}})] & (3.3) \\
 x_1 &= \frac{x - T/2}{T} \quad \text{if } x \leq \frac{T}{2} \\
 x_1 &= \frac{x + T/2}{T} \quad \text{if } x > \frac{T}{2}
 \end{aligned}$$

Figure 3.9 shows a fiber-optic interferometer signal as the coarse positioning mechanism moves against gravity and away from an optical fiber aimed at a piece of polished silicon glued onto one of the moving plates. After each cycloid pulse, the output signal from the interferometer was recorded. In this case, the bandwidth

of the interferometer signal was 0-100 kHz. The envelope of the signal decreases with the number of cycloid pulses as the distance between the plate and the fiber gets larger because the amount of light reflected back into the optical fiber decreases. The change in reflected power is a very simple way to detect the direction of translation. Here, we are using a 780 nm laser. Therefore, the distance traveled during one interference fringe is 390 nm. The total distance traveled in Figure 3.9 is 66 μm , calculated from the 169 interference fringes in the data set. 6500 cycloid pulses were required to travel this distance, which leads to an average individual step size of 10 nm. The step sizes become smaller near the end of the envelope as the sliding plates hit a mechanical stop. The mechanism can easily travel up to 2 mm, which is sufficient for positioning by eye prior to the final coarse approach. The inset of Figure 3.9 shows a zoom-in of a number of interference fringes from the data set and illustrates the uniformity of the steps against gravity.

We found both the sawtooth and cycloid waveforms yielded the best results when digitally represented by at least 100 points/cycle. The digital output we used was set to an output frequency of 330 kHz, which limits the waveform frequency to 3.3 kHz when creating a waveform with 100 points per cycle. We characterized the step size as a function of frequency and amplitude of the cycloid waveform. Figure 3.10 summarizes the step sizes as a function of these parameters. Figure 3.10(a) and 3.10(b) show the step sizes for travel against and with gravity, respectively. In general, the higher frequency cycloid drive gave the largest step size for a given amplitude. At the lower frequencies, a large change in waveform amplitude does not increase the step size as much as at the higher frequencies. Reproducible steps smaller than 10 nm were easily achieved both with and against the force of gravity. In addition, steps as large as several μm may be taken at

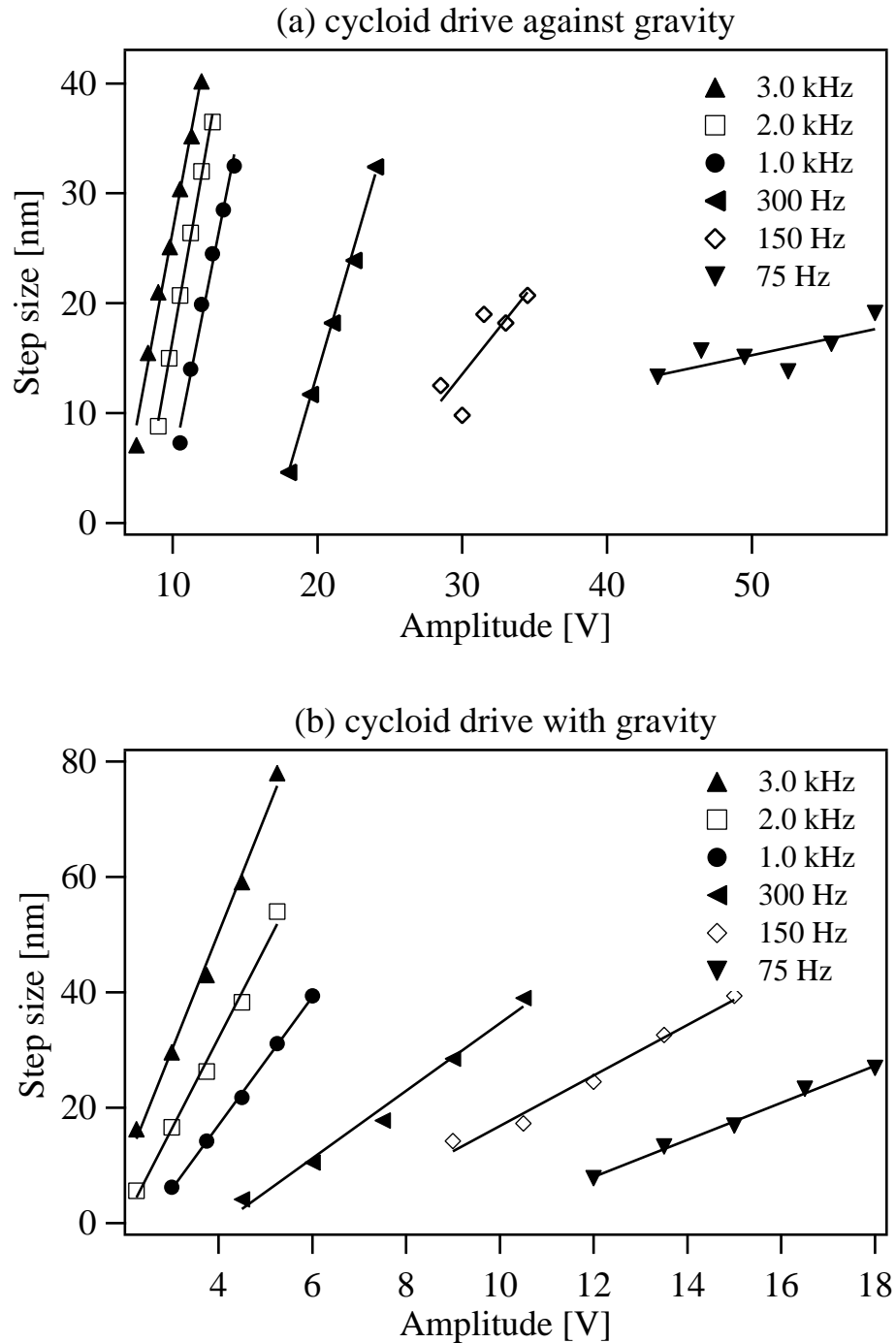


Figure 3.10: Characterization of the inertial positioning mechanism driven by the cycloid waveform. Step sizes for the cycloid waveform driving the slider are shown (a) against gravity and (b) with gravity at various frequencies.

high frequency and amplitude. A much higher amplitude is required to drive the mechanism against gravity. Finally, the higher frequency cycloid demonstrates a much more reproducible step size from one pulse to the next, which can be seen in the increased scatter in the step sizes at lower frequencies.

Step sizes ranging from 10 to 100 nm are ideal. This particular piezoelectric stack (Thorlabs, Inc., part number AE0203D04), can extend 4–5 μm at 100 V under no applied forces at room temperature. The expansion is a factor of 7–12× lower at temperatures near 4.2 K. The cantilever is mounted on one of the sliding plates of the coarse positioning mechanism. The general protocol during the approach to the surface is to take coarse steps for approximately 3/4 of the free extension, then apply a slow voltage ramp to the piezoelectric stack to ‘feel’ for the surface. During the slow voltage ramp, some measurable cantilever quantity is recorded, whether it is the simple snap-in of the oscillator due to the van der Waals force gradient or a drop in amplitude or resonance frequency of a driven cantilever. When a threshold change occurs having reached the desired distance, the piezoelectric stack retracts, pulling the translation mechanism and cantilever away from the surface, so not to smash the cantilever into the surface. Approaching a cantilever to the surface may require that contact does not occur in order to avoid triboelectric charge deposition on an insulating sample. The step sizes given up to this point have been simple before-and-after snapshots of the position of the coarse positioning mechanism. However, the dynamics of the positioning mechanism during the pulse is of great importance and this knowledge can allow the experimentalist to approach the cantilever as carefully as possible without unwanted damage.

In order to characterize the dynamics of the coarse positioning mechanism, we monitored its position by interferometry during a step downward (with gravity),

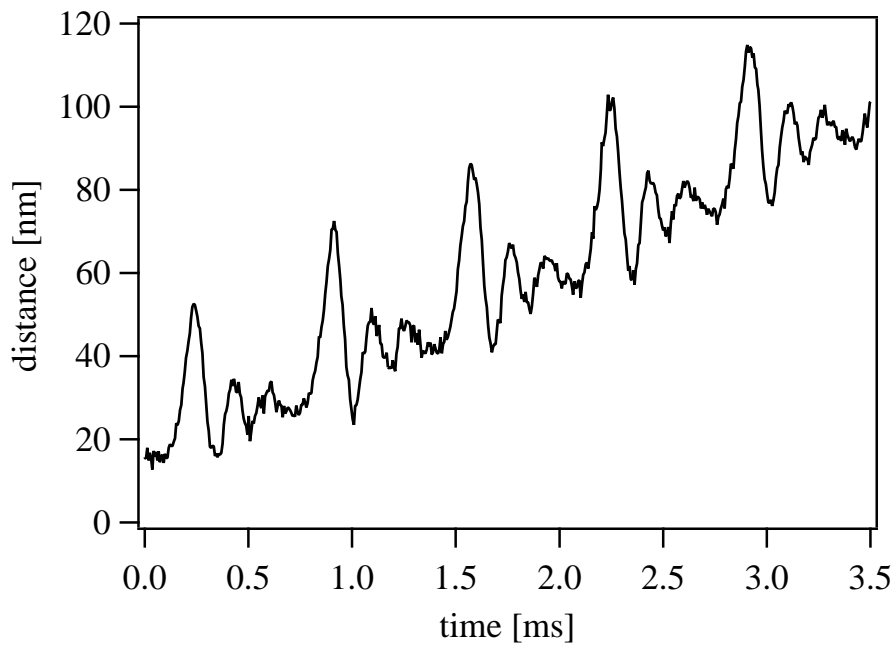


Figure 3.11: Dynamic motion of the coarse positioning mechanism driven by the cycloid waveform. For a final translation of 10 nm, almost 30 nm of ‘backlash’ or overshoot are present. The ringing after each step corresponds to a resonance of 5.5 kHz.

driven with a 3.0 kHz cycloid waveform with an amplitude of 2.0 V. The interferometer signal was acquired at 165 kHz. Figure 3.11 shows several 10 nm steps. It is important to note the overshoot of the coarse positioning. For each 10 nm step, the position of the slider moves forward almost 40 nm, with 30 nm of overshoot. It is also important to keep in mind that when a cantilever is mounted on the slider, these small steps are quite violent, exciting the cantilever and driving it momentarily. It is possible that if one is not careful during the surface approach, the cantilever might touch the surface if overshoot and cantilever excitation is not taken into account. Another interesting feature of Figure 3.11 is the ringing of translation mechanism. Note the oscillations after the initial overshoot. This corresponds to a mechanical resonance frequency of approximately 5.5 kHz. In general, the higher the resonance frequency, the better, so that the translation mechanism is not coupled to room or acoustical vibrations.

Piezoelectric materials do not move as efficiently at very low temperatures. Cooling from 298 K to 4.2 K, we expected that a larger amplitude cycloid waveform would be required. Most groups observe a factor of 7-12 \times less motion. Fortunately, the small step sizes we observed at room temperature were achieved with voltages near 10-20 V. The piezoelectric stack we used from Thorlabs has a maximum recommended applied voltage of 150 V.

In order to test the coarse positioning mechanism shown in Figure 3.7, we developed a small stage to mount the mechanism onto a test probe. The test probe was designed to fit inside a standard liquid helium transfer dewar. The translation mechanism is in direct contact with copper parts of the test vacuum probe that are submerged in helium. This ensures cooling to 4.2 K. The probe space was pumped out with a turbo-molecular pump to a high vacuum of 10^{-6}

mbar, requiring approximately 2 hours to reach this pressure. All wiring was wrapped several times around a 1/4" copper heat sink, coated with insulating GE varnish, to ensure the piezoelectric material reached the desired temperature. Before cooling, the valve between the pump and the probe was closed. The probe was then submerged in the helium transfer dewar and a small amount of helium gas was introduced into the vacuum space to promote rapid cooling. The temperature was monitored with a thermometer. The temperature was stable at 4.2 K after 1.5 hours.

Figure 3.12 summarizes our findings at 4.2 K. At room temperature, we found the cycloid waveform to drive the mechanism more efficiently than the asymmetric sawtooth waveform. However, at low temperatures, the sawtooth outperformed the cycloid. Figure 3.12(a) and 3.12(b) show 11.5 nm and 15 nm steps against and with gravity for a 3.0 kHz drive and amplitudes of 82.5 V and 77 V, respectively. Interestingly, a 1.0 kHz sawtooth waveform was able to drive the mechanism with similarly sized steps at much lower voltages, shown in Figure 3.12. In order to analyze the motion at low temperatures, the dynamics of the plates during a step taken against gravity is shown in Figure 3.12(e), acquired at 165 kHz. The step size is roughly 18 nm with an overshoot of 30 nm. Analysis of the ringing shows excitation at 1 and 5 kHz. There is also a resonance at 5 Hz. Clearly, at low temperatures the mechanism rings for a much longer period of time when compared to the time required to settle at 298 K in Figure 3.11. It should be noted that these tests were performed without vibration isolation. This is probably the source of the low frequency vibration at 5 Hz.

The major advantage of the design in Figure 3.7 is performance. The characterization shows it performs the best of all the prototypes. If operating at room

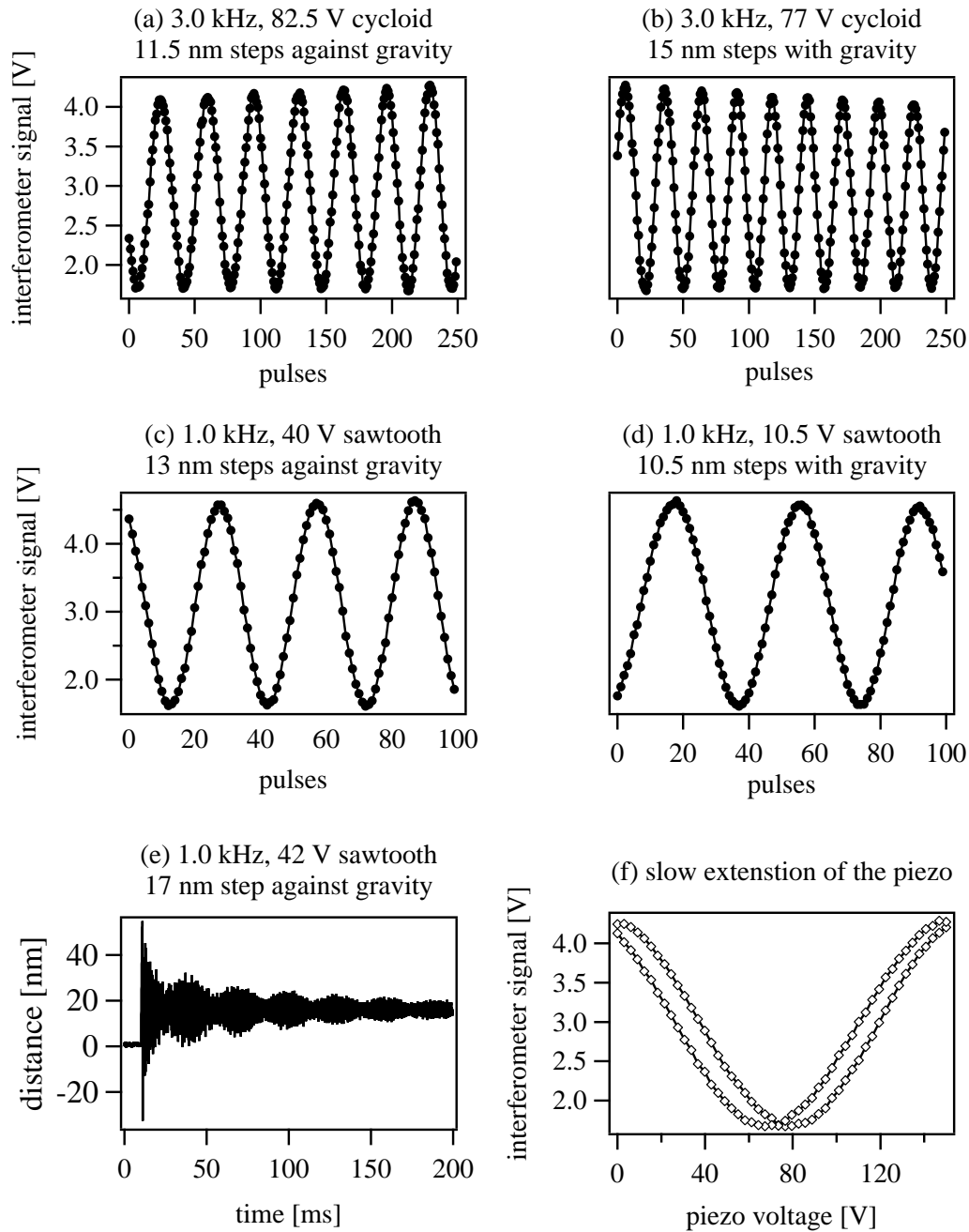


Figure 3.12: Characterization of the coarse positioning mechanism at 4.2 K.

temperature only, it is recommended that the model described here is used. However, a major drawback with this design is reliability at cryogenic temperatures. The glue holding the piezo to the mounting surface does not last through more than one cryogenic cycle. Despite testing several ‘cryogenic’ glues, we did not have success with any of them. The description of a similar glueless design is described in the following section.

3.2.2 Final design of the coarse positioning mechanism

Here we describe the final design of our variable temperature inertial coarse positioning mechanism for use in scanned probe microscopy. This reliable micropositioner has a coarse range of 2.5 mm and can take individual steps less than 10 nm from 4.2 to 340 K. It is operational in both horizontal and vertical geometries and is driven by a low voltage sawtooth waveform. This simple, compact design is both nonmagnetic and glueless. Fine positioning is achieved with the same piezo that drives the coarse positioning mechanism. We report on the design and performance of the mechanism and demonstrate its use in a contact-mode AFM image of a calibration grating taken at 4.2 K. The coarse positioning mechanism and its assembly are depicted in Figure 3.13. The two major components of this design are the brass driving plate (e) and the brass sliding plates, (d) and (f). The 2-56 screw (a), washer (b), and BeCu spring (c), Small Parts, Inc., part number Y-CS-47, serve to hold the two sliding plates against the driving plate.

The driving element for the coarse positioning mechanism is a small piezoelectric stack (Thorlabs, Inc., part number AE0203D04), which operates up to 150 V. The brass driver plate (e) is 0.085” thick and mounted to a base with 0-80 screws through the two extensions near the bottom of the piece. These extensions, ap-

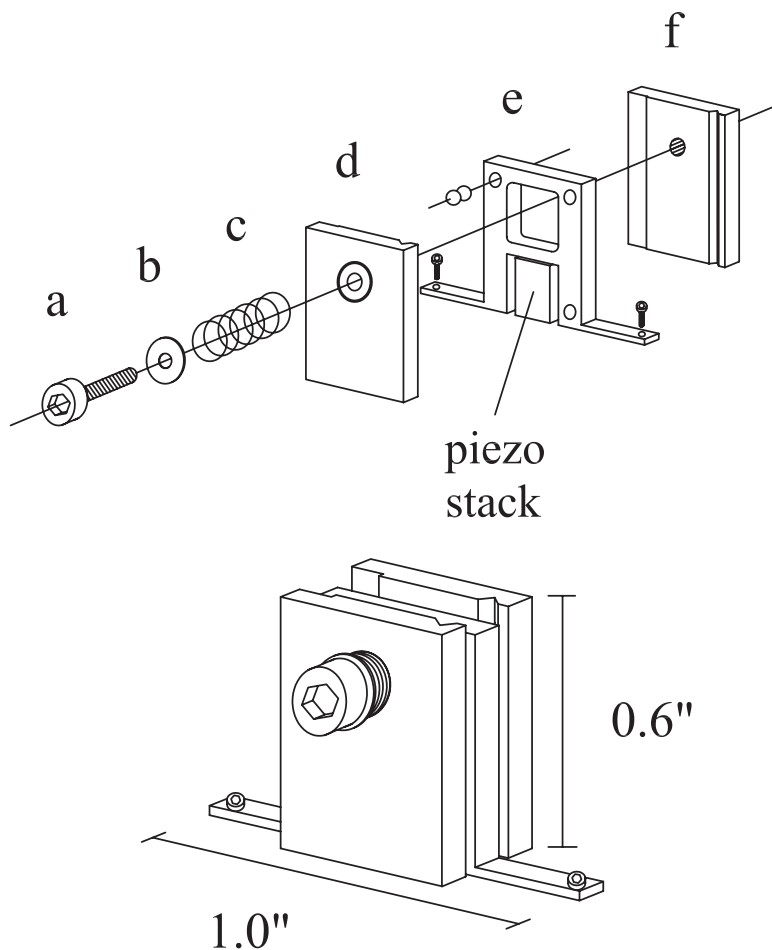


Figure 3.13: Exploded view of glueless coarse positioning mechanism. (a) 2-56 screw to hold plates together, (b) 2-56 washer, (c) BeCu spring, (d) Front brass slider plate with 2-56 clearance hole and V-groove, (e) Brass driver plate with piezoelectric stack and sapphire spheres, (f) Back brass slider plate tapped 2-56 with V-groove.

proximately 0.025" thick, exert a spring loading force on the piezoelectric stack. This eliminates the need to glue the piezoelectric stack on both ends, which we found unreliable upon successive cold cycles. Two 1/16" diameter sapphire spheres (Small Parts, Inc., part number Y-BSP-1) are placed back-to-back in each of the three 1/16" holes on the plate, as indicated in the diagram on plate (e). We have found that if a new drill bit is used for the holes, the spheres make a reliable press-fit into the brass plate. The sapphire spheres protrude from each face of the plate by approximately 0.02". With each pair of spheres in contact with each other, the planes defined on each side of the driving plate are parallel. This simplifies the assembly of the mechanism by significantly reducing tolerance and alignment constraints.

The brass slider plates, (d) and (f) of Figure 3.13, are also 0.085" thick. Each plate has a groove that acts as a track for two of the sapphire spheres on one face of the driver plate. The 90° V-groove is uniform in depth and approximately 0.015" deep. It was carefully cut using standard milling techniques and we did not find it necessary to polish the groove. We did find it important that the sapphire spheres ride along the edges of the groove, not on the faces. The flat area of the plate, which is in contact with the remaining sphere, is machined down so that the driver plate and slider plates are parallel. Plate (d) has a clearance hole that is 0.004" over the outer diameter of the 2-56 thread, while plate (e) is tapped 2-56. Prior to assembly, we clean the parts in alcohol to remove grease. When all of the plates are assembled, the two slider plates move together along the tracks provided by the driver plate. The tension in the spring is adjusted to set the necessary frictional force between the sapphire and the plates. We cut the BeCu spring in half to save space, and give the 2-56 screw approximately 3.5 turns past the free length of the

spring. This corresponds to a force of 1.7 N using the spring constant supplied by the manufacturer.

The coarse positioning mechanism is driven by a simple asymmetric sawtooth waveform 2 ms in duration. The piezoelectric stack extends under an applied voltage. During the slow ramp of the sawtooth, 1.98 ms in duration, the slider plates stick to the sapphire spheres of the driving plate due to the force of static friction. When the fast ramp of the sawtooth, 0.02 ms in duration, is reached, the inertia of the slider plates is large enough to overcome the force of static friction, resulting in a net displacement. We use a 16-bit output board (National Instruments, board PCI-6052E) operating at 50 kHz to generate the sawtooth waveform.

We are pleased to report that our vertical coarse positioning mechanism performs very well and has been extremely reliable. We have successfully built and tested three of these mechanisms in our laboratory. Over the period of two years, we have not noticed any signs of wear or loss of performance. Steps with and against gravity ranging from 7 to 75 nm have been achieved in a temperature range of 4.2–340 K. Step sizes obtained at 298 K in air and 4.2 K in helium gas are shown in Figure 3.14. All measurements were taken with a fiber-optic interferometer [53]. At 298 K in air, the downward steps are as small as 5 nm with a threshold peak-to-peak sawtooth voltage of 5 V. The upward steps begin at 7 nm, requiring 7 V. It is important to realize that for operation against gravity, the slider will travel down, not up, if a sawtooth is applied below the threshold voltage. The steps against gravity are limited to approximately 80 nm, but the steps downward can be as large as 150 nm. The step sizes certainly depend on the applied spring force, but this parameter is not difficult to set reproducibly. Remarkably, very low

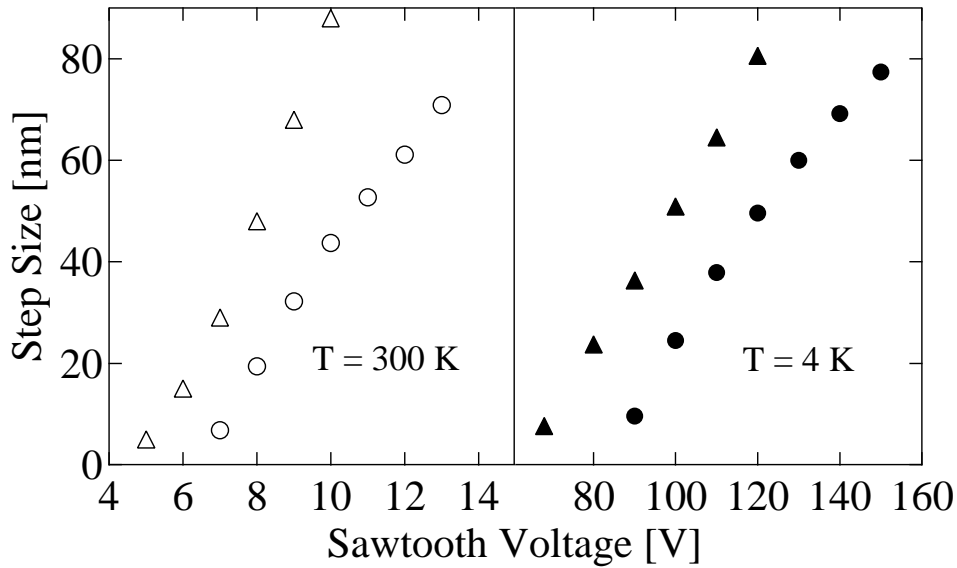


Figure 3.14: Step sizes at 298 K (left) and 4.2 K (right) vs. sawtooth peak-to-peak voltage. Triangles and circles represent steps with and against gravity, respectively.

voltage is required for room temperature operation. The fine range of the piezo at room temperature is 4.5 μm for 150 V, or 30 nm/V. The mechanism has similar performance at room temperature in high vacuum (10^{-7} Torr).

Low-temperature measurements were taken in a 1.50" diameter test can which was placed inside a liquid helium storage dewar. Helium gas was used in the can to assure that the mechanism cooled rapidly and was isothermal at 4.2 K during the tests. The steps, shown on the right in Figure 3.14, range from 7 to 80 nm both with and against gravity. This was accomplished with voltages from 70 to 150 V. The fine range at 4.2 K is 320 nm with an applied voltage of 150 V, or 2.1 nm/V. At liquid helium temperatures, it is known that piezoelectric materials lose their ability to expand by a factor of 7-10 relative to room temperature. The expansion of the piezo in this slider at 4.2 K decreased by a factor of 14. This may be due to the fact that we have brass extensions applying a different loading force to the

piezo at low temperatures as the mechanical properties of the brass change. The top of Figure 3.15 shows 7 nm steps down over a distance of 7 μm at 4.2 K. These data demonstrate how consistent the steps are over large distances. We see the same accuracy with larger steps and steps in the opposite direction. The bottom of Figure 3.15 shows several 7.5 nm downward steps at 4.2 K.

It was shown with other vertically operating coarse positioning mechanisms that the cycloid waveform is more efficient than the sawtooth [45]. In our first prototype, we glued the piezoelectric stack at both ends for mounting the slider. We found the cycloid waveform, described by Bordoni *et al.* [48], to have similar performance to the sawtooth. However, the cycloid does not work at cryogenic temperatures with the extensions of plate (e) holding the piezo under tension in Figure 3.13. Even at room temperature, the steps are larger and more uniform with the sawtooth waveform for a given peak-to-peak voltage.

Figure 3.16 shows the coarse positioning mechanism incorporated into a working contact-mode cryogenic AFM. It is straightforward to incorporate a 15° cantilever stage and optical fiber mount, as shown in Figure 3.16, without any loss in performance. We find the detection noise near a 1-10 kHz cantilever resonance is dominated by the thermo-mechanical motion of the cantilever when mounted on the stage. The plates can be easily modified for other positioning applications. Here we have interfaced the inertial positioning mechanism with a bimorph sample scanner [54] for preliminary atomic force microscopy tests.

3.2.3 Thermal stability

Besocke's design is clever since it minimizes the effects of thermal drift [39]. However, the coarse positioning mechanism described in Section 3.2.2 is susceptible

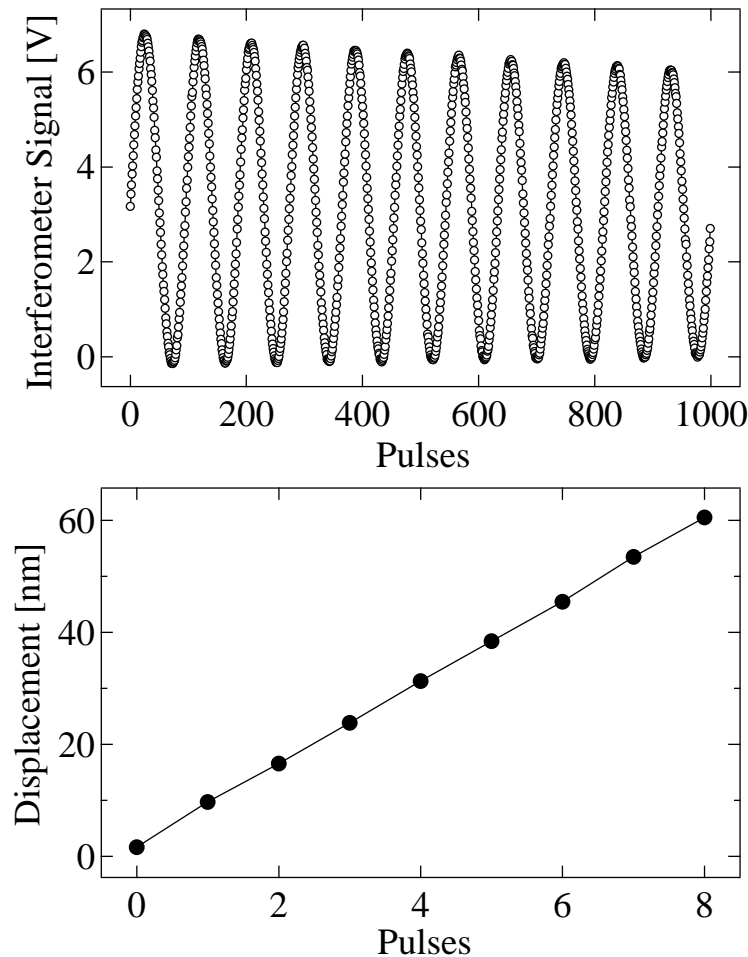


Figure 3.15: Steps measured with 1310 nm fiber optic interferometer.

(Above) Highly uniform 7 nm steps down over 7 μm at 4.2 K. Here the sliding plates move away from the optical fiber, which is indicated by the decreasing envelope of the interferometer signal. (Below) A few 7.5 nm downward steps at 4.2 K demonstrating precision positioning capability.

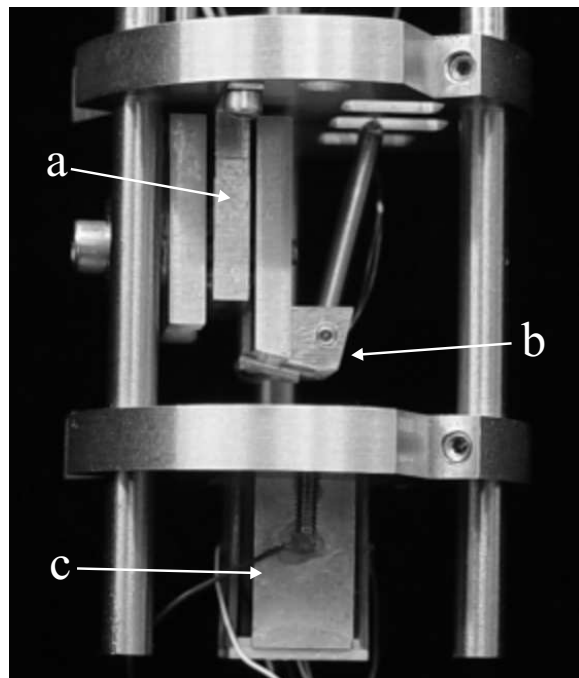


Figure 3.16: Picture of variable-temperature AFM. (a) Inertial positioning mechanism. (b) Cantilever stage and optical fiber mount. (c) Sample scanner. For scale, the horizontal plates are 1.188" in diameter and the scanner is 0.500" in length.

| Material | total drift, d | Direction |
|-----------------------|------------------|-----------|
| Brass | 37 μm | + |
| Stainless Steel | 22 μm | + |
| Macor | 14 μm | - |
| Titanium | 9 μm | - |
| <i>Brass/Titanium</i> | 2 μm | - |

Table 3.1: Thermal compensation of the coarse positioning mechanism with various materials.

to drift with a change in temperature, which could cause unwanted crashes of the cantilever into the surface during variable temperature experiments.

In order to quantify the drift, we measured the total change in displacement between the end of the inertial positioning mechanism and a plate opposite the slider during warming from 77 K to 298 K. The plate is where the sample scanner is located, so we measured what is very similar to the drift between the cantilever and the surface of the sample in a real experiment. The red arrow in Figure 3.17(a) points out the 1/16" rods used to separate the slider and the plate. Using brass rods, we found a total drift, $d = 37 \mu\text{m}$, which is quite large. In this case, the slider pulled away from the plate opposite to it upon warming. This means that upon cooling, the tip would approach the surface. We also used stainless steel, Macor (a ceramic from Corning), and titanium. The results of these experiments are summarized in Table 3.1. The direction is given as positive, +, or negative, -, which we define as movement of the end of the coarse positioning mechanism toward or away from the plate, respectively, upon cooling.

Unfortunately, all of the pure materials exhibited considerable drift. However,

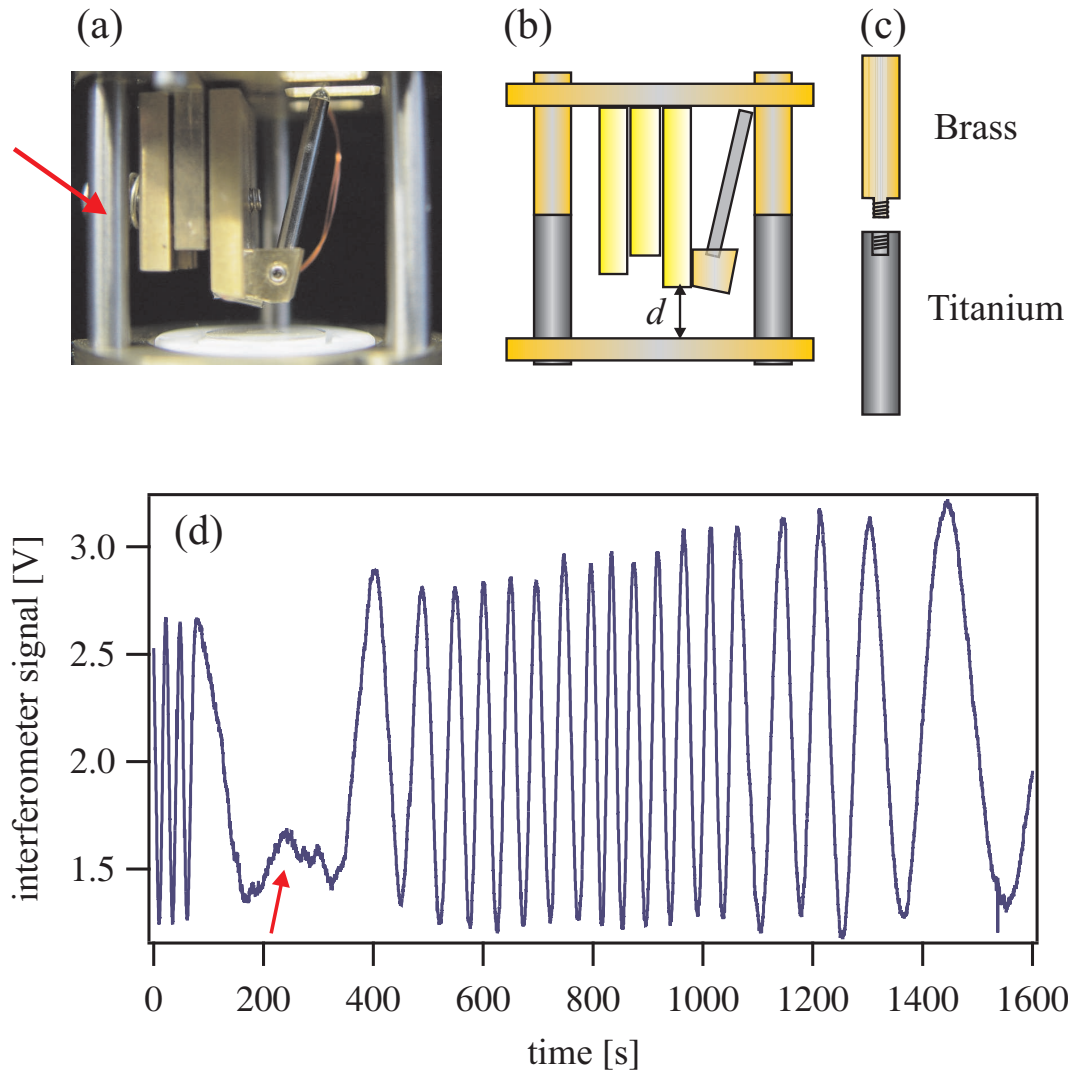


Figure 3.17: Thermal compensation of the coarse positioning mechanism.

(a) The slider with $1/16''$ rods between the slider's mounting plate (top) and the scanner plate (bottom). (b) Brass/titanium rods for thermal compensation. (c) Assembly of the rods. (d) Example of thermal drift measurement to determine the total displacement warming the apparatus from 77 K to 298 K.

we successfully decreased the total thermal drift by fabricating a rod out of brass and titanium to separate the slider and the plate, illustrated in Figure 3.17(b). Notice that brass and titanium drift in opposite directions in Table 3.1. Having both materials in the thermal path length lets us tune the thermal drift of the brass/titanium rod to counter that of the coarse positioning mechanism. We simply adjusted the ratio of brass to titanium. The assembly of the rods is depicted in Figure 3.17(c). The end of the brass rod is threaded (2-56) so that it fits tightly into the titanium rod, which is tapped (2-56). The ratio of the length of brass to titanium (Br : Ti) which worked best was 1 : 10, with total drift of only $d = 2 \mu\text{m}$ over $\Delta T = 223 \text{ K}$.

Figure 3.17d shows the interferometer signal as a function of time as the apparatus warms from 77 K to 298 K. Here, we are using approximately equal lengths of brass and titanium for the compensating rod. Counting the interference fringes gives the total distance. Interestingly, we are able to observe a phase transition of the titanium rod indicated by the red arrow of Figure 3.17d. For short period of time, the apparatus is completely stable during the transition.

This method of thermal compensation has proven very reliable. We are able to image from 4.2–340 K without worrying about the cantilever crashing into the surface. To be safe, we set the cantilever-surface distance to approximately 100 μm while varying the temperature to avoid accidental crashes as the microscope head reaches thermal equilibrium.

3.3 Sample positioning

In this microscope, the cantilever tip is approached to the surface of the sample. The sample is mounted on a piezoelectric scanner for imaging purposes. Here we

discuss the xy -scanner and the coarse positioning mechanism for positioning the sample.

3.3.1 Cryogenic bimorph piezo-based scanning stage

We have interfaced a cryogenic sample scanner first used by Siegel *et al.* [54] with the coarse positioning mechanism developed in Section 3.2.2. This scanner offers a large scan range for its size, compared to scanners based on the piezotube. The diagram of Figure 3.18(a) shows the components of the scanner: 4 bimorph piezos and 3 parts machined from Macor. The center scan stage, which is cross-hatched in Figure 3.18(a), is glued to the ends of the two bimorph piezos facing the y -direction. The opposite ends of these two piezos are glued to a square base at the bottom of the scanner. The two remaining piezos facing the x -direction are glued to the circular outer stage at the top of the scanner. These two piezos are also glued to the square base. Cyanoacrylate glues such as Krazy Glue work extremely well between piezoelectric material and Macor. The movement of the bimorph piezo is illustrated in Figure 3.18(b). Applying a voltage to the piezo causes bending in an *S*-shape. Piezos opposite each other receive the same voltage.

Figure 3.18(c) shows how the scanner was mounted into a brass plate and incorporated into the microscope. Removing the scanner is only a matter disconnecting all electrical connections from the scanner and the sample, loosening the three 2-56 set screws of the scanner’s mounting plate and sliding the scanner down the titanium rods. The scanner is typically installed by eye with a cantilever-sample distance of approximately 200–298 μm . It is useful to place a white background behind the microscope in order to determine this distance in the most careful manner possible.

The fiber-optic interferometer was used to calibrate the motion of the scanner at room temperature. We obtained a motion of 100 nm/V. This calibration has not changed over a period of 2 years. For calibration at cryogenic temperatures, we use a calibration grating with features of known size. The full details of the bimorph piezos, design of the Macor parts, scanner assembly, and the piezo amplifiers used are given in Appendix C.3.

3.3.2 Coarse positioning mechanism

In order to locate device structures and reposition the sample *in situ*, a coarse positioning mechanism was developed to work with the scanner described in Section 3.3.1. All the pieces of the positioning mechanism are attached to the cross-hatched center scanning stage of Figure 3.18(a). The positioning mechanism is based on inertial sliding. A side view of the scanner and the coarse-*xy* positioner is depicted in Figure 3.19. The sample is mounted on a small magnet glued to a polished sapphire disk. A second polished sapphire disk with a 1/8" hole in it is glued to the top of the center scan stage. A flat, 0.020" copper beryllium (CuBe) plate is glued to the bottom of the center scan stage. A second magnet is placed freely inside the scanner. When the sample/magnet/sapphire disk (shown in grey), is brought into contact with the sapphire disk glued to the center scan stage, the magnets attract, and hold the sample in place. It is important to make sure the sapphire disks are clean. Large dust particles will significantly decrease performance.

The magnets are neodymium disks purchased from Master Magnetics, Inc. The sample is mounted on a 0.100" thick, 0.375" diameter magnet. The smaller magnet inside the scanner is 0.125" thick and 0.125" in diameter. Use of the

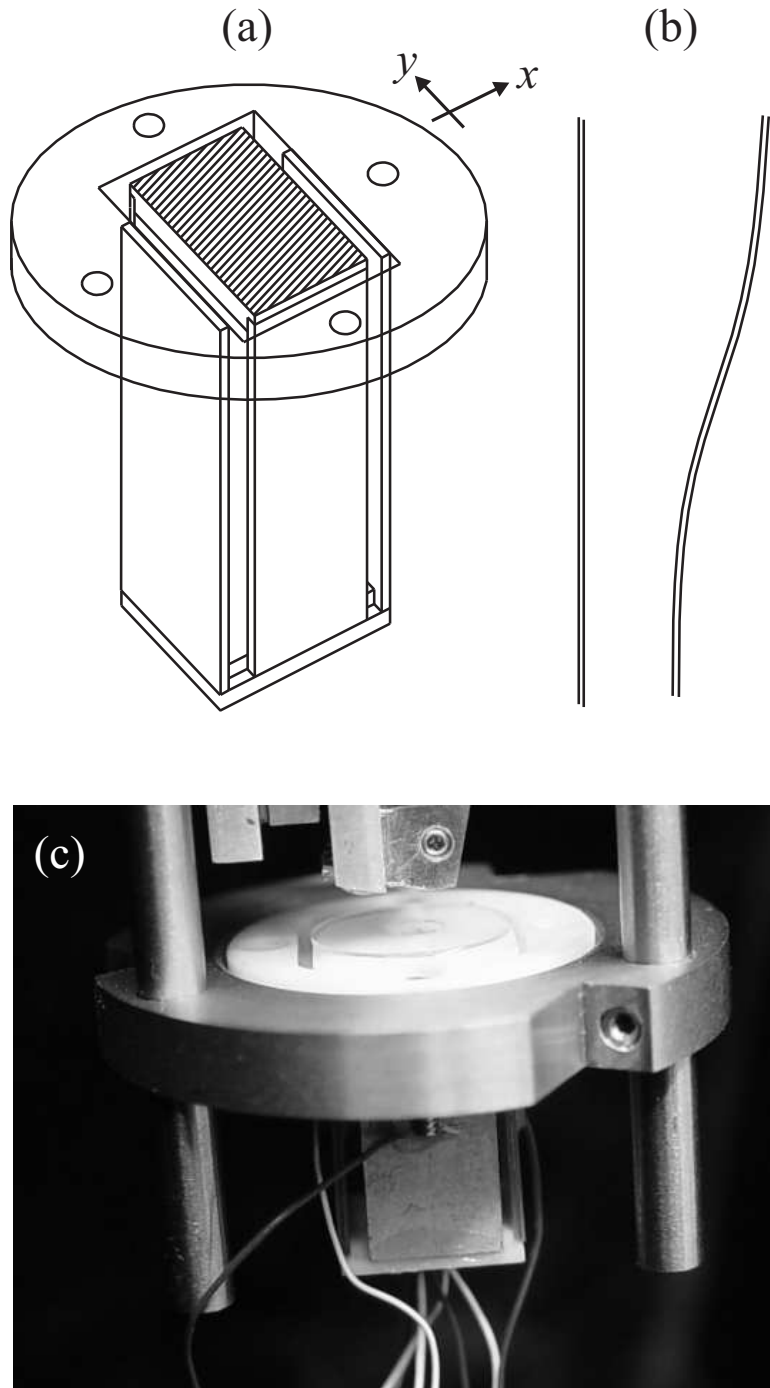


Figure 3.18: (a) Diagram of the cryogenic sample scanner. (b) Bending of the bimorph piezo at (left) zero applied voltage and (right) nonzero applied voltage. (c) Incorporation of the scanner into the scanned probe microscope. The bimorph piezos are 0.5" in length.

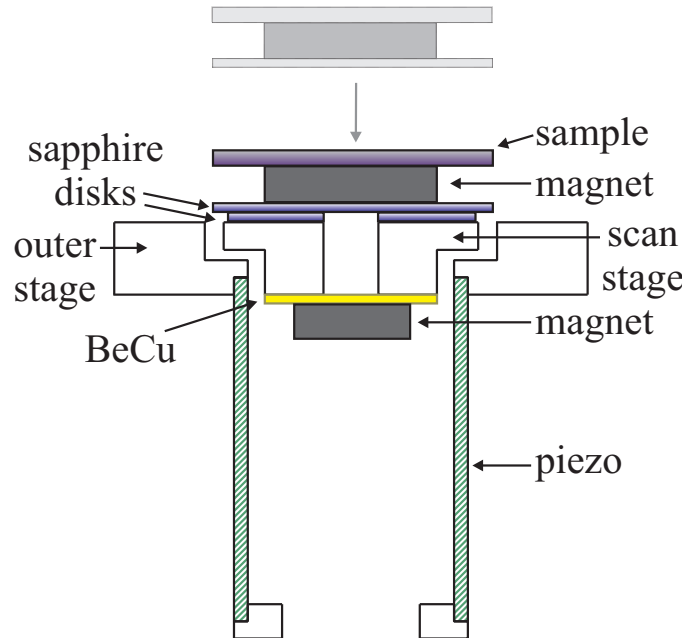


Figure 3.19: Side view of the coarse sample positioning mechanism. From this view, the bimorph piezos are attached to the outer stage. From the alternative side view, the two remaining bimorph piezos are attached to the center scan stage.

smallest magnets possible maximize the resonance frequency of the scanner, which is necessary to decouple the scanner from low frequency room vibrations. It is not critical to use these exact magnets, but they have been found to work well. The polished sapphire disks were purchased off the overrun list from Meller Optics, Inc. The disks are 0.020" thick and 0.375" in diameter. There is a 0.125" diameter hole though the disk glued (Krazy Glue) to the center scan stage. The thin CuBe plate was purchased from Small Parts, Inc.

The two magnets supply enough force to hold the sample in place while imaging. However, if an asymmetric sawtooth wave is sent to the piezos, the sapphire plates will slide against each other. It is important to switch off the RC filter that follows the piezo amplifier. Otherwise, the sawtooth will not reach the piezo. At room

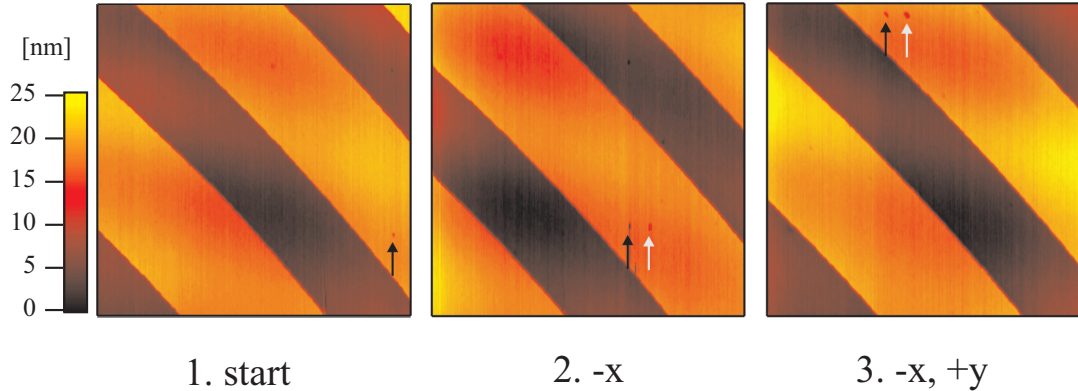


Figure 3.20: Coarse positioning of a calibration grating. $5 \mu\text{m} \times 5 \mu\text{m}$ topographical images illustrating coarse motion in the x and y directions.

temperature, a 5 kHz, 30 V sawtooth waveform will easily move the sample a few hundred nanometers. At 77 K, an amplitude of 70 V was required for 50 nm steps. Characterization of the coarse sample positioning is not as critical as the cantilever coarse positioning. Figure 3.19 demonstrates repositioning of a calibration grating at room temperature. The grating has alternating 25 nm steps every 3 μm . The $5 \mu\text{m} \times 5 \mu\text{m}$ images show how the grating is shifted by following two small dust particles, indicated by the black and white arrows. First, the grating is shifted in the $-x$ direction (middle image). Finally, the grating is shifted in the $-x$ and $+y$ directions (right image).

3.4 Mechanical design, vacuum, and vibration isolation

The microscope head is shown at the left of Figure 3.1. Only 1.2" in diameter and constructed primarily of brass, the microscope and a small copper heat sink hang from a soft bellows [24] and reside in a 1.75" diameter copper vacuum space attached to the bottom of a long stainless steel tube. The entire probe is shown in

the Appendix in Figure C.9. At the top of the stainless steel tube, we have placed fiber-optic and electrical feedthroughs into the vacuum space (Appendix C.1.2). The approach of placing the microscope at the end of a vacuum tube is common among groups who require high magnetic fields, where the magnet is placed in the bottom of the dewar, surrounding the copper end of the vacuum chamber. We also found this design compatible with initial testing in a helium transfer dewar. The entire dewar and vibration isolation system are shown in the right of Figure 3.1. A winch mechanism was implemented to raise the dewar to a 2000-pound plate where it seals against an aluminum interface. The heavy plate rests on four air legs. The turbomolecular vacuum pump, to the right of the vibration isolation stage, is vibration-isolated from the probe through a concrete block resting in sand followed by a series of flexible vacuum lines attached rigidly to the massive plate. We have found the experimental cryogenic ideas presented by Richardson and Smith [55] a great resource. A detailed description of the entire microscope is given in Appendix C.

3.4.1 Operation at cryogenic temperatures

To achieve low temperatures, the entire microscope and sample are slowly cooled using helium as an exchange gas. The exchange gas is introduced at the top of the stainless tube through a valve while the copper end of the probe, which houses the microscope, is immersed in cryogen. Once thermal equilibrium is achieved, the exchange gas is evacuated with a turbomolecular pump until a high vacuum is achieved. A series of baffles and a heat sink are used to slow heat transfer into the microscope. We have also been able to operate the experiment at higher temperatures by submersing the copper end of the probe in heated wa-

ter. Because the microscope is suspended from a soft bellows, we do not find that vibrations arising from the boiling cryogen affect our experiment.

3.5 Measuring forces and force gradients, microscopically

This section presents examples of the interaction of a micromachined cantilever with a surface. We demonstrate the response of a stationary cantilever and a cantilever driven at a constant frequency, ω . Imaging surface morphology by contact mode and intermittent contact mode is described, followed by a discussion of electrostatic force and force gradient measurements. Finally, sensitivity in air and vacuum is compared and an overview of the experimental procedure for characterization of organic films and devices by high-sensitivity electric force microscopy is given.

3.5.1 The force-distance curve

Figure 3.5 shows a measurement of the force experienced by a cantilever as it approaches and makes contact with a sodium chloride (NaCl) surface in high vacuum. Here, a force causes a deflection of the cantilever, which is monitored by the fiber-optic interferometer. The measurement of the force begins far from the surface, approximately 80 nm away where $x = 0$ nm is defined. The cantilever spring constant is overcome by the van der Waals force gradient at a distance of 75 nm, causing the cantilever to ‘jump’ to the surface. This is often referred to as ‘snap-in.’ As the cantilever is pushed further, the force crosses through 0 N, and soon experiences a force in the opposite direction. The silicon nitride cantilever used in Figure 3.21 has a resonance frequency of 8.8 kHz with a spring constant of 0.02 N/m. The total deflection of the cantilever is approximately 10 nm when

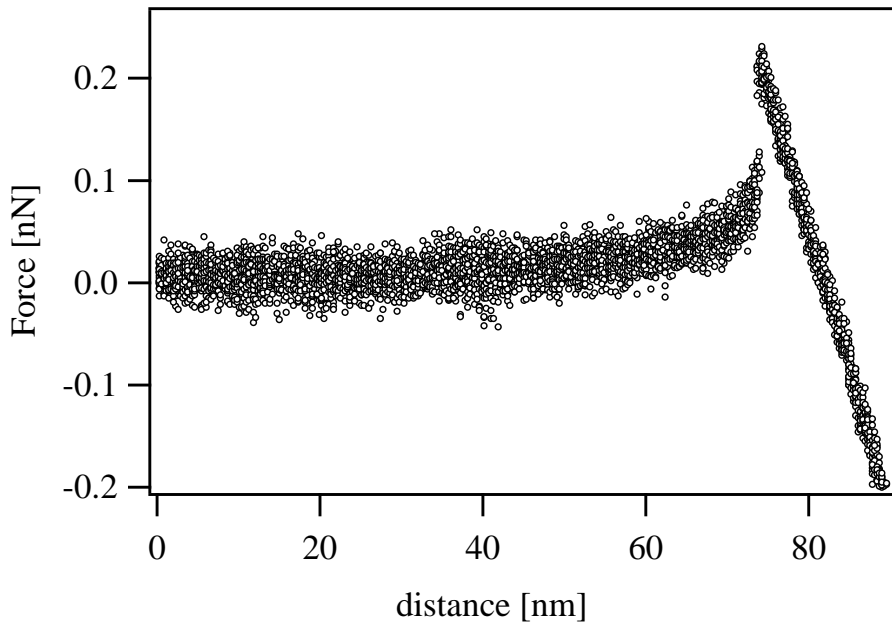


Figure 3.21: Force-distance curve on NaCl.

it snaps in. The bandwidth of the interferometer in this measurement was set to 0-100 kHz, and the signal from the interferometer was acquired at a rate of 10 kHz. A data point was taken approximately every 0.1 nm. A detailed analysis of all the components of a force-distance measurement using a fiber-optic interferometer is given in Appendix A.1.2.

3.5.2 Amplitude modulation near a surface

The cantilever is driven by a small piezoelectric crystal at the base. This design is described in Appendix A.1.3. The amplitude and phase response of the cantilever is shown in Figure 3.22.

Amplitude modulation near a surface is used for intermittent contact mode atomic force microscopy (also known as Tapping ModeTM – a trademark of Digital

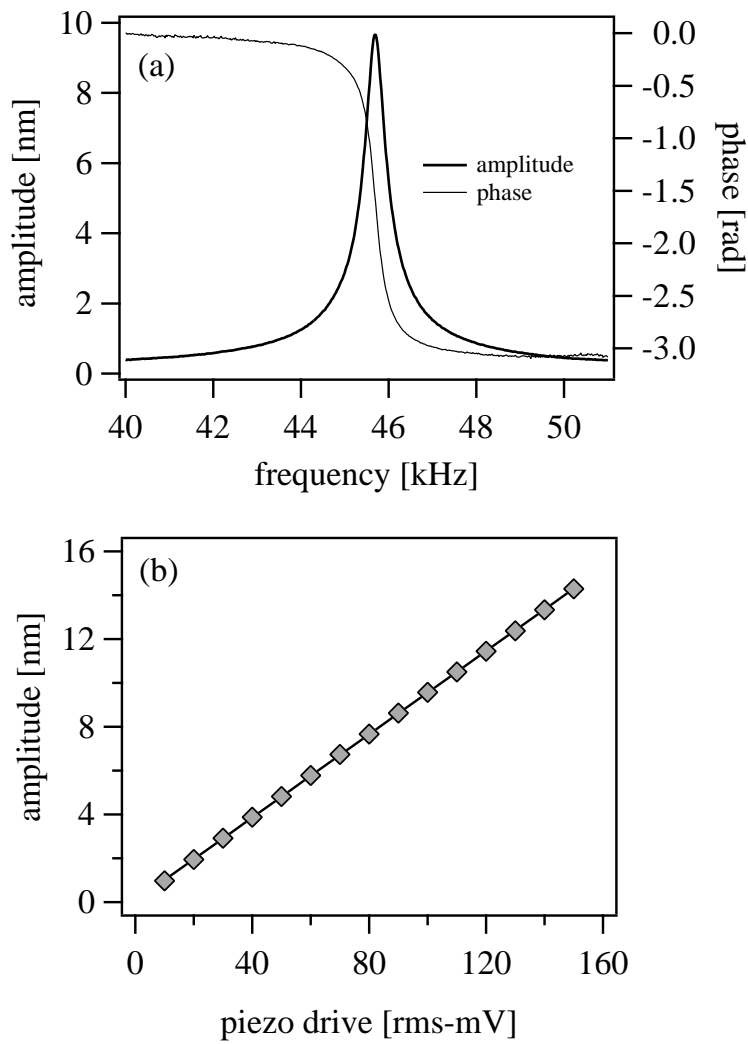


Figure 3.22: (a) Amplitude and phase response of a micromachined cantilever. (b) Cantilever amplitude as a function of piezoelectric driving voltage.

Instruments, Inc.). In this section, the interaction of a cantilever, driven at a frequency, ω , with a silicon surface in high vacuum is discussed.

Figure 3.23 shows the root mean square (rms) amplitude of the cantilever as it is brought near a silicon surface. The platinum-coated silicon cantilever has a natural resonance frequency $f_0 = 23.9$ kHz and a spring constant of 1 N/m. The cantilever is driven 0.5 kHz below resonance by a piezoelectric crystal placed at the base of the cantilever. The rms amplitude is measured with a lock-in amplifier. The time constant is set to 20 ms and the output signal is acquired at 250 Hz. The cantilever is approached slowly, requiring tens of seconds to reach the surface.

At a distance of 85 nm (solid arrow) from $x = 0$ nm, the amplitude of the cantilever begins to decrease. It is reduced by long-range attractive forces (the surface is located at a distance of $x = 138$ nm). However, the amplitude is then reduced by short-range repulsive forces. This rather abrupt change is indicated by the dotted arrow at a distance of 95 nm. The theoretical analysis of this process has been described very nicely by Garcia *et al.* [56]. Intermittent contact mode imaging is performed in the repulsive regime and is the most common technique for acquiring the topography of a material. Imaging in the attractive regime is more difficult because it occurs over such a short distance. However, it is recommended for soft samples or materials that triboelectrically charge easily. Eventually, the amplitude of the cantilever falls to zero, which occurs at a distance of 135 nm.

3.5.3 Imaging topographical features

We have created our own feedback control electronics for operation in contact and intermittent contact mode imaging. The circuitry is very similar to the proportional-integral control electronics used in many other applications, including

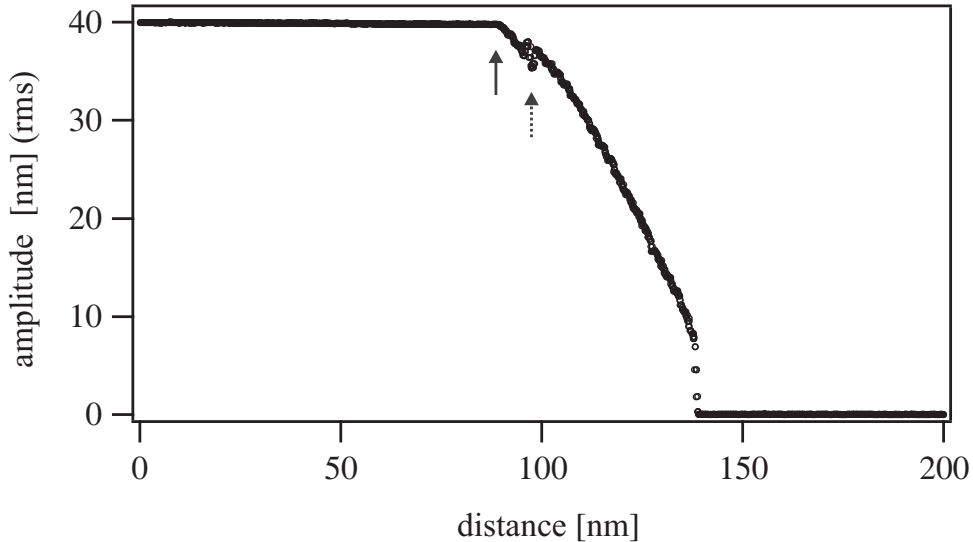


Figure 3.23: Amplitude modulation near a silicon surface. At $x = 0$ nm, the cantilever is 138 nm away from the surface.

scanning tunneling microscopy. Details of the circuit are given in Appendix D.1. For intermittent contact mode, we drive the cantilever below resonance with a small piezo at the cantilever base, resulting in a peak-to-peak amplitude of 100 nm. We approach the surface until the amplitude decreases to approximately 90 nm, at which time the feedback loop is turned on. A cantilever spring constant of 1 N/m or higher is sufficient to avoid cantilever snap-in during imaging, which occurs when the van der Waals force gradient overcomes the spring constant. For contact mode imaging, we prefer a much softer cantilever, with a spring constant of 0.02-0.1 N/m, to avoid damaging the surface. We image at constant force with less than 1 nN of force between the tip and sample.

Figure 3.24 shows a constant force contact-mode image of a calibration grating taken at 298 K and 4.2 K in helium gas. The grating has an array of 20 nm steps spaced with a period of 3 μ m. These images were acquired before vibration isolation had been set up in our laboratory.

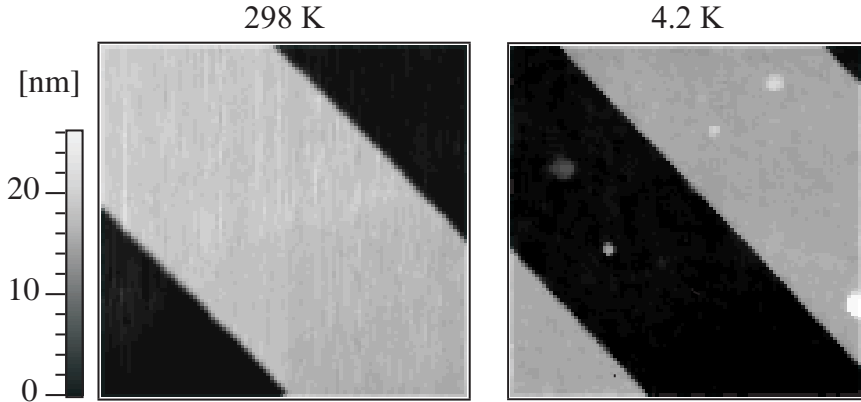


Figure 3.24: Contact-mode image of calibration grating at 298 K and 4.2 K.

The grating has 20 nm steps spaced every 3 μm .

Figures 3.25(a) and 3.25(b) are contact mode images of a graphite surface. The image was acquired at constant force with a cantilever spring constant of 0.02 N/m. The linescan in Figure 3.25(c) demonstrates very high vertical resolution. The distance between graphite layers is 0.34 nm. The arrows in Figure 3.25(c) mark the steps between adjacent graphite layers.

3.5.4 Electrostatic forces and force gradients

We discuss a simple capacitive model for the force and force gradient experienced by the cantilever in Appendix A.4. Most experiments performed at room pressure monitor the force or force gradient experienced by a cantilever by following changes in the amplitude response to a driving force at a constant frequency. Figure 3.26 illustrates how a shift in the resonance frequency causes a change in the amplitude of a cantilever driving at a constant frequency. However, working in high vacuum, it is essential to monitor the force gradient of the cantilever because the amplitude response time of the cantilever is much too long for imaging purposes. A time, $\tau = Q/\pi f_0$, where Q is the quality factor and f_0 is the resonance

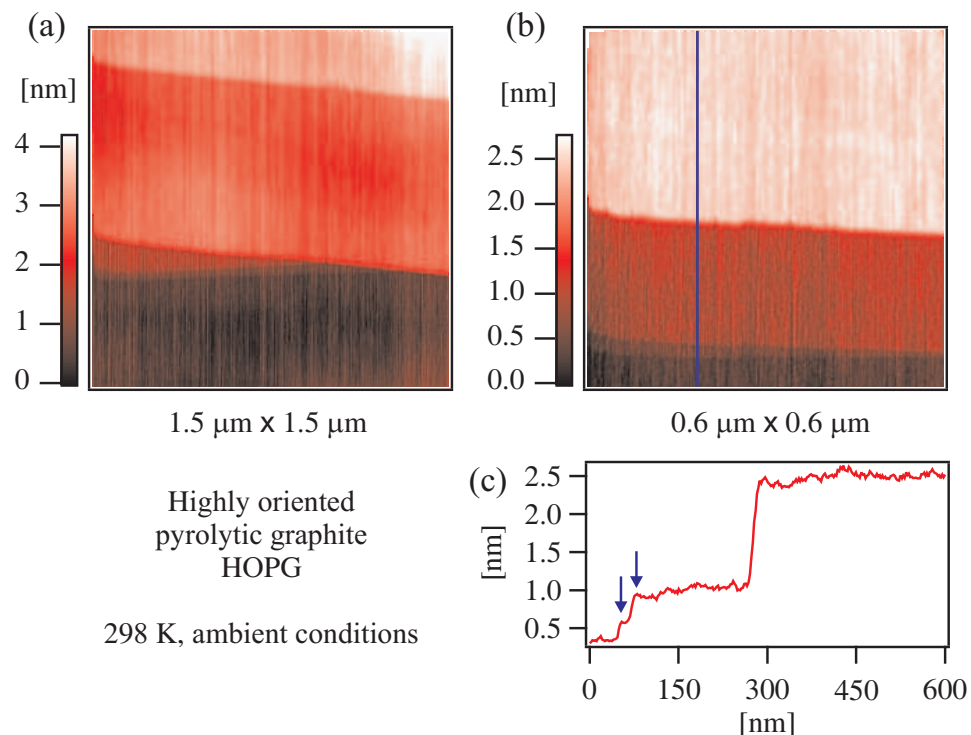


Figure 3.25: Topography of highly oriented pyrolytic graphite (HOPG). 0.2 nN constant-force, contact mode images.

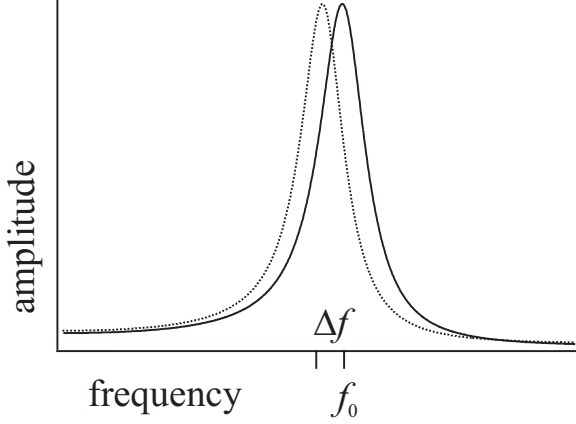


Figure 3.26: Amplitude response of the cantilever. A force gradient causes a shift of the resonance frequency.

frequency, is required for the oscillator to respond to a force. This severely limits the acquisition time since Q can be very high ($> 10^4$) in high vacuum for a 25 kHz cantilever. Instead, the resonance frequency response is measured to obtain the force gradient [57].

The growth of force microscopy past mere topographical mapping was made possible by noncontact force microscopy. Magnetic force gradients were imaged by scanning a magnetized cantilever tip over a magnetic surface [58]. Detecting electrostatic forces and force gradients was first demonstrated by Martin *et al.* [59]. The electrostatic force measured in their experiment is due to the Kelvin force present between the plates of a capacitor. This force can be derived from the energy stored in a capacitor, which is presented in Section A.3. The Kelvin force is named after Lord Kelvin's original experiment [60], and given by

$$F_z = -\frac{1}{2} \frac{\partial C}{\partial z} V^2, \quad (3.4)$$

where C is the capacitance between the tip and the sample surface, and z is the tip-surface coordinate. V is the applied potential between the cantilever and the

surface, and includes the contact potential difference, $\Delta\Phi$, which is often referred to as the surface potential. The contact potential difference includes the difference between the work function of the cantilever tip and that of the surface, as well as a number of surface effects that may alter the work function. The concept of $\Delta\Phi$ is discussed in Appendix A.2.

Equation 3.5 gives the resonance frequency of the cantilever, f , as a function of the spring constant, k , the capacitance, C , the applied potential between the cantilever and the sample, V , and the contact potential difference, $\Delta\Phi$.

$$f \approx f_0 - \frac{f_0}{4k} \frac{\partial^2 C}{\partial z^2} (V + \Delta\Phi)^2 \quad (3.5)$$

Figure 3.27 illustrates the dependence of f on the second derivative of the tip-sample capacitance, $\partial^2 C / \partial z^2$, and the potential between the tip and sample. The response of the resonance frequency as a function of the applied potential is drawn as the thick solid curve. A change in the capacitance only changes the curvature of the quadratic response (thin dotted curve in Figure 3.27). A change in the potential, which may arise from a change in $\Delta\Phi$, charge, or an applied potential, shifts the quadratic response laterally (thin solid curve in Figure 3.27).

For a more intuitive understanding of the cantilever response when part of a capacitor, consider the energy of the harmonic oscillator, $U = \frac{1}{2}kz^2$ and the energy of a capacitor, $U \sim z^{-a}$ (a is usually between 1 and 2), which are plotted in red and black, respectively, in Figure 3.28. The resulting potential, shown in blue, is similar to a harmonic oscillator with a smaller spring constant ($U \approx \frac{1}{2}(k - \Delta k)z^2$). Because $f_0 = 1/2\pi\sqrt{k/m}$, a change in the spring constant results in a change in the resonance frequency.

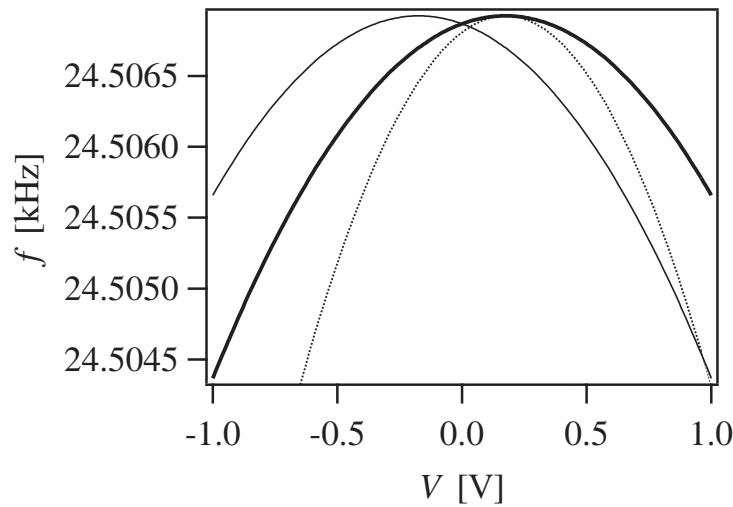


Figure 3.27: Quadratic response of the cantilever resonance frequency to the potential between the cantilever and the sample.

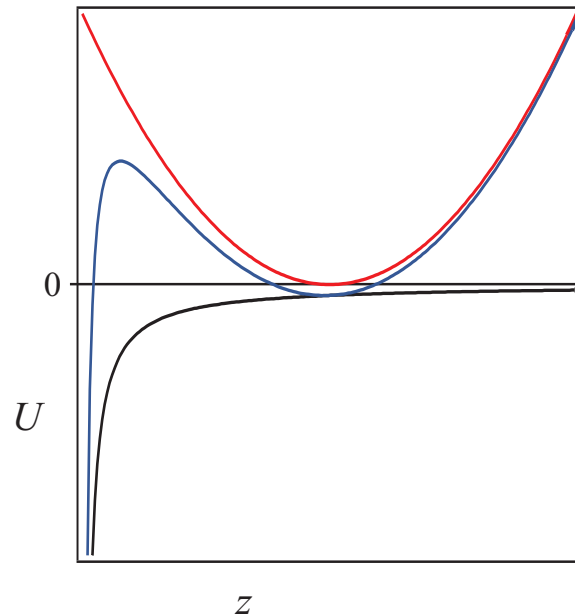


Figure 3.28: Energy of a cantilever when part of a capacitor. (Red) Energy of the harmonic oscillator. (Black) Energy of a capacitor. (Blue) Resulting energy of the system.

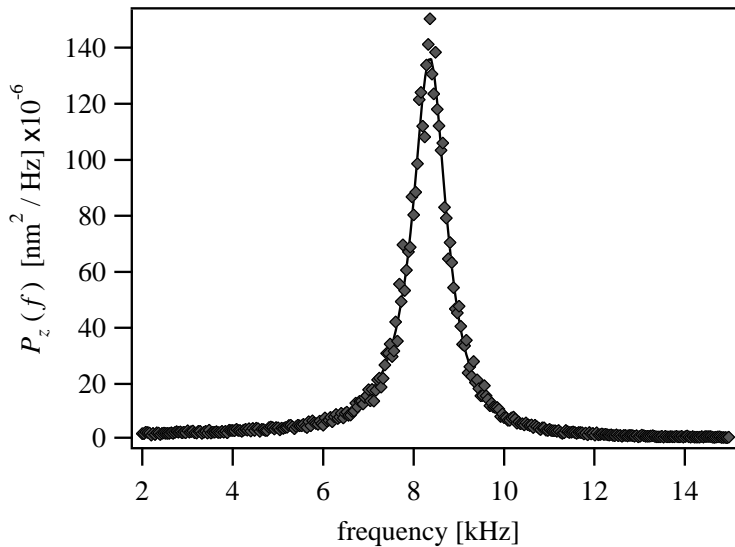


Figure 3.29: Power spectral density of a cantilever at room temperature and ambient pressure. The cantilever is driven only by thermally-induced fluctuations in position, which set the noise level of the force measurement.

3.5.5 Force sensitivity

High-sensitivity is critical for quantitative electric force microscopy. Working in ambient conditions severely limits force and force gradient sensitivity. Using a fiber-optic interferometer to detect the cantilever motion, the noise level in our experiment is limited by the thermally-induced (Brownian motion) fluctuations in position, which are set by the cantilever parameters and the temperature. At a well defined temperature, T , we can obtain the cantilever spring constant, k , the quality factor, Q , and resonance frequency, f_0 , from a power spectrum of the cantilever's thermal motion (Figure 3.29). This allows us to quantify our force and force gradient sensitivities.

| Parameter | Units | $P = 1000 \text{ mbar}$ | $P = 10^{-6} \text{ mbar}$ |
|-------------|-----------------------|-------------------------|----------------------------|
| Q | — | $50 - 150$ | $10,000 - 20,000$ |
| F_{\min} | 10^{-15} N | 100 | 8 |
| F'_{\min} | 10^{-6} N/m | 7 | 0.6 |

Table 3.2: Comparison of typical room temperature sensitivities at ambient pressure and in high vacuum obtained in a $B = 10 \text{ Hz}$ measurement bandwidth. The values for the quality factor, Q , the minimum detectable force, F_{\min} , and minimum detectable force gradient, F'_{\min} , are common for the titanium/platinum coated commercial cantilever used here. These cantilevers have a resonance frequency of $f_0 = 24\text{--}26\text{kHz}$ and a spring constant of $k = 1\text{--}2\text{N/m}$. Here F'_{\min} was obtained assuming $z_{\text{rms}} = 10 \text{ nm}$.

The minimum detectable force, F_{\min} , is given by

$$F_{\min} = \sqrt{\frac{2kk_{\text{B}}TB}{\pi Qf_0}}, \quad (3.6)$$

where F is the force between the cantilever and the surface and B is the measurement bandwidth [61]. The minimum detectable force gradient, F'_{\min} , is given by

$$F'_{\min} = \sqrt{\frac{kk_{\text{B}}TB}{\pi Qf_0 z_{\text{rms}}^2}}, \quad (3.7)$$

where z_{rms}^2 is the root mean square displacement of the driven oscillator [57].

The sensitivities reported in Table 3.2 demonstrate the great advantage of operating a scanned probe microscope in high vacuum ($1 \times 10^{-6} \text{ mbar}$). The quality factor, Q , which is proportional to the oscillator's displacement in response to an applied force, increases dramatically from $Q \sim 10^2$ to $Q \sim 10^4$. The frequency noise with $B = 10 \text{ Hz}$ and a drive of $z_{\text{rms}} = 10 \text{ nm}$ is 14 mHz, within a factor of

1.2 of the thermal limit. The force and force gradient sensitivities are improved by a factor of 10–20 at room temperature. Sensitivity improves further as the temperature is decreased and Q increases, according to Equations 3.6 and 3.7. Two electrons spaced 50 nm apart make a force of $F = 9 \times 10^{-14}$ N and a force gradient of $F' = 3.7 \times 10^{-6}$ N/m. Table 3.2 indicates the electrostatic interaction between two such electrons is already detectable using a commercial cantilever at room temperature, if operated in vacuum.

3.5.6 Overview of experimental procedures

Although an experimental procedure is given in Chapters 5 and 6, a brief summary is given here. In order to investigate a film or an operating organic device using high-sensitivity electric force microscopy, we need to work with a substrate that is compatible with the instrument. Since the microscope head is large compared to the μm -spaced channel length of most devices, electrical connections to the device must be made at least 1 cm from the channel. We use a planar interdigitated device, which significantly decreases the time required to locate a device channel *in situ* and allows us to study variability across different sections of a device gap without having to remount a sample.

After depositing the organic film onto the device substrate by spin-casting (in air) or thermal evaporation (in vacuum), we measure the device's current-voltage characteristics in high vacuum with a commercial probe station. The device is then transported to the electric force microscope. Electrical connections are made using clips, and we check each device-clip connection carefully for electrical continuity before loading the device into the electric force microscope. The microscope's vacuum space is next pumped to high vacuum for 1-2 hours until a pressure of

10^{-6} mbar is reached. It is convenient to let the tip approach the surface during this time.

We employ a titanium/platinum coated cantilever (model NSC21, MikroMasch) having a typical resonance frequency $f_0 = 25$ kHz, a spring constant $k = 1$ N/m, and a quality factor $Q \sim 10^4$ in vacuum. If topographical or electric-force gradient imaging resolution deteriorates, we replace the cantilever. Often, cantilever replacement is required after only a week under normal operating conditions.

Depending on the device, it may be necessary to locate the source-drain channel. Instead of imaging the topography of the surface until a channel is found, we apply a small potential to the electrodes or the tip. This creates a large force gradient between the metal electrodes and the tip that makes the electrodes easy to “see” in a force gradient image. The electrodes stand out even when the tip is up to 500 nm above the sample surface, making inertial repositioning using the xy sample scanner straightforward. When studying organic electronic films and devices, it often happens that unwanted particles or static charge appear in the image, so easy coarse sample positioning *in situ* is a must.

Once the device is positioned below the tip, the topography is usually obtained by intermittent contact mode imaging. The sample surface is located by recording a cantilever displacement versus distance curve and finding the “snap-in” distance at which the cantilever spring constant is overcome by the van der Waals force gradient. During this process, the height of the tip is measured using a second fiber-optic interferometer. To correct for sample tilt, we control the tip height so that it lies in a plane above the surface during electric force microscope scans. This is accomplished by acquiring force-distance curves at selected points near the edges of the image and then using this information to level the scan by adjusting

the tip height in real time while scanning.

We quantify the local potential and the capacitance derivative between the metallic probe and the sample by measuring the cantilever resonance frequency as a function of either the tip or sample potential along a line. The tip is typically grounded. When scanning over films deposited on metal, a potential is applied to the underlying metal; when scanning devices, the tip potential is referenced to either the source or drain electrode.

This open-loop approach to acquiring surface potential and capacitance information is different from standard Kelvin probe techniques since we do not modulate the applied voltage and do not rely on a feedback circuit to continuously null the potential difference between the tip and surface. Although imaging speed is reduced with our approach, the local potential and tip-sample capacitance derivative are obtained in a single linescan.

Chapter 3 references

- [1] W. R. Silveira and J. A. Marohn, Review of Scientific Instruments **74**, 269 (2003).
- [2] M. D. Kirk, T. R. Albrecht, and C. F. Quate, Review of Scientific Instruments **59**, 833 (1988).
- [3] C. W. Yuan *et al.*, Applied Physics Letters **65**, 1308 (1994).
- [4] C. W. Yuan *et al.*, Journal of Vacuum Science and Technology B **14**, 1210 (1996).
- [5] A. Volodin, K. Temst, C. V. Haesendonck, and Y. Bruynseraede, Applied Physics Letters **73**, 1134 (1998).
- [6] R. E. Thomson, Review of Scientific Instruments **70**, 3369 (1999).
- [7] M. T. Woodside *et al.*, Physica E **6**, 238 (2000).
- [8] N. Suehira *et al.*, Applied Surface Science **157**, 343 (2000).
- [9] A. Volodin, K. Temst, C. V. Haesendonck, and Y. Bruynseraede, Physica C **332**, 156 (2000).
- [10] H. J. Hug *et al.*, Review of Scientific Instruments **70**, 3625 (1999).
- [11] J. Rychen, T. Ihn, P. Studerus, A. Herrmann, and K. Ensslin, Review of Scientific Instruments **70**, 2765 (1999).
- [12] C. B. Prater *et al.*, Journal of Vacuum Science and Technology B **9**, 989 (1991).
- [13] Q. Dai, R. Vollmer, R. W. Carpick, D. F. Ogletree, and M. Salmeron, Review of Scientific Instruments **66**, 5266 (1995).
- [14] T. R. Albrecht, P. Grütter, D. Rugar, and D. P. E. Smith, Ultramicroscopy **42**, 1638 (1992).
- [15] H. J. Hug *et al.*, Review of Scientific Instruments **64**, 2920 (1993).
- [16] K. Moloni, B. M. Moskowitz, and E. D. Dahlberg, Geophysical Research Letters **23**, 2851 (1996).
- [17] D. V. Pelekhov and G. Nunes, Czech. Journal of Physics **46**, 2833 (1996).
- [18] D. V. Pelekhov, J. B. Becker, and G. Nunes, Applied Physics Letters **72**, 993 (1998).

- [19] D. V. Pelekhov, J. B. Becker, and G. Nunes, Review of Scientific Instruments **70**, 114 (1999).
- [20] R. Euler, U. Memmert, and U. Hartmann, Review of Scientific Instruments **68**, 1776 (1997).
- [21] W. Allers, A. Schwarz, U. D. Schwarz, and R. Wiesendanger, Review of Scientific Instruments **69**, 221 (1998).
- [22] M. Vogel, B. Stein, H. Pettersson, and K. Karrai, Applied Physics Letters **78**, 2592 (2001).
- [23] N. Suehira, Y. Tomiyoshi, Y. Sugawara, and S. Morita, Review of Scientific Instruments **72**, 2971 (2001).
- [24] M. Roseman and P. Grütter, Review of Scientific Instruments **71**, 3782 (2000).
- [25] P. Weitz, E. Ahlswede, J. Weis, K. V. Klitzing, and K. Eberl, Applied Surface Science **157**, 349 (2000).
- [26] D. Rugar, C. S. Yannoni, and J. A. Sidles, Nature **360**, 563 (1992).
- [27] J. A. Sidles and D. Rugar, Physical Review Letters **70**, 3506 (1993).
- [28] O. Zuger and D. Rugar, Applied Physics Letters **63**, 2496 (1993).
- [29] K. Wago, O. Zuger, R. Kendrick, C. S. Yannoni, and D. Rugar, Journal of Vacuum Science and Technology B **14**, 1197 (1996).
- [30] M. A. Lantz *et al.*, Physical Review Letters **84**, 2642 (2000).
- [31] A. Schwarz, W. Allers, U. D. Schwarz, and R. Wiesendanger, Physical Review B **61**, 2837 (2000).
- [32] W. Allers, A. Schwarz, U. D. Schwarz, and R. Wiesendanger, Applied Surface Science **140**, 247 (1999).
- [33] A. D. Drake and D. C. Leiner, Review of Scientific Instruments **55**, 162 (1984).
- [34] D. Rugar, H. J. Mamin, R. Erlandsson, J. E. Stern, and B. D. Terris, Review of Scientific Instruments **59**, 2337 (1988).
- [35] K. J. Bruland *et al.*, Review of Scientific Instruments **70**, 3542 (1999).
- [36] T. Albrecht, P. Grütter, D. Rugar, and D. Smith, Ultramicroscopy **42-44**, 1638 (1992).
- [37] E. M. Muller, *Charge trapping in pentacene field-effect transistors*, PhD thesis, Cornell University, Ithaca, NY, 2005.

- [38] D. Miller and N. Moshegov, Journal of Vacuum Science and Technology A **19**, 386 (2001).
- [39] K. Besocke, Surface Science **181**, 145 (1987).
- [40] S. H. Pan, Piezoelectric motor: International Patent Publication Number WO 93/19494, International Bureau, World Intellectual Property Organization (1993).
- [41] A. K. Gupta and K. W. Ng, Review of Scientific Instruments **72**, 3552 (2001).
- [42] D. W. Pohl, Review of Scientific Instruments **58**, 54 (1987).
- [43] P. Niedermann, R. Emch, and P. Descouts, Review of Scientific Instruments **59**, 368 (1988).
- [44] J. W. Lyding, S. Skala, J. S. Hubacek, R. Brockenbrough, and G. Gammie, Review of Scientific Instruments **59**, 1897 (1988).
- [45] C. Renner, P. Niedermann, A. D. Kent, and O. Fischer, Review of Scientific Instruments **61**, 965 (1990).
- [46] O. Probst, S. Grafstrom, J. Kowalski, R. Neumann, and M. Wortge, Journal of Vacuum Science and Technology B **9**, 626 (1991).
- [47] B. L. Blackford, M. H. Jericho, and M. G. Boudreau, Review of Scientific Instruments **63**, 2206 (1992).
- [48] F. Bordoni, G. Degasperis, S. Dibattista, and G. S. Spagnolo, Sensors and Actuators A: Physics **45**, 173 (1994).
- [49] F. Mugele, A. Rettenberger, J. Boneberg, and P. Leiderer, Review of Scientific Instruments **69**, 1765 (1998).
- [50] S. R. Garner, S. Kuehn, J. M. Dawlaty, N. E. Jenkins, and J. A. Marohn, Applied Physics Letters **84**, 5091 (2004).
- [51] S. R. Garner, *Force-Gradient Detection of Nuclear Magnetic Resonance*, PhD thesis, Cornell University, Ithaca, NY, 2005.
- [52] D. D. Smith, J. A. Marohn, and L. E. Harrell, Review of Scientific Instruments **72**, 2080 (2001).
- [53] D. Rugar, H. J. Mamin, and P. Guethner, Applied Physics Letters **55**, 2588 (1989).
- [54] J. Siegel, J. Witt, N. Venturi, and S. Field, Review of Scientific Instruments **66**, 2520 (1995).

- [55] R. C. Richardson and E. N. Smith, *Experimental Techniques in Condensed Matter Physics at Low Temperatures*, Addison-Wesley, 1988.
- [56] R. Garcia and A. San Paulo, Ultramicroscopy **82**, 79 (2000).
- [57] T. R. Albrecht, P. Grütter, D. Horne, and D. Rugar, Journal of Applied Physics **69**, 668 (1991).
- [58] Y. Martin and H. K. Wickramasinghe, Applied Physics Letters **50**, 1455 (1987).
- [59] Y. Martin, D. W. Abraham, and H. K. Wickramasinghe, Applied Physics Letters **52**, 1103 (1988).
- [60] Lord Kelvin, Philosophical Magazine **46**, 82 (1898).
- [61] K. Y. Yasumura *et al.*, Journal of Microelectromechanical Systems **9**, 117 (2000).

CHAPTER 4
CHARGE TRANSPORT AND INJECTION IN A MODEL
ORGANIC SEMICONDUCTOR

In this chapter, the molecularly doped polymer system is introduced. The chemical and structural nature of the triarylamine is discussed, followed by a summary of the key findings concerning charge transport theory and experiment. We next examine space-charge limited current (SCLC) in solids. Finally, the fundamental theories commonly used to describe charge injection in organic materials are presented. These theories are tested microscopically in Chapter 5.

4.1 Overview of the molecularly doped polymer system

Molecularly doped polymers are a class of organic materials offering unique chemical and electrical properties. The molecularly doped polymer system consists of small organic molecules dispersed into a host polymer, creating an amorphous matrix of molecules positioned randomly in space. Figure 4.1 shows the structure of the triarylamine we have investigated, N,N'-diphenyl-N-N'-bis(3-methylphenyl)-(1,1'-biphenyl)-4,4'-diamine, or more simply, TPD. Host polymers include polystyrene

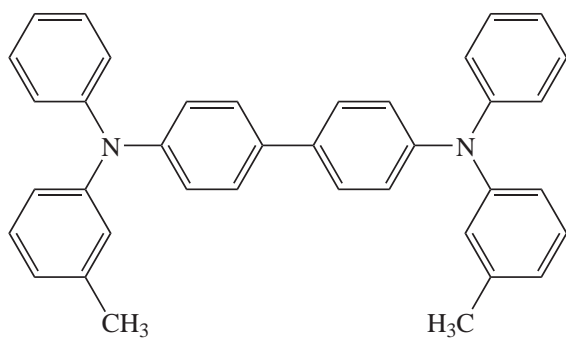


Figure 4.1: Structure of the triarylamine, N,N'-diphenyl-N-N'-bis(3-methylphenyl)-(1,1'-biphenyl)-4,4'-diamine, TPD.

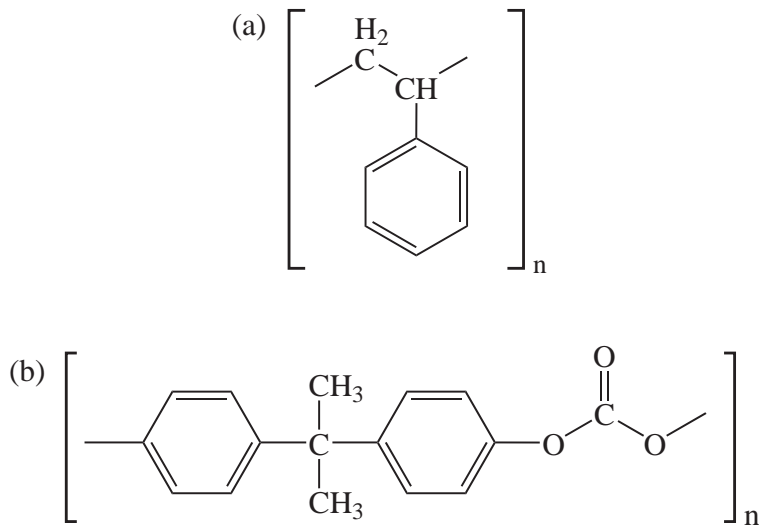


Figure 4.2: Structures of the host polymers (a) polystyrene and (b) polycarbonate.

(PS) and polycarbonate (PC), shown in Figure 4.2(a) and 4.2(b), respectively.

Molecularly doped polymers offer a wide range of chemical and physical tunability. By varying the polarity of the host polymer, one can vary the electrostatic environment of the dispersed molecules. Similarly, the polarity of the dopant molecule used as the conductive center is easily varied by altering the structure of the triarylamine. Because charge transport occurs by thermally activated hopping between adjacent molecules, the charge mobility, μ , is a strong function of temperature. Finally, the mobility is easily tuned over several orders of magnitude by varying the concentration of the dopant molecules.

4.2 Chemical nature of the triarylamine

In most charge transport and injection studies, the chemical nature of the triarylamine is ignored, and the focus is instead yielded to physics. Here, we explore what is known about the chemistry of TPD and other triarylamine derivatives. If

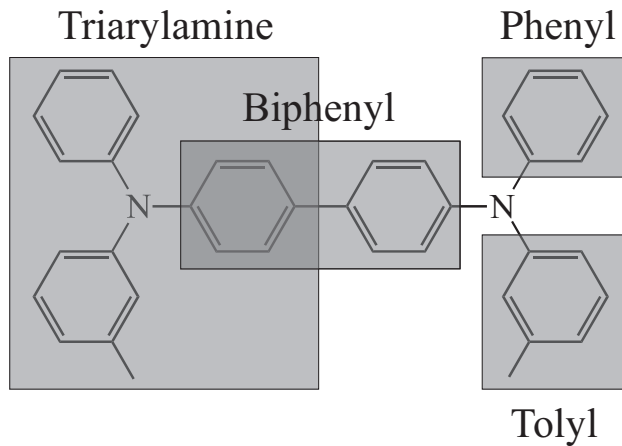
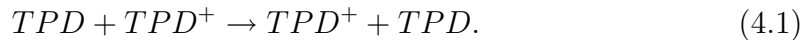


Figure 4.3: Chemical moieties of the triarylamine, N,N'-diphenyl-N,N'-bis(3-methylphenyl)-(1,1'-biphenyl)-4,4'-diamine, TPD.

we are to understand charge injection and transport at the most fundamental level, the chemical and physical view of the molecule will have to merge. Charge transport is described by the simple chemical reaction between adjacent molecules,



The structure of TPD, shown in Figure 4.3, is composed of two triarylamine groups and one biphenyl linkage. Of the three groups bonded to the center nitrogen atom, one of the aryl groups is a phenyl group (C_6H_5) and the other is a tolyl group ($CH_3C_6H_4$). The tolyl group breaks one degree of symmetry in the TPD molecule. Often, the classification of triarylamine and triphenylamine are used interchangeably.

Theoretical investigations have found the nature of the TPD molecule is best understood by considering its components, namely the two triarylamines linked by a biphenyl segment. Sakanoue *et al.* found that amines such as dimethyl aniline, which has only one phenyl group bonded to the central nitrogen, underwent significant structural changes during charge transfer [1]. Upon ionization to a cationic

state, the bonds surrounding the nitrogen atom change from tetrahedral (sp^3) to planar (sp^2). However, triarylamine, completely surrounded by bulkier aromatic phenyl groups, was found to be planar (sp^2) in both the neutral and charged species. Smaller structural changes of the amine seem to best facilitate charge transfer. The phenyl and tolyl groups form a propeller-like geometry surrounding the nitrogen atom with a torsion angle of approximately 40° , which were found to decrease only a few degrees upon removing an electron [2]. Crystallography has confirmed the planar geometry of the nitrogen atom in triphenylamine [3].

Theoretical investigations have also uncovered the importance of the biphenyl linkage. The biphenyl segment of TPD is central to the molecule's unique transport and charge transfer properties and makes it much different from triphenylamine. The electronic properties of oligophenylenes, which are similar in nature to the biphenyl moiety, have been investigated theoretically [4]. Zojer *et al.* found that the individual rings in oligophenylenes are highly aromatic, such that delocalization occurs only on the individual ring when neutral. Adjacent rings are not coplanar. Their calculations indicate that the phenyl rings twist approximately 40° in a neutral molecule to reach an energy minimum. The angle between the rings decreases by up to 20° when an electron is removed from one of the rings, causing the geometry to become more quinoid-like. Removing another electron, creating a doubly charged species, causes the rings to fall into the same plane, which is a nearly perfect quinoid structure.

A theoretical study of the central biphenyl segment of the TPD molecule confirms that the change in geometry upon ionization to a cationic radical state is similar to the changes that occur in the biphenyl segment of oligophenylenes. However, quite unexpectedly, the geometrical changes that occur in the triphenylamine

moiety of TPD are different from triphenylamine alone [2]. The phenyl rings participating in the biphenyl segment become more planar, which again is more similar to a quinoid-like configuration. However, the terminal tolyl and phenyl rings become more orthogonal in order to compensate for this change.

We have seen that TPD is hardly the flat molecule depicted in Figure 4.1. In an amorphous solid solution, one might expect several conformations to be found. It is possible for the phenyl and tolyl groups to rotate about the C–N σ -bond. It is also possible for rotation to occur between the two phenyl rings that join the amines, where the carbon-carbon bond is also mostly σ in nature.

Theoretical calculations by Malagoli *et al.* have found that there are six stable conformers within 0.1 kcal/mol of each other [5]. The magnitude of the molecular dipole moment depends on the position of the tolyl group. This fascinating result emphasizes how disorder is inherent in TPD films. The dipole moment for the six cis and trans conformers found in this study are given in Figure 4.4. The average dipole moment is $\mu_d = 0.382$ D. Clearly, the tolyl group has a rather dramatic effect on the dipole moment. They also studied the effects of various constituents such as the methoxy group ($-\text{OCH}_3$), the cyano group ($-\text{CN}$), and other fluorinated compounds. It was found that the molecular dipole moment increased by up to an order of magnitude in some cases. Time of flight studies have shown that the mobility decreases substantially with such substitution [6], presumably from electrostatic variations surrounding each TPD-based molecule.

The potential for chemical tunability is a great advantage of organic molecules. Due to the inductive effects of various substituents, the energies of the highest occupied molecular orbital (HOMO) and lowest unoccupied molecular orbital (LUMO) have been calculated to shift up to 0.5 eV by Cornil *et al.* [7]. However, photo-

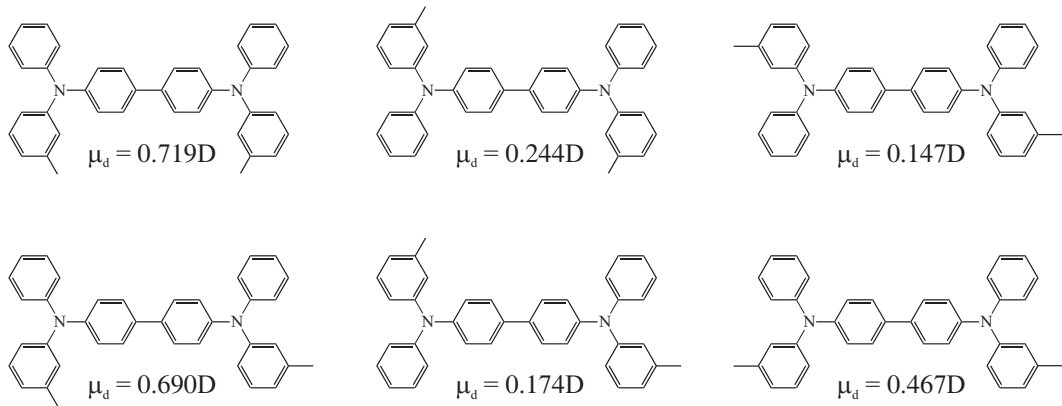


Figure 4.4: Six stable conformers of TPD and the associated dipole moment, μ_d , [5].

electron spectroscopy studies show that the energy gap is not altered. This holds much promise for the fine tuning of energy barriers at the charge injecting interface. However, the trade off for improved charge injection will most likely be a lower mobility, as Maldonado *et al.* have found.

We have found that the charge transfer chemistry of the triarylamine, TPD, is more than just the sum of its parts. The amine and biphenyl groups combine to form a chemical system capable of efficient charge transfer. The presence of the tolyl group leads to a variety of stable conformers and dipole moments. Chemical substitution, while advantageous for tuning the energy levels of the HOMO and LUMO, may decrease the mobility.

4.3 Charge transport in molecularly doped polymers

In this section, we describe the fundamental properties and characterization techniques of charge transport in the molecularly doped polymer system. This is not meant to be an exhaustive review, but a summary of the ideas relevant to this work. For a comprehensive review, please refer to *Organic Photoreceptors for*

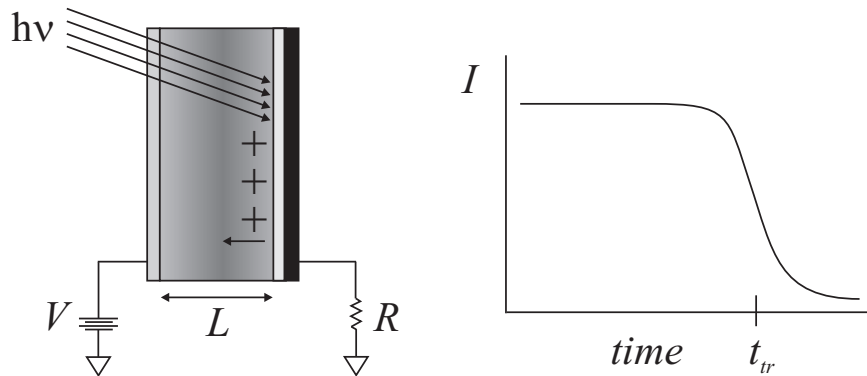


Figure 4.5: Time of flight experiment.

Xerography, written by P. M. Borsenberger and D. S. Weiss [8].

4.3.1 Time of flight technique

The molecularly doped polymer system is used heavily in the xerography industry. In fact, this organic material can be found on the belt of almost any copy machine. The film is used to transport positive charge (holes) which annihilate electrons on the surface of the low mobility film. This technique allows one to pattern charge on the surface of the organic film. The remaining electrons attract the toner which is transferred to the paper to create an image.

In order to improve the copying process, companies such as Xerox put forth an enormous effort to understand charge transport in molecularly doped polymers. The time of flight technique allows for the study of the mobility, μ , without having to consider charge injection. The mobility is an intrinsic property of a material, defined by the drift velocity, v , per unit electric field, E .

$$\mu = \frac{v}{E} \quad (4.2)$$

The time of flight technique [9] is commonly used to measure charge mobilities in organic materials and has been particularly useful for understanding charge

transport in molecularly doped polymers. Figure 4.5 illustrates the experiment. A fast laser pulse enters a transparent electrode on the left, travels through the organic film and creates a sheet of electron/hole pairs where it is absorbed at the thin film on the right electrode. In this case, the electrons quickly enter the right electrode. The holes enter the organic film. As the holes traverse the organic film from left to right, a current, I , is generated and recorded. As they reach the left electrode, the current decays. The tail of the current reflects broadening of the charge sheet due to repulsion and diffusion. The charge mobility is found by relating the transit time, t_{tr} , to the length of the sample, L , the mobility, μ , and the electric field, E , to give [8]

$$t_{tr} = \frac{L}{\mu E} = \frac{L^2}{\mu V}. \quad (4.3)$$

4.3.2 Hopping transport and the Gaussian disorder model

Organic molecules in the molecularly doped polymer system are held together in the solid phase primarily by van der Waals interactions. They do not interact in such a way to cause significant delocalization. Because of this, the transport of charge in the molecularly doped polymer system has been successfully described by the passing of charge between adjacent molecules, illustrated in Figure 4.6. This type of charge transport, which involves localization of charge, has been termed hopping transport. The localized charge polarizes the surrounding molecules very quickly, and this has been called the “small polaron” [10].

This brief description of the Gaussian disorder model primarily follows the review of charge transport by Bässler [11]. The key feature of this model is the functional form of the density of localized energy states (Equation 4.4). The ener-

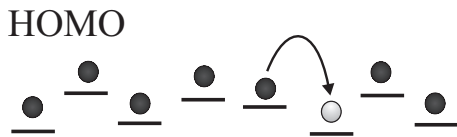
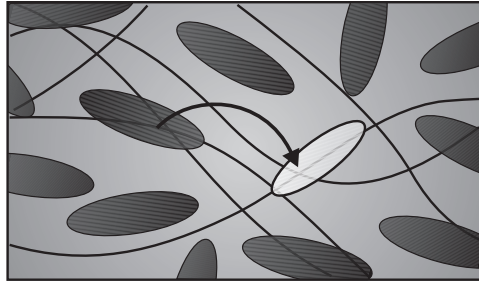


Figure 4.6: Hopping transport between adjacent molecules.

gies, E , involved in charge transport are taken to have a Gaussian distribution,

$$g(E) = \frac{1}{\sqrt{2\pi\sigma^2}} e^{-E^2/2\sigma^2}. \quad (4.4)$$

The localized charges move by hole transport in the HOMO. The difference between the average energy of the HOMO and LUMO is the energy gap, $E_{\text{gap}} \sim 3 \text{ V}$. This is represented in Figure 4.7. The range of energies is thought to arise from variations of the electrostatic environment surrounding the organic molecules. Each site has a different environment due to random van der Waals and dipole-dipole interactions, which will cause a variation of the polarization energy of a particular site [8]. By the central limit theorem, the random electrostatic environment leads to an approximately Gaussian density of site energies, with a width σ between 50 and 150 mV in typical molecularly doped polymers [12]. The distance between hopping sites is also described as a Gaussian distribution, an excellent assumption considering the amorphous nature of the molecularly doped polymer.

The hopping rate between molecules, described by Miller and Abrahams [13], is used in the Gaussian disorder model. In the original paper, Miller and Abra-

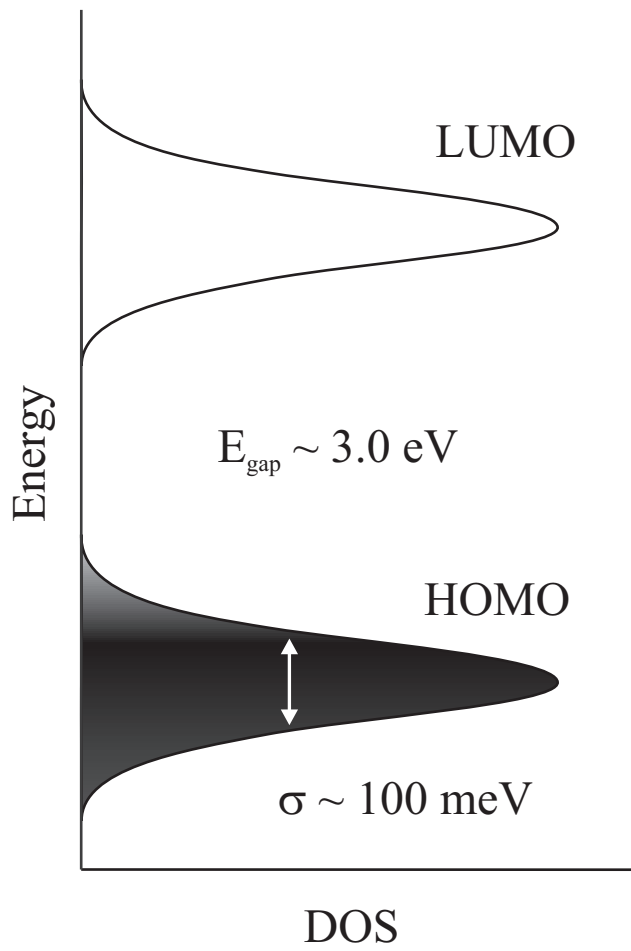


Figure 4.7: Gaussian distribution of localized states for the molecularly doped polymer.

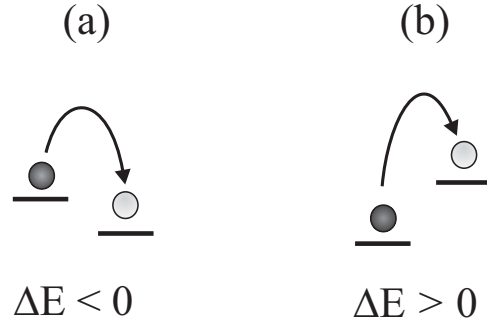


Figure 4.8: (a) Hopping downhill in energy. (b) Hopping uphill in energy.

ham sought to explain charge transport in doped inorganic semiconductors at low temperatures. The transport is no longer delocalized in a doped semiconductor at low temperatures, but occurs by hopping between localized states. The model indicates the hopping rate between molecules is determined by wavefunction overlap and is therefore an exponentially decaying function of the distance between sites, r , and the difference between the final and initial states, ΔE . The rate, R , is given by

$$R = R_0 e^{-r/r_0} e^{-\Delta E/k_B T}, \text{ for } \Delta E > 0, \quad (4.5)$$

$$R = R_0 e^{-r/r_0}, \text{ for } \Delta E < 0,$$

where R_0 is a prefactor for the hopping rate and r_0 is a scaling factor for the hopping distance, r [13].

For $\Delta E > 0$, the rate is determined in part by a Boltzmann factor. For $\Delta E < 0$, the rate does not depend on the energy difference. These two cases are illustrated in Figure 4.8(a) and 4.8(b). We can see that increasing the distance, r , between the molecules decreases R in both cases. To conserve energy, charge-transfer is followed by phonon emission or absorption. Although the Miller-Abrahams theoretical description has been very successful, there has also been work done to

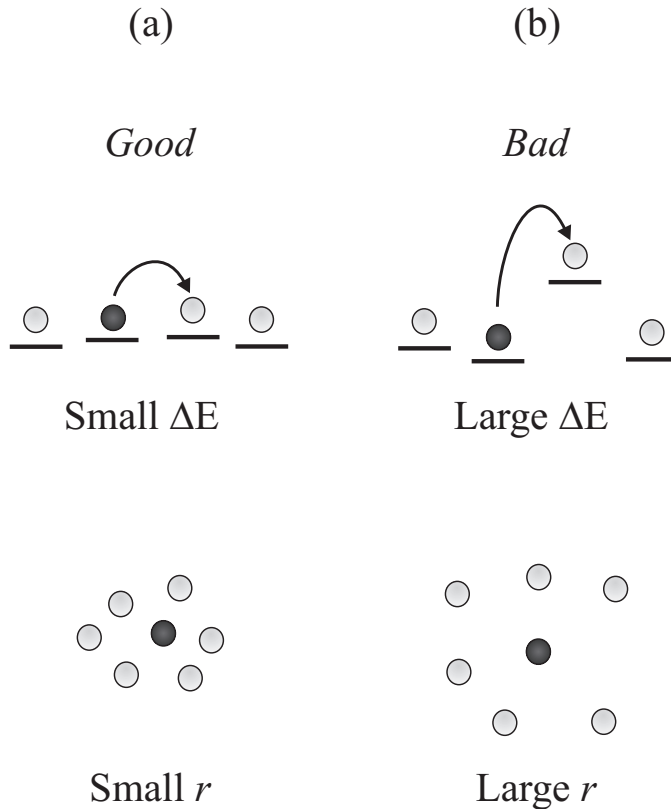


Figure 4.9: (a) “Good” hops: Closely spaced energy levels and small intermolecular distances. (b) “Bad” hops: Large difference in energy levels and large intermolecular distances.

explain the charge-transfer event in terms of Marcus theory [1].

We can summarize the model in terms of “good” and “bad” hops (Figure 4.9). Hopping is much easier between energy levels that are closely spaced and when the intermolecular distance is small (Figure 4.9(a)). On the other hand, hopping is inhibited when large energies are required and when the intermolecular distance is large (Figure 4.9(b)). Therefore, a large width, σ , of the density of localized states, $g(E)$, makes charge transport more difficult, as does a lower concentration molecularly doped polymer. The width, σ , can be minimized by decreasing electrostatic variations due to large dipoles.

Concentration dependence of the mobility

One of the great advantages of studying the molecularly doped polymer system is the tunability of the mobility by varying the concentration. The concentration dependence of the mobility, μ , is predicted nicely by the Gaussian disorder model. First, the zero-field mobility, μ_0 , which is the part of the mobility that depends on the average intersite distance, r , is proportional to the mean square intersite distance, r^2 (units: m²). To make sense of this, consider the mobility of a single hop – a larger hop will give a higher mobility, given that the time between hops is the same. Second, μ_0 is proportional to the hopping rate, which goes as $R_0 e^{-r/r_0}$ (Equation 4.6, units: s⁻¹). Shorter time spent on a molecule leads to a higher mobility. Finally, μ_0 is scaled by the available energy, making it inversely proportional to the thermal energy per charge, $k_B T/e$ (Units: V⁻¹). Therefore,

$$\mu \propto \frac{e}{k_B T} R_0 r^2 e^{-r/r_0}, \quad (4.6)$$

which has the correct units m² V⁻¹ s⁻¹. For example, Schein *et al.* plot ln μ/r^2 versus r and demonstrate an excellent fit in TPD-PC for concentrations ranging from 25-80 % weight [14].

Temperature dependence of the mobility

The theory also correctly predicts the temperature dependence of μ . If a small number of charge carriers are introduced into a Gaussian density of localized states at E = 0, it is found, analytically, that the average energy after equilibration, $\langle E_\infty \rangle$, is

$$\langle E_\infty \rangle = \frac{\sigma^2}{k_B T}. \quad (4.7)$$

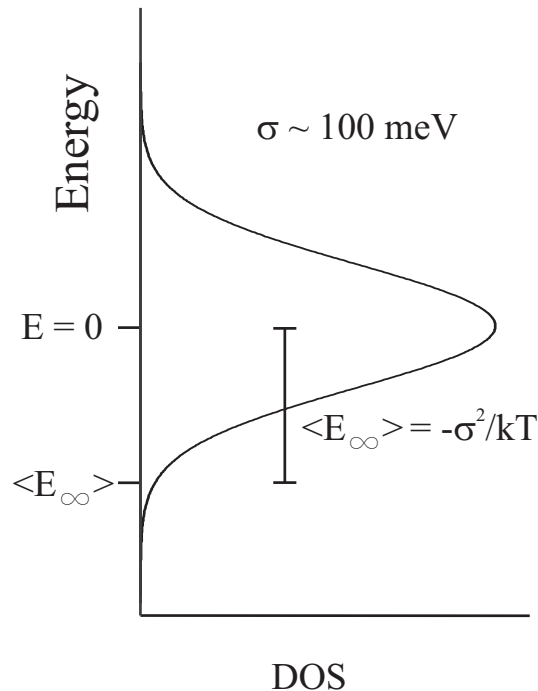


Figure 4.10: Dilute charge carrier energies in a Gaussian distribution of localized states. Charge carriers placed at $E = 0$ will relax to $\langle E_\infty \rangle$.

This is illustrated in Figure 4.10 for the case of a small number of electrons placed into an empty LUMO (the equivalent case is holes in the HOMO). The small number of charges equilibrates in the tail of the Gaussian density of localized states. It equilibrates so deep into the tail, $\sim 4\sigma$, that the density of states is very small, and considerable thermal activation is required for charge transport. On average, the activation energy, E_a , required will be, $\sigma^2/k_B T$, the distance from $\langle E_\infty \rangle$ to $E = 0$.

Therefore, although we might expect the temperature dependence of the mobility to follow an Arrhenius-like behavior,

$$\mu = \mu_0 e^{-E_a/k_B T}, \quad (4.8)$$

the activation energy carries a temperature dependence leading to a non-Arrhenius

form,

$$\mu = \mu_0 e^{-\sigma^2/(k_B T)^2}. \quad (4.9)$$

Therefore, by measuring the temperature dependence of the mobility, σ is found.

Electric field dependence of the mobility

So what does the Gaussian disorder model predict for the electric field dependence of the mobility? From the hopping rate given by Equation 4.6, we see that $\mu \propto \exp(-\Delta E/k_B T)$ for $\Delta E > 0$ (Figure 4.11(a)). In an applied electric field, E , the energy between two levels will be lowered by eEr when the electric field is parallel to the direction of the hop (Figure 4.11(b)). Therefore, the mobility should go as

$$\mu \propto e^{eEr/k_B T}. \quad (4.10)$$

Unfortunately, the Gaussian disorder model does not accurately predict the electric field dependence of the mobility. This is quite surprising considering the great success of the model in explaining temperature and concentration dependences of the mobility. Experiments have shown the mobility to depend exponentially on the square root of the electric field [15],

$$\mu \propto e^{\beta_\mu \sqrt{E}}. \quad (4.11)$$

Although the effects of trapping give a Poole-Frenkel-like, \sqrt{E} -dependence of the mobility [16] as shown in Equation 4.11, molecularly doped polymers are trap-free. Another explanation is required.

In this section, we found the Gaussian disorder model gives a powerful description of the charge transport properties of molecularly doped polymers. It successfully describes the concentration and temperature dependence of the mo-

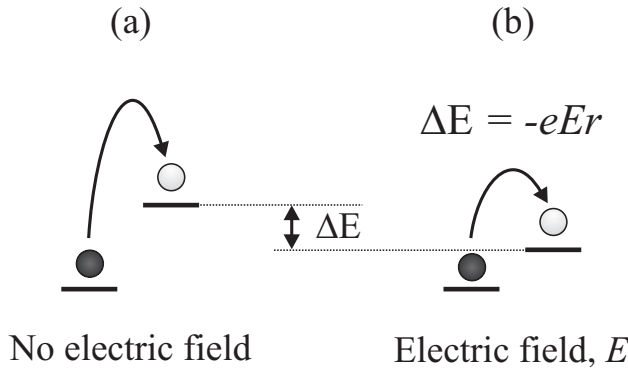


Figure 4.11: Barrier lowering - Gaussian disorder model. Difference in energy levels (a) without and (b) with an applied electric field.

bility. However, an understanding of the electric field dependence of the mobility was not extracted from this theory.

4.3.3 \sqrt{E} , dipoles, and the correlated disorder model

We are left with the mobility dependence of $\ln \mu \propto \sqrt{E}$, which is much different than $\ln \mu \propto E$, predicted from the Gaussian disorder model. What is behind the unexpected dependence of the mobility on the electric field?

The dipolar contribution to the width, σ , of the density of localized states is key to understanding the dependence of the mobility on the electric field as well as gaining a microscopic chemical and physical understanding of the molecularly doped polymer system. In a molecularly doped polymer, the dopant molecule and the host polymer usually have a dipole moment. The mobility has been correlated to the randomly placed dipoles. Larger dipoles lead to a lower mobility because the randomly placed dipoles lead to a variation of the electrostatic environment, adding to the energetic variations that arise from van der Waals interactions [17].

Order from disorder

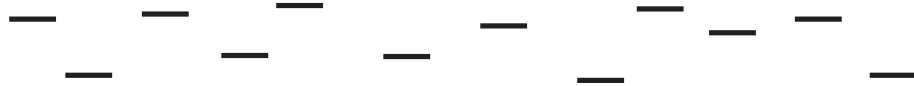
A breakthrough occurred when Novikov and Vannikov calculated the electrostatic potential from randomly oriented dipoles. They found that the potential is strongly correlated and that clusters of potential of similar magnitude are created in a 3-dimensional lattice of randomly oriented dipoles [18]. The clusters are of different sizes and shapes. They explain that this surprising result arises from the long range nature of the potential from a dipole, which goes as $1/r^2$, with r as the distance between dipoles. Their work finds that the correlation between the site energies as a function of position, $E(\mathbf{r})$, is given by

$$C(\mathbf{r}) = \langle E(\mathbf{r})E(0) \rangle \propto \frac{1}{r}. \quad (4.12)$$

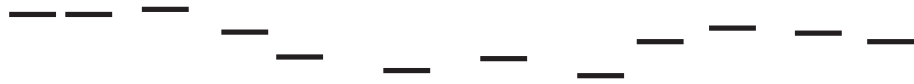
This means that two molecules near each other will not find themselves in a randomly different electrostatic potential, but will experience a similar electrostatic potential due to the long range interaction of the surrounding dipoles. This effect falls off as $1/r$ and leads to the clustering of the potential of different shapes and sizes. Neighboring sites will not have randomly assigned energies as described in the Gaussian disordered model; they will have similar energies. The energy landscape becomes much smoother from one site to the next, as shown in Figure 4.12. Compared the model that assumes no correlation between individual dipoles, larger cluster sizes will appear more frequently [19].

The work of Novikov and Vannikov was followed by a Monte Carlo simulation that incorporated the correlated energies into the Gaussian disorder model [20]. They found excellent agreement with the experimentally observed electric field dependence of the mobility. This simulation was followed by an exciting calculation by Dunlap, Parris, and Kenkre [21]. Using the fact that the site energies are

Noncorrelated energies



Correlated energies

**Figure 4.12:** Noncorrelated and correlated energy levels.

correlated due to the long range interaction of the dipole, they were able to show, analytically, the electric field dependence of the mobility as $\mu \propto \exp(\beta_\mu \sqrt{E})$, finally unraveling the Poole-Frenkel-like behavior of charge transport in the molecularly doped polymer!

An excellent discussion of the physical picture behind the field dependence of the mobility has been published by Dunlap and Kenkre [22]. In Equation 4.10, we found that $\mu \propto \exp(eEr/k_B T)$, predicted by the Gaussian disorder model since the energy barrier between adjacent sites will be lowered by an amount eEr (Figure 4.11(b)). An important parameter is r , the distance between the sites. In the Gaussian disorder model, r is just the average intersite distance since the energies are not correlated and fluctuate randomly – each site is a potential bottleneck. However, when the energies are correlated, r takes on a different meaning: the distance between a peak and a valley of the smoothly varying energetic landscape becomes the bottleneck. Because of the energetic correlation, short valleys are quite shallow and long valleys are deep. So which valley is more important to the electric field dependence of the mobility? It turns out that an intermediate valley

acts as the most critical bottleneck. Short valleys are shallow and therefore do not contribute significantly to the transit time of a charge. Long valleys, with large r , have barriers that are significantly reduced by the electric field, eEr . The culprit is a valley with a distance $r \propto E^{-1/2}$. This distance, when used in Equation 4.10, results in the Poole-Frenkel-like mobility

$$\mu = \mu_0 e^{\beta_\mu \sqrt{E}}, \quad (4.13)$$

where β_μ is a function of temperature.

In summary, the accepted description of charge transport in molecularly doped polymers is the correlated disorder model [18, 20, 21, 23–26]. The transport of injected holes occurs by hopping between the HOMO of adjacent molecules. Electrostatic interactions with the permanent dipole moments of distant molecules allow for a large number of independent contributions to the energy of an ionized molecule. By the central limit theorem, this leads to an approximately Gaussian density of site energies, with a width σ between 50 and 150 mV in typical molecularly doped polymers. This correlated disorder is the central feature that allows this model to correctly explain the surprising Poole-Frenkel-like dependence of the mobility on electric field found in molecularly doped polymers.

4.4 Space-charge limited conduction

In this section, we discuss the voltage dependence of the current density in trap free molecularly doped polymers. This is much different from what one would expect for an ohmic device. We explore how the buildup of space-charge in the bulk material is the cause of the V^2 -dependence of the current density. For clarity, we will consider the current due to electrons. An excellent discussion of space-charge

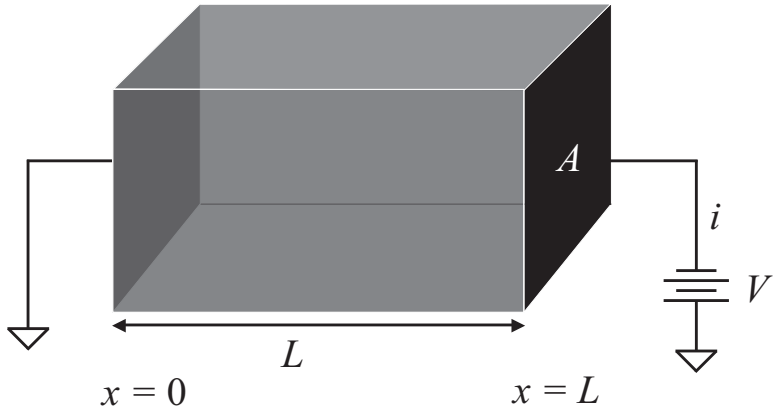


Figure 4.13: Parallel plate device.

limited current (SCLC) is presented in the text by Lampert and Mark [27].

Let us consider the current density, potential, electric field, and charge density for a molecularly doped polymer film between two electrodes (Figure 4.13). In Figure 4.13, electrons are injected at $x = 0$ and collected at $x = L$, where we have applied a positive voltage, V . We assume an ohmic contact, meaning the electrode can supply any current density.

The charge transport properties presented here are derived in Appendix B.1 and are adapted from the Child-Langmuir current solved in the text by Kusse [28]. The primary result is the current density, J_{SCL} , is proportional to V^2 ,

$$J_{\text{SCL}} = \frac{9}{8} \mu \epsilon \frac{V^2}{L^3}. \quad (4.14)$$

The potential (Equation 4.15), electric field (Equation 4.16), and charge density (Equation 4.17) are given as a function of distance from the injecting to the collecting electrode (also listed in Appendix B.1 as Equations B.9).

$$\phi(x) = \left(\frac{8J}{9\epsilon\mu} \right)^{1/2} x^{3/2} \quad (4.15)$$

$$E(x) = - \left(\frac{2J}{\epsilon\mu} \right)^{1/2} x^{1/2} \quad (4.16)$$

$$\rho(x) = - \left(\frac{\epsilon J}{2\mu} \right)^{1/2} x^{-1/2} \quad (4.17)$$

Table 4.1: Typical SCLC parameters for a molecularly doped polymer device and the resulting current, J_{SCL} .

| | |
|---------------------------|---|
| $V(0) = 0$ | [V] |
| $V(L) = 50$ | [V] |
| $\mu = 1 \times 10^{-9}$ | $\left[\frac{\text{m}^2}{\text{Vs}} \right]$ |
| $\epsilon = 3 \epsilon_0$ | $\left[\frac{\text{C}^2}{\text{Nm}^2} \right]$ |
| $J_{\text{SCL}} = 0.597$ | $\left[\frac{\text{A}}{\text{m}^2} \right]$ |

We now consider parameters typical for a molecularly doped polymer. Table 4.1 lists parameters and the resulting current density calculated from Equation 4.14. Using Equations 4.15, 4.16, and 4.17, we can calculate the potential, electric field, and charge density, respectively, from the parameters in Table 4.1. This is shown in Figure 4.14.

It is clear from Figure 4.14 that the potential (Equation 4.15) is lowered by the excess electrons (the space-charge) between the injecting and collecting electrodes. This gives a qualitative picture for the functional form of the current density, $J_{\text{SCL}} \propto V^2$. If $J = Q/t$, the planar charge density, Q , originates from the capacitance between the bulk insulator and the collecting electrode, and can be approximated as $Q = CV = eV/L$. Now, the time, t , is just the transit time for an electron to travel a distance L . So, $t = L/v$, where v is the velocity given by $v = \mu E \approx \mu V/L$. This simple approximation gives

$$J_{\text{SCL}} \approx \mu \epsilon \frac{V^2}{L^3}, \quad (4.18)$$

which is very close to Equation 4.14.

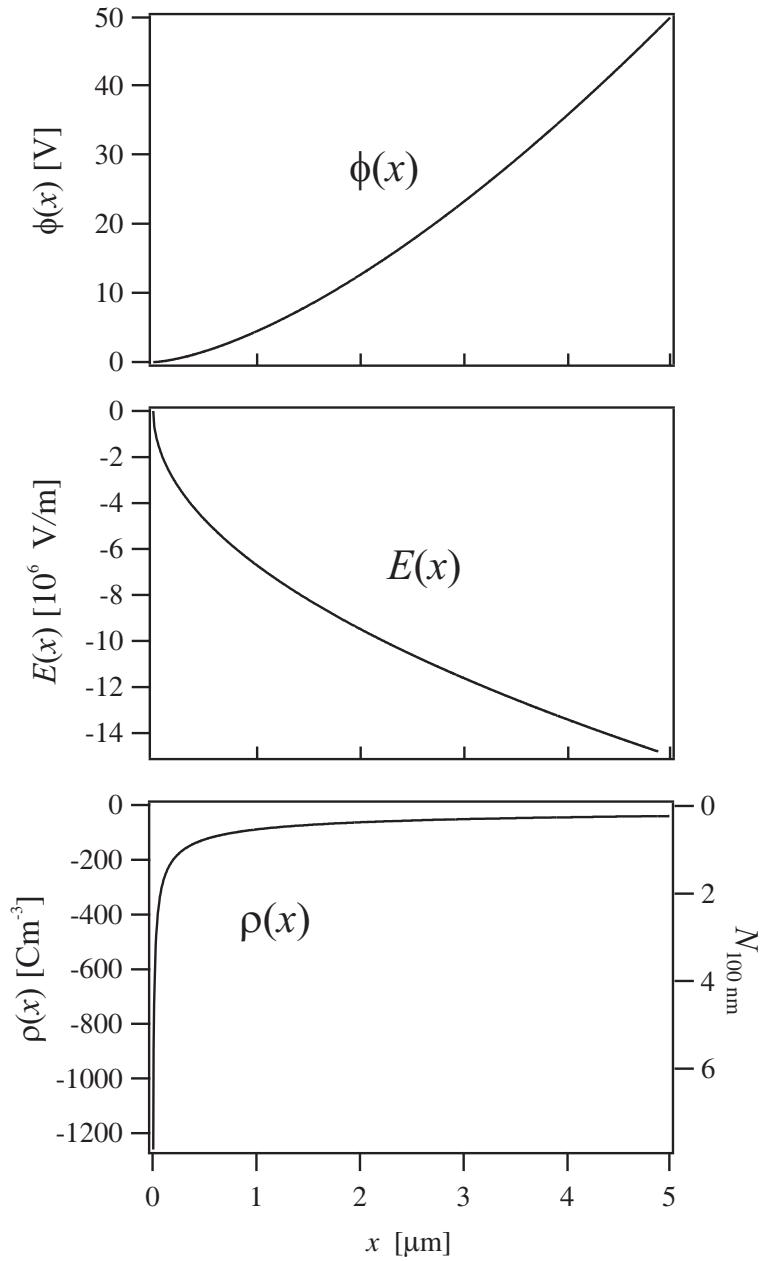


Figure 4.14: Potential, $\phi(x)$ (top), electric field, $E(x)$ (middle), and charge density, $\rho(x)$ (bottom) calculated from the parameters in Table 4.1. The x -axis begins at $x = 0$ and ends at $x = L$, with $L = 5 \mu\text{m}$. The right axis on the charge density plot is the number of charges in a $(100 \text{ nm})^3$ volume, $N_{100 \text{ nm}}$.

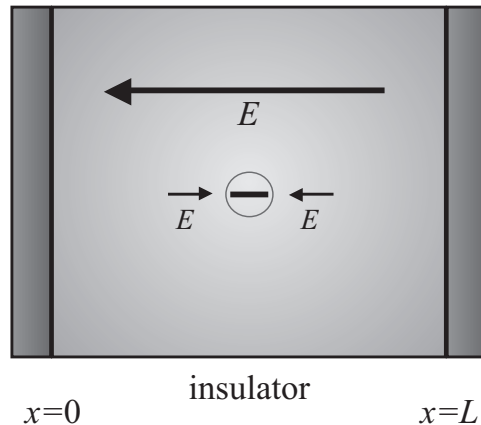


Figure 4.15: Electric field altered by space-charge. The simplest case is one electron between the electrodes.

The electric field in Figure 4.14 follows the boundary condition, $E(0) = 0$. The electric field is highest at the collecting electrode and goes as $-x^{1/2}$ (Equation 4.16). The asymmetric electric field can be qualitatively understood by considering only one electron between the injecting and extracting electrodes [28], illustrated in Figure 4.15. The large field from the electrodes points from left to right. The field from the electron decreases the large field on the left of the electron and increases the field on the right of the electron.

The charge density in Figure 4.14 illustrates how the space-charge density varies from the injecting electrode to the collecting electrode. Near the injecting electrode, $\rho(x)$ is very large and decays as $-x^{-1/2}$ (Equation 4.17). On the right axis, labeled $N_{100 \text{ nm}}$, the charge density is scaled to the number of electrons in a volume of $(100 \text{ nm})^3$. Less than $1 e^-/(100 \text{ nm})^3$ is responsible for the change in the potential across most of the device. Electric force microscopy has a typical resolution of 100 nm. At best, we can expect $\sim 1 e^-$ below the tip according to this model!

Background charge carriers

Background charge carriers are almost always present in molecularly doped polymer films [29]. They are responsible for Ohmic charge transport prior to the onset of space-charge limited current. These carriers most likely arise from accidental doping or autoionization. The background charge carrier density could also be due to photodegradation during sample preparation. The density of charge carriers, N_0 , has been found to be highly dependent on sample preparation and history [29]. Regardless of the source, these “dark” carriers are compensated by a counterion and cause Ohmic conduction to dominate over SCLC at low voltages.

Ohm’s law gives a current density, J_Ω , of

$$J_\Omega = \sigma E = \mu \rho E = \mu \rho \frac{V}{L}, \quad (4.19)$$

where $\sigma = \mu \rho$ is the conductivity, and as before, μ is the mobility, $\rho = eN_0$ is the Ohmic charge density, E is the electric field, V is the applied voltage, and L is the device length.

In TPD-PC films, Abkowitz *et al.* increased the density of the charge carrier, TPD^+ , by oxidizing a fraction of the TPD molecules [29]. The reduced counterions do not participate in conduction, but are accompanied by an equal density of TPD radical cations. The authors note that the presence of small amounts of the doubly charged cation, TPD^{++} , cannot be ruled out.

Figure 4.16 shows Ohmic and space-charge currents, J_Ω and J_{SCL} , as well as the resulting current-voltage curve expected when both processes occur. These current-voltage curves are calculated from J_Ω (Equation 4.19) and J_{SCL} (Equation 4.14), with $\mu = 2 \times 10^{-9} \text{ m}^2 \text{V}^{-1} \text{s}^{-1}$, $\rho = 16 \text{ Cm}^{-3}$ ($\rho = eN_0$, with $N_0 = 1 \times 10^{20} \text{ m}^{-3}$), $L = 5 \text{ } \mu\text{m}$, and $\epsilon = 3\epsilon_0$. The effects of the background charge

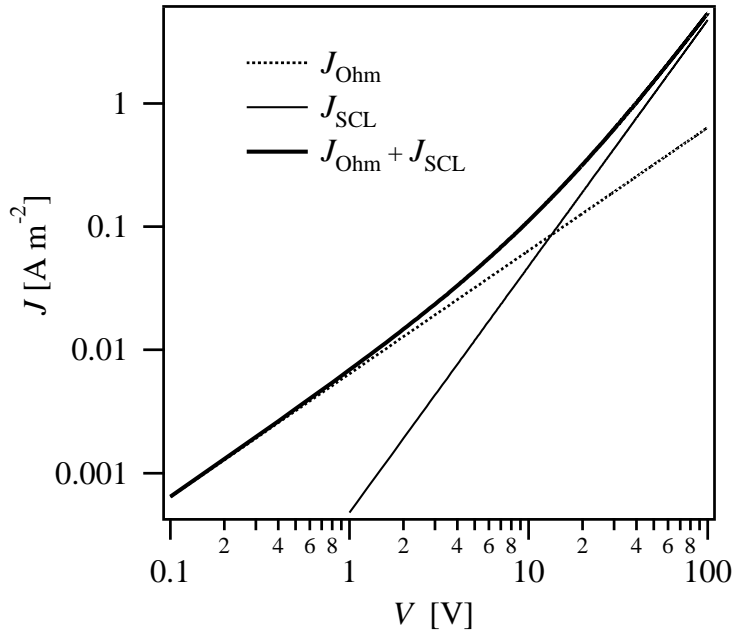


Figure 4.16: Ohmic, J_Ω , and space-charge limited currents, J_{SCL} .

carriers are pronounced at low electric fields. If we compare the value of N_0 used above to the density of TPD molecules in a 50% weight TPD-PS film, $N_{\text{TPD}} = 2.66 \times 10^{26} \text{ m}^{-3}$, we can see that less than 1 ionization in 10^6 TPD molecules is easily observable in a current-voltage curve.

The progression from Ohmic conduction to SCLC is usually explained by the increasing density of injected charge carriers with the applied voltage. As the number of injected carriers becomes greater than the background charge density, N_0 , SCLC dominates over Ohmic charge transport.

However, Abkowitz and Pai give a more detailed explanation – a condition that must hold for the current to be interpreted as due to Ohmic conduction. The transit time, t_{tr} , of a charge carrier must be longer than the “dielectric” (or Ohmic) relaxation time, τ_Ω [29]. In other words, the injected charge density cannot significantly perturb the background charge density, N_0 , to have Ohmic

conduction. The sample remains neutral. Also, the converse is that the transit time has to be smaller than the relaxation time ($t_{tr} < \tau_\Omega$) for SCLC to dominate transport, when the sample is no longer neutral, but is filled with space-charge.

Considering charge density in a conductive material in more detail, Stratton gives a very straightforward explanation [30]. Starting with the continuity equation,

$$\nabla \cdot \mathbf{J} + \frac{\partial \rho}{\partial t} = \nabla \cdot \sigma \mathbf{E} + \frac{\partial \rho}{\partial t} = 0, \quad (4.20)$$

and the divergence of the electric field,

$$\nabla \mathbf{E} = \frac{\rho}{\epsilon}, \quad (4.21)$$

to get

$$\frac{\partial \rho}{\partial t} + \frac{\sigma}{\epsilon} \rho = 0, \quad (4.22)$$

which has the solution

$$\rho = \rho_0 e^{-\sigma t / \epsilon}. \quad (4.23)$$

A time constant is defined as $\tau_\Omega = \epsilon / \sigma$.

Suppose that an initial charge density, ρ_0 , is placed in a material with a nonzero conductivity. Equation 4.23 says that in a time, τ_Ω , the charge will have decayed through Ohmic currents.

How is this related to Ohmic conduction and SCLC? For the current-voltage curve in Figure 4.16, the conductivity is $\sigma = 3.2 \times 10^{-8} \Omega^{-1} m^{-1}$, giving a time constant $\tau_\Omega = 0.83$ ms. Most of the injected charge that traverses the sample in a time longer than τ_Ω will be carried by Ohmic transport. On the other hand, most of the injected charge that traverses the sample in a time shorter than τ_Ω will not travel via background charge carriers. The transit time, t_{tr} is approximately equal

to τ_Ω when the carrier velocity is $v = L/\tau = \mu V/L$. The voltage required for this to be true is 15 V, which is precisely the voltage at which $J_\Omega = J_{SCL}$ in Figure 4.16.

4.5 Models of charge injection

Because their charge-transport properties are so well understood, molecularly doped polymers now serve as an excellent proving ground for theories of metal/organic charge injection [31–39]. In this section, key features of the Mott-Gurney and Schottky interfaces are discussed. Energy barrier lowering due to the image force is described, followed by an overview of thermionic emission theory. Finally, the diffusion-limited thermionic emission theory of charge injection at the metal/inorganic semiconductor interface by Schottky and the diffusion-limited thermionic emission theory of charge injection at the metal/insulator interface by Emtage and O’Dwyer are summarized.

4.5.1 The Mott-Gurney interface

In this section, we discuss the main features of the Mott-Gurney model of a metal/insulator interface [27, 40, 41]. We will again consider the injection of electrons into the conduction band, which is analogous to the LUMO. Keep in mind that hole injection in TPD films occurs by the opposite process: hole injection from the metal into the valence band or HOMO.

The Mott-Gurney model

The formation of the Mott-Gurney interface is illustrated in Figure 4.17. Figure 4.17(a) shows the metal and the insulator before contact. The metal is characterized by the work function, ϕ_m , and the insulator by the electron affinity, χ . The

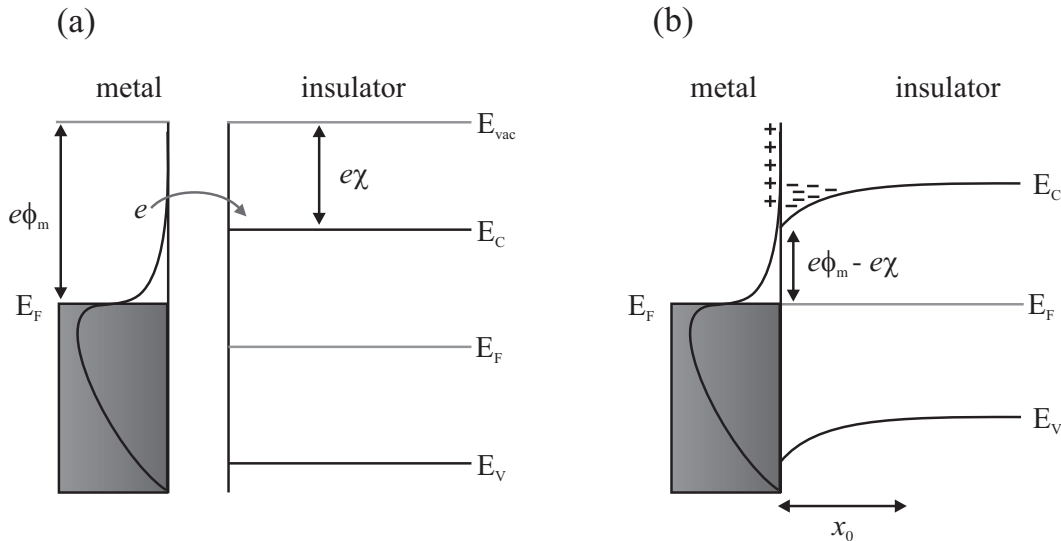


Figure 4.17: The Mott-Gurney interface for electron injection. (a) Metal and insulator before contact. The vertical curve represents the density of states for the metal. (b) Formation of the Mott-Gurney interface after contact. An accumulation of electrons resides in the conduction band.

density of states for the metal is represented by the vertical curve, which crosses the Fermi level of the metal, E_F . As the metal makes contact with the insulator, high energy electrons in the tail states fall into the conduction band of the insulator, creating an accumulation region of width x_0 . An equal and opposite positive charge resides at the surface of the metal. This is shown in Figure 4.17(b). The barrier for electron injection is $e\phi_m - e\chi$, where e is the electron charge.

Interesting physical quantities [27] may be calculated as a result of this model. The length scale, x_0 , of the space-charge region is given by

$$x_0 = \sqrt{\frac{2k_B T \epsilon \epsilon_0}{e \rho_0}}, \quad (4.24)$$

where ρ_0 is the density of electrons in the insulator at the interface, and is approximately

$$\rho_0 \approx 2e \left(\frac{mk_B T}{2\pi\hbar^2} \right)^{3/2} e^{-e(\phi_m - \chi)/k_B T}. \quad (4.25)$$

It is assumed that the density of states in the insulator at the boundary is the same as the metal. m is the effective mass for electrons in the insulator, which we will take as the free electron mass. For molecularly doped polymers, a good approximation to the pre-exponential term in Equation 4.25 is the density of small molecules in the organic film. In the case of TPD molecules, we refer ro the density of TPD as N_{TPD} , so that $\rho_0 = eN_{\text{TPD}}$. The electric field in the metal is zero, but it is not in the insulator. Mott and Gurney find that the planar charge density at the interface is

$$\sigma_0 = \left(\frac{2k_B T \epsilon \epsilon_0 \rho_0}{e} \right)^{1/2}. \quad (4.26)$$

Figure 4.18 shows ρ_0/e , x_0 , and σ_0/e for $\phi_m - \chi = 0.30$ mV, a typical barrier for hole injection between Au and TPD-PS . It is clear that the interfacial charge density is a strong function of temperature. At 298 K, there are approximately 0.44 charge carriers in a 100 nm × 100 nm area, the typical resolution of an EFM experiment. Of course, the carrier density is a strong function of the barrier height. The length scale for the accumulation region in the insulator, x_0 (Equation 4.24), is ≈ 200 nm at 298 K, and increases to several μm for temperatures lower than 200 K.

4.5.2 The Schottky interface

In this section, we review the basic principles of the Schottky barrier, which is created when a crystalline inorganic semiconductor makes contact with a metal. This is a nice starting point for modeling charge injection from a metal into organic materials. The following discussion of the Schottky interface follows the discussion in Chapter 4 of Reference [42] by Sze. Although charge transport in a molecularly doped polymer occurs via hole injection into the HOMO, we will again consider

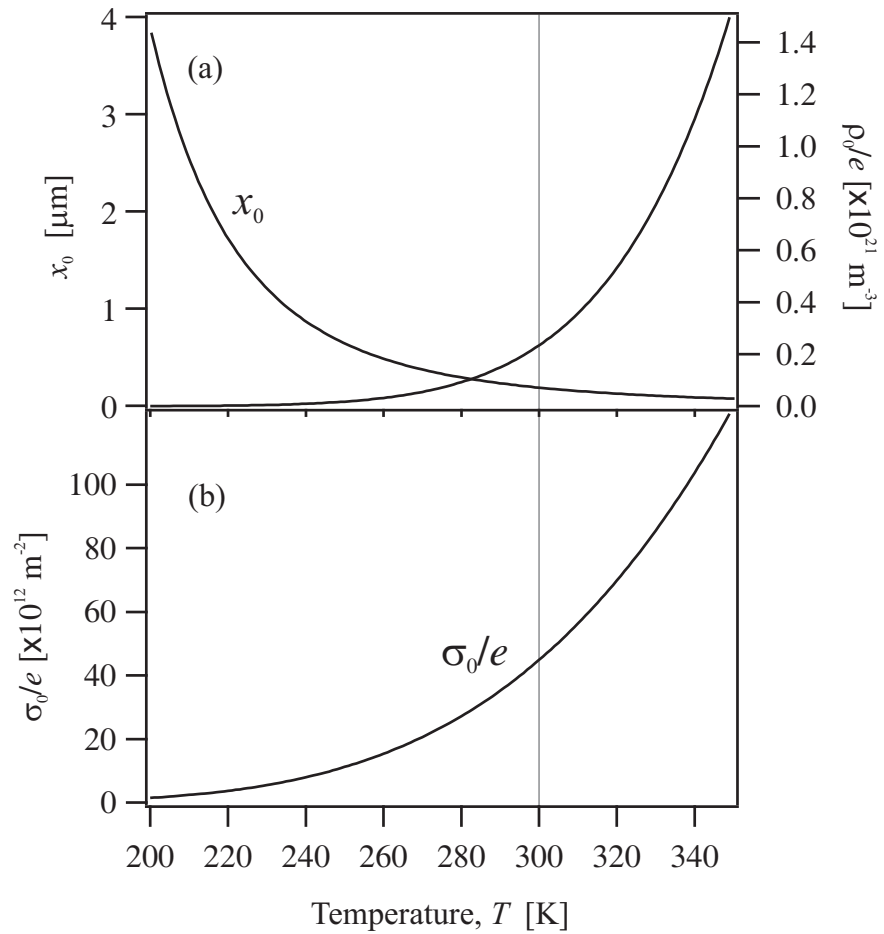


Figure 4.18: Mott-Gurney parameters for a typical Au/TPD-PS interface with a barrier of $\phi_m - \chi = 0.30 \text{ mV}$. (a) Carrier density, ρ_0/e , at the interface and the length scale, x_0 , of the accumulation region. (b) The planar carrier density, σ_0/e , in the insulator at the interface. The vertical line marks 300 K.

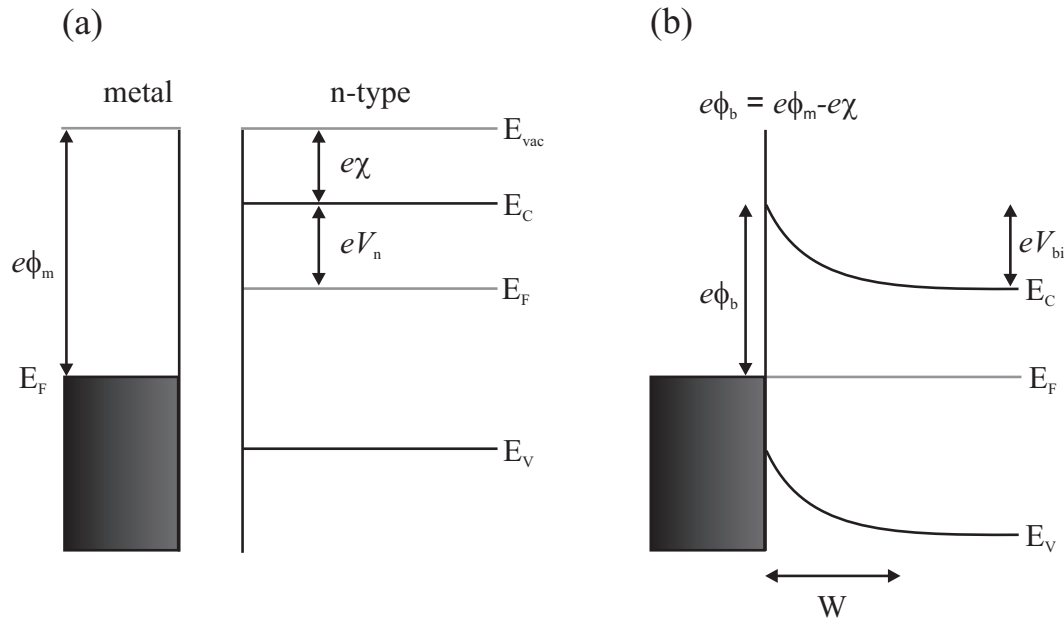


Figure 4.19: Schottky interface for electrons. (a) Metal and n-type semiconductor before contact. (b) Formation of the Schottky interface, ϕ_b , after contact.

the analogous case of electron injection into the conduction band (similar to the LUMO) for simplicity, keeping in mind that the basic result is the same.

The Schottky model

Figure 4.19(a) shows a metal and a n-type semiconductor before contact. The difference between the Fermi level of the metal, E_F , and the vacuum level, E_{vac} , sets the work function, $e\phi_m$. The semiconductor is described by delocalized energy bands: the conduction band, E_C , and the valence band, E_V . The Fermi level, E_F , is midway between the bands in an intrinsic semiconductor and shifted off center if the semiconductor is doped. The distance from the vacuum level to the conduction band, which is the electron affinity, has an energy $e\chi$. The distance from the conduction band to the Fermi level is the energy, eV_n .

Upon making contact, electrons will flow from the higher potential of the semiconductor to the lower potential of the metal until the Fermi levels of the two materials become equal. This is illustrated in Figure 4.19(b). As electrons leave the semiconductor, positive donors are left behind and the potential in the bulk semiconductor is lowered by an amount, eV_{bi} , at a distance, W , from the interface. The depletion of charge causes band bending in the semiconductor near the interface. The barrier for an electron to pass from the metal into the conduction band of the semiconductor, known as the Schottky barrier, ϕ_b , is given by

$$e\phi_b = e\phi_m - e\chi. \quad (4.27)$$

From this, one can already see that minimizing the alignment of the metal work function and the band energies is critical to charge injection.

The width, W , of the barrier is approximately

$$W \approx \sqrt{\frac{2\epsilon\epsilon_0 V_{\text{bi}}}{eN_D}}, \quad (4.28)$$

where ϵ is the dielectric constant of the semiconductor, and N_D is the donor density [42].

Energy barrier lowering

Energy barrier lowering occurs for charges near the metal surface [42]. When an electron is injected into the conduction band, it experiences an attractive Coulomb force with the image charge it creates in the metal (Figure 4.20(a)). If the electron is a distance x from the metal/semiconductor interface, from basic electrostatics the force, F , is

$$F = -\frac{e^2}{4\pi\epsilon\epsilon_0(2x)^2}. \quad (4.29)$$

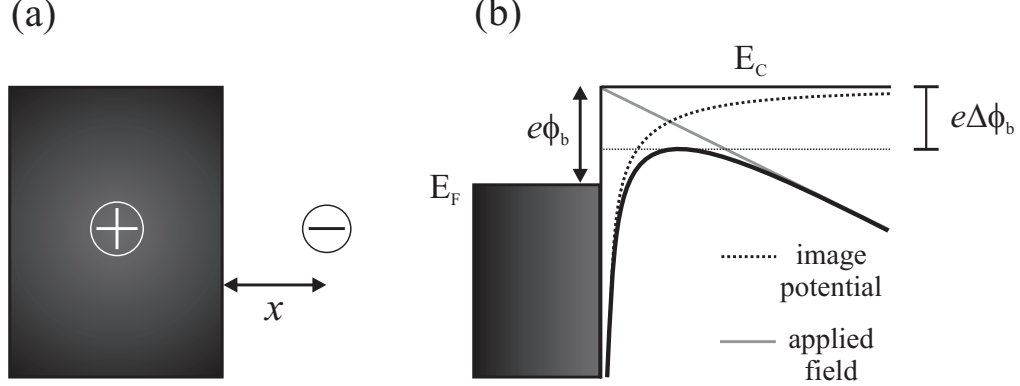


Figure 4.20: Energy barrier lowering for electron injection. (a) The formation of an image charge. (b) Energy barrier lowering, $\Delta\phi_b$, due to the image force and the applied field.

The potential energy is obtained by integrating this force from $x = 0$ to $x = \infty$ (the energy to move the charge infinitely away from x), which gives

$$U = -\frac{e^2}{16\pi\epsilon\epsilon_0 x}. \quad (4.30)$$

This potential energy, which goes as $1/x$, is illustrated by the dotted curve in Figure 4.20(b). An applied electric field E tilts the potential energy by $U = -eEx$ (the grey solid line in Figure 4.20(b)). The resulting potential near the interface is

$$e\phi(x) = e\phi_b - eEx - \frac{e^2}{16\pi\epsilon\epsilon_0 x}, \quad (4.31)$$

and is drawn as the thick solid line in Figure 4.20(b).

The barrier for injecting an electron from the metal to the conduction band of the semiconductor is lowered by an amount, $e\Delta\phi_b$ [42], and is given by

$$e\Delta\phi_b = e\sqrt{\frac{eE}{4\pi\epsilon\epsilon_0}}. \quad (4.32)$$

For simplicity, the barrier lowering is condensed to a parameter, β_s ,

$$\frac{e\Delta\phi_b}{k_B T} = \beta_s \sqrt{E}, \quad (4.33)$$

where β_s is defined as

$$\beta_s = \sqrt{\frac{e^3}{4\pi\epsilon\epsilon_0(k_B T)^2}}. \quad (4.34)$$

The basic features of an interface between a metal and an inorganic semiconductor have been described. We will now discuss two basic models for injection, thermionic emission theory and the related charge injection theory by Schottky.

Thermionic emission theory

Thermionic emission theory, developed by Bethe, is a charge injection process that depends on thermal energy to overcome the energy barrier between the metal and the inorganic semiconductor [42, 43]. The current density is given by

$$J = \frac{4\pi e m^* (k_B T)^2}{h^3} e^{-e\phi_b/k_B T} \quad (4.35)$$

where m^* is the effective mass of the charge, h is Planck's constant, and ϕ_b is the barrier height. This model assumes that the barrier height is large compared to $k_B T$ and that thermal equilibrium exists at the interface. Equation 4.35 is broken up into calculating the current from the metal to the semiconductor and the current from the semiconductor to the metal. The current arises solely from the kinetic (thermal) energy of the charges, which are given by Fermi-Dirac statistics. Electrons with an energy high in the tail states of the Fermi distribution will be able to pass the injection barrier, which is similar to how the emission of electrons into vacuum is described. This model does not account for the energy barrier lowering, but it can be incorporated into Equation 4.35, which is known as the Richardson-Schottky Equation [44],

$$J = \frac{4\pi e m^* (k_B T)^2}{h^3} e^{-e\phi_b/k_B T} e^{\beta_s \sqrt{E}}. \quad (4.36)$$

The Schottky model for diffusion-limited thermionic emission into a semiconductor

The Schottky model is quite different from thermionic theory of Bethe. Most importantly, the Schottky model accounts for the shape of the potential in the semiconductor near the Schottky interface, shown in Figure 4.20(a), and the collisions that electrons experience in the depletion region at the interface [42]. In Bethe's model, the injection is dominated by the energies of the charge carriers, but in Schottky's model, the injection is dominated by charge transport and diffusion in the charged depletion region [45].

This is not meant to be a rigorous derivation of Schottky's diffusion model, but a simple consolidation of the various components of the approximate expression for the current given in Equation 4.39. We proceed to incorporate the field dependent mobility and barrier lowering to obtain Equation 4.41. More detailed models describing charge injection at the Schottky interface can be found in the text by Sze [42].

Unlike the original thermionic emission theory given by Equations 4.35 and 4.36, the Schottky model accounts for the diffusive current at the interface. Starting with the simple Ohmic expression for the current density,

$$J = \mu \rho_0 E, \quad (4.37)$$

and using the following expression for the density of carriers injected into the inorganic semiconductor,

$$\rho_0 = e N_C e^{-e\phi_b/k_B T}, \quad (4.38)$$

we have

$$J = \mu E e N_C e^{-e\phi_b/k_B T}, \quad (4.39)$$

where N_C is the density of states in the conduction band. If we include the barrier lowering, $\beta_s\sqrt{E}$, from Equation 4.33, and the field dependent mobility, $\mu = \mu_0 \exp(\beta_\mu\sqrt{E})$, from Equation 4.13, we obtain

$$J = \mu_0 E e N_C e^{-e\phi_b/k_B T} e^{(\beta_\mu + \beta_s)\sqrt{E}}. \quad (4.40)$$

To simplify this a little, condense terms into ρ_0 in the expression for the current density and we have

$$J = \mu_0 \rho_0 E e^{(\beta_\mu + \beta_s)\sqrt{E}}. \quad (4.41)$$

To summarize, the diffusion-limited thermionic emission theory by Schottky includes:

- The Schottky interface – the potential of the charged depletion region.
- A diffusion current.
- Energy barrier lowering.

This model of charge injection is used in Chapter 5 to understand charge injection from a metal into an organic semiconductor, the molecularly doped polymer. While the model is extremely useful, we must keep in mind that it describes charge injection into a crystalline semiconductor with delocalized energy bands, including transport through a depletion region. As we found in Sections 4.3.2 and 4.5.1, organic materials transport charge via localized sites, and often form an accumulation region rather than a depletion region.

4.5.3 Emtage and O'Dwyer's model for diffusion-limited thermionic emission into an insulator

We now introduce the theory of charge injection by Emtage and O'Dwyer [46]. In 1965, Simmons pointed out a major problem [47] with the application of thermionic emission theory [43] to insulators with very low mobility. Delocalization that occurs in semiconductors leads to charge transport that takes place with a large mean free path. On the other hand, insulators have relatively little delocalization, and a very short mean free path between transport events. Insulators lose much more energy during transport, which is why they have such a low charge mobility. The current predicted by thermionic emission theory (Equation 4.35) would require an enormous charge density in the insulator, based on a simple Ohmic argument. In fact, the charge density would be so large that it would diffuse back into the metal!

In 1966, Emtage and O'Dwyer presented a new model [46] for charge injection into an insulator to deal with the unrealistic charge densities discussed by Simmons [47]. The key features of this model include:

- The insulator is trap-free.
- There are no electrons available for conduction in its ‘normal’ state.
- The bulk transport is separable from the injection process.
- Energy barrier lowering.
- A diffusion current.

This theory already appears more appropriate than the Schottky models for charge injection into an organic material.

Emtage and O'Dwyer give the current in two parts, one limit appropriate for low electric fields and the other for high electric fields. Marohn has derived an expression for the current that works at all fields and includes the field dependence of the mobility [48]. The current is given by

$$J \approx \mu_0 \rho_0 E \frac{e^{\beta_\mu \sqrt{E}}}{\beta_s \sqrt{E} K_1(\beta_s \sqrt{E})}. \quad (4.42)$$

Here, K_1 is a modified Bessel function of the second kind. ρ_0 is given by the density of TPD molecules $\rho_0 = eN_{\text{TPD}} \exp(-e\phi_b/k_B T)$. The energy barrier lowering exponent, β_s , is given by Equation 4.34.

In a more recent approach, Scott and Malliaras have calculated the recombination of a charge and its image charge at the interface due to the attractive potential [35]. While they found good agreement with Emtage and O'Dwyer, they discovered, however, that fully accounting for recombination leads to a lower current, even in high electric fields. In an important study of charge injection into TPD-PC, Shen *et al.* found that the current density is indeed proportional to the mobility of the organic [37], as predicted by Scott and Malliaras and Equation 4.42.

In Chapter 5, the diffusion-limited thermionic emission theory of Emtage and O'Dwyer is used to test, microscopically, the injection of charge from a metal into a molecularly doped polymer.

4.6 Conclusions

The molecularly doped polymer has been crucial in the development of charge transport theory for organic materials. It is also a perfect testing ground for the commonly assumed charge injection theories presented in this chapter. In Chapter 5, we test these theories using high-sensitivity electric force microscopy.

Chapter 4 references

- [1] K. Sakanoue, M. Motoda, M. Sugimoto, and S. Sakaki, Journal of Physical Chemistry A **103**, 5551 (1999).
- [2] M. Malagoli and J. L. Bredas, Chemical Physics Letters **327**, 13 (2000).
- [3] A. N. Sobolev, V. K. Belsky, I. P. Romm, N. Y. Chernikova, and E. N. Guryanova, Acta Crystallographica C**41**, 967 (1985).
- [4] E. Zojer, J. Cornil, G. Leising, and J. L. Bredas, Physical Review B **59**, 7957 (1999).
- [5] M. Malagoli, M. Manoharan, B. Kippelen, and J. L. Bredas, Chemical Physics Letters **354**, 283 (2002).
- [6] J.-L. Maldonado *et al.*, Chemistry of Materials **15**, 994 (2003).
- [7] J. Cornil *et al.*, Journal of Physical Chemistry A **105**, 5206 (2001).
- [8] P. M. Borsenberger and D. S. Weiss, *Organic Photoreceptors for Xerography*, Marcel Dekker, Inc., New York, 1998.
- [9] J. R. Haynes and W. Shockley, Physical Review **81**, 835 (1951).
- [10] J. D. Write, *Molecular Crystals*, Cambridge University Press, 1995.
- [11] H. Bässler, Physica Status Solidi (B) **175**, 15 (1993).
- [12] A. Nemeth-Buhin, C. Juhasz, V. I. Arkhipov, and H. Bässler, Philosophical Magazine Letters **74**, 295 (1996).
- [13] A. Miller and E. Abrahams, Physical Review **120**, 745 (1960).
- [14] L. B. Schein and J. X. Mack, Chemical Physics Letters **149**, 109 (1988).
- [15] L. B. Schein, A. Peled, and D. Glatz, Journal of Applied Physics **66**, 686 (1989).
- [16] P. N. Murgatroyd, Journal of Physics D - Applied Physics **3**, 151 (1969).
- [17] A. Dieckmann, H. Bässler, and P. M. Borsenberger, Journal of Chemical Physics **99**, 8136 (1993).
- [18] S. V. Novikov and A. V. Vannikov, Journal of Physical Chemistry **99**, 14573 (1995).
- [19] S. Novikov, Physica Status Solidi (B) **218**, 43 (2000).
- [20] Y. N. Gartstein and E. M. Conwell, Chemical Physics Letters **245**, 351 (1995).

- [21] D. H. Dunlap, P. E. Parris, and V. M. Kenkre, Physical Review Letters **77**, 542 (1996).
- [22] D. H. Dunlap and V. M. Kenkre, Journal of Imaging Science and Technology **43**, 437 (1999).
- [23] S. V. Novikov, D. H. Dunlap, V. M. Kenkre, P. E. Parris, and A. V. Vannikov, Physical Review Letters **81**, 4472 (1998).
- [24] P. E. Parris, D. H. Dunlap, and V. M. Kenkre, Physica Status Solidi (B) **218**, 47 (2000).
- [25] S. V. Novikov and A. V. Vannikov, Molecular Crystals and Liquid Crystals **361**, 89 (2001).
- [26] R. E. Parris, V. M. Kenkre, and D. H. Dunlap, Physical Review Letters **8712**, 126601 (2001).
- [27] M. A. Lampert and P. Mark, *Current Injection in Solids*, Academic Press, Inc., New York, 1970.
- [28] B. Kusse and E. Westwig, *Mathematical Physics*, John Wiley and Sons, Inc., 1998.
- [29] M. Abkowitz and D. M. Pai, Philosophical Magazine B **53**, 193 (1986).
- [30] J. A. Stratton, *Electromagnetic Theory*, McGraw-Hill Book Company, New York & London, 1941.
- [31] M. A. Abkowitz and H. A. Mizes, Applied Physics Letters **66**, 1288 (1995).
- [32] Y. N. Gartstein and E. M. Conwell, Chemical Physics Letters **255**, 93 (1996).
- [33] A. Ioannidis, J. S. Facci, and M. A. Abkowitz, Journal of Applied Physics **84**, 1439 (1998).
- [34] U. Wolf, V. I. Arkhipov, and H. Bässler, Physical Review B **59**, 7507 (1999).
- [35] J. C. Scott and G. G. Malliaras, Chemical Physics Letters **299**, 115 (1999).
- [36] M. A. Baldo and S. R. Forrest, Physical Review B **6408**, 1948 (2001).
- [37] Y. L. Shen, M. W. Klein, D. B. Jacobs, J. C. Scott, and G. G. Malliaras, Physical Review Letters **86**, 3867 (2001).
- [38] J. C. Scott, Journal of Vacuum Science and Technology A **21**, 521 (2003).
- [39] Y. Shen, A. Hosseini, M. H. Wong, and G. G. Malliaras, ChemPhysChem **5**, 16 (2004).

- [40] N. F. Mott and R. W. Gurney, *Electronic Processes in Ionic Crystals*, Clarendon Press, Oxford, 1940.
- [41] J. A. Marohn and D. H. Dunlap, Marohn Group Report, *unpublished* (2003).
- [42] S. M. Sze, *Physics of Semiconductor Devices*, Wiley-Interscience Publication, 1981.
- [43] H. A. Bethe, MIT Radiation Laboratory Reports , 43 (1942).
- [44] A. J. Dekker, *Solid State Physics*, Prentice-Hall, Inc., New Jersey, 1957.
- [45] E. H. Rhoderick, Journal of Physics D - Applied Physics **3**, 1153 (1970).
- [46] P. R. Emtage and J. J. O'Dwyer, Physical Review Letters **16**, 356 (1966).
- [47] J. G. Simmons, Physical Review Letters **15**, 967 (1965).
- [48] J. A. Marohn, Marohn Group Report, *unpublished* (2004).

CHAPTER 5

MICROSCOPIC VIEW OF CHARGE INJECTION IN A MODEL ORGANIC SEMICONDUCTOR

Organic electronic materials are particularly well suited for constructing high-efficiency solar cells and light emitting diodes [1], and inexpensive solution processable thin-film transistors [2]. A fundamental understanding of how charge is injected from a metal to a π -conjugated organic system is essential to the design and operation of such organic electronic devices. Despite a growing body of phenomenological knowledge [3], a predictive microscopic theory of the charge injection process remains elusive [4].

In these studies, a molecularly doped polymer system is investigated to help elucidate, microscopically, how charge is injected from a metal into a disordered π -conjugated organic material. This work demonstrates:

- The use of a well-studied organic system to probe the interface energetics locally at a “good” contact.
- The measurement of the local charge density at the organic/metal interface as a function of electric field, which can be used to test models of charge injection. We find the charge density at this interface increases with electric field much faster than is predicted by diffusion-limited thermionic emission theory.
- A direct microscopic observation of the transition from Ohmic conduction to the space-charge limited conduction (SCLC) mechanism.

5.1 Introduction

Many theories have been proposed to describe charge injection into hopping transport organic materials. Early models were adapted from inorganic semiconductor injection theories such as Schottky injection and Fowler-Nordheim field emission. Recent theories have sought to describe the charge injection process as thermally-assisted tunneling from the metal to localized states [5], tunneling into polaron levels in polymers [6], thermally-assisted injection into an energetically disordered dielectric [7, 8], or as diffusion-limited thermionic emission [9, 10]. Factors playing a role in metal-to-organic charge injection include the charge mobility in the organic layer [9–11], the dependence of the mobility on electric field [12] and on charge density [13, 14], trapping of injected charges at the interface due to the image potential [15, 16], interface dipoles arising from charge transfer [17] or interfacial chemistry [18], and disorder in these interface dipoles [19]. Intriguing effects such as a dramatic time evolution of charge injection have been observed [20].

Testing microscopic theories of charge injection requires a separation of bulk and contact effects. One approach is to model the current-voltage behavior of devices of different length [21]. This is possible in systems in which the contact contributes significantly to the device resistance. In the case of a “good” contact, the device current is space-charge limited and independent of the contact resistance. A more direct approach to disentangling bulk and contact effects has been to use conducting-probe potentiometry [22] and scanned probe potentiometry [23–25] to follow voltage discontinuities at the metal/organic interface in a device. Studies of the temperature dependence of the poly(3-hexylthiophene)/metal contact resistance have recently led Bürgi *et al.* to call into question diffusion-limited thermionic emission theories (Section 2.4.3) [25].

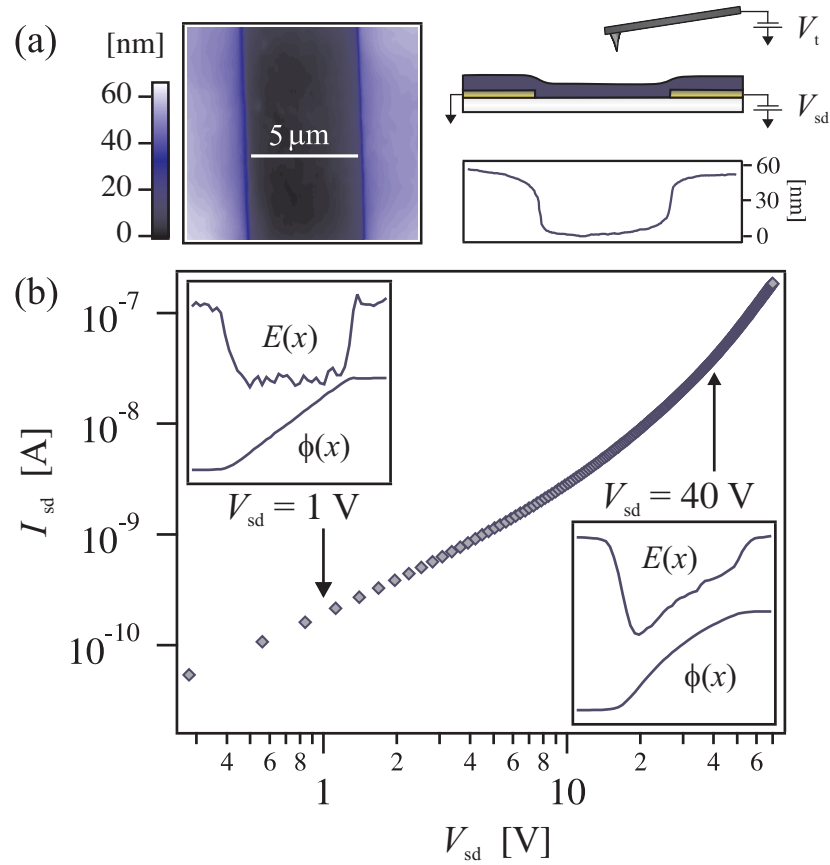


Figure 5.1: 50% weight TPD-PS film topography and current-voltage curve.

(a) Topographic image (left) and linescan (right), acquired by intermittent-contact atomic force microscopy. (b) Current, I_{sd} , versus applied source-drain voltage, V_{sd} . The inset shows linescans of normalized potential, $\phi(x)$, and electric field, $E(x)$, at low and high voltage, demonstrating the transition from Ohmic conduction to SCLC.

In this chapter, we use high-sensitivity electric force microscopy to investigate charge injection from a metal to a π -conjugated system through a *good* metal-organic contact, the behavior of which should provide a stringent test of thermionic emission theories of charge injection. We have studied the interface between gold and a triarylamine, N,N'-diphenyl-N-N'-bis(3-methylphenyl)-(1,1'-biphenyl)-4,4'-diamine (TPD), dispersed in polystyrene (PS). This system, introduced in Chapter 4, was chosen because bulk transport of holes in TPD-PS is well understood, free of charge trapping effects [11,12,20,26,27], has relatively well characterized interface energetics [18], and, most importantly, because this contact easily supports space-charge limited conduction.

5.2 Experimental

Preparation of the organic device

The organic device studied here consists of a TPD-PS film which conducts charge between two coplanar electrodes (Figure 5.1). Interdigitated gold electrodes were patterned on quartz by optical lithography. The source-drain gap was 5 μm , the length of each electrode was 3 mm, and there were 67 electrodes in total. Electrodes were formed by evaporating a 50 \AA adhesion layer of chromium followed by 500 \AA of gold at a rate of 0.4 $\text{\AA}/\text{s}$ by electron beam in high vacuum. The resulting metal films appeared polycrystalline by atomic force microscopy with a surface roughness of 0.65 nm. The quartz substrate was cleaned by sonication in acetone, toluene, and isopropanol followed by UV/ozone treatment. 50% weight TPD-PS was prepared by dissolving 15 mg of TPD (supplied by Xerox Corporation) and 15 mg of PS (MW = 2.0×10^6 , PD = 1.09; Aldrich) in 3 mL of dry tetrahydro-

furan (≤ 10 ppm water, BakerDRY Ultra Low Water THF, part No. 9446-10) for 2.5 hours. The solution was spin-cast in air onto the cleaned quartz substrates at 1900 rpm for 15 s, yielding amorphous films having a thickness of 100 nm and a surface roughness of 0.7 nm (Figure 5.1(a)). During spin-casting, helium gas was flowed through the spinner apparatus to minimize the effects of humidity. When the humidity in the laboratory was too high, spin-casting resulted in films with voids and rough topography. Samples were transferred into vacuum for characterization within an hour of preparation.

Electrical characterization

The electrical characteristics show an evolution from Ohmic conduction at low voltages, with the current proportional to the applied potential ($I_\Omega \propto V$), to space-charge limited conduction (SCLC) at high voltages, with the current proportional to the square of the applied potential ($I_{\text{SCL}} \propto V^2$), shown in Figure 5.1(a). At low voltages we expect an Ohmic current density

$$J_\Omega = \mu_0 e N_0 \frac{V}{L} e^{\beta_\mu \sqrt{V/L}}, \quad (5.1)$$

where L is the channel length, e is the electron charge, N_0 is the density of intrinsic free carriers, β_μ accounts for the Poole-Frenkel-like field dependence of the mobility in TPD-PS [26] and μ_0 is the zero field mobility. In Equation 5.1, we neglect the field dependence of the mobility, a valid approximation at low voltage.

When the voltage is high enough so that the total injected charge exceeds the total intrinsic (compensated) charge, the space-charge alters the voltage dependence of the current density. A simple argument for the V^2 dependence of the current is given in Appendix B.2 and the transition is discussed in detail in

Section 4.5.1. In the space-charge limit the current is given by the modified Mott-Gurney equation [28],

$$J_{\text{SCL}} = \frac{9}{8} \mu_0 \epsilon \frac{V^2}{L^3} e^{0.89\beta_\mu \sqrt{V/L}}, \quad (5.2)$$

where μ_0 is the extrapolated zero-field mobility and $\epsilon \simeq 3\epsilon_0$ is the TPD-PS dielectric constant. Equation 5.2 is derived for parallel plate electrodes. However, as an approximation, we have applied the model to our device which uses coplanar electrodes. Above 2 V, both Equation 5.1 for Ohmic conduction and Equation 5.2 for space-charge limited conduction fit the current equally well, and it is difficult to distinguish Ohmic conduction from space-charge limited conduction based solely on the current-voltage characteristics. The conduction mechanism(s) can, however, be unambiguously assigned using high-sensitivity electric force microscopy, as we will now show.

High-sensitivity electric force microscopy

We imaged the potential, $\phi(x)$, and tip-sample capacitance derivative in a TPD-PS/Au device using a custom-built electric force microscope operating at room temperature in a vacuum of 10^{-6} mbar [29]. The microscope is described in detail in Chapter 3 and Appendix C. The microscope employs a Ti-Pt coated cantilever (model NSC21; MikroMasch) having a resonance frequency $f_0 = 28$ kHz, a spring constant $k = 1$ N/m, and a typical quality factor $Q = 2 \times 10^4$ in vacuum. Once the source-drain gap was located by intermittent-contact mode atomic force microscopy, the source was grounded and a voltage V_{sd} was applied to the drain. The cantilever was scanned along a line 100 nm above the surface across the source-drain channel. At each position x and V_{sd} the cantilever resonance frequency f was recorded while the cantilever tip voltage V_t was varied. The cantilever was

made the resonant element in a self-oscillating positive feedback loop [30]. The frequency of cantilever self oscillation was measured to a fractional accuracy of $\sim 10^{-7}$, for a drive amplitude of 20 nm and a gate time of 0.1 s.

The capacitive tip-sample force gradient (Section 3.5.4 and Appendix A.4) leads to a resonance frequency of

$$f(V_t, x) = f_0 - \frac{f_0}{4k} \frac{\partial^2 C}{\partial z^2}(x) (V_t - \phi(x))^2, \quad (5.3)$$

where C is the tip-sample capacitance, z is the tip-sample separation, and $\phi(x)$ is the device potential. Varying V_t within ± 2 V of $\phi(x)$, f was found to be quadratic in V_t to within a percent. Fitting f to Equation 5.3, we obtained the capacitance derivative, $\partial^2 C / \partial z^2$, and ϕ as a function of both x and V_{sd} .

5.3 A microscopic view of space-charge limited conduction

We observed the onset of space-charge limited conduction (SCLC) directly using high-sensitivity electric force microscopy. Holes are injected into the highest occupied molecular orbital (HOMO) in TPD-PS. At low voltage, $\phi(x)$ drops linearly between the hole-injecting electrode (right electrode) and the hole-extracting electrode (left electrode), shown in the left inset of Figure 5.1(b). The lateral electric field, $E(x)$, calculated by differentiating the potential, is uniform and symmetric within the device gap at low voltages, as expected for Ohmic conduction. At high voltages (right inset of Figure 5.1(b)), $\phi(x)$ reveals a non-uniform electric field associated with a buildup of space-charge. To our knowledge, this is the first microscopic observation of SCLC.

We have also used electric force microscopy to determine if the contact is “good” or “bad” by looking for a potential drop at the contact, which indicates that the

resistance of the metal/organic contact is larger than the resistance of the film. Unlike the polythiophene film investigated by Bürgi *et al.* [24, 25], there is not a discernable voltage drop at the organic/metal interface in our TPD-PS device.

The potential profiles strongly suggest that Equation 5.1 is the appropriate model at low voltages. We fit the current density from 0-2 V to J_Ω to determine the density of free charge carriers, N_0 , ignoring the electric field dependence of the mobility by setting $\beta_\mu = 0$. We take $\mu_0 = 2 \times 10^{-9} \text{ m}^2/\text{Vs}$ from Yuh *et al.* [26] and compute the current density as $J = I/A$ where $A = 1.1 \times 10^{-8} \text{ m}^2$, the cross sectional area of the device assuming a sheet charge of height 55 nm (the electrode height). We find $N_0 = 2.8 \times 10^{14} \text{ cm}^{-3}$. We have found this value is independent of channel length. These carriers are thought to arise from impurities, but their chemical nature remains a mystery. The potentiometry also justifies fitting the data from 50-70 V to J_{SCL} . We find $\mu_0 = 2.0 \times 10^{-9} \text{ m}^2/\text{Vs}$ and $\beta_\mu = 0.60 \times 10^{-3} (\text{m/V})^{1/2}$, which is in agreement with Yuh *et al.* [26].

Figure 5.2(a) shows the potential $\phi(x)$ for V_{sd} varying from 2 to 40 V. Let us consider the measured electric field in some detail. The electric field, Figure 5.3(a), is obtained from the potential: $E(x) = -d\phi/dx$. We now compare the experimental potential and electric field against the theoretical potential and electric field based on the model of space-charge limited conduction discussed in Chapter 4. In Section 4.5.1, we calculated the theoretical potential, electric field and charge density for electron injection. We now calculate $\phi(x)$ and $E(x)$ for hole injection with an applied voltage $V_{\text{sd}} = 40 \text{ V}$, using $\epsilon = 3\epsilon_0$ and $\mu = 2 \times 10^{-9} \text{ m}^2 \text{ V}^{-1}\text{s}^{-1}$. We ignore the field dependence of the mobility. Figure 5.4 shows the comparison of the experimental and theoretical potential (Figure 5.4(a)) and electric field (Figure 5.4(b)). Qualitatively, the theoretical potential and electric field appears to

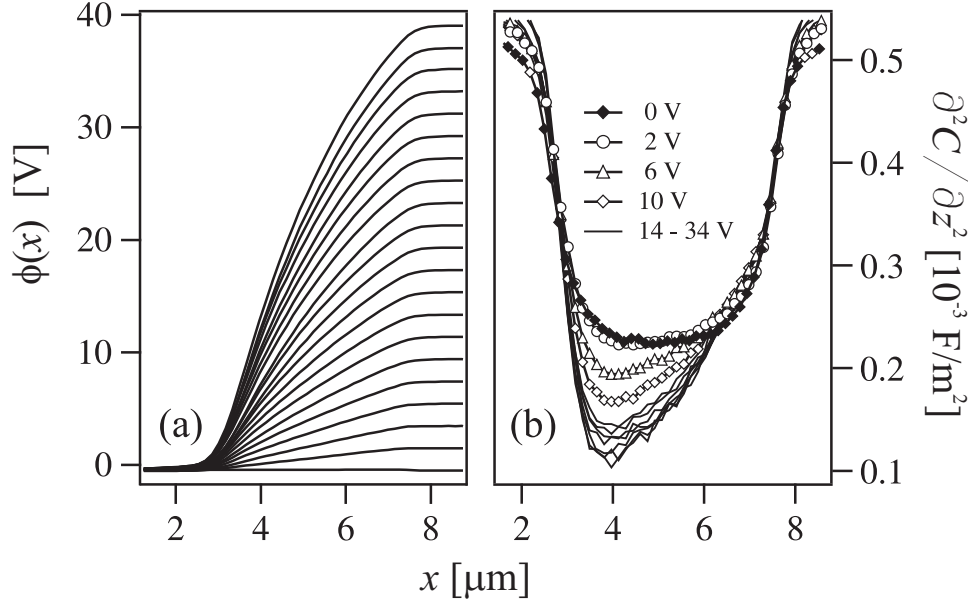


Figure 5.2: (a) The potential, $\phi(x)$, versus distance x across the source-drain gap. The source-drain bias, V_{sd} , was varied from 0 to 40 V. (b) The second derivative of the tip-surface capacitance, $\partial^2 C / \partial z^2$, for various V_{sd} .

match the experimental profiles quite well. The discrepancy between the measured and predicted electric field is well outside the measurement noise. The approximately constant slope of E in the bulk implies a uniform charge density. We currently attribute this discrepancy with the standard Mott-Gurney prediction to deviations from the idealized one-dimensional conduction between two parallel plate electrodes.

Figure 5.5(a) qualitatively shows what is expected during the transition from Ohmic conduction to SCLC. Initially, conduction occurs via the background charge carriers, N_0 , and the bulk is neutral. As the injected charge increases, a positive space-charge builds up in the bulk of the organic material.

The behavior of the electric field at the interface can be used to quantify the extent to which the current density is space-charge limited. If the injecting contact

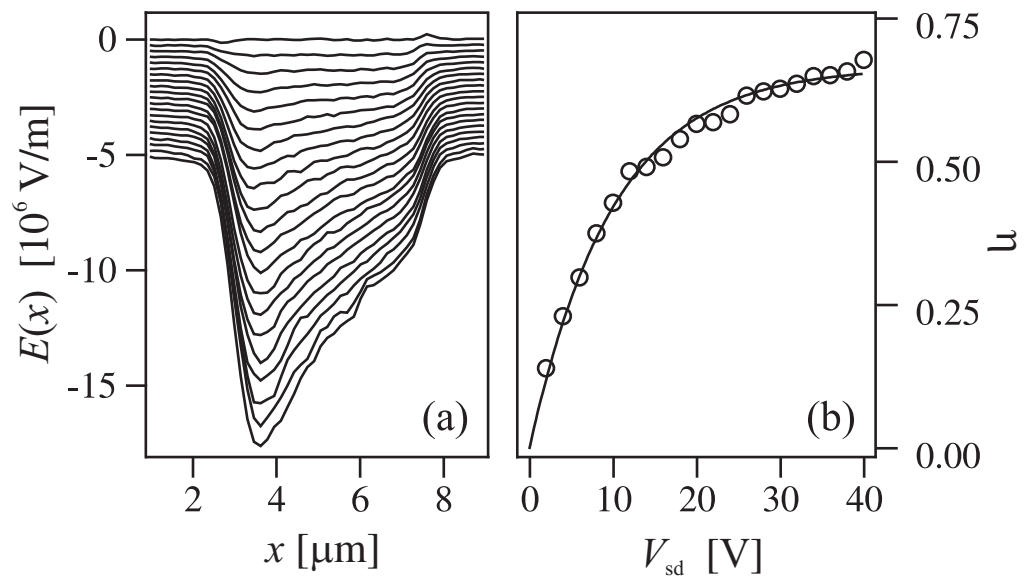


Figure 5.3: (a) Electric field from source to drain. The source-drain bias V_{sd} is varied in 2 V steps from 0 to 40 V. For clarity, each curve has been offset vertically downward by $0.25 \times 10^6 \text{ V/m}$ from the $V_{sd} = 0$ curve. (b) Degree to which SCLC dominates transport.

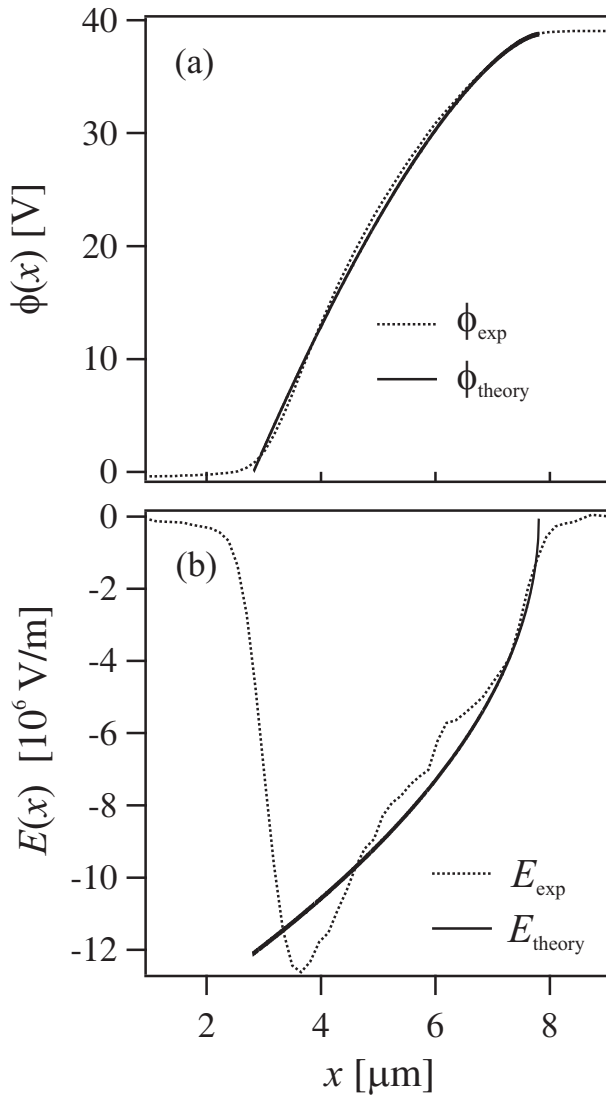


Figure 5.4: Comparison of experimental and theoretical potential $\phi(x)$ and electric field $E(x)$. The theoretical prediction is based on the Mott-Gurney model. The potential is shown in (a) and the electric field in (b). We have chosen to compare the two at $V_{\text{sd}} = 40 \text{ V}$. Experimental values are represented by the dotted lines and the theoretical prediction by the solid lines.

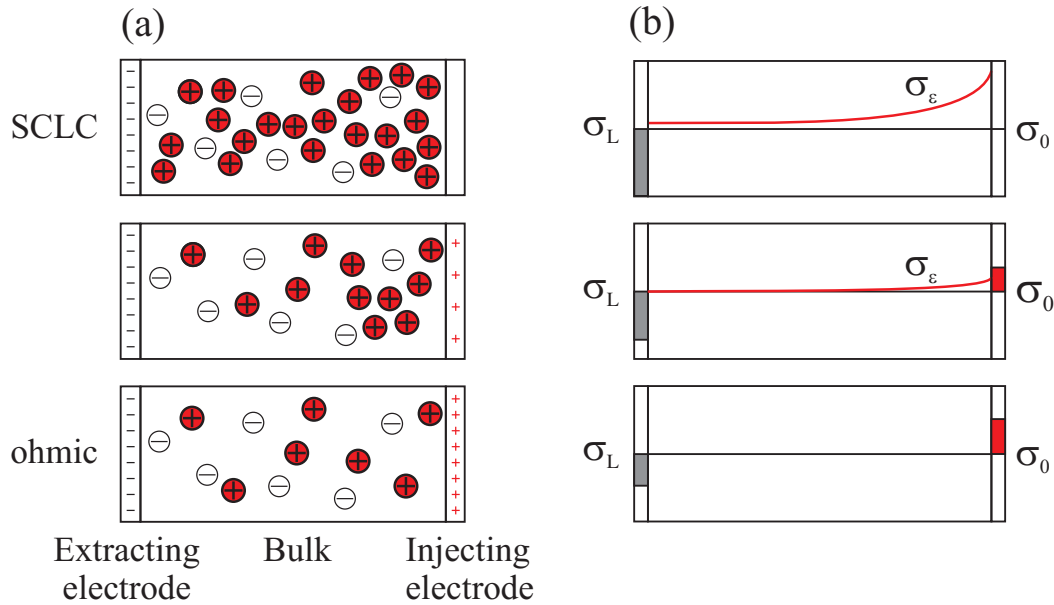


Figure 5.5: (a) Qualitative picture of the transition from Ohmic conduction to SCLC. (b) Charge densities at the extracting electrode, bulk, and injecting electrode during the transition.

is supplying the material's space-charge limited current, then we expect the steady-state planar charge density in the material σ_ϵ to become comparable to that at the extracting electrode, σ_L , and much larger than that at the injecting electrode σ_0 . By Gauss' law, $\sigma_L = \epsilon E_L$ and $\sigma_0 = -\epsilon E_0$, and by charge conservation, $\sigma_\epsilon = \epsilon(E_0 - E_L)$. The evolution from Ohmic conduction to SCLC is illustrated by the charge densities in the extracting electrode, bulk organic, and injecting electrode of Figure 5.5(b). A quantitative measure of the degree to which SCLC dominates transport is therefore $\eta \equiv -\sigma_\epsilon/\sigma_L = (E_L - E_0)/E_L$. As defined, $\eta = 0$ for purely Ohmic currents and $\eta = 1$ when the current is due purely to space-charge. Figure 5.3(b) shows η as a function of V_{sd} . The data fits well to $\eta = \eta_\infty(1 - \exp(-V/V_0))$ with $\eta_\infty = 0.667 \pm 0.007$; $V_0 = 10.0 \pm 0.4$ V, which agrees with a calculated crossover from J_Ω to J_{SCL} of 12 V.

The second derivative of the tip-sample capacitance, $\partial^2 C / \partial z^2$ (Equation 5.3), shown in Figure 5.2(b), also evolves dramatically as the system undergoes the transition from Ohmic conduction to SCLC. The capacitance is large over the gold electrodes, and the general shape of the linescan reflects sample topography. If the capacitance is a function of the total charge density, the behavior of the capacitance between the source and drain suggests, rather surprisingly, that the bulk becomes depleted of free carriers near the extracting electrode as the space-charge limit is approached, leaving behind immobile charged acceptors. On the other hand, if the capacitance between the tip and the sample is related to the dielectric relaxation time ($\tau_\Omega \approx 0.8$ ms), it is possible that the capacitance between the tip and the film is lower near the extracting electrode because the holes travel fastest in this area. A more detailed understanding of probe-sample capacitance is necessary in order to understand the evolution of the tip-sample capacitance.

5.4 Evaluating models of charge injection

A great advantage of EFM is the ability to measure electric fields microscopically. We can observe how the current density depends on the electric field at the interface. By combining the current density with the local electric field, we can infer the mobility-charge density product at the interface using $\mu\rho = J/E$. This allows us to evaluate models of charge injection. We will evaluate simple thermionic emission theory, Schottky's diffusion-limited thermionic emission theory for charge injection into a semiconductor, and Emtnage and O'Dwyer's model for diffusion-limited thermionic emission into an insulator. These models were introduced in Section 4.5.

5.4.1 Thermionic emission theory

Thermionic emission is a charge injection model that depends on thermal energy required to overcome the energy barrier between the metal and the extended states of an inorganic semiconductor. Although it is not expected thermionic emission theory will fully explain charge injection at the Au/TPD-PC interface, we can test the theory to understand its limitations. The Richardson-Schottky equation [31,32] for the current density is

$$J = \frac{4\pi em^*(k_B T)^2}{h^3} e^{-e\phi_b/k_B T} e^{\beta_s \sqrt{E}}, \quad (5.4)$$

where e is the electron charge, m^* is the effective mass of the charge, k_B is Boltzmann's constant, T is the temperature, h is Planck's constant, ϕ_b is the energy barrier and β_s accounts for the energy barrier lowering.

We compare the theoretical current predicted by this theory to the experimental current as functions of the local electric field measured by electric force microscopy. Figure 5.6 shows the experimental current density as a function of the electric field. We stringently apply Equation 5.4, by holding the pre-exponential factor,

$$\frac{4\pi em^*(k_B T)^2}{h^3}, \quad (5.5)$$

and the energy barrier lowering parameter,

$$\beta_s = \sqrt{\frac{e^3}{4\pi\epsilon\epsilon_0(k_B T)^2}}, \quad (5.6)$$

to the theoretical values of $1.08 \times 10^{11} \text{ Am}^{-2}$ and $0.85 \times 10^{-3} (\text{m/V})^{1/2}$, respectively. Also, for the predicted current, we use a barrier height of $\phi_b = 300 \text{ mV}$, which is an estimate derived from the difference between the work function of gold and ionization potential of TPD-PS [18]. The predicted current density is 7 orders of magnitude larger than the measured current density (Figure 5.6). This is precisely

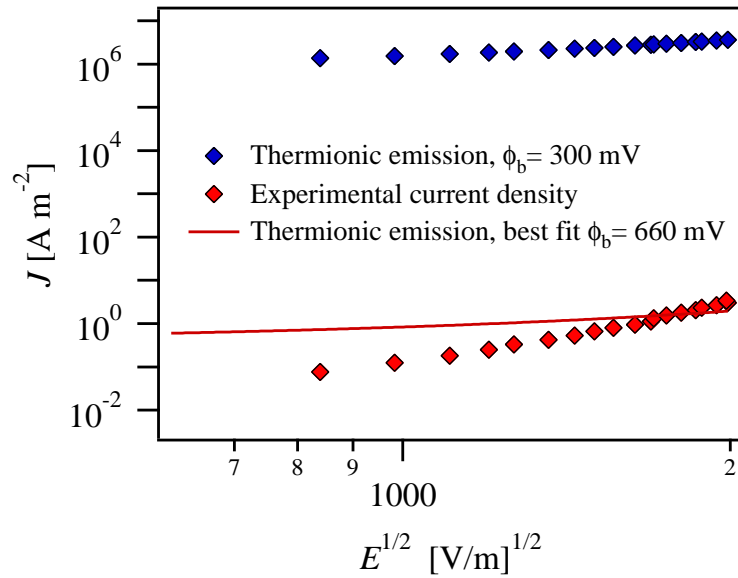


Figure 5.6: Comparison to thermionic emission theory.

the problem pointed out by Simmons [32], discussed in Section 4.5.3. If we allow ϕ_b to vary, we obtain the best fit (red solid line in Figure 5.6) with $\phi_b = 660 \text{ mV}$, which is much too high based on other literature [18] as well as our own measurements described below. We also note the experimental current density rises much faster than the thermionic emission model would predict. The model does not include the mobility of organic, which would cause the current to rise faster with electric field. It also assumes that the current is due only to the kinetic energies of the charge carriers, when diffusion across the interface most likely plays a critical role in charge injection. Thermionic emission theory explains charge injection into extended states extremely well, but fails for injection into localized states. It is more appropriate to consider the drift and diffusion in the semiconducting material, rather than kinetic energies alone, when modeling charge injection into low mobility materials.

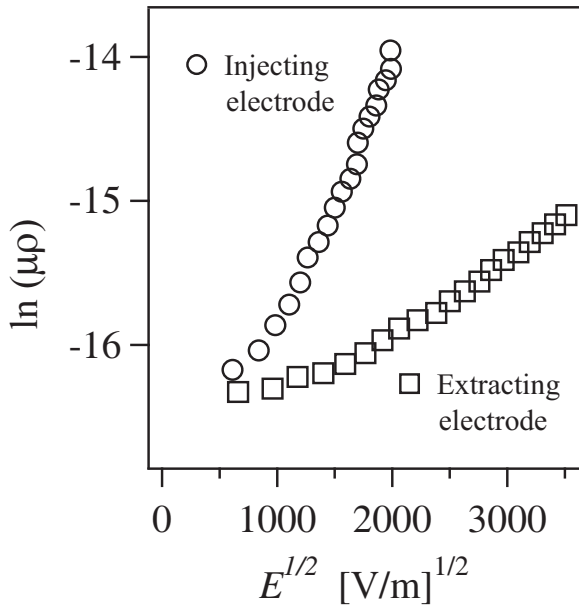


Figure 5.7: The charge density mobility product ($\mu\rho$) as a function of electric field for the injecting and extracting electrodes. Examining $\mu\rho$ as a function of electric field allows us to evaluate models of charge injection.

5.4.2 The Schottky model for diffusion-limited thermionic emission into a semiconductor

For low mobility inorganic semiconductors, the Schottky model of diffusion-limited thermionic emission for charge injection at a metal/semiconductor interface is more appropriate than thermionic emission [33]. The Schottky model describes charge injection into a crystalline semiconductor with delocalized energy bands, including drift and diffusion through a depletion region in the semiconductor.

In this analysis, we will use the mobility-charge density product, given by $J/E = \mu\rho$, which is shown for both electrodes in Figure 5.7. We will focus on the injecting electrode.

In Section 4.5.2, the Schottky barrier and injection model was introduced and

described. In Equations 4.38 and 4.41 we found

$$J = \mu_0 \rho_0 E e^{(\beta_\mu + \beta_s)\sqrt{E}}, \quad (5.7)$$

with

$$\rho_0 = e N_C e^{-e\phi_b/k_B T}. \quad (5.8)$$

Rearranging and using $J/E = \mu\rho$, we have

$$\frac{J}{E} = \mu\rho = \mu_0 \rho_0 e^{\beta\sqrt{E}}, \quad (5.9)$$

defining $\beta = \beta_\mu + \beta_s$. In Section 4.5.2, we considered electron injection into the conduction band. Here, we are considering hole injection into the HOMO of TPD-PS. The injection barrier, ϕ_b , now depends on the alignment of the Fermi level of the metal and the HOMO. Also, the density of states we are interested in is the density of TPD sites, $N_C = N_{\text{TPD}}$.

Using the Schottky model, Equation 5.9 describes the charge injection quite well (Figure 5.8(a)). The Schottky barrier for hole injection is shown in Figure 5.8(b). At the injecting electrode, the energy barrier lowering exponent, β_s , was fixed at its theoretical value of $\beta_s = 0.85 \times 10^{-3} (\text{m/V})^{1/2}$ and $\beta_\mu = 0.60 \times 10^{-3} (\text{m/V})^{1/2}$ was used from the current-voltage characterization, giving a $\beta = \beta_s + \beta_\mu = 1.45 \times 10^{-3} (\text{m/V})^{1/2}$. At the extracting electrode, β was allowed to vary, and the best fit yielded $\beta = 0.59 \times 10^{-3} (\text{m/V})^{1/2}$. The zero-field charge density $\rho_0 = e N_{\text{TPD}} \exp(-\phi_b/(k_B T))$ depends on the TPD density N_{TPD} and on the injection barrier ϕ_b ; $\mu_0 \rho_0$ was restricted to be the same at both electrodes (the fits meet at zero electric field). Under this constraint, $\mu_0 \rho_0 = 36 \times 10^{-9} \text{ A/Vm}$. The resulting injection barrier, $\phi_b = 360 \text{ mV}$, is reasonable.

The Schottky model assumes a Schottky interface, which is plausible considering we know background carriers exist due to the presence of acceptor molecules.

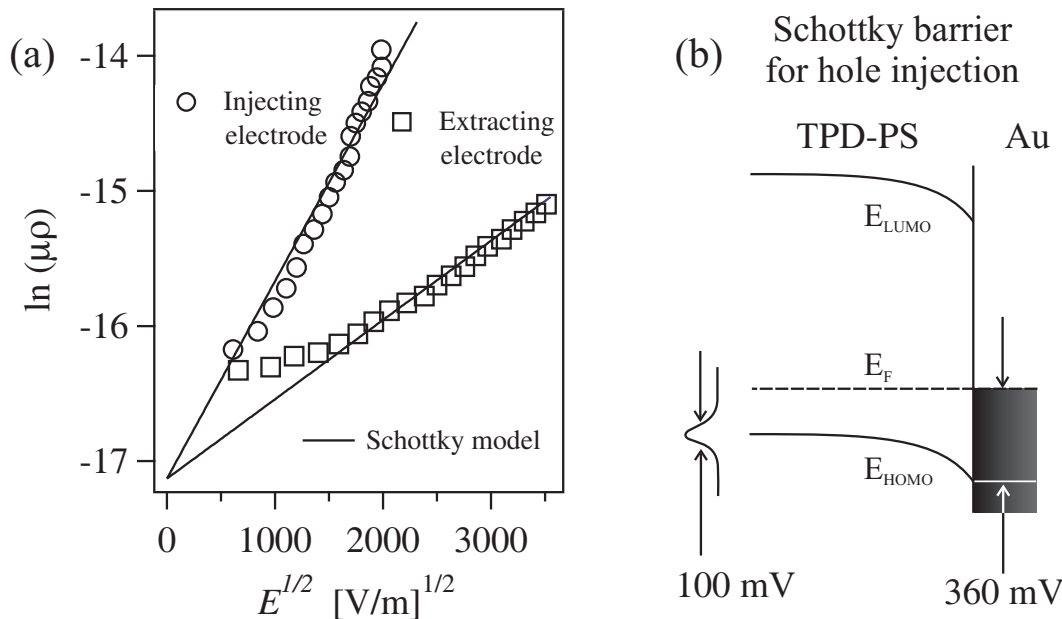


Figure 5.8: Testing the Schottky model of charge injection and extraction.
 (a) Modeling $\mu\rho$ as a Schottky barrier. (b) The Schottky barrier for hole injection into the HOMO.

In order to form a Schottky barrier for hole injection, prior to contact between the gold and TPD-PS, the Fermi level of the gold must be higher than the chemical potential of the TPD-PS. Therefore, equilibrium is reached via electron transfer from the metal to the empty HOMO states of the organic, leaving a depletion of positive charge carriers at the interface. An equivalent way to describe this is that the background density of holes will transfer to the metal at the interface. For the Au/TPD-PS interface, this would result in a negatively charged depletion region due to the remaining negatively charged acceptor molecules. As we will show, this assumption does not hold for our sample.

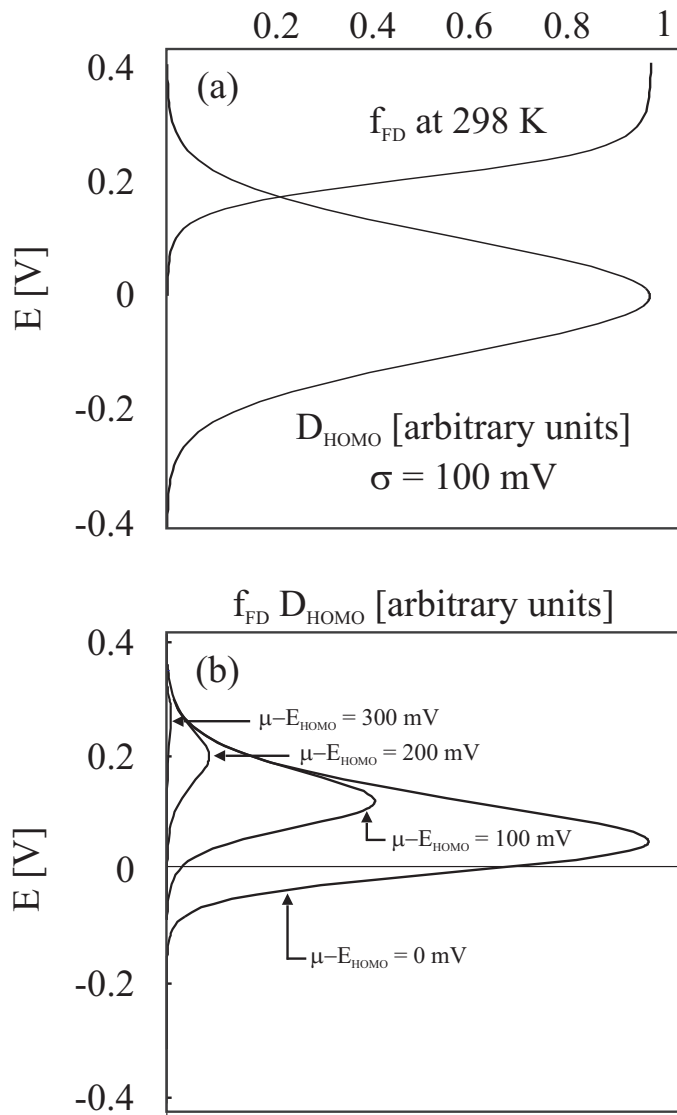


Figure 5.9: Calculating the chemical potential, μ , of TPD. (a) The density of states of the HOMO, D_{HOMO} , centered at $E_{HOMO} = 0$ with $\sigma = 100$ mV and the Fermi-Dirac distribution function, f_{FD} , with $\mu - E_{HOMO} = 200$ mV. (b) The product, $f_{FD}D_{HOMO}$, which gives the density of holes for the values of $\mu - E_{HOMO} = 0, 100, 200$, and 300 mV.

The chemical potential of TPD-PS

Although the chemical identity, concentration, and energy levels of the acceptor states giving rise to the bulk free carriers are not known, we can use Fermi-Dirac statistics to determine the chemical potential (Fermi level), μ , of holes in the bulk TPD-PS from the measured density N_0 of bulk free carriers. Assuming a Gaussian density of highest occupied molecular orbitals (HOMO) of width $\sigma = 100 \text{ mV}$ [12], the density of states for the HOMO, D_{HOMO} , is

$$D_{\text{HOMO}} = \frac{N_{\text{TPD}}}{\sqrt{2\pi\sigma^2}} e^{-(E-E_{\text{HOMO}})^2/2\sigma^2} \quad (5.10)$$

where $N_{\text{TPD}} = 2.66 \times 10^{20}/\text{cm}^3$ is the concentration of TPD molecules. The Fermi-Dirac distribution for holes is

$$f_{\text{FD}} = \frac{1}{1 + e^{(\mu-E)/k_B T}}. \quad (5.11)$$

Integrating $f_{\text{FD}} D_{\text{HOMO}}$ over all energies gives the density of holes for a given value of $\mu - E_{\text{HOMO}}$.

$$N_0 = \frac{N_{\text{TPD}}}{\sqrt{2\pi\sigma^2}} \int_{-\infty}^{+\infty} \frac{e^{-(E-E_{\text{HOMO}})^2/2\sigma^2}}{1 + e^{(\mu-E)/k_B T}} dE \quad (5.12)$$

Numerically, we find $(\mu - E_{\text{HOMO}})/e = 540 \text{ mV}$, which is consistent with the material being a *p*-type organic semiconductor.

From $(\mu - E_{\text{HOMO}})/e = 540 \text{ mV}$, we have constructed the energy level diagram of Figure 5.10. The difference between the Fermi level of the gold, E_F , and E_{HOMO} is $\sim 300 \text{ mV}$, established by our and other experiments [18]. Therefore, since $\mu > E_F$, equilibrium between the Fermi level of the gold and the chemical potential of the TPD-PS film is reached by transfer of electrons from TPD-PS to Au, resulting in accumulation, not depletion, of holes in the organic.

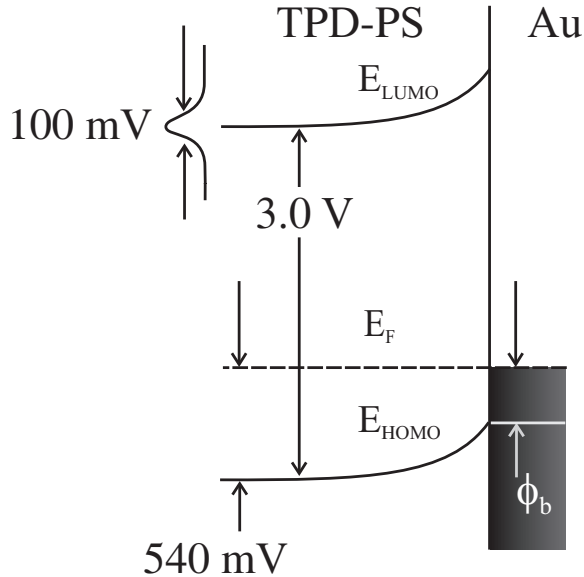


Figure 5.10: Proposed energy level diagram for the TPD-PS/Au interface.

5.4.3 Emtage and O'Dwyer's model for diffusion-limited thermionic emission into an insulator

The accumulation of charge carriers at the interface is much like the Mott-Gurney interface described in Chapter 4. In this situation, the diffusion-limited thermionic emission theory of Emtage and O'Dwyer [9], which describes the injection of charge from a metal into an insulator, is the most appropriate model of charge injection. We have revisited their model and derived an exact analytical equation for $\rho(E)$ at the injecting electrode valid at all fields. The mobility-charge density product, $\mu\rho$ is

$$\mu\rho = \frac{J}{E} \approx \mu_0\rho_0 \frac{e^{\beta_s\sqrt{E}}}{\beta_s\sqrt{E}K_1(\beta_s\sqrt{E})}. \quad (5.13)$$

Here, K_1 is a modified Bessel function of the second kind. The charge density, ρ_0 , is given by the effective density of TPD molecules: $\rho_0 = e N_{\text{TPD}} \exp(-e\phi_b/k_B T)$.

The fit to this theory, Fit 1 of Figure 5.11 and Table 5.1, with the injection

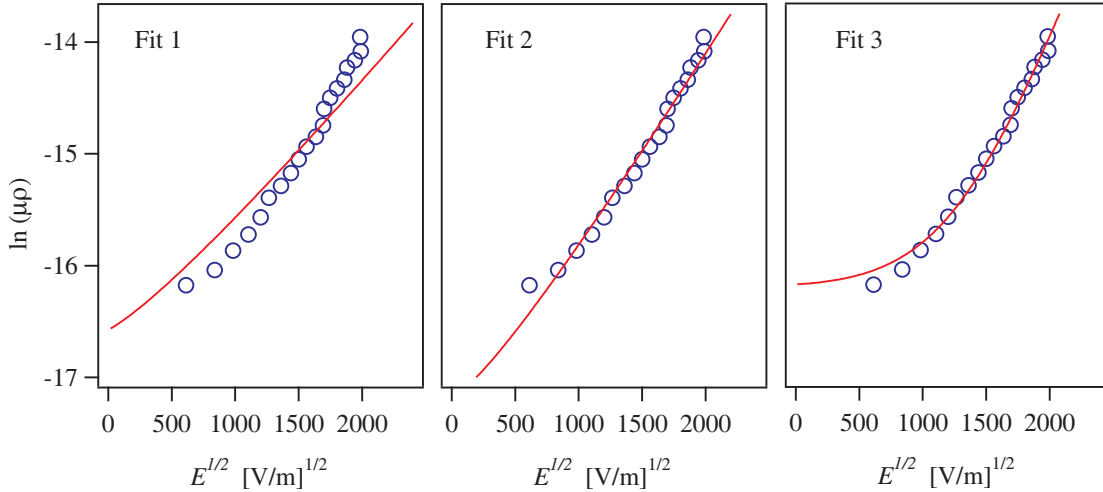


Figure 5.11: Modeling $\mu\rho$ at the hole-injecting electrode with the diffusion-limited thermionic emission theory of Emtage and O'Dwyer. The fits (solid red lines) are described in Table 5.1.

barrier as the only free parameter, is quite poor. The resulting injection barrier of $\phi_b = 350$ mV is reasonable. However, with this stringent test of the Emtage and O'Dwyer model, we can see that the current rises faster with electric field than the theory predicts. If β_s is allowed to vary, as it is in Fit 2 of Figure 5.11 and Table 5.1, we find that $\beta_s = 1.4 \times 10^{-3}$ (m/V) $^{1/2}$, approximately 1.6 \times larger than expected. For Fit 2, $\phi_b = 370$ mV, which is also reasonable.

If we introduce, *ad hoc*, the measured density N_0 of bulk free carriers into the theory to account for the comparatively large current density observed at low electric fields, the fit does not improve from Fit 2. Good agreement is achieved if we allow the energy barrier lowering exponent, β_s , to vary. Fit 3 of Figure 5.11 and Table 5.1 gives $\phi_b = 420$ mV and $\beta_s = 2.5 \times 10^{-3}$ (m/V) $^{1/2}$, approximately 2.9 \times larger than expected.

Might β_s be large simply because we have underestimated the local electric field at the interface with our measurement? This is unlikely. While the electric field

Table 5.1: Modeling $\mu\rho$ at the hole-injecting electrode with the diffusion-limited thermionic emission theory of Emtage and O'Dwyer. In each fit, $\beta_\mu = 0.60 \times 10^{-3} (\text{m/V})^{1/2}$. In Fit 1, we constrained to $\beta_s = \sqrt{\frac{e^3}{4\pi\epsilon\epsilon_0(k_B T)^2}}$. In Fit 2 and Fit 3, β_s was allowed to vary. *In Fit 3, N_0 has been introduced.

| | model | equation for $\mu\rho$ | parameter | fit value | units |
|-------|---------|--|----------------|----------------|---|
| Fit 1 | Emtage | $\frac{\mu_0 \rho_0 \exp(\beta_\mu \sqrt{E})}{\beta_s \sqrt{E} K_1(\beta_s \sqrt{E})}$ | $\mu_0 \rho_0$ | 63.4 ± 3.0 | $10^{-9} [\frac{\text{A}}{\text{Vm}}]$ |
| | | | ϕ_b | 350 | [mV] |
| Fit 2 | Emtage | $\frac{\mu_0 \rho_0 \exp(\beta_\mu \sqrt{E})}{\beta_s \sqrt{E} K_1(\beta_s \sqrt{E})}$ | $\mu_0 \rho_0$ | 34.3 ± 3.0 | $10^{-9} [\frac{\text{A}}{\text{Vm}}]$ |
| | | | β_s | 1.4 ± 0.1 | $10^{-3} [\frac{\text{m}}{\text{V}}]^{1/2}$ |
| | | | ϕ_b | 370 | [mV] |
| Fit 3 | Emtage* | $\mu_0 \left(\frac{\exp(\beta_\mu \sqrt{E})}{\beta_s \sqrt{E} K_1(\beta_s \sqrt{E})} + e N_0 \right)$ | $\mu_0 \rho_0$ | 5.0 ± 0.6 | $10^{-9} [\frac{\text{A}}{\text{Vm}}]$ |
| | | | β_s | 2.5 ± 0.1 | $10^{-3} [\frac{\text{m}}{\text{V}}]^{1/2}$ |
| | | | ϕ_b | 420 | [mV] |

is known to diverge near a thin, planar electrode [34], the divergence is relatively gradual in the lateral dimension. We do not observe an enhanced electric field, however, at any voltage, within 100 nm of either electrode. The organic film is thicker than the planar electrodes and covers them completely, which could alter the expected field predicted by Reference [34]. However, large β_s has been observed in Monte-Carlo simulations of charge injection incorporating energetic disorder [15].

The results presented in this chapter are typical for 50% weight TPD-PS films with gold electrodes. However, occasionally, variability in the mobility has been observed. In one case, β_s was a factor of two larger on an identical device. This suggests that the large β_s is due to the material and is not solely a geometric property. The mobility for this device was an order of magnitude lower than we found previously. This would imply that we have more energetic disorder in this film, consistent with our hypothesis that energetic disorder enhances β_s .

Comparison to the work of others

In a study complimentary to ours, Bürgi *et al.* [25] have used EFM to study contact resistance versus gate voltage and temperature in a polythiophene field-effect transistor. They also call into question widely used theories of charge injection. They find the activation energy of the contact resistance is not accounted for by diffusion-limited thermionic emission theory, which predicts that the total activation energy at the contact is the sum of the activation energy of the mobility, the injection barrier, and the effect of barrier lowering. This is in agreement with our finding that a larger β_s is required in a model organic semiconductor with a good contact.

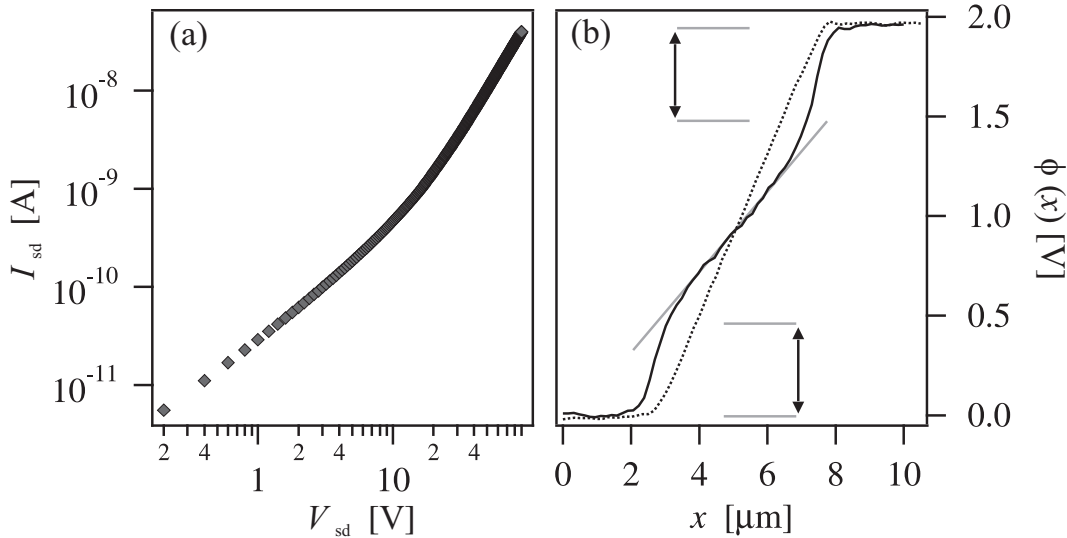


Figure 5.12: I-V curve and potential profiles of an aged device. (a) Current-voltage curve of an aged TPD-PS film on interdigitated gold electrodes. (b) Comparison of potential profiles of a new device (dotted line) and an aged device (full line) at $V_{sd} = 2$ V.

5.5 Effects of film degradation

We have observed the effects of aging of the organic film on charge injection at the Au/TPD-PS interface. In Section 5.1, the resistance of the TPD-PS film was set by the resistance of the bulk and not by the resistance of the TPD-PS/Au contact, because all of the applied voltage was dropped in the bulk of the film (Figure 5.2(a)). Bulk-limited conduction is achieved when the charge density available at the organic/metal interface for injection, ρ_0 , exceeds the density of bulk intrinsic carriers in the film, N_0 . From the shape of the lateral electric field, it was clear that the bulk current was carried by thermally-ionized carriers at low voltage and by injected space-charge at high voltage.

When $\rho_0 < N_0$, the current through the film is contact limited, although it is not obvious from the current-voltage curve of a device with a “bad” contact

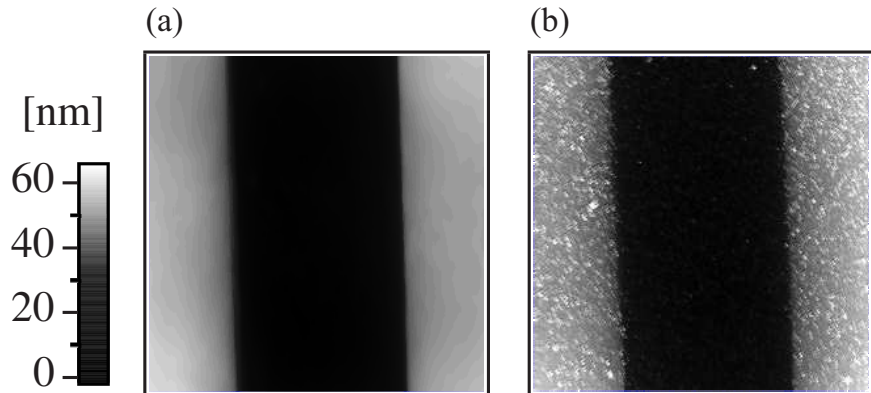


Figure 5.13: Crystallization of a TPD-PS film. (a) $10 \mu\text{m} \times 10 \mu\text{m}$ topographical image of a new TPD-PS film with interdigitated gold electrodes. (b) $10 \mu\text{m} \times 10 \mu\text{m}$ topographical image of an aged TPD-PS film with interdigitated gold electrodes.

(Figure 5.12(a)). The corresponding potential profile for a contact-limited device is shown in Figure 5.12(b) (solid line). In this device a substantial fraction of the applied voltage is dropped near the electrodes instead of in the bulk of the film. Here, electric force microscopy is used to follow the degradation of a TPD-PS/Au contact. Crystallization of TPD results in a film whose current becomes contact limited over time even though it was bulk limited initially.

We find that crystallization of TPD in polystyrene proceeds spontaneously if the TPD-PS film is stored in air for a few days. This can be seen by comparing the organic film's topography immediately after the film was spin-cast (Figure 5.13(a)) to a topographic image acquired after crystallization (Figure 5.13(b)). Crystallization of TPD from neat amorphous films [35–37] and solid solutions with polycarbonate [38, 39] is well established.

As TPD crystallizes out of polystyrene, the resistance of the TPD-PS/Au contact increases. The voltage drops at the source and drain contacts are comparable

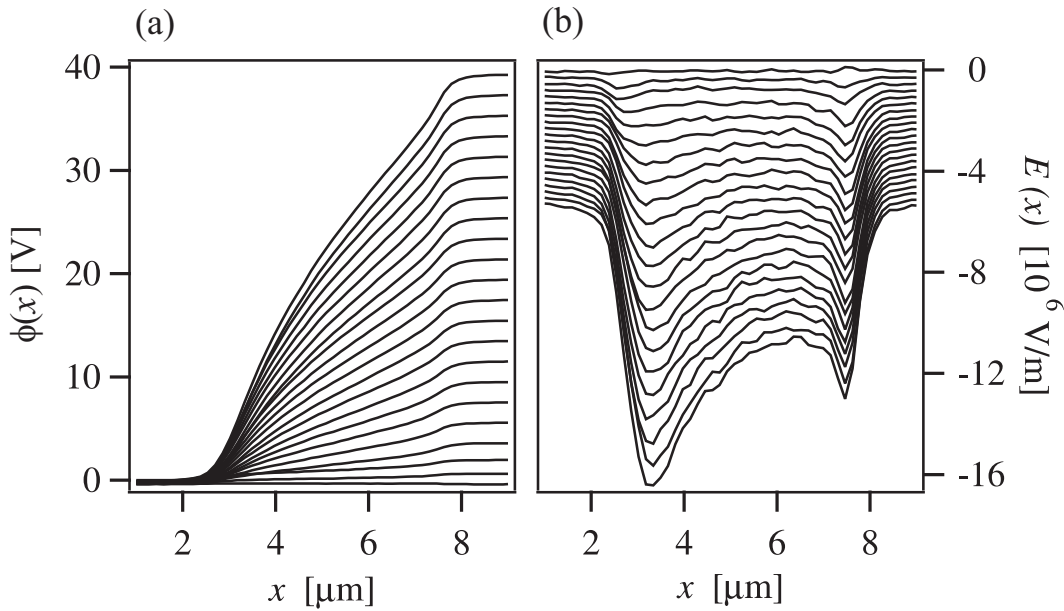


Figure 5.14: Potential and electric field profiles of an aged device. (a) $\phi(x)$ and (b) $E(x)$.

at low voltage (Figure 5.12(b), solid line) and remain symmetric when the applied voltage is reversed. At higher voltages, a slight voltage drop is still evident at the injecting electrode (Figure 5.14(a)). Nevertheless, the injecting contact has become “good” enough at high voltage to supply space-charge limited current, as evidenced by the raised potential in the device (Figure 5.14(a)) and the non-constant electric field profile inside the bulk of the film (Figure 5.14(b)). Qualitatively, the TPD-PS/Au contact in the TPD-crystallized device evolves from quite “bad” to “better” as the applied voltage is increased, and the interfacial electric field rises.

The current evolves from being bulk limited ($\rho_0 > N_0$) to being contact limited ($\rho_0 < N_0$). Fitting the current density observed at high-voltage to Equation 5.2, we can extract μ_0 (and β). Having estimated μ_0 , we fit the current density at low voltage to Equation 5.1, accounting for the voltage drop at the contacts, to obtain N_0 . Table 5.2 compares μ_0 and N_0 before and after crystallization. We find that μ_0

| | N_0 | μ_0 |
|------------------------|-----------------------------------|---|
| Before crystallization | $2 \times 10^{20} \text{ m}^{-3}$ | $1.6 \times 10^{-9} \text{ m}^2/\text{Vs}$ |
| After crystallization | $2 \times 10^{20} \text{ m}^{-3}$ | $7.0 \times 10^{-11} \text{ m}^2/\text{Vs}$ |

Table 5.2: Comparison of the zero-field hole mobility, μ_0 , and the density of intrinsic carriers, N_0 , before and after TPD crystallization.

decreases upon crystallization, presumably because the mean distance required to hop between TPD molecules has increased at grain boundaries. We find that the concentration of bulk intrinsic charge is not dramatically affected by crystallization. We can therefore conclude that the current has become contact limited because ρ_0 has decreased – the contact has degraded. Crystallization of TPD could either raise the injection barrier or decrease the density of states available for injection by, for example, reducing the energetic disorder present in the film.

Short lifetimes of organic light emitting diodes are a major problem in organic electronics. Crystallization of neat TPD at room temperature has long been associated with a loss of electroluminescence efficiency in light emitting diodes [35,36]. At elevated temperatures (near the glass transition temperature in neat TPD films), the loss of luminescence efficiency has been correlated with increased roughness, again suggesting crystallization, which was assumed to cause poor injection [37]. In this section we have used electric force microscopy to show that crystallization leads to both a decreased bulk mobility and a poor contact at both electrodes.

5.6 Conclusions

We have examined charge injection and space-charge in a model organic semiconductor by combining electric force microscopy and charge transport measurements. We have directly observed the transition from Ohmic conduction to space-charge limited conduction, microscopically, for the first time. Interfacial charge density was calculated from the measured current and inferred electric field. The charge density increases with electric field much faster than expected. We find that diffusion-limited thermionic emission theories, when strictly applied, do not completely describe the electric field dependence of the charge density at the metal/organic interface of this well-studied organic semiconductor. This strongly suggests that disorder plays an important role in charge injection, consistent with recent theoretical work [8, 15, 40]. Finally, we have observed the effects of film crystallization on charge injection, which led to a decreased bulk mobility and a poor contact at both electrodes.

5.7 Future directions

Variable temperature studies will give the activation energy of the injection barrier and allow us to better understand the nature of the acceptor molecules responsible for the background charge carriers, N_0 . Also, a more complete theoretical understanding of the tip-sample capacitance will help better quantify charge densities in the sample. By developing a field-effect transistor based on a molecularly doped polymer, we can infer the charge density at the interface and compare the results to the work of Bürgi *et al.* on polythiophene. If charge injection is a function of disorder, it should be possible to induce more disorder by doping

the molecularly doped polymer with a molecule having a large dipole moment to observe an increase in β_s . However, this may prove challenging since we observe considerable variation in β_s from similar samples.

The work presented in this chapter is based on the analysis of linescans across the source-drain channel. By measuring the space-charge current and imaging the potential in two dimensions in a sample with a more interesting geometry, such as a sharp electrode, it may be possible to observe current diffusion directly. Finally, it would be very interesting to observe the motion of a small packet of charge induced by creating electron/hole pairs with light – a microscopic time-of-flight experiment.

Chapter 5 references

- [1] P. Peumans, A. Yakimov, and S. R. Forrest, *Journal of Applied Physics* **93**, 3693 (2003).
- [2] H. E. Katz and Z. Bao, *Journal of Physical Chemistry B* **104**, 671 (2000).
- [3] Y. L. Shen, A. R. Hosseini, M. H. Wong, and G. G. Malliaras, *ChemPhysChem* **5**, 16 (2004).
- [4] J. C. Scott, *Journal of Vacuum Science and Technology A* **21**, 521 (2003).
- [5] M. A. Abkowitz and H. A. Mizes, *Applied Physics Letters* **66**, 1288 (1995).
- [6] E. M. Conwell and M. W. Wu, *Applied Physics Letters* **70**, 1867 (1997).
- [7] V. I. Arkhipov, E. V. Emelianova, Y. H. Tak, and H. Bässler, *Journal of Applied Physics* **84**, 848 (1998).
- [8] U. Wolf, V. I. Arkhipov, and H. Bässler, *Physical Review B (Condensed Matter)* **59**, 7507 (1999).
- [9] P. R. Emtage and J. J. O'Dwyer, *Physical Review Letters* **16**, 356 (1966).
- [10] J. C. Scott and G. G. Malliaras, *Chemical Physics Letters* **299**, 115 (1999).
- [11] Y. L. Shen, M. W. Klein, D. B. Jacobs, J. C. Scott, and G. G. Malliaras, *Physical Review Letters* **86**, 3867 (2001).
- [12] P. M. Borsenberger and D. S. Weiss, *Organic Photoreceptors for Xerography*, Optical Engineering, Marcel Dekker, Inc., New York, 1998.
- [13] Y. Roichman and N. Tessler, *Appl. Phys. Lett.* **80**, 1948 (2002).
- [14] C. Tanase, E. J. Meijer, P. W. M. Blom, and D. M. de Leeuw, *Physical Review Letters* **91**, 216601 (2003).
- [15] Y. N. Gartstein and E. M. Conwell, *Chemical Physics Letters* **255**, 93 (1996).
- [16] M. N. Bussac, D. Michoud, and L. Zuppiroli, *Physical Review Letters* **81**, 1678 (1998).
- [17] X. Crispin *et al.*, *Journal of the American Chemical Society* **124**, 8131 (2002).
- [18] M. Abkowitz, J. S. Facci, and J. Rehm, *Journal of Applied Physics* **83**, 2670 (1998).
- [19] M. A. Baldo and S. R. Forrest, *Physical Review B* **6408**, 1948 (2001).

- [20] A. Ioannidis, J. S. Facci, and M. A. Abkowitz, Journal of Applied Physics **84**, 1439 (1998).
- [21] B. H. Hamadani and D. Natelson, Applied Physics Letters **84**, 443 (2004).
- [22] K. Seshadri and C. D. Frisbie, Applied Physics Letters **78**, 993 (2001).
- [23] T. Hassenkam, D. R. Greve, and T. Bjørnholm, Advanced Materials **13**, 631 (2001).
- [24] L. Bürgi, H. Sirringhaus, and R. H. Friend, Applied Physics Letters **80**, 2913 (2002).
- [25] L. Bürgi, T. J. Richards, R. H. Friend, and H. Sirringhaus, Journal of Applied Physics **94**, 6129 (2003).
- [26] H. J. Yuh and D. M. Pai, Molecular Crystals and Liquid Crystals **183**, 217 (1990).
- [27] S. Heun and P. M. Borsenberger, Physica B **216**, 43 (1995).
- [28] P. N. Murgatroyd, Journal of Physics D - Applied Physics **3**, 151 (1970).
- [29] W. R. Silveira and J. A. Marohn, Review of Scientific Instruments **74**, 267 (2003).
- [30] T. R. Albrecht, P. Grütter, D. Horne, and D. Rugar, Journal of Applied Physics **69**, 668 (1991).
- [31] A. J. Dekker, *Solid State Physics*, Prentice-Hall, Inc., New Jersey, 1957.
- [32] J. G. Simmons, Physical Review Letters **15**, 967 (1965).
- [33] E. H. Rhoderick, Journal of Physics D - Applied Physics **3**, 1153 (1970).
- [34] K. J. Donovan, N. E. Fisher, and E. G. Wilson, Synthetic Metals **28**, D557 (1989).
- [35] L. M. Do, E. M. Han, Y. Niidome, and M. Fujihira, Journal of Applied Physics **76**, 5118 (1994).
- [36] P. F. Smith, P. Gerroir, S. Xie, A. M. Hor, and Z. Popovic, Langmuir **14**, 5946 (1998).
- [37] H. Fujikawa, M. Ishii, S. Tokito, and Y. Taga, Materials Research Society Symposium Proceedings **621**, 1 (2000).
- [38] E. M. Han, L. M. Do, M. Fujihira, H. Inada, and Y. Shirota, Journal of Applied Physics **80**, 3297 (1996).

- [39] F. Khan, A. M. Hor, and P. R. Sundararajan, *Journal of Physical Chemistry B* **108**, 117 (2004).
- [40] V. I. Arkhipov, U. Wolf, and H. Bässler, *Physical Review B (Condensed Matter)* **59**, 7514 (1999).

CHAPTER 6

VARIATION OF THE SURFACE POTENTIAL IN A MODEL ORGANIC SEMICONDUCTOR

We observe a surprising variation of the surface potential in thin films of a molecularly doped polymer system composed of the small molecule, triarylamine N,N'-diphenyl-N-N'-bis (3-methylphenyl) - (1,1'-biphenyl) -4,4'-diamine, known as TPD, dissolved in host polymers, polystyrene (PS) and polycarbonate (PC). High-sensitivity electric force microscopy is used to quantify the potential and capacitive contributions to the force gradient between the organic film and a sharp cantilever probe. A 60–100 mV peak-to-peak variation of the surface potential occurs on a 100–200 nm length scale, is uncorrelated with surface topography and consistently appears under a number of chemical and physical conditions. This large spatial variation of the surface potential is a large source of energetic disorder and is currently unaccounted for in charge injection and transport theories.

6.1 Introduction

High-sensitivity electric force microscopy is a powerful technique used to determine the local distribution of charge in organic electronic materials. Deposition and imaging of charge on organic insulators [1, 2] has been used to study tribo-electrification microscopically, with the sensitivity to detect single charge recombination events [3]. Correlations between morphology and work function in various thiophene polymers have been observed [4, 5].

Energetic disorder, a measure of the width, σ , of the density of localized states is an important component of the charge transport theories of amorphous solid solutions of π -conjugated molecules [6, 7], yet it has not been observed directly.

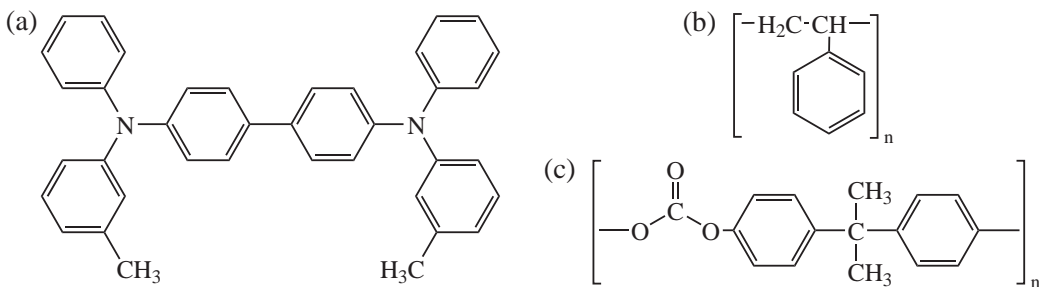


Figure 6.1: Chemical structures. (a) The triarylamine, TPD. (b) Polystyrene (PS) (c) Polycarbonate (PC).

Detailed bulk Kelvin probe and ultraviolet photoelectron spectroscopy studies have been used to determine the degree of band bending, the formation of an interface dipole layer and Fermi level alignment in organic semiconductor/metal systems [8,9]. The density of localized states is thought to exhibit significant broadening from the random orientation of dipoles at the interface [10]. However, spatial variations in band bending and in interface dipole layers have also yet to be directly observed.

In this chapter, an experimental effort to determine the cause of the large spatial variation of the surface potential observed in thin films of a model π -conjugated system is described. Our conclusions provide new insight into the electronic environment of disordered organic semiconducting molecules.

The molecularly doped polymer system

The triarylamine, TPD, is dispersed into a host polymer, polystyrene (PS) or polycarbonate (PC), shown in Figure 6.1. This molecularly doped polymer system was introduced in Chapter 4, where we discussed relevant charge transport and injection theories. This system has proven extremely useful for understanding charge transport [6,11] and injection [12–14] in molecularly doped polymers. Fur-

thermore, extremely flat films are prepared by spin-casting from solution, which greatly reduces the effort involved in disentangling contributions of the surface potential and capacitance to the force gradient measured by high-sensitivity electric force microscopy. This study follows our investigation of charge injection and space-charge limited conduction in TPD-PS [15].

6.2 Possible causes of the surface potential variation

Figures 6.2(a) and 6.2(b) show a typical force gradient image and linescan of the variation of the surface potential, $\Delta\Phi$. The sample is a thin, spin-cast film of molecularly doped polymers on a substrate(Figure 6.2(c)).

Figure 6.3 illustrates possible causes of the surprising spatial variation we have discovered in films of the molecularly doped polymers, TPD-PC and TPD-PS. Possible causes of a spatial variation of the surface potential, $\Delta\Phi$, include:

- Local charges or the work function variation of the underlying substrate
- Charge interface dipole between TPD and the underlying metal film [8,9,16]
- An accumulation region near the metal/organic interface [17]
- Uncompensated charge at the surface of the polymer film [1,2]
- Energetic disorder from surface & bulk dipoles [6,7,18]
- Aggregation of TPD molecules [19,20]
- Degree of disorder at the bulk versus the interface [10]
- Background charge carriers – ionized acceptors/donors [11]

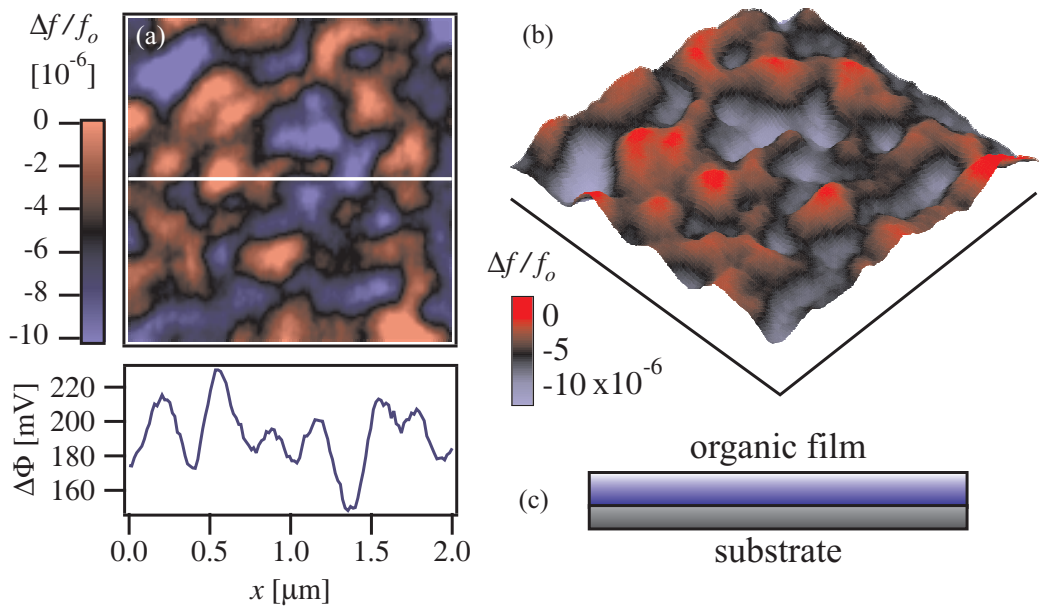


Figure 6.2: (a) Force gradient image and linescan of the surface potential, $\Delta\Phi$, over a thin molecularly doped polymer film. (b) Another view of the force gradient image shown in (a). (c) Representation of a thin organic film deposited on a substrate.

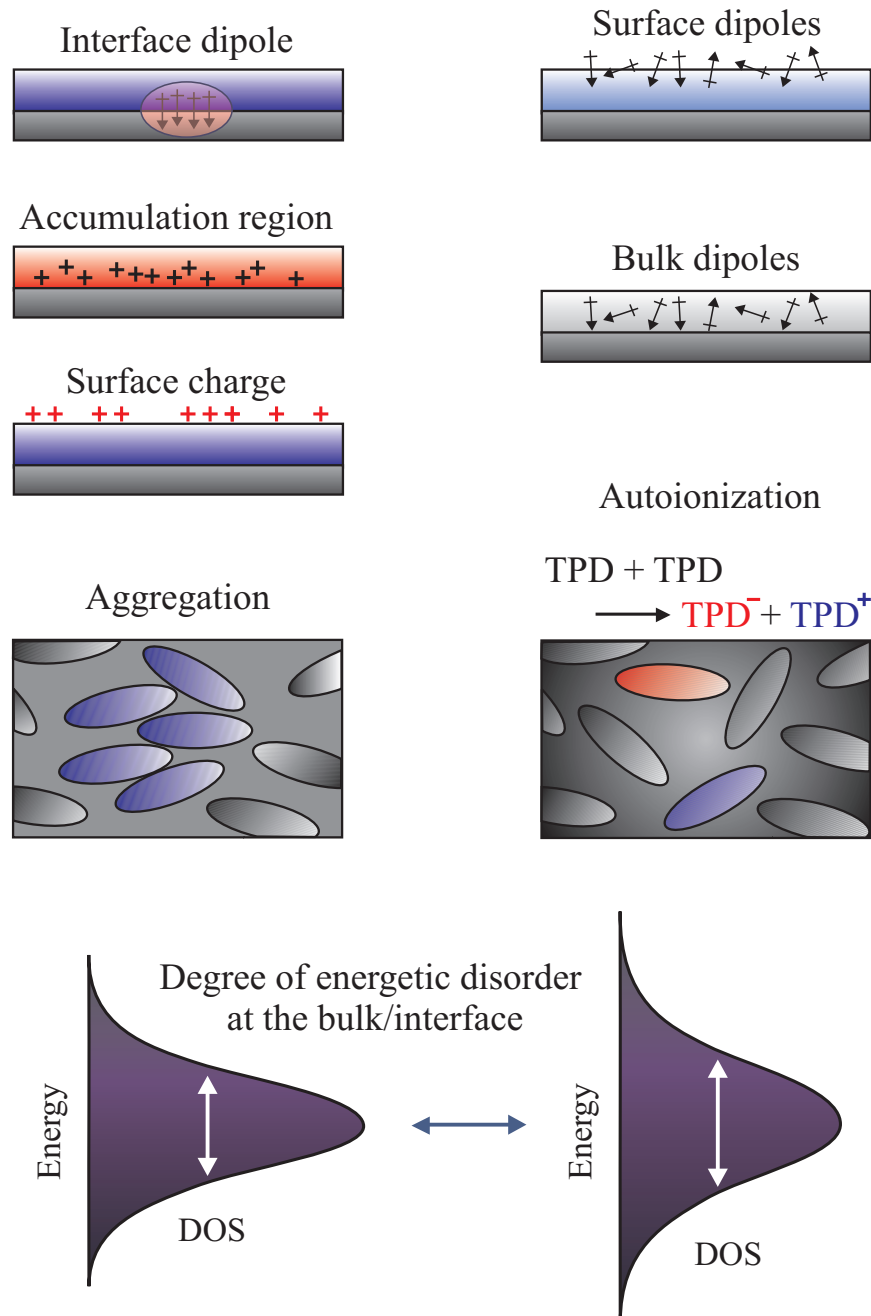


Figure 6.3: Possible causes of the spatial variation of the surface potential shown in Figure 6.2(a).

6.3 Experimental procedures

We discuss the preparation of gold, aluminum, and SiO₂ substrates. A procedure is given to create uniform films of TPD-based molecularly doped polymers by spin-casting. Finally, imaging the force gradient above organic thin films by high-sensitivity electric force microscopy is described.

6.3.1 Preparation of the substrate

Polycrystalline gold films were formed by evaporating 50 Å of chromium, which served as an adhesion layer, followed by 500 Å of gold on silicon at a rate of 0.4 Å/s by electron beam evaporation in high vacuum. The resulting metal films appeared polycrystalline by atomic force microscopy with a surface roughness 0.65 nm rms and 40–50 nm grain size. Epitaxially grown gold on mica was obtained from Molecular Imaging (part no. 61-100). The atomically flat terraces of epitaxial Au⟨111⟩ are typically several hundreds of nanometers across. Aluminum was deposited on silicon at a rate of 0.4 Å/s by electron beam evaporation in high vacuum, yielding 50–65 nm polycrystalline grains and surface roughness 1 nm rms. Here a native aluminum oxide of 1-2 nm is expected upon exposure to ambient conditions prior to film deposition [21].

For device fabrication, 300 nm films of SiO₂ were thermally grown on heavily doped n⁺Si, and interdigitated gold electrodes with a 5 μm spacing were patterned on top of the oxide. The 50 nm thick gold electrodes with a 5 nm chromium adhesion layer were prepared the same way as the polycrystalline gold films. However, because this is a lift-off technique, the gold film was exposed to a number of organic solvents in order to remove the gold and the photoresist polymer remaining

in the gap. Prior to solution-casting the organic film, we sonicated the substrate in acetone, methanol, and ethanol for 10 minutes then removed organics from the substrate by UV-ozone treatment for 10 minutes. We also fabricated a similar device in which gold electrodes were deposited with a 5 μm separation onto a quartz substrate [15]. In order to study the channel length dependence, devices with 2–10 μm channels were fabricated on a quartz substrate.

6.3.2 Preparation of the molecularly doped polymer films

Films of 50% weight TPD-PS (or PS) were prepared by first dissolving 15 mg of TPD and 15 mg of PS (MW = 2.0×10^6 , PD = 1.09; Aldrich) into 3 mL of dry tetrahydrofuran (≤ 10 ppm water) for 2.5 hours. The TPD and polycarbonate used here was supplied by Xerox, Inc. The concentration of TPD was decreased and the amount of host polymer was held constant for lower concentration TPD solutions, leading to consistent film thicknesses. The solution was then spin-cast in air onto the substrate at 2000 rpm for 15 s, yielding amorphous films with a typical thickness of 100 nm and a surface roughness of 0.65 nm (rms). To obtain films with a thickness of 20 nm, the concentrations of both the TPD and the host polymer were decreased to approximately 5 mg/mL and spin-cast at 2500 rpm for 15 s. Film thicknesses were measured by surface profilometry. Samples were prepared in air and transferred into high vacuum for electrical and scanned probe characterization within an hour of preparation.

6.3.3 Electric force microscopy and image interpretation

We imaged the film topography by intermittent contact mode atomic force microscopy and measured the local surface potential and tip-surface capacitance

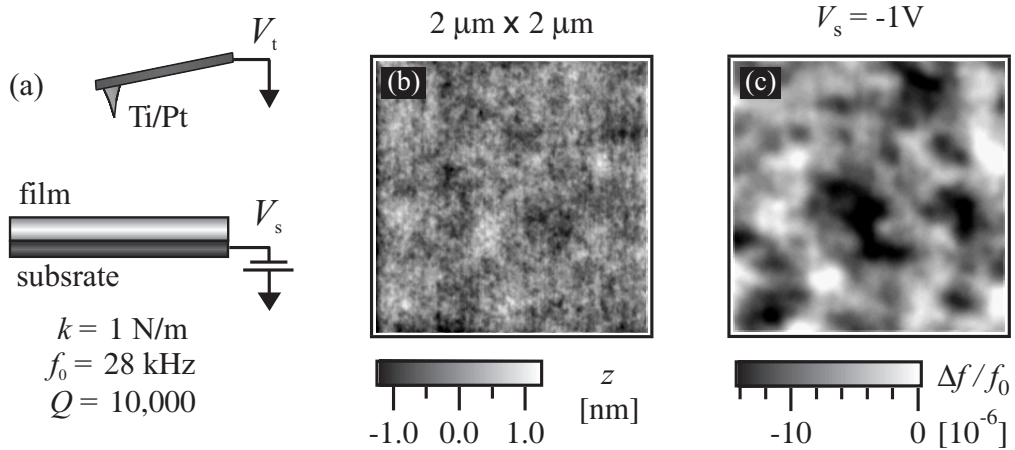


Figure 6.4: (a) Electrical convention between the cantilever tip and the sample surface. (b) Topography of a 120 nm thick film of 50% weight TPD-PC on polycrystalline gold. (c) Force gradient image of the same area ($2 \mu\text{m} \times 2 \mu\text{m}$).

in noncontact mode with a custom-built electric force microscope operating at room temperature in a vacuum of 10^{-6} mbar [22]. The microscope employed a Ti-Pt coated cantilever (model NSC21; MikroMasch) having a typical resonance frequency, $f_0 = 23\text{-}28$ kHz, a spring constant, $k = 1 \text{ N/m}$, and a quality factor, $Q \sim 10^4$, in vacuum.

Figure 6.4(a) illustrates the electrical convention between the cantilever tip and the sample. The tip is set to ground and a potential, V_s , is applied to the metal film underlying the molecularly doped polymer. In some cases, V_t is applied. Figures 6.4(b) and 6.4(c) show the topography obtained by intermittent contact mode imaging and a force gradient image of the same area in greyscale for comparison. Here the sample is a 120 nm thick 50% weight TPD-PC film on polycrystalline gold. We do not observe a correlation between the topography of these extremely flat polymer films (0.65 nm rms) and the force gradient images.

The contrast in the force gradient image arises from spatial variations of the

surface potential and capacitance between the cantilever and the surface of the sample. We measure the force gradient with an amplitude of 15 nm at a tip-surface distance of 65 nm. The interaction between the sharp probe and the sample are primarily electrostatic at this distance. Modeling the interaction as a capacitor (refer to Appendix A.4 and Section 3.5.4), the force gradient between the tip and the sample along the z -axis leads to a cantilever resonance frequency as a function of the applied surface potential, V_s ,

$$\frac{\Delta f}{f_0} = -\frac{1}{4k} \frac{\partial^2 C}{\partial z^2} (V_s - \Delta\Phi)^2, \quad (6.1)$$

$$f(V_s) = f_0 - \frac{f_0}{4k} \frac{\partial^2 C}{\partial z^2} (V_s - \Delta\Phi)^2, \quad (6.2)$$

where C is the tip-sample capacitance and $\Delta\Phi$ is the contact potential difference between the cantilever tip and the sample. $\Delta\Phi$ is dependent on the work functions of the tip and sample as well as uncompensated charge in the sample. We refer to $\Delta\Phi$ as the surface potential. When V_s was within ± 2 V of $\Delta\Phi$, f was quadratic in V_s to within a percent. Modeling f in this way (Equation 6.2) allows us to infer the second derivative of capacitance, $\partial^2 C / \partial z^2$ (labeled C'' in linescans), and $\Delta\Phi$, spatially.

Force gradient imaging

When imaging the force gradient, the applied surface potential, V_s , is held constant on the conductive substrate underlying the polymer film, as referenced to the cantilever tip. Force gradient images are acquired by scanning the sample and keeping the tip-sample distance constant by adjusting the cantilever height so that it traces out a plane parallel to the flat polymer surface. There is no contact between the tip and the surface during imaging. The height is obtained

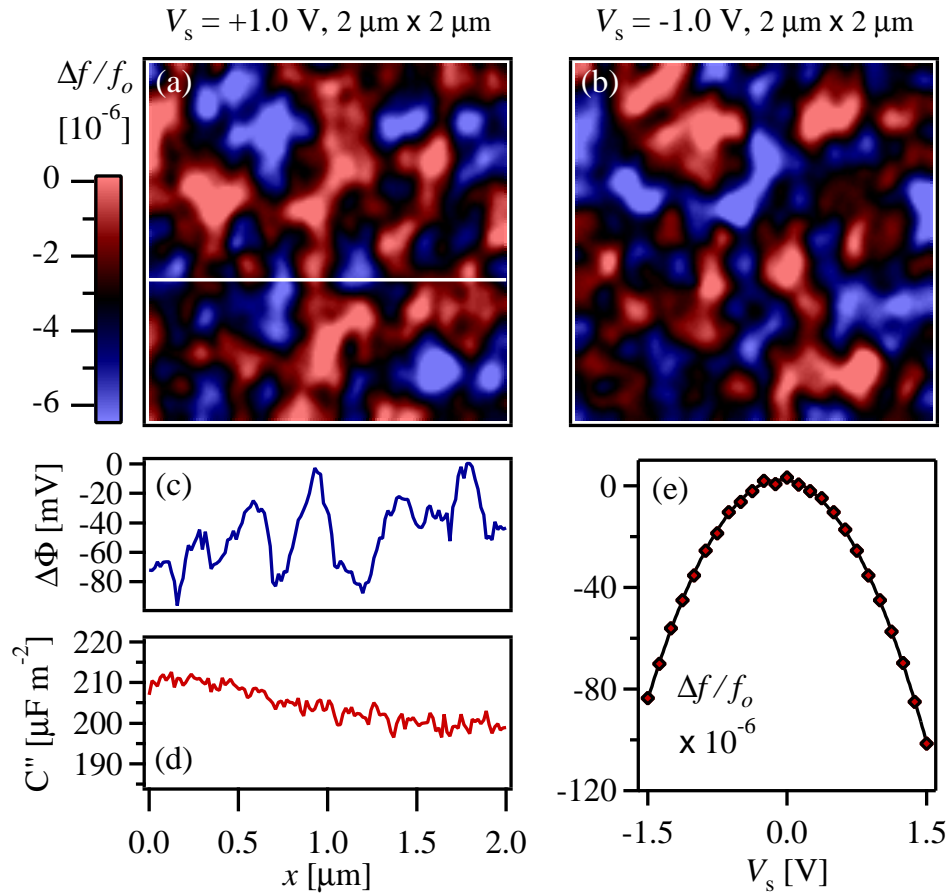


Figure 6.5: 120 nm thick film of 50% weight TPD-PC on polycrystalline gold. (a) and (b) show force gradient images ($2 \mu\text{m} \times 2 \mu\text{m}$) of the same area acquired at opposite bias, V_s . (c) The surface potential variation, $\Delta\Phi$, and (d) the capacitance derivative, $\partial^2 C / \partial z^2$, across the horizontal line indicated in image (a). (e) The resonance frequency shift of the cantilever as a function of applied surface potential, V_s .

by acquiring force-distance curves or estimated from the capacitance derivative, if necessary, to avoid tip-sample contact when triboelectric charging is a problem. Force gradient images are presented as a relative shift in resonance frequency, $\Delta f/f_0$. The force gradient, $\partial F_z/\partial z$, is related to the relative frequency shift by $\Delta f/f_0 \approx -1/2k \partial F_z/\partial z$.

Figures 6.5(a) and 6.5(b) are $2\mu\text{m} \times 2\mu\text{m}$ force gradient images of the same area over a 120 nm thick, 50% weight TPD-PC film on polycrystalline gold. These two images have inverted contrast because they are acquired on opposite sides of the f - V_s curve, shown in Figure 6.5(e). Here, the primary contribution to the images is a variation of $\Delta\Phi$. The image in Figure 6.5(a) was recorded with $V_s = 1.0$ V and the image in Figure 6.5(b) was recorded with $V_s = -1.0$ V. A positive change in $\Delta\Phi$, shifting the f - V_s curve to the right, causes decrease in f when imaging with negative V_s . However, a positive change in $\Delta\Phi$ will cause an increase in f when imaging with positive V_s , which explains the inverted contrast. A change in the capacitance will symmetrically alter the curvature of the f - V_s curve. The capacitance derivative depends on the tip-surface distance, z , according to z^{-n} , where n is between 1 and 2. Therefore, an increase in the tip-surface distance will decrease the capacitance. If a force gradient image arises from capacitive changes alone, such as would be caused by variations of the topography or a changing dielectric constant, images taken with opposite V_s will appear the same. This is not observed, confirming image contrast arises primarily from variations of the surface potential.

Linescans for quantifying $\Delta\Phi$ and $\partial^2C/\partial z^2$

In order to quantify the primary components of the force gradient, the cantilever was scanned along a line 65 nm above the surface in the plane from which the image was acquired. At each position x the cantilever resonance frequency f was recorded as a function of the applied surface potential, V_s . This gives a f - V_s curve for each point along the line. Figure 6.5(e) shows the quadratic response of the resonance frequency to the applied surface potential. Fitting each curve to Equation 6.2 yields $\Delta\Phi(x)$ and $\partial^2C/\partial z^2(x)$. The root mean square spatial variation of $\Delta\Phi$, is labeled $\Delta\Phi_{rms}$. In comparing the various polymer films we have investigated, these values are obtained from representative linescans, typically 2-5 μm in length.

6.4 Varying the chemical and physical environment of TPD

The surprising observation of a large variation of the surface potential, $\Delta\Phi$, over TPD-based molecularly doped polymer films is detailed in this section. We observed the effect under a variety of chemical and physical conditions, which we examined to uncover the source of the inhomogeneity. The experiments in this section are presented in detail, but a concise summary of the numerous studies is given in Section 6.5.

6.4.1 Molecularly doped polymer films on gold

The basic observation of the variation of $\Delta\Phi$ over a TPD-PC film on gold is discussed. Polycrystalline gold and epitaxially grown gold films are also investigated as a possible source of the variation of $\Delta\Phi$.

50% weight TPD-PC films on polycrystalline gold

In Figure 6.5, we have quantified the contributions of the $\Delta\Phi$ and $\partial^2C/\partial z^2$ to the force gradient in 50% weight TPD-PC film on polycrystalline gold. The maximum variation (peak-to-peak) of the potential in the linescan of Figure 6.5(d) is $\Delta\Phi_{pp} = 97$ mV. The root mean square (rms) value of the potential variation is $\Delta\Phi_{rms} = 22$ mV. The variation occurs on a 100-200 nm length scale. Linescans taken from over ten different areas on 4 separate films give an average $\Delta\Phi_{rms} = 17.5$ mV. The variation ranged from $\Delta\Phi_{rms} = 11-22$ mV.

The linescans in Figure 6.5(c) and 6.5(d) indicate that the force gradient arises from changes in $\Delta\Phi$. The small variation of $\partial^2C/\partial z^2$ is due to small changes in the tip-surface height and slight variation of the thickness of the film. The change in capacitance is consistent with a 2 nm change in tip-sample height, based on the height-dependence of the capacitance derivative. During the scan, the height of the scanning stage lowers as the piezoelectric material extends, which explains why the capacitance derivative decreases as the scan distance, x , increases. We have observed large changes in capacitance on poorly prepared films, where the presence of 10-100 nm sized voids have formed. Therefore, we are able to rule out the variation arising from defects such as pinholes and bubbles based on the nearly constant tip-surface capacitance. However, this leaves open the possibility that the variation of $\Delta\Phi$ might arise from a bulk charge, surface charge, or dipoles.

Comparison to a bare polycrystalline gold film

It is also possible the measured variation of the potential arises from an inhomogeneous work function of the underlying gold film. The work function of gold depends on which crystal orientation is exposed. For $\langle 100 \rangle$, $\langle 110 \rangle$, and $\langle 111 \rangle$

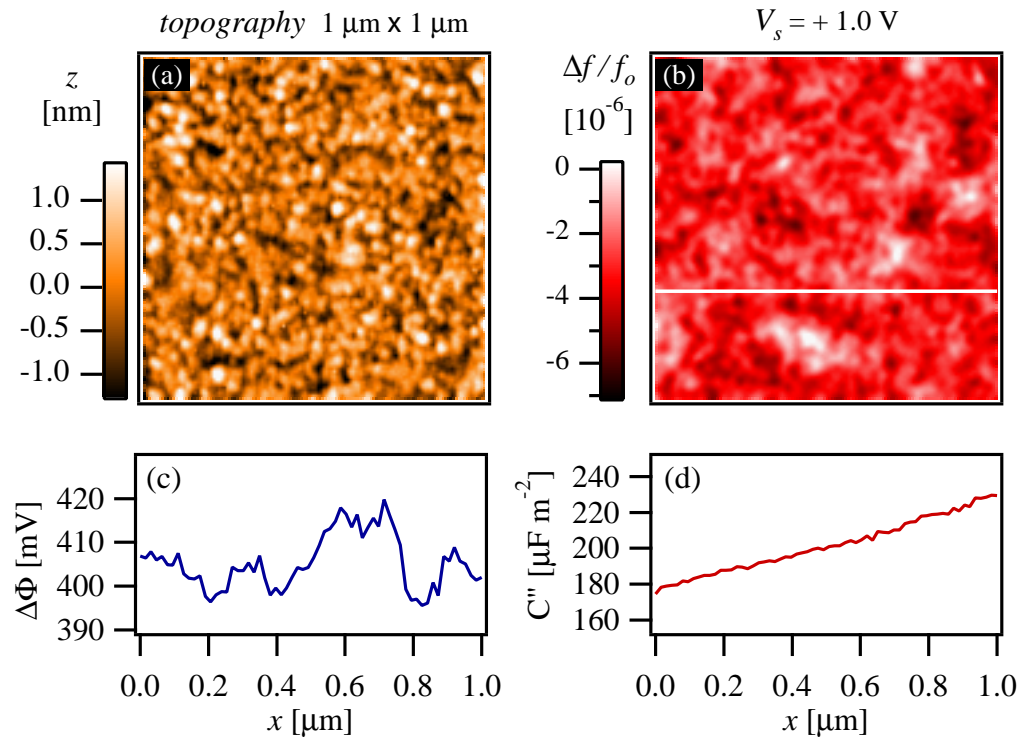


Figure 6.6: Polycrystalline gold films. (a) Topography of the polycrystalline film and (b) the corresponding force gradient image ($1 \mu\text{m} \times 1 \mu\text{m}$). (c) Linescan of the surface potential with $\Delta\Phi_{\text{rms}} = 6 \text{ mV}$. (d) The capacitance derivative, $\partial^2 C / \partial z^2$.

crystal faces, the work function, measured by the photoelectric effect, is 5.47 eV, 5.37 eV, and 5.31 eV, respectively [23]. In addition, the work function may fluctuate up to 100 mV depending on the surface conditions, such as the presence of water or oxygen [24], which are certainly present during sample preparation in ambient conditions.

Figure 6.6 summarizes our findings for a bare polycrystalline gold substrate. Most importantly, we found $\Delta\Phi_{\text{rms}} = 6$ mV for the gold film shown in Figure 6.6, compared to the typical $\Delta\Phi_{\text{rms}} = 17.5$ mV variation observed for TPD-PC films on Au. For polycrystalline gold, we found an average $\Delta\Phi_{\text{rms}} = 6.3$ mV, with a range of 3–11 mV. The surface potential, $\Delta\Phi$, varies on a length scale larger than the grain size of the polycrystalline Au, which is typically 40–50 nm as measured by atomic force microscopy. In addition, the capacitance derivative, which should reflect the topography, is not resolved. This is most likely due to spatial averaging considering the finite cantilever tip radius of 50 nm and tip-surface distance of 100 nm, which limits resolution in the force gradient images and corresponding linescans to approximately 100 nm.

Films of epitaxially grown gold

In order to further examine the role of the gold substrate, we studied epitaxially grown gold surfaces with a single crystal orientation – much different than polycrystalline gold. Here, atomically flat terraces of $\text{Au}\langle 111 \rangle$ are typically several hundreds of nanometers across, as shown in Figure 6.7(a). Figure 6.7(b) shows a force gradient image over the same area. The force gradient image resembles the topography of the sample, which indicates the primary contribution to the image is a variation of $\partial^2 C / \partial z^2$. The image in Figure 6.7(c) and the corresponding lines-

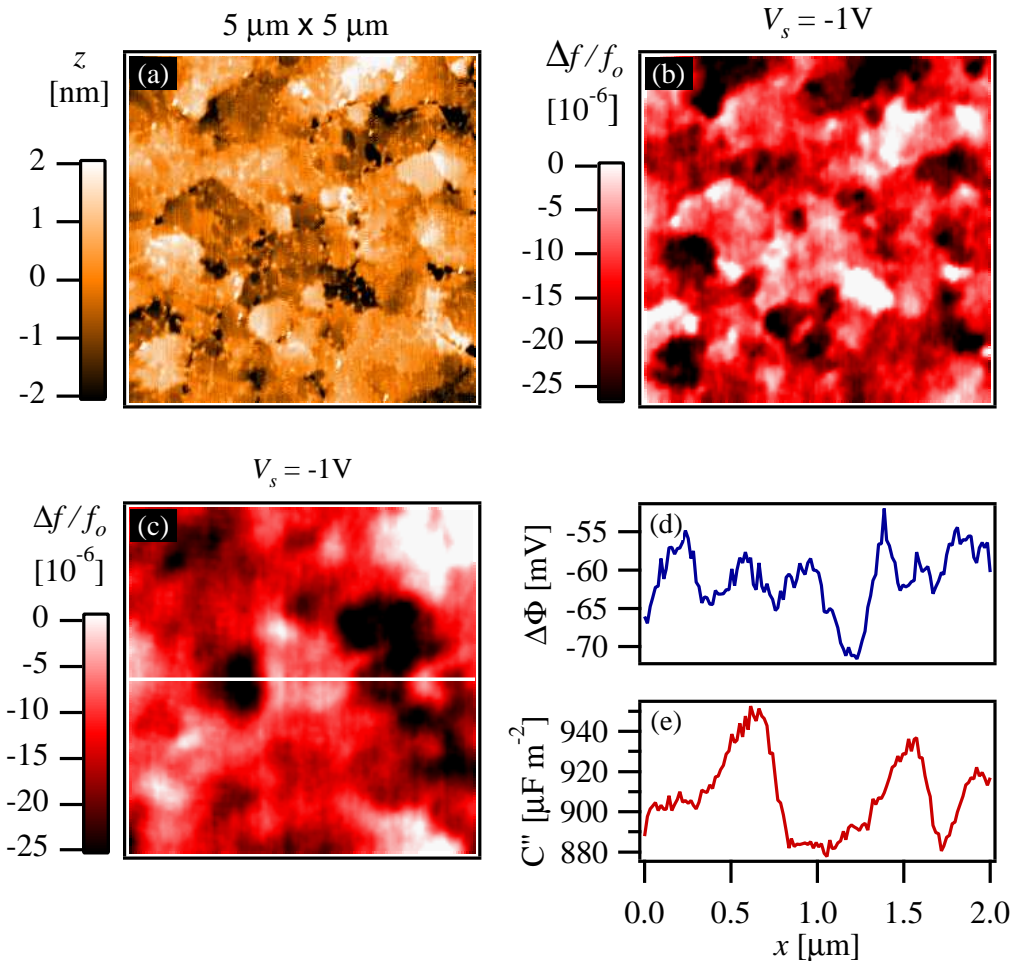


Figure 6.7: Epitaxially grown gold on mica. (a) Surface topography, $5 \mu\text{m} \times 5 \mu\text{m}$, (b) the corresponding force gradient image. (c) $2 \mu\text{m} \times 2 \mu\text{m}$ force gradient image and linescans showing (d) the variation of surface potential, $\Delta\Phi_{\text{rms}} = 3 \text{ mV}$, and (e) the capacitance derivative, $\partial^2 C / \partial z^2$.

cans demonstrate how $\Delta\Phi$ (Figure 6.7(d)) and $\partial^2C/\partial z^2$ (Figure 6.7(e)) contribute to the force gradient. The potential for the image shown varies by $\Delta\Phi_{\text{rms}} = 3 \text{ mV}$, although we have found larger variations. We found an average potential variation of $\Delta\Phi_{\text{rms}} = 7.8 \text{ mV}$. This is still much smaller than $\Delta\Phi_{\text{rms}} = 17.5 \text{ mV}$ for 50% weight TPD-PC films on gold.

Unlike the linescan of polycrystalline Au (Figure 6.6(d)), changes in $\partial^2C/\partial z^2$ trace the changing tip-surface distance because they occur on a larger length scale. The capacitance derivative shown in Figure 6.7(e) follows the horizontal line through the force gradient image of Figure 6.7(c) and the topography of the gold film. To a lesser degree, we observe that the surface potential, $\Delta\Phi$, also affects the force gradient as the work function changes at steps on the Au⟨111⟩ surface.

50% weight TPD-PC films on epitaxially grown gold

We have also found a large variation of the surface potential in 50% weight TPD-PC films on epitaxially grown Au. Figures 6.8(a) and 6.8(b) show $2\mu\text{m} \times 2\mu\text{m}$ force gradient images of a 100 nm thick, 50% weight TPD-PC film. The inverted contrast of the two images indicates a variation of $\Delta\Phi$ is the primary cause of the contrast in the force gradient images. The force gradient varies significantly on a 200 nm length scale, as it did with TPD-PC films on a polycrystalline gold substrate (Figure 6.5). The linescans of Figures 6.8(c) and 6.8(d) also show similar variation of $\Delta\Phi$ and $\partial^2C/\partial z^2$ when compared with the polycrystalline gold substrate. The potential varies by $\Delta\Phi_{\text{rms}} = 19 \text{ mV}$. Figure 6.8(e) is a larger, $5 \mu\text{m} \times 5 \mu\text{m}$ force gradient image, which includes the boxed region imaged in Figures 6.8(a) and 6.8(b). We find an average $\Delta\Phi_{\text{rms}} = 16 \text{ mV}$. The potential variation ranged from $\Delta\Phi_{\text{rms}} = 12\text{--}19 \text{ mV}$.

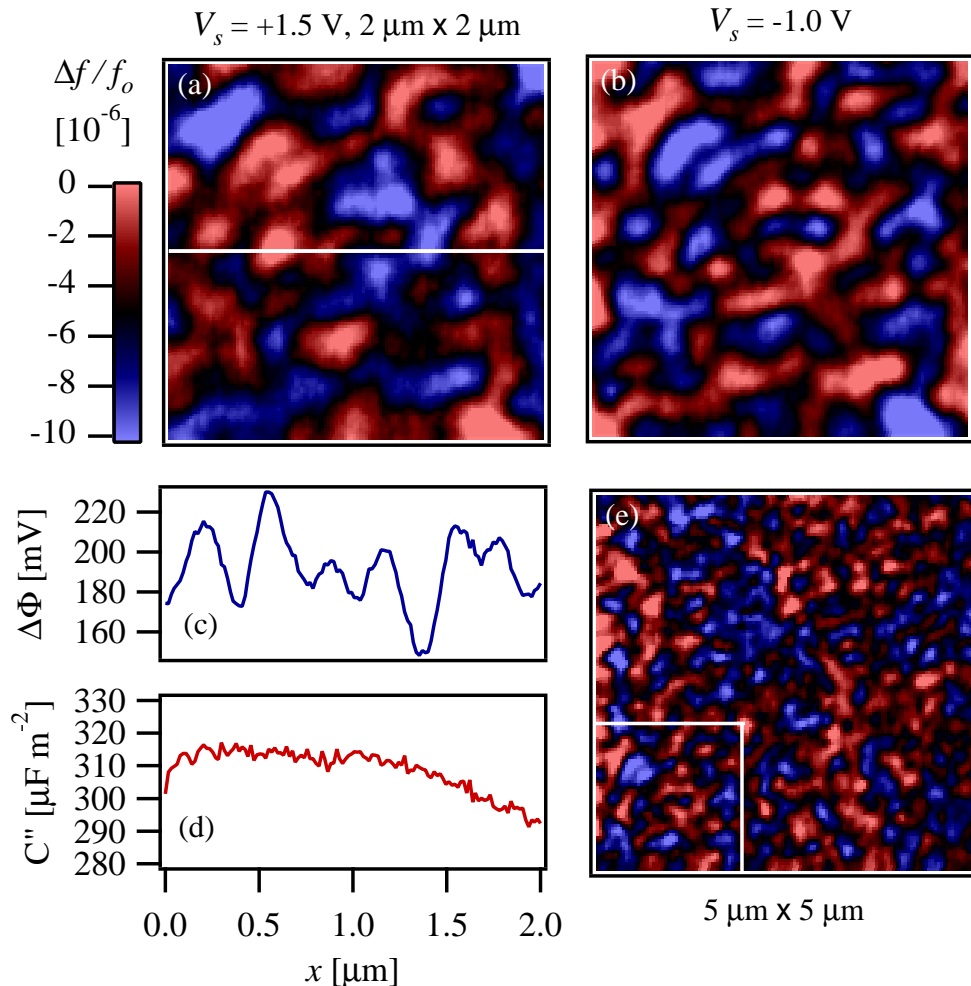


Figure 6.8: 100 nm thick film of 50% weight TPD-PC on epitaxially grown gold. Images (a) and (b) show $2 \mu\text{m} \times 2 \mu\text{m}$ force gradient images. Linescans (c) and (d) show variations in the potential ($\Delta\Phi_{\text{rms}} = 19 \text{ mV}$) and capacitance derivative, $\partial^2 C / \partial z^2$, respectively, for the line shown in (a). Image (e) shows a larger $5 \mu\text{m} \times 5 \mu\text{m}$ force gradient image including the area imaged in (a) and (b), indicated by the boxed area in the lower left hand corner.

Conclusions

The studies of both polycrystalline and epitaxially grown Au films support the conclusion that the large variation of $\Delta\Phi$ in films of TPD-PC on gold is not simply due to the underlying gold film. This work also shows the variation of the force gradient arises primarily from changes in the potential.

6.4.2 Varying the interface energetics

The formation of an interface dipole is substrate dependent [16]. Also, an accumulation region, predicted by the Mott-Gurney model (Section 4.5.1), should decrease for an interface with a larger injection barrier. An aluminum film or a silicon oxide (SiO_2) surface creates a much different interface with TPD than does gold. Aluminum has a significantly smaller work function, and SiO_2 is an insulator. If the variation of $\Delta\Phi$ arises from a spatially varying interface dipole or accumulation region, we might expect to see a difference in the magnitude or length-scale of the spatial variation of $\Delta\Phi$ for TPD films on aluminum and (SiO_2).

We found the variation of $\Delta\Phi$ for TPD-PC films on polycrystalline and epitaxially grown gold films is much larger than that of bare gold in Section 6.4.1. It is well known that highly purified TPD forms an interface dipole with gold under ultrahigh vacuum conditions (Figure 6.9(a)). The interface dipole decreases in magnitude on metal films with a lower work function. The magnitude of the interface dipole is -1.15 V on a clean gold surface [16, 25], significantly increasing the hole injection barrier. It is thought that the TPD molecule repels the electrons tailing off the metal surface, altering the surface dipole of the metal. However, there is also evidence of charge transfer at the interface of indium-tin oxide [26].

In Section 4.5.1, the Mott-Gurney model predicts an accumulation of charge

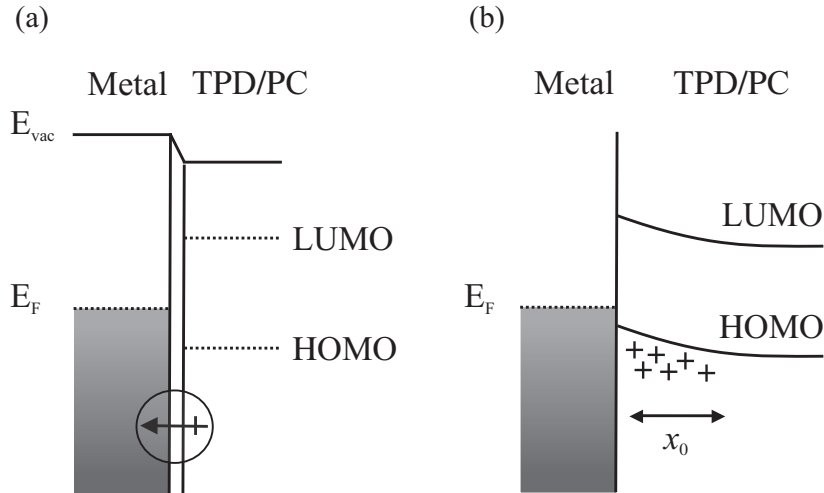


Figure 6.9: (a) The interface dipole between clean gold and purified TPD [16,25]. (b) The accumulation region (holes), as predicted by the Mott-Gurney model of the insulator/metal interface (Section 4.5.1).

carriers at the metal/insulator interface. The formation of an accumulation of holes at the metal/TPD interface is illustrated in Figure 6.9(b). The charge density at the interface, ρ_0 (Equation 4.25), is $\sim 262 \text{ C/m}^3$ at 298 K with an injection barrier of 300 mV, a density of TPD, $N_{\text{TPD}} = 2.66 \times 10^{26} \text{ m}^{-3}$, and a dielectric constant, $\epsilon = 3$. This is approximately 1.6 charges in a $(100 \text{ nm})^3$ volume. For aluminum, the measured work function is at least 1 V lower than gold. With a conservative barrier of 1.0 V, $\rho_0 \sim 1.8 \times 10^{-10} \text{ C/m}^3$, several orders of magnitude less than the predicted charge density at the TPD-PC/Au interface. If the variation is due to a spatially varying accumulation region, due to, for example, a spatial variation in orbital energies [18], this large decrease in the charge density should alter the variation of $\Delta\Phi$ considerably.

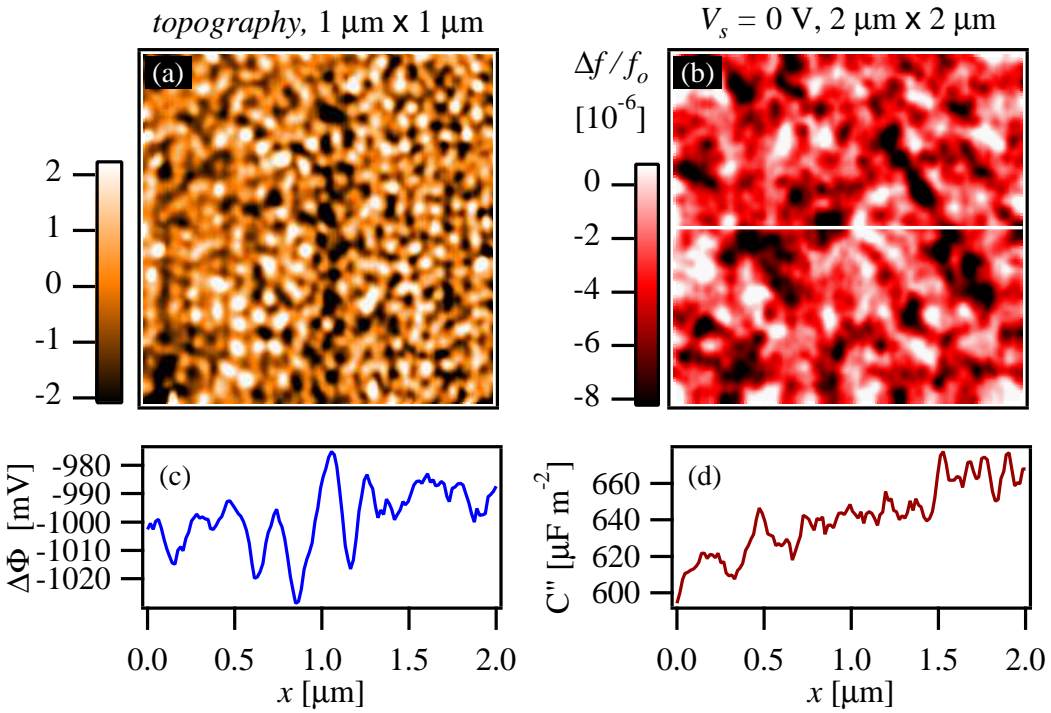


Figure 6.10: Polycrystalline aluminum film with a native oxide. (a) Topography ($1 \mu\text{m} \times 1 \mu\text{m}$) showing 65 nm grains. (b) $2 \mu\text{m} \times 2 \mu\text{m}$ force gradient image with contributions from both the surface potential, $\Delta\Phi$, and capacitance derivative, $\partial^2 C / \partial z^2$, shown in linescans (c) and (d), respectively. The potential varies by $\Delta\Phi_{\text{rms}} = 11 \text{ mV}$.

Aluminum films

The topography of aluminum substrate with a native oxide is shown in Figure 6.10(a). The film is 50 nm thick and the topography shows 65 nm grains and a surface roughness of 1 nm rms. Figure 6.10(b) is a $2 \mu\text{m} \times 2 \mu\text{m}$ force gradient image acquired with $V_s = 0 \text{ V}$. Aluminum has a work function less than that of the platinum-titanium cantilever tip by $\sim 1 \text{ V}$, so this rather large contact potential difference is sufficient to bring out contrast in the force gradient images without an applied bias. The linescan of Figure 6.10(c) has a potential variation of $\Delta\Phi_{\text{rms}} = 11 \text{ mV}$. We found the average variation was $\Delta\Phi_{\text{rms}} = 9.3 \text{ mV}$. The aluminum grains are slightly larger than the gold grains, allowing the variation of tip-surface distance in the linescan of $\partial^2 C / \partial z^2$ (Figure 6.10(d)) to be resolved.

50% weight TPD-PC films on aluminum

Figure 6.11(a) and 6.11(b) are force gradient images of a 110 nm thick film of 50% weight TPD-PC on a polycrystalline aluminum film with a native oxide. The variation of the potential is $\Delta\Phi_{\text{rms}} = 16.5 \text{ mV}$, shown in Figure 6.11(c). The images shown in Figure 6.11(a) and 6.11(b) are acquired under opposite bias, V_s , indicating the potential is the primary component of the force gradient. This is supported by the nearly constant capacitance derivative shown in Figure 6.11. We find an average $\Delta\Phi_{\text{rms}} = 17 \text{ mV}$.

Because a spatially varying interface dipole or accumulation region should be much smaller at the aluminum/TPD interface, it is unlikely that the variation of $\Delta\Phi$ is caused by these effects. We also prepared a 90 nm thick film of 50% weight TPD-PS, changing the host polymer from polycarbonate to polystyrene. We found no significant change. The average variation of the potential was $\Delta\Phi_{\text{rms}} = 16.3 \text{ mV}$

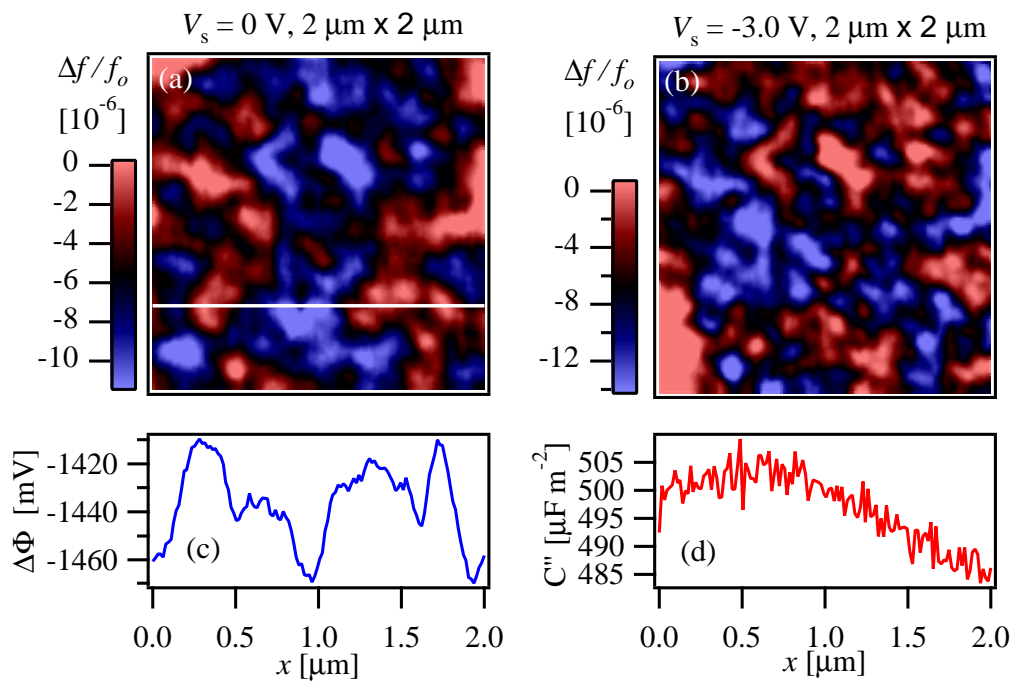


Figure 6.11: 110 nm film of 50% weight TPD-PC on a polycrystalline aluminum film with a native oxide. 2 $\mu\text{m} \times 2 \mu\text{m}$ force gradient images acquired under opposite bias are shown in (a) and (b). (c) The potential varies by $\Delta\Phi_{\text{rms}} = 16.5 \text{ mV}$. (d) The capacitance derivative, $\partial^2 C/\partial z^2$.

for the TPD-PS film.

50% weight TPD-PS films on SiO₂

Figure 6.12(a) shows the topography of a 100 nm film of 50% weight TPD-PS on polycrystalline gold electrodes patterned on a SiO₂ substrate. The film has the same thickness on the SiO₂ as it does on the gold electrodes. Figure 6.12(b) is a force gradient image of the TPD-PS device. From the force gradient image of Figure 6.12(c), note the spatial variation of the force gradient over the SiO₂. This suggests that the variation of $\Delta\Phi$ may be similar over gold and the oxide, which would rule out a spatially varying interface dipole and an accumulation region as the cause of the observed potential variation.

The linescan of Figure 6.12(d) shows a large variation of $\Delta\Phi$. Over the SiO₂, $\Delta\Phi_{rms} = 38$ mV on average. This variation is much larger than what is observed for a TPD-PS film on a gold substrate. Unfortunately, the variation arises from charges on the SiO₂ surface itself. We find that on bare SiO₂ and polished quartz surfaces, $\Delta\Phi$ varies by hundreds of mV, making it very difficult to draw conclusions with TPD films on SiO₂.

The linescan of Figure 6.12(e) shows the variation of the potential drop, $\phi(x)$, with an applied potential of 1.5 V to the left (hole-injecting) electrode. It is interesting to note that the features in the linescan of Figure 6.12(d) ($\Delta\Phi$) are observable on top of the potential drop, $\phi(x)$ (Figure 6.12(e)), across the device when it is “on.” If the variation of $\Delta\Phi$ is due to an inhomogeneous distribution of charges in TPD-PS, they are not mobile at this electric field.

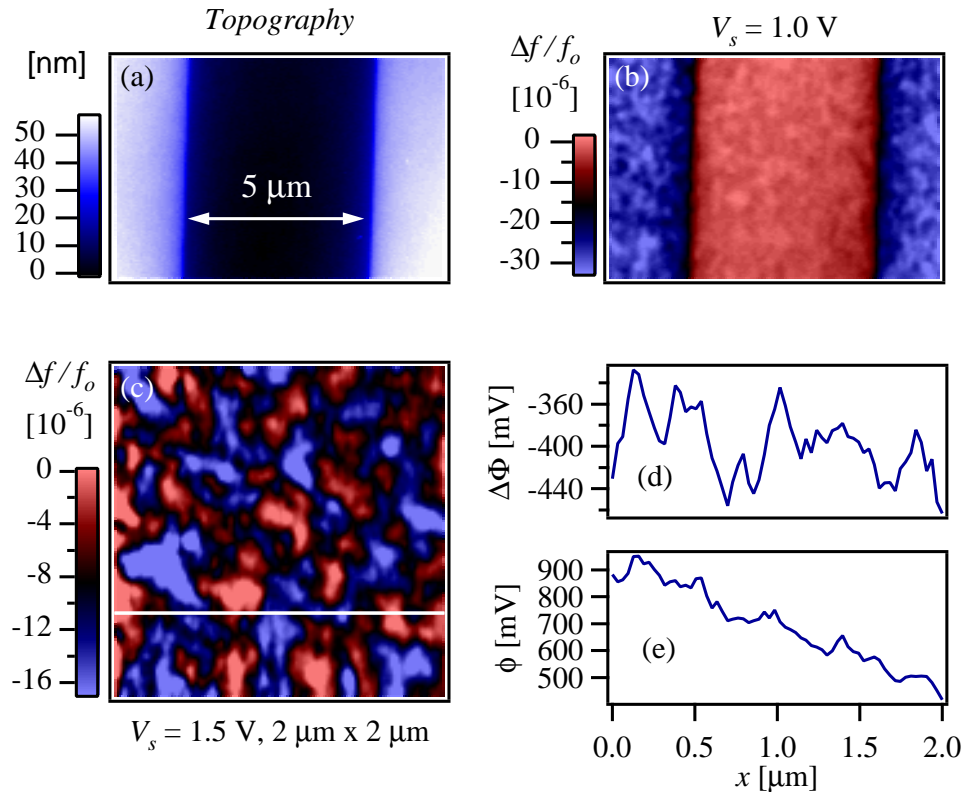


Figure 6.12: Interdigitated device: A 100 nm film of 50% weight TPD-PS on 55 nm polycrystalline gold electrodes with a 5 μm spacing. (a) Film topography and (b) force gradient image of the same area. (c) Force image over the SiO_2 region and (d) the potential, $\Delta\Phi$, across the linescan indicated in (c). (e) Linescan over the same line in (d) with an applied potential of 1.5 V to the left (hole-injecting) electrode.

Conclusions

It is unlikely a spatially varying interface dipole or accumulation region is the cause of the variation of the surface potential, considering the drastic difference between the energetics of gold and aluminum interfaces with TPD-PC. Due to the surface charging of SiO₂, it is difficult to draw conclusions about the TPD-PS/SiO₂ interface.

6.4.3 Surface charges on low mobility organic films

We investigated whether the observed variation of $\Delta\Phi$ is due to native or triboelectric deposition of surface charge. There is precedent for depositing uncompensated surface charge on an insulating surface using an electric force microscope tip, so this is a concern [1].

Charge deposited on top of an insulating film will contribute to $\Delta\Phi$ by an amount

$$\Delta\Phi = \frac{\sigma d}{\epsilon\epsilon_0} \quad (6.3)$$

where σ is the surface charge density, d is the film thickness, and ϵ is the film dielectric constant. This relationship is derived from a parallel plate model with a dielectric and vacuum between the capacitor plates and a surface charge density, σ [27].

Surface charge deposition on 50% weight TPD-PC and TPD-PS films

Triboelectric charge deposition from tip-surface contact was not observed at room temperature in 50% weight TPD-PC or TPD-PS films on gold, presumably because the mobility is high enough to dissipate surface charges before imaging. Attempts to deposit charge with applied potentials up to ± 10 V between the

tip and surface did not alter $\Delta\Phi$. While charge deposition may have occurred, it dissipated within 100 ms, the time required to retract the cantilever tip and monitor the force gradient.

However, positive surface charges were deposited on 50% weight TPD-PC/Au films at 77 K nearly every time the tip contacted the surface, without an applied potential between the tip and sample. At low temperatures, the mobility of the film is several orders of magnitude lower [11], effectively halting the dissipation of charge throughout the polymer film. To further investigate the dependence of the charge deposition as a function of mobility, we studied low concentration TPD-PC and TPD-PS films, as well as pure polycarbonate films. An image of triboelectric charge deposition at low temperatures is shown in Section 6.4.5, Figure 6.18(a).

Low concentration TPD-PS films

Charge deposition was observed at room temperature in 5% weight TPD-PS, where the mobility is 5 orders of magnitude lower than 50% TPD-PS [11, 28]. The charges were deposited without an applied potential between the tip and sample. The tip was slowly approached to the surface and allowed to contact the surface as the van der Waals attractive potential became greater than that of the cantilever, known as ‘snap-in.’ The tip was in contact with the surface for 300 ms.

Figure 6.13(a) and 6.13(b) are force gradient images before and after charge deposition, respectively. The images are acquired with a negative V_s . The positive charge on the surface screens the field from the underlying gold (negative potential), leading to a smaller force gradient between the cantilever tip and substrate. This is why the surface charges appear as a bright spot. Figure 6.13(c) shows the potential profile across the charged region. A more negative V_s is required to null

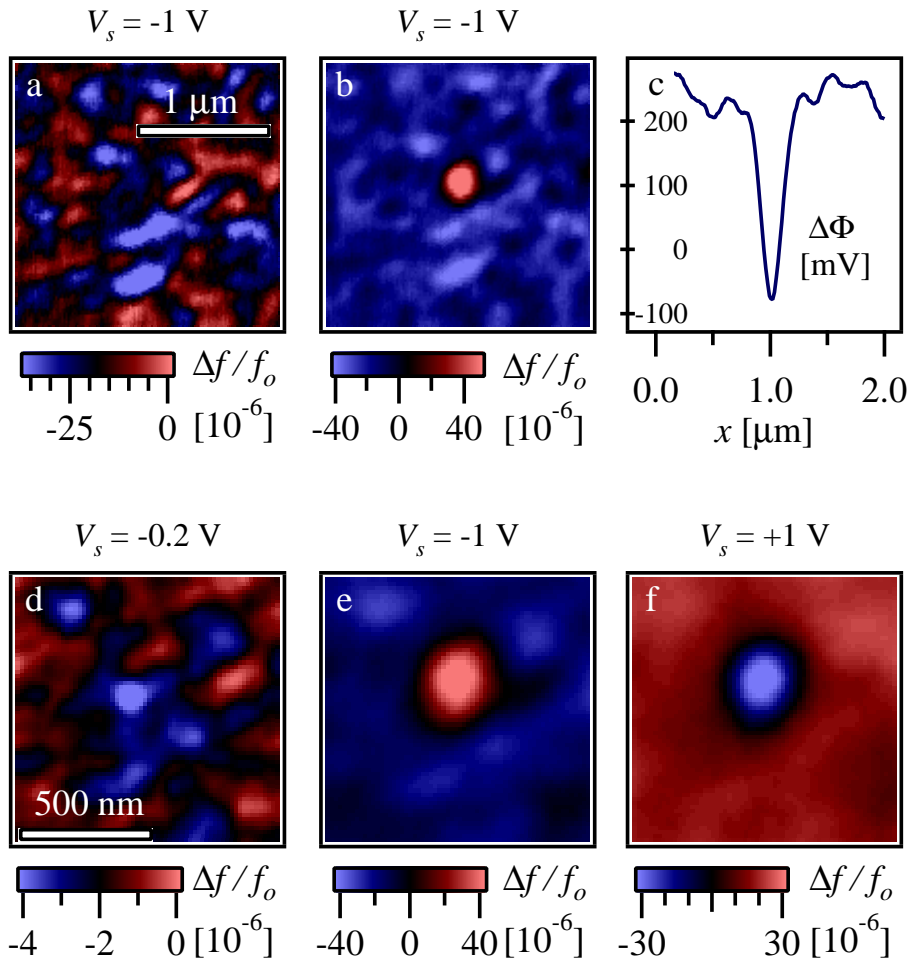


Figure 6.13: Charge deposition on 5% weight TPD-PS: 100 nm thick TPD-PS film on polycrystalline gold. (a) $2 \mu\text{m} \times 2 \mu\text{m}$ force gradient image prior to tip-sample contact. (b) Force gradient image after contact indicating deposition positive charge on the surface. (c) The change in potential, $\Delta\Phi$, over the charged area. (d) $1 \mu\text{m} \times 1 \mu\text{m}$ force gradient image with an applied potential close to the contact potential difference between the tip and sample (the null point). Images of the same area with potentials of $V_s = -1 \text{ V}$ and $V_s = +1 \text{ V}$ are shown in (e) and (f), respectively.

the potential between the tip and sample, consistent with positive surface charges.

Figure 6.13(d) shows a 500 nm × 500 nm image of the charged area with the applied potential near the null point ($V_s \approx \Delta\Phi$). The surface charges appear as a small force gradient, since the force arises from only the image charge in the tip. Figures 6.13(e) and 6.13(f) illustrate how uncompensated surface charges appear in a force gradient image when the bias of V_s is reversed. Like a change in the work function, force gradient images of surface charge under opposite bias (V_s) exhibit inverted contrast. Using Equation 6.3, we calculate ~ 10 positive charges reside on the surface of the polymer, concentrated where the tip touched the surface of the 5% weight TPD-PS film. Like polycarbonate and 50% weight TPD-PS at low temperatures, we did not observe diffusion of the charge spot over the course of 24 hours.

It is interesting that we observe the deposition of only positive charges on the surface. Terris *et al.* [2] observed deposition of positive and negative charges on films of polymethyl methacrylate (PMMA) under ambient conditions. However, they noted a higher probability of depositing positive charges and suggested that adsorbed water may play a role. We see deposition of positive charges in high vacuum, where water should be absent, on polycarbonate and low mobility TPD-PC and TPD-PS films. In the case of TPD, the molecule could donate an electron from the HOMO into the tip, leaving positive charges behind. This would dissipate quickly if the mobility is sufficient. It would remain if the mobility is low, which is our observation.

Surprisingly, we find that decreasing the concentration did not lead to a significantly smaller variation of the potential. The potential varied from $\Delta\Phi_{rms} = 17.5$ mV to $\Delta\Phi_{rms} = 16$ mV as the TPD concentration is dropped from 50% weight

to 5% weight.

Polycarbonate films

Unlike 50% weight TPD-PC films at room temperature, pure polycarbonate films (on polycrystalline gold), which are highly insulating, were found to accept charges from the cantilever tip under intermittent contact mode AFM imaging. We first imaged a $1\mu\text{m} \times 1\mu\text{m}$ area with both the surface potential, V_s , and tip potential, V_t , at ground. The contact potential difference between the tip and surface was less than -40 mV. The tip was lifted from the surface, and a force gradient image was acquired with the gold substrate potential at $V_s = +1.0$ V. Figure 6.14(a) is the topographic image. The variations in the subsequent force gradient image of the same area, Figure 6.14(b), correspond to a peak-to-peak potential variation of $\Delta\Phi_{\text{pp}} = 106$ mV due to deposited charge. The charge distribution is not uniform over the area despite having equal contact time with the surface-tapping probe. Depending on the deformation of the polymer film as the cantilever ‘taps’ the film, the surface area of the contact region will vary. Some areas of the polycarbonate appear to be more susceptible to triboelectric charging, which maybe be related to the surface morphology.

The force gradient image of Figure 6.14(b) includes the charged area plus a larger area which was “untouched” by intermittent contact mode imaging. The force gradient images are acquired with a positive potential to the surface, V_s . Thus, the presence of positive surface charges on the insulating film above the electrode increases the force gradient [1]. It is clear that charges were deposited only in the square region in the lower left-hand corner of Figure 6.14(c), where contact was made by the tip during topographical imaging. The potential varia-

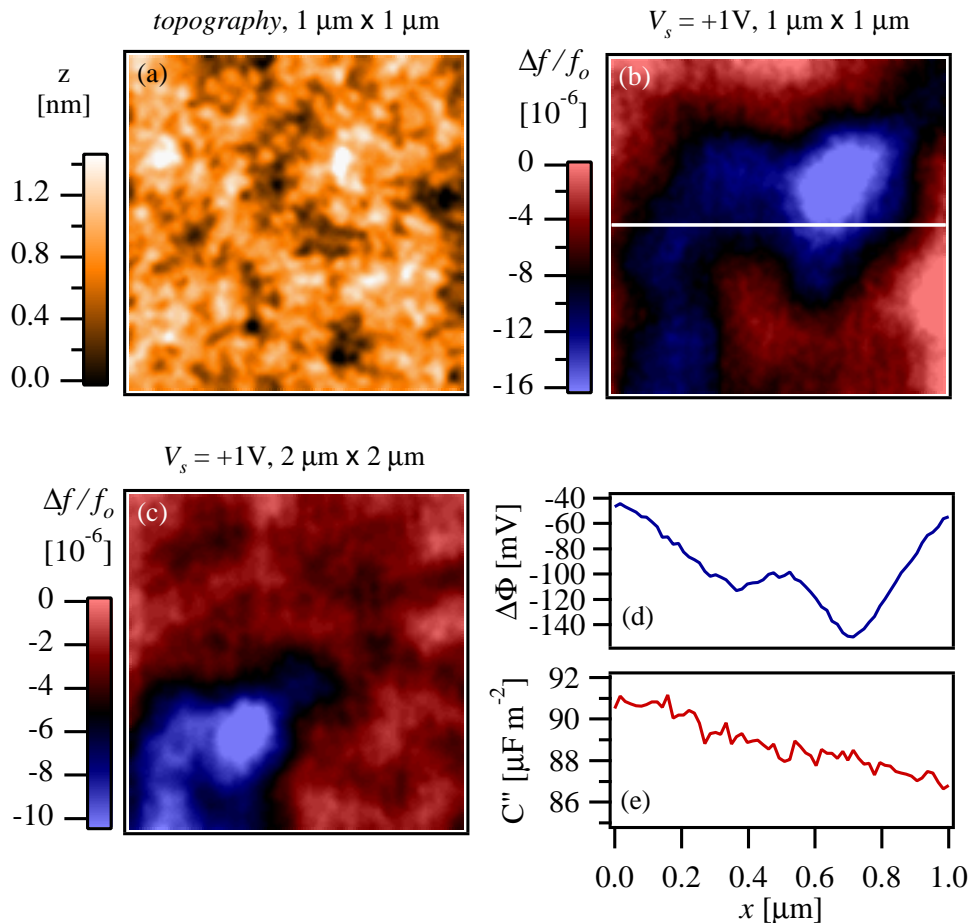


Figure 6.14: Polycarbonate: 100 nm polycarbonate film on polycrystalline gold. (a) Film topography ($1 \mu\text{m} \times 1 \mu\text{m}$), obtained by intermittent contact mode AFM. (b) Force gradient image of the same area after obtaining topography, charging the surface. (c) Force gradient image of a larger area ($2 \mu\text{m} \times 2 \mu\text{m}$) showing positive surface charges (the blue area) deposited by the tip. (d) Linescan from image (b) illustrating the change of $\Delta\Phi$ across the charged area. (e) Linescan showing the capacitance derivative, $\partial^2 C / \partial z^2$.

tion, $\Delta\Phi$, over the untouched region was only $\Delta\Phi_{\text{rms}} = 6 \text{ mV}$, which is very similar to the variation we observed on the bare gold substrates. The change in potential over the charged region ($\Delta\Phi_{\text{pp}} = 106 \text{ mV}$) corresponds to a change in the surface charge density of only $\sim 2.5 e^+/(100 \text{ nm})^2$. We did not observe dissipation of the charged area over the period of 24 hours.

Conclusions

High concentration TPD-PC and TPD-PS films do not support the formation of a long-lived surface charges at room temperature. However, lowering the temperature to 77 K decreases the mobility so that surface charges are easily sustained. Low concentration TPD-PC and TPD-PS films also support surface charges due to the decreased mobility. It is unlikely that the variation of $\Delta\Phi$ is due to a surface charge density on the 50% weight TPD-PC and TPD-PS films.

Of equal importance, we discovered that the variation of $\Delta\Phi$ was small for untouched polycarbonate films. This is evidence that the variation of $\Delta\Phi$ is due to TPD molecules.

6.4.4 Varying the degree of energetic disorder

Electrostatic interactions with the dipole moment of distant molecules allow for a large number of independent contributions to the energy of an ionized molecule. This leads to an approximately Gaussian density of site energies, with a width, σ , between 50 and 100 mV in typical molecularly doped polymers [6, 7, 18]. In this section, we vary the electrostatic environment of the TPD molecule by (1) adding small molecules with a large dipole moment and (2) changing the host polymer from polystyrene (PS) to a more polar host, polycarbonate (PC). If the variation of

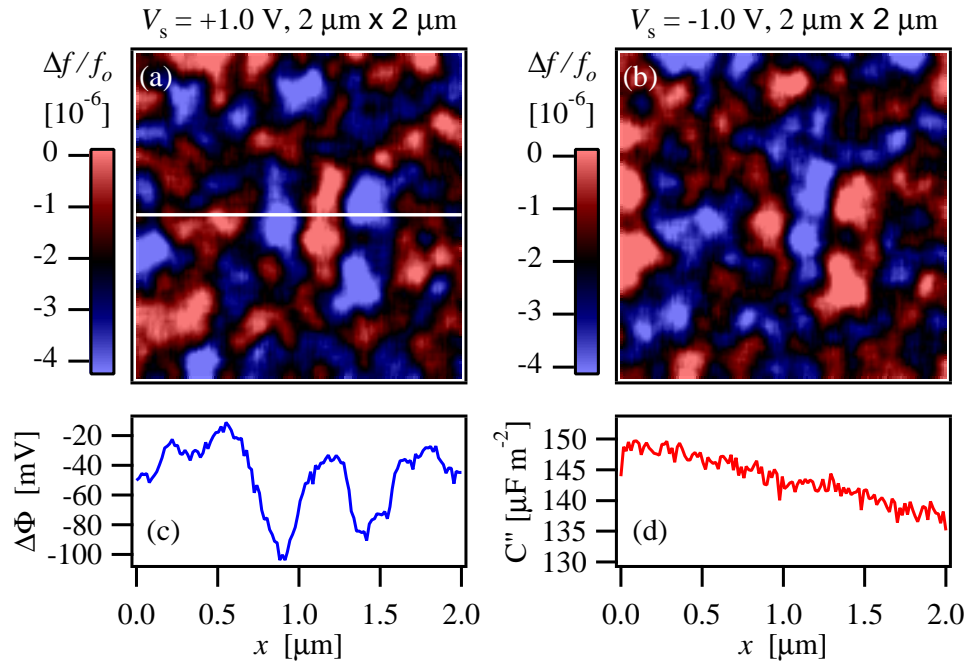


Figure 6.15: Dipole doping: 100 nm film of 49% TPD, 49%PC, and 2% butyl sulfone, by weight. (a) 2 $\mu\text{m} \times 2 \mu\text{m}$ force gradient images acquired under opposite bias in (a) and (b). The potential varies by $\Delta\Phi_{\text{rms}} = 22.5$ mV shown in linescan (c). The capacitance derivative, $\partial^2 C / \partial z^2$, is shown in (d).

$\Delta\Phi$ is caused by correlated energetic disorder due to long range dipole interactions, increasing σ should increase the variation of $\Delta\Phi$.

Dipole doping the molecularly doped polymer

A small molecule, butyl sulfone, was added to the TPD/PC film (Figure 6.16). Butyl sulfone has a dipole moment of approximately $\mu_d = 4.3$ D [29], significantly larger than that of TPD ($\mu_d = 1.5$ D [19]), polycarbonate ($\mu_d = 1.0$ D per repeat unit [19]), and polystyrene ($\mu_d = 0.36$ D per repeat unit [29]). The dipole moment of butyl sulfone comes from the double bonds between the sulfur and the two oxygen atoms. The butyl groups, attached to the sulfur atom, help dissolve the

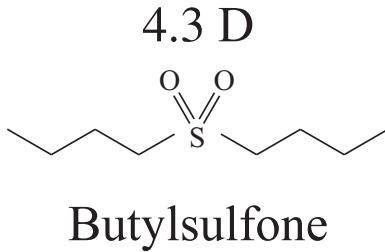


Figure 6.16: Butyl sulfone. $\mu_d = 4.3$ D.

molecule in relatively nonpolar solvents and prevent phase separation. Young *et al.* found that butyl sulfone decreased the mobility in a different molecularly doped polymer, TTA/PS, by 1 order of magnitude at 2% weight [29].

Dispersing molecules with large dipoles into the molecularly doped polymer system did not significantly increase the variation of $\Delta\Phi$. Figure 6.15(a) and 6.15(b) show $2 \mu\text{m} \times 2 \mu\text{m}$ force gradient images of a 100 nm film composed of 49% weight TPD, 49% weight PC, and 2% weight butyl sulfone ($\mu_d = 4.3$ D) on polycrystalline gold. At this concentration, there are approximately 8.5 TPD molecules per butyl sulfone. The linescan of Figure 6.15(c) shows a variation of $\Delta\Phi_{\text{rms}} = 22.5$ mV. On average, we found $\Delta\Phi_{\text{rms}} = 19$ mV, which is 2 mV larger than the variation observed in films of 50% TPD-PC on gold.

We then increased the amount of butyl sulfone to 10% by weight, amounting to 1.6 TPD molecules per butyl sulfone. The average variation was found to be $\Delta\Phi_{\text{rms}} = 21.6$ mV. Although this appears to be a measurable increase, we find $\Delta\Phi_{\text{rms}} = 19.5$ mV without including one outlier with $\Delta\Phi_{\text{rms}} = 30$ mV. Young *et al.* report that doubling the concentration of the dipole does not double the negative effect on charge transport [29].

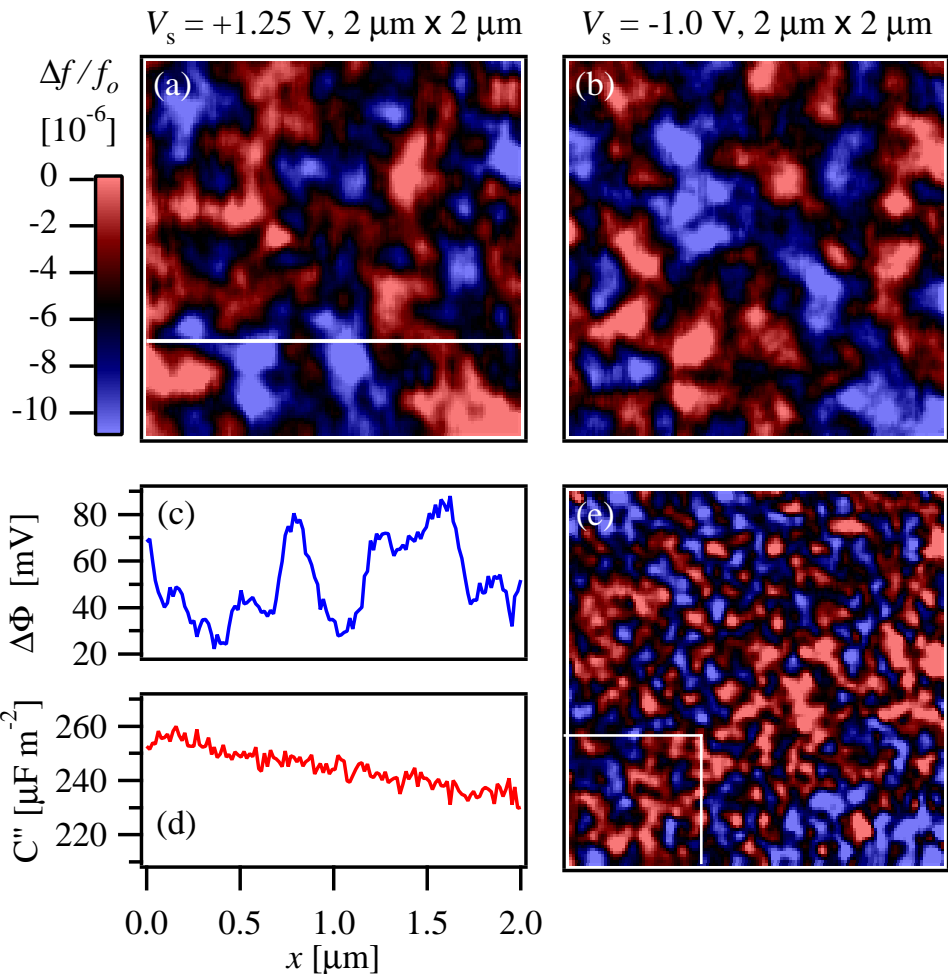


Figure 6.17: Polystyrene host polymer: 100 nm film of 50% weight TPD-PS on epitaxially grown gold. (a) $2 \mu\text{m} \times 2 \mu\text{m}$ force gradient images acquired under opposite bias in (a) and (b). The potential varies by $\Delta\Phi_{\text{rms}} = 16.8 \text{ mV}$ shown in linescan (c). The capacitance derivative, $\partial^2 C / \partial z^2$, is shown in (d). (e) A larger, $5 \mu\text{m} \times 5 \mu\text{m}$ image, with the area of images (a) and (b) outlined in the boxed area.

Varying the host polymer

Although the host polymer is often described as an inert ‘binder’ that serves to randomly disperse the small hole conducting molecules, it is well known that the host polymer plays a significant role in the transport properties of molecularly doped polymers [6, 28]. The orientation of TPD molecules is a critical step in the thermally assisted hopping of charge. Polycarbonate, shown in Figure 6.1(c), contains a large dipole arising from the carbonyl group ($\mu_d = 1.0$ D per repeat unit [19]) that not only increases energetic disorder, but may restrict the available orientations of the TPD molecules. This might explain why polystyrene, a polymer without a large dipole ($\mu_d = 0.1$ D per repeat unit [19]), has a larger mobility for similar TPD concentrations [6, 19].

We find there is a slight decrease in the variation of the potential, $\Delta\Phi$, in films of 50% weight TPD in polycarbonate (PC) and polystyrene (PS). Figure 6.17(a) and 6.17(b) are $2 \mu\text{m} \times 2 \mu\text{m}$ force gradient images acquired under opposite bias. The variation of the potential shown in Figure 6.17(c) is $\Delta\Phi_{\text{rms}} = 16.8$ mV. On average, we find a variation $\Delta\Phi_{\text{rms}} = 16$ mV, which is very close to the variation $\Delta\Phi_{\text{rms}} = 17$ mV we found for 50% weight TPD-PC on epitaxially grown gold (Figure 6.8). Decreasing the energetic disorder by changing the host polymer from polycarbonate to polystyrene did not lead to a significant change in the variation of the potential, $\Delta\Phi$.

Conclusions

Altering the electrostatic environment of the TPD molecules by increasing energetic disorder with large dipoles increased the variation of $\Delta\Phi$ by ~ 1.5 mV. Also, decreasing the energetic disorder by using a nonpolar host polymer, polystyrene,

decreased $\Delta\Phi$ by ~ 1 mV. These changes are small and it is difficult to conclude that controlling the energetic disorder has resulted in a change of the variation of $\Delta\Phi$ without more experiments. The effects of dipole doping and changing the host polymer on charge transport properties are much more dramatic [6, 29]. However, the change in $\Delta\Phi_{\text{rms}}$ is in the expected direction for the addition of butyl sulfone and the polycarbonate/polystryrene comparison.

6.4.5 The potential variation at low temperatures

In Section 4.5.1, the Mott-Gurney model for the metal/insulator interface predicts an accumulation of charge carriers at the metal/insulator interface. The formation of an accumulation of holes at the metal/TPD interface is depicted in Figure 6.9(b). In Section 6.4.2, we found that the aluminum substrate did not cause a change in the variation of $\Delta\Phi$ despite the significantly larger injection barrier of the TPD-PC/Al interface.

However, in order to further explore the possibility the variation of the potential, $\Delta\Phi$, is caused by a temperature activated process of space-charge buildup at the metal/organic interface, we investigated the $\Delta\Phi$ at cryogenic temperatures. At 77 K, the charge density at the interface, ρ_0 (Equation 4.25), predicted by the Mott-Gurney model is several orders of magnitude smaller than at 298 K.

For a 100 nm thick film of 50% weight TPD-PC on thermally evaporated gold, we find that $\Delta\Phi_{\text{rms}}$ does not exhibit an observable temperature dependence. Figure 6.18(a) is a force gradient image of the film after contact with the titanium-platinum cantilever tip. Triboelectric charging occurred nearly every time contact was made, as the charge mobility of the film is several orders of magnitude lower at 77 K [6]. Care was taken to avoid touching the surface. Figure 6.18(b) is a

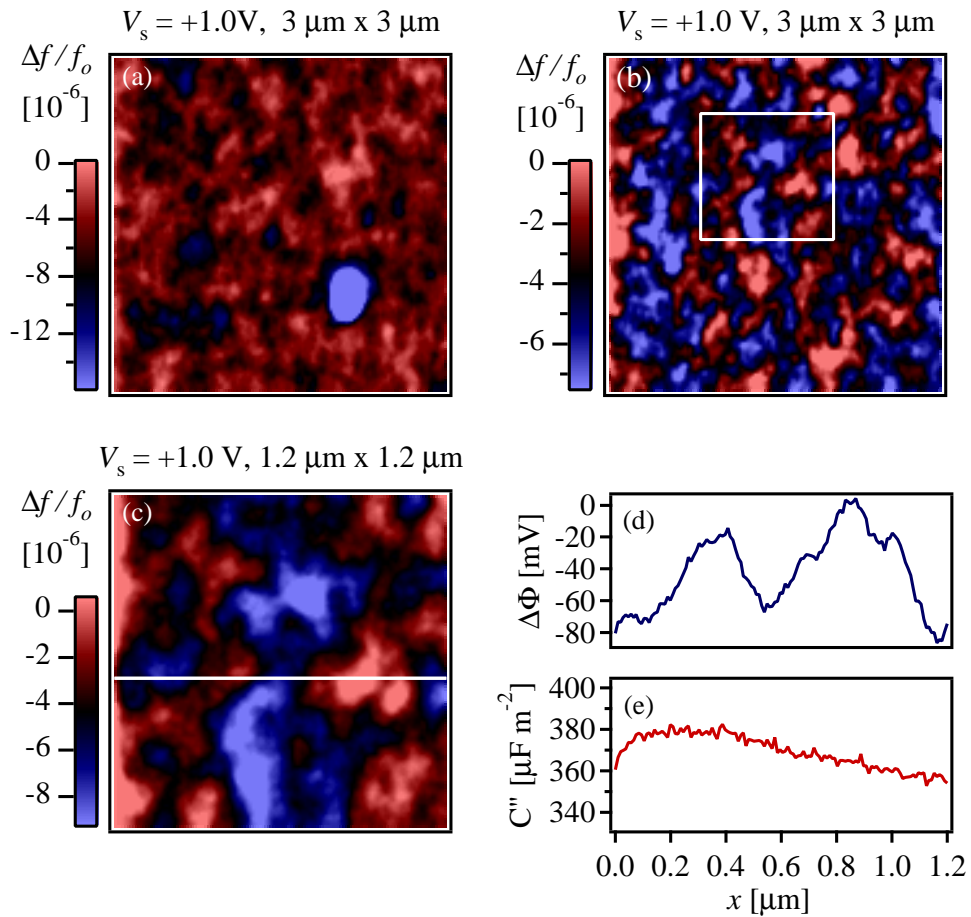


Figure 6.18: 100 nm thick 50% weight TPD-PC film on polycrystalline gold.

The potential variation at low temperature (77 K) shows a similar variation of $\Delta\Phi$. (a) Force gradient image showing where charge was deposited by the cantilever tip. (b) Untouched area: The boxed area in (b) indicates the area imaged in (c) and the corresponding linescans of (d) $\Delta\Phi$, and (e) $\partial^2 C/\partial z^2$.

$3 \mu\text{m} \times 3 \mu\text{m}$ force gradient image of an untouched area. The variation of $\Delta\Phi$ is similar, spatially. The $1.2 \mu\text{m} \times 1.2 \mu\text{m}$ area outlined in Figure 6.18(b) is the area imaged in Figure 6.18(c). The corresponding linescans of the potential, $\Delta\Phi$, and the capacitance derivative, $\partial^2 C / \partial z^2$, are shown in Figure 6.18(d) and 6.18(e), respectively. We find an average $\Delta\Phi_{\text{rms}} = 16.8 \text{ mV}$.

Conclusions

We do not find the variation of $\Delta\Phi$ is temperature activated. This is in agreement with the experiment described in Section 6.4.2; an aluminum substrate did not cause a change in the variation of $\Delta\Phi$ despite a significantly larger injection barrier of the TPD-PC/Al interface compared to TPD-PC/Au. These experiments strongly suggest that the variation of $\Delta\Phi$ is not due to a spatial variation of the accumulation region.

6.4.6 Thickness dependence of the potential variation

To explore whether $\Delta\Phi$ is a surface or volume effect, we characterized a much thinner film. A 25 nm film of 50% weight TPD-PC on epitaxially grown gold was prepared. The variation of the surface potential, $\Delta\Phi_{\text{rms}}$, was only slightly smaller. The variation of the potential was $\Delta\Phi_{\text{rms}} = 15.3 \text{ mV}$, compared to $\Delta\Phi_{\text{rms}} = 17.5 \text{ mV}$ for the 100 nm film. We will refer to this result in Section 6.8, where models of surface dipoles, bulk dipoles, surface charges, and bulk charges are discussed.

6.5 Summary of chemical and physical perturbations

In Table 6.1, the values of the average variation of $\Delta\Phi$ are listed for the experiments in Sections 6.4.1 through 6.4.6.

Summary and discussion of experiments in Section 6.4

In Section 6.4.1, the variation of the potential over 100 nm thick 50% weight TPD-PC films on gold was significantly larger than the potential variation over the bare gold substrates (polycrystalline and epitaxially grown gold films). We also found the change in the capacitance derivative was small, allowing us to rule out the presence of small pinholes (or voids) and aggregates larger than ~ 50 nm.

In Section 6.4.2, experiments were performed to explore the possibility of a spatially varying interface dipole and an accumulation region. The aluminum substrate did not affect the variation of the potential, $\Delta\Phi$, despite having a much lower work function than gold. The bare surfaces of SiO_2 and quartz exhibited large variations of the potential which prevented us from drawing conclusions from TPD-PC and TPD-PS films on these insulating substrates.

In Section 6.4.3, the deposition of surface charges was investigated. 50% weight TPD-PC films did not sustain a surface charge density at room temperature. However, at low temperatures the mobility is many orders of magnitude lower and surface charge was easily sustained. Similarly, at low concentrations (5% weight TPD-PC), surface charge was sustained due to low mobility. It is unlikely the variation of the potential over 50% weight TPD-PC films arises from surface charges based on these experiments. The variation of the potential was only slightly lower for 5% weight TPD-PC on gold. Finally, insulating polycarbonate films were easily charged, but show little variation of the potential if untouched. This strongly

Table 6.1: Summary: Variation of the potential, $\Delta\Phi$, in TPD-based molecularly doped polymer films under different chemical and physical conditions. The concentrations of TPD, the host polymer, and the added dipole, butyl sulfone, are given in weight percent. The film thickness, t , is given in nanometers. The substrate is polycrystalline Au (pAu), epitaxially grown gold (eAu), Aluminum (Al), or silicon dioxide (SiO_2).

| | TPD | host | dipole | t [nm] | substrate | T [K] | $\Delta\Phi_{\text{rms}}$ [mV] |
|---|-----|----------|---------|----------|----------------|---------|--------------------------------|
| A | 50% | PC, 50% | — | 120 | pAu | 298 | 17.5 |
| B | 50% | PC, 50% | — | 100 | pAu | 77 | 16.8 |
| C | — | — | — | 55 | pAu | 298 | 6.3 |
| D | — | — | — | 50 | eAu | 298 | 7.8 |
| E | 0% | PC, 100% | — | 120 | pAu | 298 | 6.0 |
| F | 50% | PC, 50% | — | 100 | eAu | 298 | 16.0 |
| G | 50% | PC, 50% | — | 25 | eAu | 298 | 15.3 |
| H | 49% | PC, 49% | X , 2% | 100 | pAu | 298 | 19.0 |
| I | 45% | PC, 45% | X , 10% | 100 | pAu | 298 | 21.6 |
| J | 5% | PC, 95% | — | 60 | eAu | 298 | 16.1 |
| K | 50% | PS, 50% | — | 100 | eAu | 298 | 16.0 |
| L | 50% | PC, 50% | — | 90 | Al | 298 | 17.0 |
| M | 50% | PS, 50% | — | 90 | Al | 298 | 16.3 |
| N | — | — | — | 50 | Al | 298 | 9.3 |
| O | 50% | PS, 50% | — | 100 | SiO_2 | 298 | 38.0 |

suggests that TPD molecules are responsible for the variation of the potential in TPD-PC and TPD-PS films.

In Section 6.4.4, energetic disorder was increased by doping the molecularly doped polymer with butyl sulfone, a molecule with a large dipole moment. A slight increase in the variation of the potential was found. Energetic disorder was decreased by changing the host polymer from polycarbonate (polar) to polystyrene (nonpolar). A slight decrease in the variation of the potential was observed. However, these changes are within ± 2 mV, which is the typical deviation of the root mean square variation of the surface potential observed with similarly prepared films.

In Section 6.4.5, the variation of the potential did not exhibit a temperature dependence. The variation was the same at 298 K and 77 K. This agrees with the conclusion of the experiment with an aluminum interface (Section 6.4.2); the variation of the surface potential is not due to a spatially varying accumulation region at the interface.

Finally, in Section 6.4.6, the variation of the potential decreased only slightly for a thin, 25 nm film of 50% weight TPD-PC (typical thickness: 100 nm). This experimental result is explored with a calculation of randomly placed bulk charges in Section 6.8.2.

From the list of likely causes of the potential variation in Section 6.2, we are left with the following possibilities:

- Aggregation of TPD molecules [19, 20]
- Energetic disorder from surface and bulk dipoles [6, 7, 18]
- Background carriers – ionized acceptors/donors [11]

Aggregation of TPD molecules: Although the capacitance derivative is nearly constant for most TPD-PC and TPD-PS films, it is not possible to rule out aggregation on a length-scale smaller than the resolution of the EFM measurement, which is approximately 60-100 nm. We were able to resolve 65 nm grains of polycrystalline aluminum in Section 6.4.2 by EFM, but the 40-50 nm grains of polycrystalline Au were not observed in the capacitance derivative in Section 6.4.1. In Chapter 5, we found significant crystallization after exposure to ambient conditions. Therefore, we know crystal growth is initiated at some point.

Energetic disorder from surface & bulk dipoles: Randomly oriented surface and bulk dipoles are known to create clusters of similar electric potential at a variety of length scales [18]. Therefore, this is another possible cause of the variation of $\Delta\Phi$. We discuss recent theoretical work which has explored this possibility Section 6.8.1.

Background charge carriers – ionized acceptors/donors: From Chapter 5, we found the density of background charge carriers, $N_0 = 2.8 \times 10^{20} \text{ m}^{-3}$, in a 50% weight TPD-PS film. Abkowitz and Pai suggest the charges arise from a photoreaction during sample preparation or impurities [11]. They may also arise from autoionization of TPD molecules in the tail states. We characterize the density of background carriers further in Section 6.7 and consider a theoretical model for random distributions of bulk charge in Section 6.8.2.

6.6 Interaction between the cantilever and sample

Observations of the tip-surface distance dependence of the capacitance derivative and the potential are discussed in this section. These studies were performed to better understand the tip-surface interaction and for comparison to theoretical

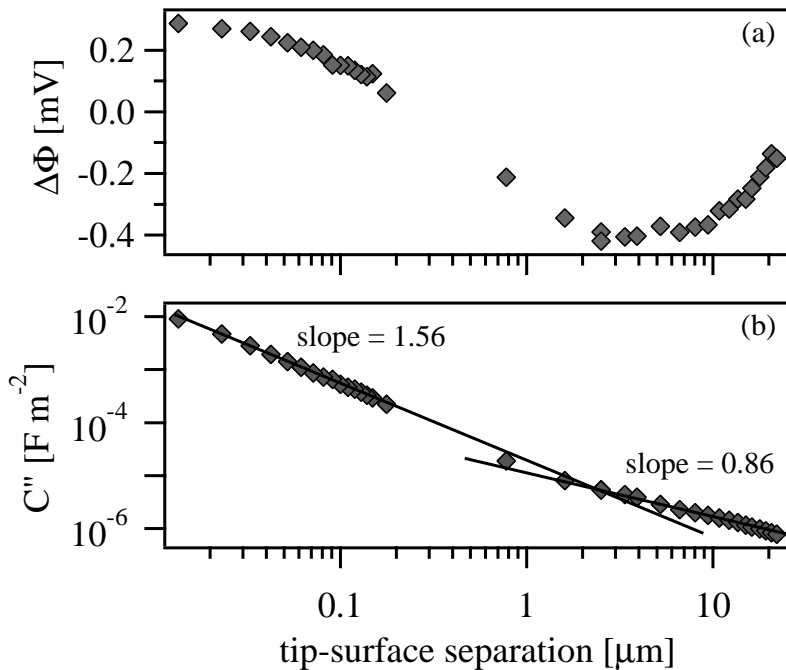


Figure 6.19: Height dependence of (a) the potential, $\Delta\Phi$, and (b) the capacitance derivative, $\partial^2C/\partial z^2$, between a platinum cantilever and an epitaxially grown gold surface.

modeling.

We use a titanium-platinum coated triangular (V-shaped) cantilever from MicroMasch (part NSC21/Ti-Pt). The cantilever is 290 μm long with beams that are 40 μm wide and 2 μm thick. The tip has a cone angle of 30° and a total tip height of 15-20 μm . The metal coating consists of a 10 nm platinum film on a 20 nm titanium sublayer. When coated, the tip has a typical radius of curvature of 40-50 nm. Measuring the resonance frequency, f , as a function of the applied surface potential, V_s , allows us to infer the potential, $\Delta\Phi$, and the second derivative of the tip-surface capacitance, $\partial^2C/\partial z^2$.

Figure 6.19(a) shows the height dependence of the potential, $\Delta\Phi$, over an epi-

taxially grown substrate. It is likely the distance-dependence arises from different work functions on the cantilever tip and the rest of the cantilever body. At small distances to the surface, the sharp cantilever tip is the primary structure involved in the interaction with the surface, but at larger distances, the contributions from the electronic properties of entire cantilever, including the surface of the pyramidal tip and the surface of the underside of the cantilever, become more important. Even along the surface of the cone of the cantilever tip, it is possible to have over 100 mV variations in the work function in a polycrystalline metallic film. In our work, we have observed 100-200 mV changes in the work function of the tip upon touching the surface or exposing the cantilever to ambient conditions for a few hours. While this happens only rarely, the occurrence highlights a limit in the absolute quantification of the surface potential between experiments or even force-distance curves. It is very likely the tip can pick up material or lose a small amount of the metal film, altering the work function. In order for the electronic properties of the cantilever to remain constant, great care must be taken to keep the environment or experiment from altering the tip.

Figure 6.19(b) gives the corresponding height-dependence of $\partial^2C/\partial z^2$. At small distances, $z < 1 \mu\text{m}$, the capacitance derivative fits very well to a power law, $\partial^2C/\partial z^2 \propto z^{-n}$. The exponent, $n = 1.56$, is in between that expected for a sphere ($n = 2$) and a cone ($n = 1$) [30], similar to what Krauss *et al.* [31] have observed for an irregular pyramidal cantilever tip. At distances larger than $1 \mu\text{m}$, we find $n = 0.86$. This has also been observed by Belaidi *et al.* and is attributed to the lateral surface of the cantilever tip. It is important to note that the characteristics vary from one cantilever to the next.

We have also characterized the height dependence of the tip-surface capacitance

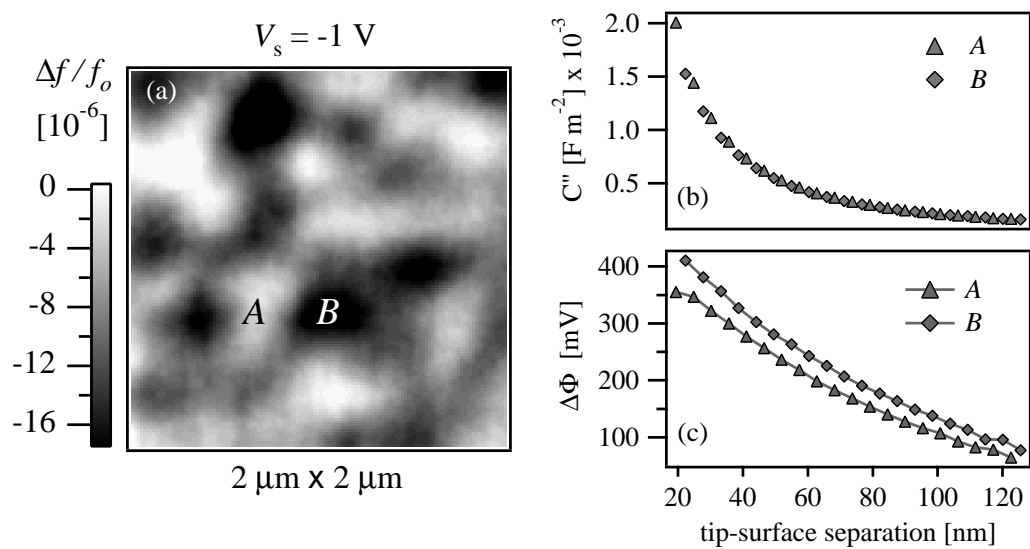


Figure 6.20: 100 nm film of 50% weight TPD-PC on epitaxially grown gold.
 (a) Force gradient image showing a typical variation. The height dependence of (b) the surface potential, $\Delta\Phi$, and (c) the tip-surface capacitance derivative, $\partial^2 C / \partial z^2$, at points A and B from the force gradient image shown in (a).

derivative, $\partial^2 C / \partial z^2$, and the potential, $\Delta\Phi$, over a 100 nm film of 50% weight TPD-PC on epitaxially grown gold. Figure 6.20(a) shows a $2 \mu\text{m} \times 2 \mu\text{m}$ force gradient image illustrating the typical variation we observe. We have chosen two points, *A* and *B*, to characterize the height dependence where $\Delta\Phi$ changes most significantly. Figure 6.20(b) shows the height dependence of the capacitance derivative at *A* and *B*. The measurements indicate the film thickness and dielectric properties are nearly the same at the two points. The capacitance derivative follows $\partial^2 C / \partial z^2 \propto z^{-1.33}$, only slightly less than what we observed over the bare Au substrate ($n = 1.56$). The height dependence of $\Delta\Phi$ shown in Figure 6.20(c) demonstrates that despite a significant change in $\Delta\Phi$ with z , the difference between the potentials at the two points is always different. There is a larger difference in $\Delta\Phi$ at smaller tip-surface distances, as the resolution of the technique improves the closer the cantilever is to the surface. These data also support the conclusion that the force gradient arises from a changing potential, not a variation of the capacitance.

In Figure 6.21, we show the height dependence of the potential variation. The force gradient images have been converted to images of potential by assuming all of the change in the force gradient arises from a shift in $\Delta\Phi$ and calculating the potential from a frequency-voltage (f - V_s) curve.

6.7 The density of background charge carriers

In this section, we characterize the density of background charge carriers and compare it to the expected density of background charge carriers based on Fermi-Dirac statistics.

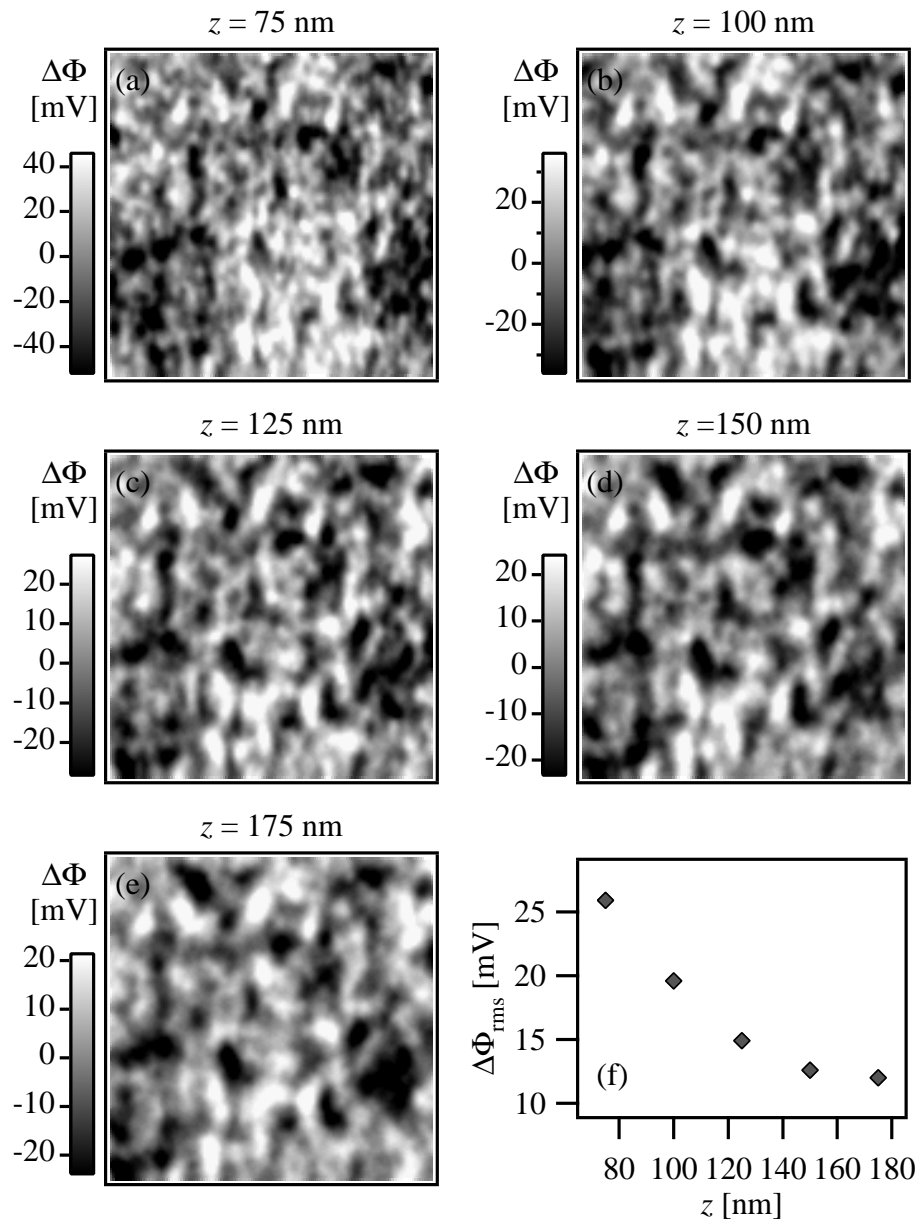


Figure 6.21: Height dependence of $\Delta\Phi_{\text{rms}}$.

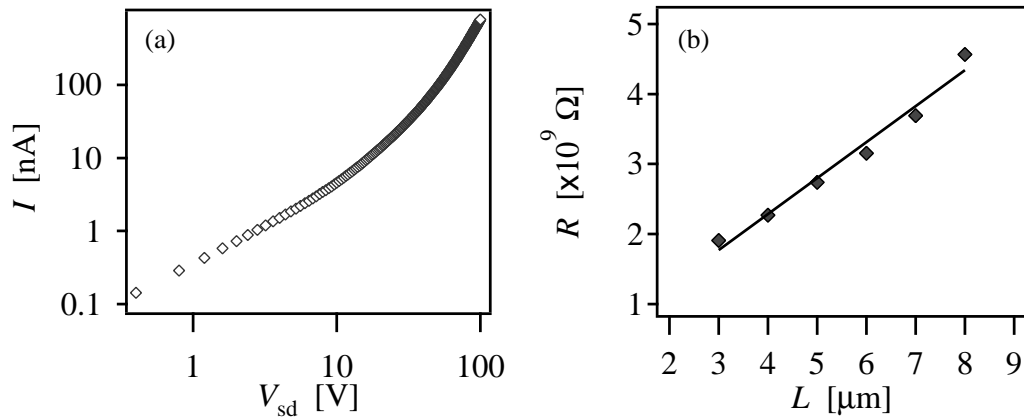


Figure 6.22: (a) Current-voltage curve for a 5 μm channel. (b) Resistance versus channel length.

6.7.1 Electrical characterization

We have investigated the current-voltage characteristics of a 100 nm film of 50% weight TPD-PS on coplanar gold electrodes in order to characterize the number of background charge carriers present in the organic film. Gold was chosen because it provides an Ohmic contact with TPD-PS [15]. Abkowitz *et al.* suggest accidental doping arises from photodegradation and leads to single and possibly double charged radical cations of TPD [11]. It also seems possible that “intact” TPD molecules in the tail states of the Gaussian DOS may play the role of donor and acceptor (autoionization).

Figure 6.22(a) shows a current-voltage curve for a 50% weight TPD-PS device with a 5 μm channel and an effective cross-sectional area of $2.75 \times 10^{-8} \text{ m}^2$. We fit the linear region of the curve, prior to the onset of space-charge limited conduction (SCLC), between $V_{sd} = 0 \text{ V}$ to $V_{sd} = 5 \text{ V}$, using Ohm’s law,

$$J_\Omega = \frac{I}{A} = eN_0\mu \frac{V}{L}, \quad (6.4)$$

where J_Ω is the current density, I is the current, A is the area, N_0 is the carrier

density, μ is the mobility, and L is the channel length. Figure 6.22(b) shows the dependence of the resistance, R , on channel length, L . $R \propto L$, supporting the use of J_Ω to calculate the number of background charge carriers, N_0 . We have used a mobility of $2.0 \times 10^{-6} \text{ cm}^2 \text{ V}^{-1}\text{s}^{-1}$ [28].

The density of background charge carriers, $N_0 = 2.1 \times 10^{14} \text{ cm}^{-3}$, is very close to what we found in Chapter 5. The density of TPD molecules in a 50% weight TPD-PS film is $N_{\text{TPD}} = 2.66 \times 10^{20} \text{ cm}^{-3}$. Therefore, approximately 1 in 10^6 of TPD molecules is responsible for the Ohmic current at low voltages. Interestingly, this is approximately $0.2 e^+$ for a volume of $(100 \text{ nm})^3$. In addition, there must be $0.2 e^-$ in the same volume to account for the negatively charged acceptor centers.

6.7.2 Expected density of charge carriers

As we found in Chapter 5, integrating the product of the Fermi-Dirac distribution, f_{FD} , and the density of states, D_{HOMO} , over all energies gives the density of holes, N_h , for a given value of $\mu - E_{\text{HOMO}}$,

$$N_h = \frac{N_{\text{TPD}}}{\sqrt{2\pi\sigma_h^2}} \int_{-\infty}^{+\infty} \frac{e^{-(E-E_{\text{HOMO}})^2/2\sigma_h^2}}{1 + e^{(\mu-E)/k_B T}} dE, \quad (6.5)$$

where we have labeled σ_h the width of the Gaussian density of states for holes in the HOMO. In the denominator, we make the approximation, $1 + \exp(\mu - E)/k_B T \approx \exp(\mu - E)/k_B T$, which is true if $(\mu - E)/k_B T \gg 1$. Therefore, N_h is approximately

$$N_h = \frac{N_{\text{TPD}}}{\sqrt{2\pi\sigma_h^2}} \int_{-\infty}^{+\infty} e^{-(E-E_{\text{HOMO}})^2/2\sigma_h^2} e^{-(\mu-E)/k_B T} dE. \quad (6.6)$$

Similarly, for electrons in the LUMO, the density of electrons, N_e , is given by

$$N_e = \frac{N_{\text{TPD}}}{\sqrt{2\pi\sigma_e^2}} \int_{-\infty}^{+\infty} e^{-(E_{\text{LUMO}}-E)^2/2\sigma_e^2} e^{-(E-\mu)/k_B T} dE. \quad (6.7)$$

where σ_e is the Gaussian density of states for electrons in the LUMO. Evaluating the integral, the density of holes and electrons is given by:

$$N_h \approx N_{\text{TPD}} e^{\frac{1}{2} \frac{\sigma_h^2}{(k_B T)^2}} e^{-\left(\frac{\mu - E_{\text{HOMO}}}{k_B T}\right)} \quad (6.8)$$

$$N_e \approx N_{\text{TPD}} e^{\frac{1}{2} \frac{\sigma_e^2}{(k_B T)^2}} e^{-\left(\frac{E_{\text{LUMO}} - \mu}{k_B T}\right)} \quad (6.9)$$

Assuming the TPD-PS film is undoped ($N_h = N_e$), and the width of the HOMO and LUMO are equivalent ($\sigma_h = \sigma_e$), the intrinsic concentration of electrons and holes, N_i , is

$$N_i = N_{\text{TPD}} e^{\frac{1}{2} \frac{\sigma^2}{(k_B T)^2}} e^{-\frac{E_{\text{gap}}}{2k_B T}} \quad (6.10)$$

where $E_{\text{gap}} = E_{\text{HOMO}} - E_{\text{LUMO}}$.

Table 6.2 summarizes calculations of the expected density of intrinsic charge carriers. In Table 6.2(A), the value of N_i , calculated with $\sigma = 100$ mV [6] and $E_{\text{gap}} = 3.05$ V [32], is much smaller than the measured N_0 . Allowing E_{gap} to decrease to 1.11 V (Table 6.2(B)) or σ to increase to 242 mV (Table 6.2(C)) gives the measured value of N_0 . Clearly, N_i is a strong function of the band gap and energetic disorder.

The polarization energy, P_{\pm} , is a stabilizing energy resulting from polarization of the dielectric medium surrounding a polaron and justifies lowering E_{gap} by ~ 1 V in π -conjugated organic materials [33, 34]. The ‘charge gap,’ defined by the difference between the ionization energy and the electron affinity (measured by cyclic voltammetry), is 3.52 V for TPD [35]. From the ‘charge gap,’ it is appropriate to include the stabilizing effect of the polarization energy to obtain the transport gap, E_t [33]. An estimate of the polarization energy, P_{\pm} , based on the size of the molecule, is given by

$$P_{\pm} = \frac{e^2}{2R} \frac{1}{4\pi\epsilon_0} (1 - 1/\kappa), \quad (6.11)$$

Table 6.2: (A) Expected density of intrinsic charge carriers, N_i , for $\sigma = 100$ mV [6] and the optical bandgap, $E_{\text{gap}} = 3.05$ V [32]. (B) The energy gap, E_{gap} , is allowed to decrease in order to obtain $N_i = N_0 = 2.1 \times 10^{20}$ m $^{-3}$. (C) The width of the density of states, σ , is allowed to increase in order to obtain $N_i = N_0 = 2.1 \times 10^{20}$ m $^{-3}$. (D) The polarization energy is included, lowering the energy gap. σ is only slightly increased from 100 mV for the calculation of N_i to obtain agreement with the measured N_0 . The temperature in each case is 298 K.

| | σ [mV] | E_{gap} [V] | N_i [m $^{-3}$] | remarks |
|---|---------------|----------------------|----------------------|-----------------------|
| A | 100 | 3.05 | 0.9×10^4 | expected |
| B | 100 | 1.11 | 2.1×10^{20} | vary E_{gap} |
| C | 242 | 3.05 | 2.1×10^{20} | vary σ |
| D | 124 | 1.32 | 2.1×10^{20} | include P_{\pm} |

where R is the radius of the molecule and κ is the relative dielectric constant [36].

From the theoretical study by Cornil *et al.* [37], the electronic wavefunction for the TPD molecule has been used to estimate the radius, $R = 4.3 \text{ \AA}$. The charge density on TPD is primarily located on the nitrogen atoms and, to a lesser extent, on the central biphenyl portion of the molecule [37]. Using $R = 4.3 \text{ \AA}$ and $\kappa = 3$ for the model given in Equation 6.11 [36], the polarization energy is $P_{\pm} = 1.1 \text{ V}$, and the estimated transport gap is $E_t = 1.32 \text{ V}$. In Table 6.2(D), we calculated N_i with the transport gap and a slightly increased width of the density of states ($\sigma = 124 \text{ mV}$) in order to obtain $N_i = N_0 = 2.1 \times 10^{20} \text{ m}^{-3}$. This estimation is very reasonable and strongly suggests the background charge carriers may be the intrinsic charge carriers.

Conclusions

From the electrical characterization of TPD-PS/Au devices and previous literature [11], we *know* background charge carriers are present in the molecularly doped polymer at low concentrations (1 in 10^6). By calculating the expected density of intrinsic charge carriers and including the polarization energy, it appears likely the background charge carriers arise from the autoionization of TPD molecules. In Section 6.8, we model the potential above a dielectric film on a metal. Randomly placed charges are put into the dielectric to model the expected potential from the background charge carriers.

6.8 Theoretical modeling

In this section, the variation of the potential expected from randomly oriented dipoles is discussed. This is followed by calculations of the potential expected

from randomly dispersed charges in a dielectric film in order to determine if the background charge carriers create a large enough potential to cause the variation discovered in TPD-based molecularly doped polymer films.

6.8.1 Modeling random surface and bulk dipoles

J. A. Marohn and D. H. Dunlap have recently modeled the potential from randomly oriented bulk and surface dipoles with parameters similar to what one would expect from a 100 nm 50% weight TPD-PC and TPD-PS films [38]. In their model, the cantilever probe is approximated as a point charge. The calculation is similar to the work by Novikov and Vannikov, who found that the potential is strongly correlated and that clusters of potential of similar magnitude are created in a 3-dimensional lattice of randomly oriented dipoles, which represent TPD molecules [18].

For the surface dipole model, the resulting rms potential variation is approximately $30\times$ too small. The calculation for the potential expected from bulk dipoles is larger, but still an order of magnitude less than the experimentally observed variation of the surface potential of TPD-PC and TPD-PS films. While random dipoles have been shown to create various sizes of potential similar in magnitude and account for the \sqrt{E} -dependence of the mobility [7,18], it appears the variation of the potential we observe is too large to arise from randomly oriented dipoles. However, it is still possible aggregation of TPD molecules would increase the potential.

6.8.2 Potential from charges dispersed in a dielectric film

We have calculated the potential expected above a random distribution of equal numbers of positive and negative charges in a thin dielectric film on a metal sub-

strate. The cantilever is approximated as a point charge. The calculation is meant to simulate the background charge carriers, N_0 , randomly dispersed in a TPD-based molecularly doped polymer film on gold. We found $N_0 = 2.1 \times 10^{20} \text{ m}^{-3}$ in a 50% weight TPD-PS film in Section 6.7.

The potential from a charge in a dielectric film on a metal

The following point-probe model calculates the potential, ϕ , above a charge, q , in a dielectric film on a metal (Figure 6.23) [39]. The potential is given by,

$$\phi(\rho, h) = \frac{q}{4\pi\epsilon_0} \int_0^\infty dk J_0(k\rho) e^{-kh} a(k), \quad (6.12)$$

where

$$a(k) = \frac{2}{\epsilon_r + 1} \left(\frac{e^{-kd} - e^{kd}}{1 + \beta e^{-2kt}} \right), \quad (6.13)$$

and

$$\beta = \frac{\epsilon_r - 1}{\epsilon_r + 1}. \quad (6.14)$$

The lateral displacement of the point probe from the buried charge is given by ρ , and the charge is a depth, $-d$, from the surface of the film ($z = 0$). The film thickness is $-t$. The dielectric constant of the film is ϵ and the relative dielectric constant is given by $\epsilon_r = \epsilon/\epsilon_0$. J_0 is a Bessel function of the first kind. The integral in Equation 6.12 was calculated numerically with Mathematica and Matlab.

Single charge calculations

We have calculated the potential, ϕ , due to a single positive charge residing in a dielectric film using a point-charge model. In a realistic experiment, a 100 nm uniform film of a molecularly doped polymer, typically 50% weight TPD-PS, is spin-cast onto a gold substrate. Electric force microscopy is performed with a

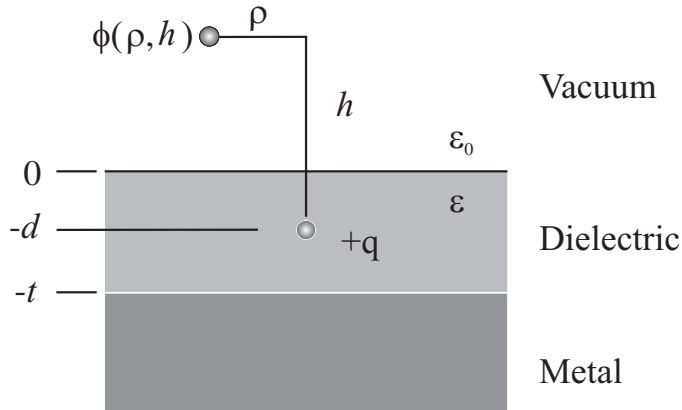


Figure 6.23: Geometry of the metal-dielectric-vacuum interface and the parameters used to calculate the potential from a charge in the dielectric film.

tip-surface height, h , of 50–60 nm. The relative dielectric constant of the material is taken as $\epsilon_r = 2.5$. These parameters are illustrated in the diagram of Figure 6.24(b). We seek to understand how the depth of the charge, d , in the dielectric film and the tip-sample distance, h , affect the calculated potential, ϕ , from a single charge in order to better understand the variation of $\Delta\Phi$ observed with films of TPD-based molecularly doped polymers.

Figure 6.24(a) shows a simulated image of the potential over a single positive charge placed on the surface of the dielectric ($d = 0$ nm). The $1 \mu\text{m} \times 1 \mu\text{m}$ image is composed of 256×256 pixels and was calculated with a tip height, $h = 50$ nm, and a film thickness, $t = 100$ nm. The maximum of the potential, measured directly above the positive charge at this height is +12.6 mV. Figure 6.24(c) shows a linescan of the potential through the middle of the image shown in Figure 6.24(a). Notice that the width of the peak is rather large, approximately 200 nm at the full width at half maximum.

Figure 6.25 shows the tip-surface distance and charge-depth dependence of the potential. The thick solid curve labeled *surface charge* shows the tip-surface

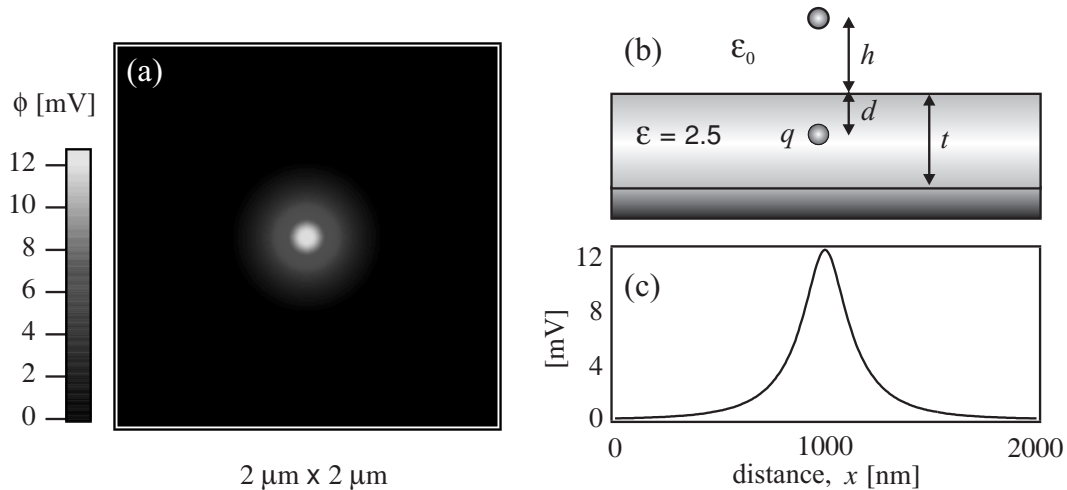


Figure 6.24: (a) $1 \mu\text{m} \times 1 \mu\text{m}$ image of the potential from a single positive charge placed on the surface of a 100 nm thick dielectric film. (b) Diagram illustrating the charge-depth, d , tip height, h , and film thickness, t . (c) Linescan through the midline of the image shown in (a).

distance dependence of the potential for a single charge placed at $d = 0 \text{ nm}$, which defines the surface of the dielectric film. Once the charge is inside the dielectric film, ϕ falls off significantly at very small distances, $h < 10 \text{ nm}$. It is interesting that at larger distances, the potential for all charge-depths decreases proportional to z^{-2} , which is the expected behavior of a simple dipole composed of two separated charges.

As noted before, the potential from a single charge at the surface is approximately 200 nm wide at a tip-surface distance $h = 50 \text{ nm}$. Figure 6.26 illustrates further lateral broadening of the potential when the charge is placed within the dielectric film. Here, the charge is 50 nm deep in a 100 nm thick film with the potential measured at a tip height, $h = 50 \text{ nm}$. The potential above the buried charge is 3.8 mV, approximately 3 times smaller than the potential of the surface charge. Buried charges are not only more difficult to detect because of the

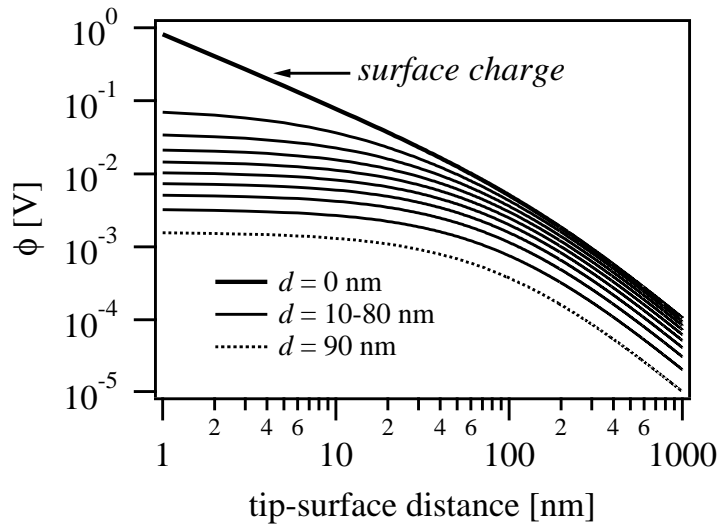


Figure 6.25: The tip-surface distance, h , and surface charge-depth, d , dependencies of the calculated potential, ϕ .

smaller potential, but they appear wider because they are farther from the tip.

The dependence of the potential on the charge-depth, d , at a typical experimental tip-surface distance $h = 50$ nm is shown in Figure 6.27. Near the surface, the potential is approximately 12 mV, but at a charge-depth larger than 80 nm, the potential is less than 2 mV. Charges residing at the dielectric-metal interface will be difficult to resolve due to the small potential they create at the position of the cantilever tip.

Random distribution of charge in a dielectric film

We have calculated the potential variation expected from placing equal numbers (N_0) of positive and negative charges randomly in space throughout a 100 nm thick dielectric film on a metal substrate. The experimental potential variation is labeled $\Delta\Phi_{\text{rms}}$ and the theoretical/calculated variation is labeled $\Delta\phi_{\text{rms}}$.

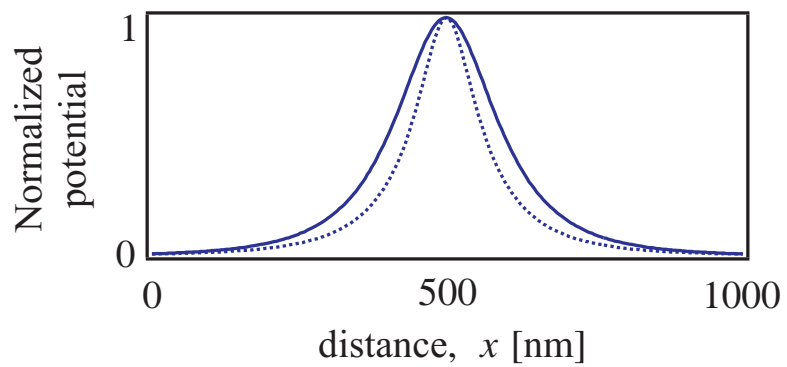


Figure 6.26: Broadening of the potential. The dashed line shows a surface charge and the solid line shows a buried charge, $d = 50$ nm, in a 100 nm film.

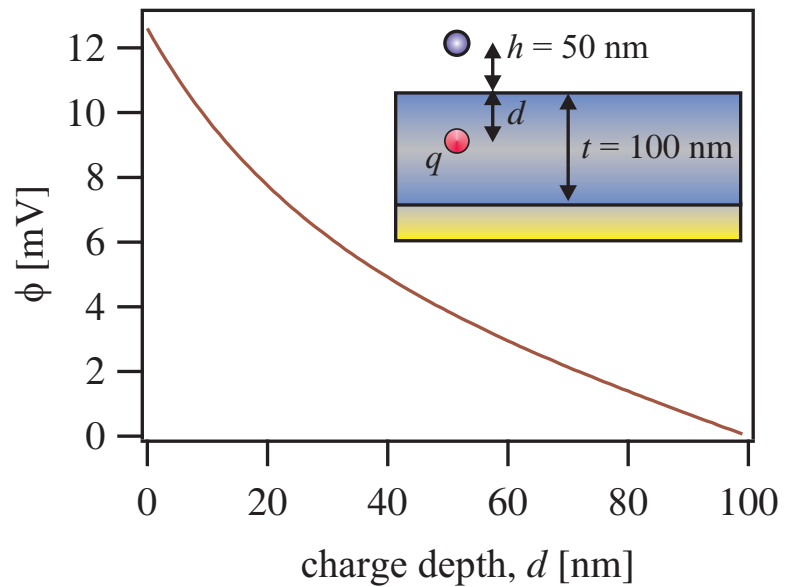


Figure 6.27: Charge-depth dependence of the potential, ϕ , calculated 50 nm above the surface.

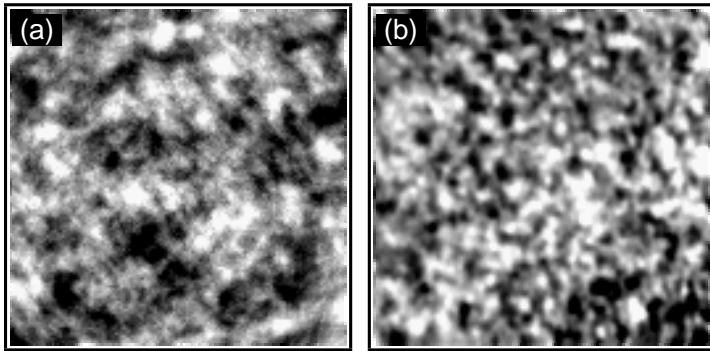


Figure 6.28: (a) $4 \text{ } \mu\text{m} \times 4 \text{ } \mu\text{m}$ simulated image of a 100 nm film with $N_0 = 2.8 \times 10^{20} \text{ m}^{-3}$. (b) A real $4 \text{ } \mu\text{m} \times 4 \text{ } \mu\text{m}$ force gradient image of a 100 nm thick 50% weight TPD-PS film on epitaxially grown gold.

Figures 6.28(a) and 6.28(b) compare a $4 \text{ } \mu\text{m} \times 4 \text{ } \mu\text{m}$ simulated image with a $4 \text{ } \mu\text{m} \times 4 \text{ } \mu\text{m}$ force gradient image of a 50% weight TPD-PS film acquired with an applied potential of 1.0 V between the cantilever and the underlying metal film. For the calculation, the tip-surface distance was set to $h = 50 \text{ nm}$ and the charge concentration to $N_0 = 2.8 \times 10^{20} \text{ m}^{-3}$ [15], which is the concentration of charge carriers we observed in Chapter 5. The tip-surface distance of the experimental image was also $h = 50 \text{ nm}$. As before, we use $\epsilon_r = 2.5$ for the calculation of ϕ .

The peak-to-peak variation we observe for a TPD-PC film on gold is typically $\Delta\Phi_{\text{pk-pk}} \approx 60\text{-}100 \text{ mV}$ with a root mean square variation of approximately $\Delta\Phi_{\text{rms}} \approx 16 \text{ mV}$. $\Delta\phi_{\text{pk-pk}} = 55 \text{ mV}$ and $\Delta\phi_{\text{rms}} = 7.3 \text{ mV}$ for the simulated image.

Belaïdi *et al.* find that the point charge model underestimates the force by over 25% at tip-surface distances greater than 10 nm [40], which may explain the small difference between experimental and theoretical results in this comparison.

Film thickness, tip-surface distance and concentration dependence of the calculated potential variation

In this section, we calculate the variation of ϕ for randomly placed charge sites in a dielectric film. We consider the effects of the film thickness, t , the tip-sample height, h , and the concentration of charges, N_0 . We use the results of a procedure written in Matlab. For all images, the scale bar is adjusted to include 94% of the full vertical scale. The accuracy of the Matlab calculation was set to 10^{-4} for the in this section.

Figure 6.29 shows two images calculated with the same concentration of acceptors and holes, but with different film thickness, t . The charge concentration, N_0 , is $2.8 \times 10^{20} \text{ m}^{-3}$. The potential variation, $\Delta\phi_{\text{rms}} = 4.5 \text{ mV}$ for a 20 nm thick dielectric film compared to $\Delta\phi_{\text{rms}} = 6.4 \text{ mV}$ for a 100 nm thick dielectric film. Surprisingly, it does not appear the potential is a very strong function of the thickness considering a dramatic decrease in film thickness did not significantly decrease the variation of the potential. In Section 6.4.6, we found the potential variation, $\Delta\Phi_{\text{rms}} = 15.3 \text{ mV}$ for a 20 nm thick TPD-PS film on gold compared to $\Delta\Phi_{\text{rms}} = 17.5 \text{ mV}$ for a 100 nm thick TPD-PS film on gold.

The dependence of $\Delta\phi$ on the tip-surface distance, h , is shown in Figure 6.30. In this calculation, we set $N_0 = 5 \times 10^{20} \text{ m}^{-3}$ and $t = 100 \text{ nm}$ for the $2 \mu\text{m} \times 2 \mu\text{m}$ simulated images of Figure 6.30(a)-(g). The tip-surface distance, h , varies from 50-200 nm for the images of Figure 6.30(a)-(g). Considerable loss of the lateral resolution in the simulated images is observed as h increases. Figure 6.30h plots $\delta\phi_{\text{rms}}$. As h is increased, the variation decreases.

We compare this to the variation of $\Delta\Phi_{\text{rms}}$ with tip-surface distance in the experiment described in Section 6.6. The data is shown in Figure 6.21 for a 100 nm

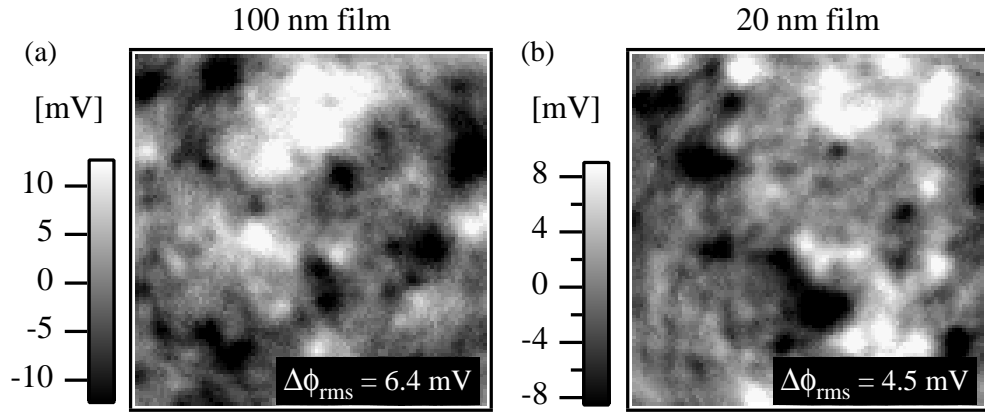


Figure 6.29: Set of $2 \mu\text{m} \times 2 \mu\text{m}$ simulated images of a 100 nm thick dielectric film (a) and a 20 nm thick dielectric film (b).

thick 50% weight TPD-PC film on epitaxially grown gold. From a tip-surface distance of 75 nm to 175 nm, $\Delta\Phi_{\text{rms}}$ dropped from 25 mV to 12 mV. For the system in Figure 6.30, the calculated potential, $\Delta\phi_{\text{rms}}$, dropped from 5.2 mV to 2.7 mV for the same change in tip-surface distance. Although the magnitudes are different, the relative decrease in the potential variation is the same for the experiment and the calculation.

Finally, we have calculated the concentration dependence of the potential over a 100 nm dielectric with a tip-surface height of 50 nm. Here, the concentration of the randomly placed positive and negative charges was varied over an order of magnitude. Figure 6.31(a) and Table 6.3 show the concentration dependence of the potential. The images associated with the potential variation are illustrated in Figure 6.32(a)-(l). The image size is $2.5 \mu\text{m} \times 2.5 \mu\text{m}$ with 128×128 pixels. Figure 6.31(b) shows the concentration dependence of the square of the calculated potential variation, $\Delta\phi_{\text{rms}}^2$, suggesting agreement with $\Delta\phi_{\text{rms}} \propto \sqrt{N_0}$.

In Section 6.4.3, decreasing the concentration of TPD did not lead to a sig-

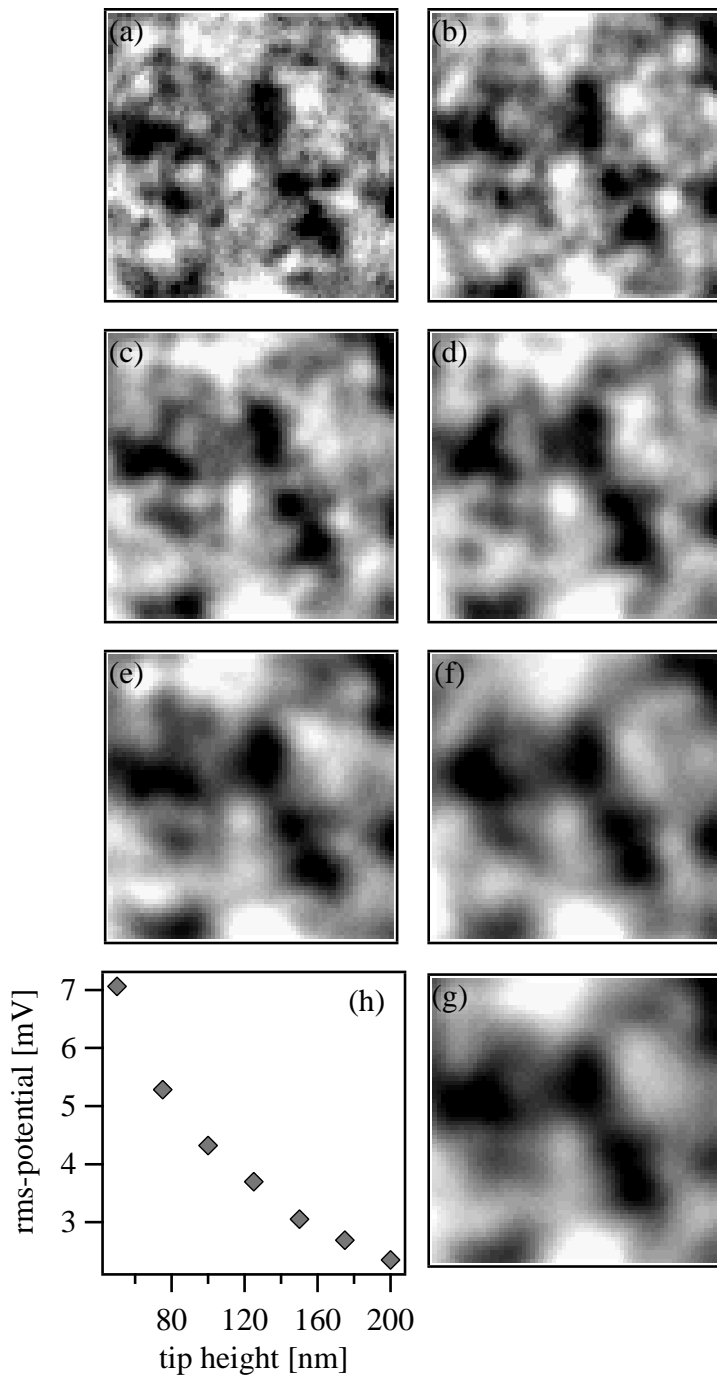


Figure 6.30: (a-g) 2 μm × 2 μm simulated images of $\Delta\phi$ at tip-surface distances ranging from 50–200 nm. (h) Dependence of $\Delta\phi_{\text{rms}}$ on the tip-height, h .

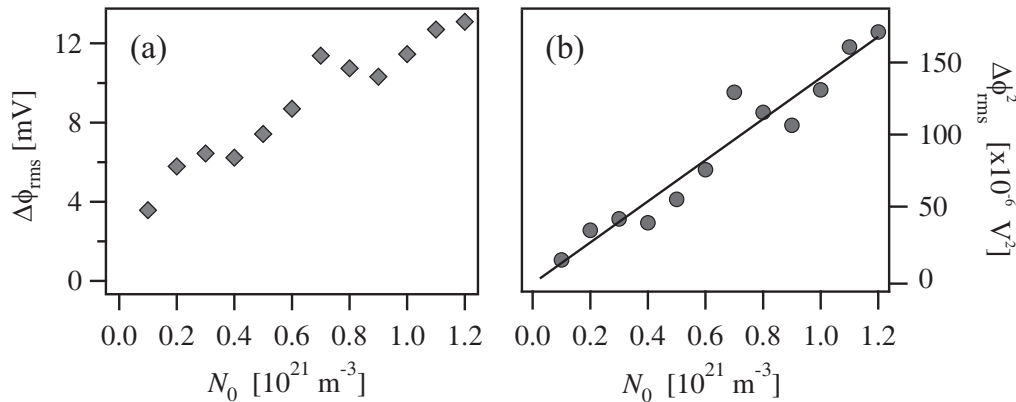


Figure 6.31: (a) Concentration dependence of the calculated potential variation, $\Delta\phi_{\text{rms}}$. The associated images are listed in Figure 6.32. (b) Concentration dependence of the square of the calculated potential variation, $\Delta\phi_{\text{rms}}^2$.

nificantly smaller variation of the potential. The potential varied from $\Delta\Phi_{\text{rms}} = 17.5 \text{ mV}$ to $\Delta\Phi_{\text{rms}} = 16 \text{ mV}$ as the TPD concentration is dropped from 50% weight to 5% weight. However, the concentration of TPD, N_{TPD} is not necessarily proportional to the density of background charge carriers, N_0 .

In order to compare the theoretical results to experiment, N_0 must be controlled. Abkowitz and Pai increased N_0 in TPD-PC by oxidizing TPD to TPD^+ with a salt [11]. More recently, Shen *et al.* were able to control N_0 in similar molecularly doped polymer system [13].

Summary

In Section 6.8.1, the potential calculated from randomly oriented surface and bulk dipoles is too small to account for the variation of $\Delta\Phi$ we observe over TPD-based molecularly doped polymer films. It is unlikely that the potential arises from energetic disorder due to random dipoles. However, it is possible aggregation might create a larger effect.

| Image | N_0 [10^{21} m $^{-3}$] | $\Delta\phi_{\text{rms}}$ [mV] |
|----------------|-------------------------------|--------------------------------|
| Figure 6.32(a) | 0.1 | 3.6 |
| Figure 6.32(b) | 0.2 | 5.8 |
| Figure 6.32(c) | 0.3 | 6.4 |
| Figure 6.32(d) | 0.4 | 6.2 |
| Figure 6.32(e) | 0.5 | 7.4 |
| Figure 6.32(f) | 0.6 | 8.7 |
| Figure 6.32(g) | 0.7 | 11.3 |
| Figure 6.32(h) | 0.8 | 10.6 |
| Figure 6.32(i) | 0.9 | 10.1 |
| Figure 6.32(j) | 1.0 | 11.3 |
| Figure 6.32(k) | 1.1 | 12.7 |
| Figure 6.32(l) | 1.2 | 12.0 |

Table 6.3: Concentration dependence of the calculated potential, $\Delta\phi_{\text{rms}}$. The associated images are shown in Figure 6.32(a)–(l).

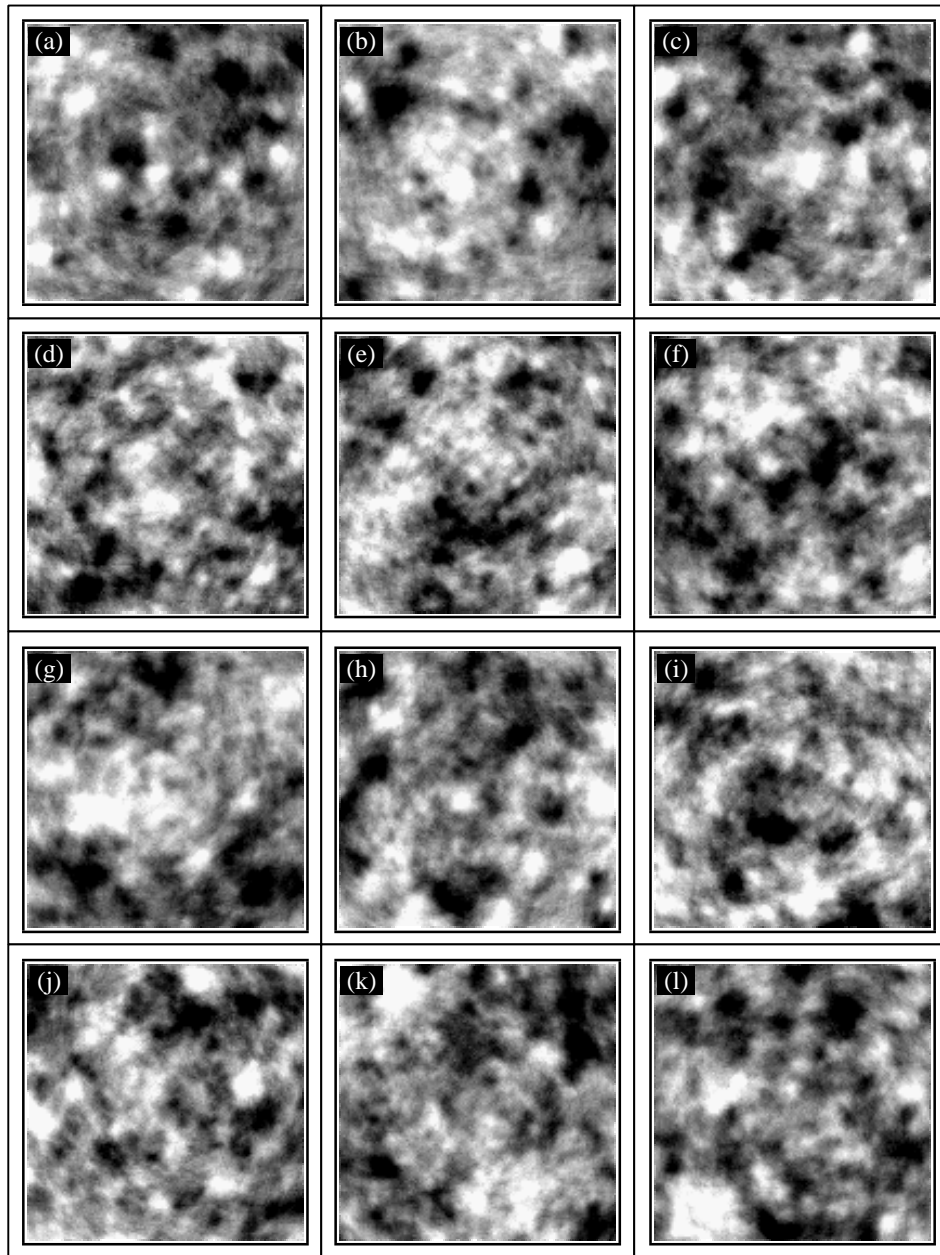


Figure 6.32: Concentration dependence of the calculated potential variation.

2.5 $\mu\text{m} \times 2.5 \mu\text{m}$ images. The associated potential variations are listed in Table 6.3(a)–(l).

From the calculations of a single charge in a dielectric film, we were able to gain intuition about the potential of a charge as a function of depth in a dielectric medium and the tip-surface distance dependence. Also, the lateral resolution from a single charge in the dielectric is quite broad, even for the point probe model used here.

Calculating the potential over a dielectric film with randomly positioned charges was extremely enlightening. For a concentration of background charges similar to what we would measure in a TPD-PC or TPD-PS film, the variation of the calculated potential is approximately $2\text{-}3\times$ smaller than the measured potential variation. It also varies on a slightly larger length scale. It is possible that N_0 measured from the current-voltage characteristics is only a lower limit. This number represents the charges that are mobile. A fraction of these charges could be trapped. Also, Belaidi *et al.* find the point probe model underestimates the force by over 25% at tip-height distances greater than 10 nm [40].

By varying the thickness of the film, we found the calculated potential did not drop dramatically going from a 100 nm thick film to a 20 nm thick film, which is in agreement with the experimental observation. The dependence of the potential variation on the tip-surface distance is in very good agreement with experimental observations over a distance of 100 nm. Finally, the concentration dependence of the potential variation suggests experiments should be performed in which N_0 is controlled by oxidizing a known fraction of TPD molecules.

6.9 Conclusions

Energetic disorder is a central issue for charge transport and injection in organic semiconductors. The large spatial variation of the surface potential in molecularly

doped polymer films was a very surprising discovery and is a significant source of energetic disorder. In order to uncover the cause of the variation, we studied TPD-based molecularly doped polymers under a number of chemical and physical conditions.

By investigating bare gold films, we were able to eliminate the possibility the variation of the surface potential is due to variations of the work function of the gold substrate. Comparing the TPD-PC/Au interface with the TPD-PC/Al interface suggested a spatially varying interface dipole was not creating the large potential variation. Observations of the potential variation over TPD-PC/Au at low temperatures indicates a spatial variation of the accumulation region at the metal/organic interface is also not the cause.

High concentration TPD-PC films did not sustain a surface charge density, leading to the conclusion that the potential variation is not due to a simple uncompensated static surface charge. Low mobility TPD-PC films, achieved at either low concentrations or low temperatures, were easily charged at the surface, yet showed similar variations of the surface potential in untouched areas as high mobility TPD-PC films. Furthermore, films of pure polycarbonate exhibited a very small surface potential variation, which justified focusing on the chemical environment of the TPD molecule.

However, controlling the degree of energetic disorder did not clarify the matter. Only very small changes in the potential variation were observed by doping the molecularly doped polymer film with large dipoles and by changing the polarity of the host polymer. The likelihood the potential variation arises from background charge carriers solidified as the density of these compensated charges, obtained by electrical characterization, appeared well matched with the spatial variation of the

potential.

Theoretical studies provided considerable insight. Calculations indicate the expected potential from randomly oriented surface or bulk dipoles is too small to account for the large variation of the potential outside the TPD films. Calculations of the potential from a charge in a dielectric film on a metal substrate were extremely valuable and support the conclusion that the variation of the potential is due to the presence of background charge carriers due to the ionization of TPD. By placing a density of positive and negative charges randomly in the dielectric film at the same concentration of background charges we expect in TPD-based molecularly doped polymer films, images were calculated and compared to experimental observations. Although the magnitude of the calculated variation is smaller than that of the experiment, the result is very encouraging. For both calculation and experiment, the potential variation did not decrease significantly as the film thickness was decreased. Also, the dependence of the potential variation on the tip-surface distance is in excellent agreement with experimental observations over large distance.

In conclusion, we have observed a large variation of the surface potential over thin films of the molecularly doped polymers, TPD-PC and TPD-PS. The variation is a considerable source of energetic disorder. The experiments and calculations in this chapter strongly support the conclusion that the potential variation is caused by background charge carriers. These carriers are responsible for the Ohmic current at low electric fields. The chemical environment leading to the formation of these carriers, the radical cation, TPD^+ , must be very different from the majority of TPD molecules, since the concentration is on the order of 1 in 10^6 . The variation of the potential we observe is unaccounted for in charge injection and transport

theories at this time. Finally, this study underscores the ability of high-sensitivity electric force microscopy to reveal an unexpected phenomenon even in a nominally well understood π -conjugated system.

6.10 Future directions

Doping the TPD molecules will provide a way to intentionally increase the number of background charge carriers, which we predict should increase the variation of the surface potential. It will also be interesting to follow the potential variation of a film as it crystallizes. This will provide much insight into how charge is rearranged during the molecularly doped polymer's transition from amorphous to crystalline. In order to detect the correlated energetic disorder due to randomly oriented dipoles [7, 18], it will be necessary to develop highly purified materials, clean substrates, and investigate molecules with large dipole moments. Scanning tunneling microscopy should be explored as a potential method to observe the variation from dipolar energetic disorder.

Chapter 6 references

- [1] B. D. Terris, J. E. Stern, H. J. Mamin, and D. Rugar, *Applied Physics Letters* **53**, 2717 (1988).
- [2] B. D. Terris, J. E. Stern, D. Rugar, and H. J. Mamin, *Physical Review Letters* **63**, 2669 (1989).
- [3] C. Schönenberger and S. F. Alvarado, *Physical Review Letters* **65**, 3162 (1990).
- [4] O. A. Semenikhin, L. Jiang, T. Iyoda, K. Hashimoto, and A. Fujishima, *Journal of Physical Chemistry* **100**, 18603 (1996).
- [5] O. A. Semenikhin, L. Jiang, T. Iyoda, K. Hashimoto, and A. Fujishima, *Electrochimica Acta* **42**, 3321 (1997).
- [6] P. M. Borsenberger and D. S. Weiss, *Organic Photoreceptors for Xerography*, Optical Engineering, Marcel Dekker, Inc., New York, 1998.
- [7] D. H. Dunlap, P. E. Parris, and V. M. Kenkre, *Physical Review Letters* **77**, 542 (1996).
- [8] H. Ishii *et al.*, *Physica Status Solidi (A)* **201**, 1075 (2004).
- [9] S. Kera *et al.*, *Physical Review B* **70**, 085304 (2004).
- [10] M. A. Baldo and S. R. Forrest, *Physical Review B* **6408** (2001).
- [11] M. Abkowitz and D. M. Pai, *Philosophical Magazine B* **53**, 193 (1986).
- [12] Y. L. Shen, M. W. Klein, D. B. Jacobs, J. C. Scott, and G. G. Malliaras, *Physical Review Letters* **86**, 3867 (2001).
- [13] Y. L. Shen *et al.*, *Physical Review B* **68** (2003).
- [14] Y. L. Shen, A. R. Hosseini, M. H. Wong, and G. G. Malliaras, *ChemPhysChem* **5**, 16 (2004).
- [15] W. R. Silveira and J. A. Marohn, *Physical Review Letters* **93**, 116104 (2004).
- [16] N. Hayashi, E. Ito, H. Ishii, Y. Ouchi, and K. Seki, *Synthetic Metals* **121**, 1717 (2001).
- [17] N. F. Mott and R. W. Gurney, *Electronic Processes in Ionic Crystals*, Clarendon Press, Oxford, 1940.
- [18] S. V. Novikov and A. V. Vannikov, *Journal of Physical Chemistry* **99**, 14573 (1995).

- [19] F. Khan, A.-M. Hor, and P. R. Sundararajan, *Pure Applied Chemistry* **76**, 1509 (2004).
- [20] F.-M. Han, L.-M. Do, M. Fujihira, T. Inada, and Y. Shirota, *Journal of Applied Physics* **80**, 3297 (1996).
- [21] U. Memmert and P. R. Norton, *Surface Science* **203**, L689 (1988).
- [22] W. R. Silveira and J. A. Marohn, *Review of Scientific Instruments* **74**, 267 (2003).
- [23] D. R. Lide, *Handbook of Chemistry and Physics*, CRC Press, Cleveland, Ohio, 2004.
- [24] D. E. Eastman, *Physical Review B* **2**, 1 (1970).
- [25] A. Kahn, N. Koch, and W. Gao, *Journal of Polymer Science: Part B: Polymer Physics* **41**, 2529 (2003).
- [26] M. Knupfer and H. Peisert, *Physica Status Solidi (A)* **201**, 1055 (2004).
- [27] J. A. Marohn, Marohn Group Report, *unpublished* (2003).
- [28] H.-J. Yuh and D. M. Pai, *Philosophical Magazine Letters* **62**, 61 (1990).
- [29] R. H. Young and J. J. Fitzgerald, *Journal of Chemical Physics* **102**, 2209 (1995).
- [30] S. Belaidi, P. Girard, and G. Leveque, *Journal of Applied Physics* **81**, 1023 (1997).
- [31] T. D. Krauss and L. E. Brus, *Physical Review Letters* **83**, 4840 (1999).
- [32] H. Fujikawa, S. Tokito, and Y. Taga, *Synthetic Metals* **91**, 161 (1997).
- [33] I. G. Hill, A. Kahn, Z. G. Soos, and R. A. Pascal, *Chemical Physics Letters* **327**, 181 (2000).
- [34] E. V. Tsiper and Z. G. Soos, *Physical Review B* **64**, 195124 (2001).
- [35] Z. Y. Xie *et al.*, *Synthetic Metals* **108**, 81 (2000).
- [36] E. V. Tsiper and Z. G. Soos, *Physical Review B* **68**, 085301 (2003).
- [37] J. Cornil *et al.*, *Journal of Physical Chemistry A* **105**, 5206 (2001).
- [38] J. A. Marohn and D. H. Dunlap, *in preparation* (2005).
- [39] J. A. Marohn, Marohn Group Report, *unpublished* (2005).
- [40] S. Belaidi, P. Girard, and G. Leveque, *Journal of Applied Physics* **81**, 1023 (1997).

APPENDIX A

HARMONIC OSCILLATOR MEASUREMENTS

A.1 Thermal energy and the harmonic oscillator

A harmonic oscillator in equilibrium with a bath of temperature, T , has an energy expectation value for each mode equal to $k_B T/2$. Therefore,

$$\frac{1}{2} k \langle x^2 \rangle = \frac{1}{2} k_B T, \quad (\text{A.1})$$

where $k_B = 1.38 \times 10^{-23}$ J K $^{-1}$ is Boltzmann's constant and T is the absolute temperature. Here $\langle x^2 \rangle$ is mean-square displacement x_{rms}^2 . The mean-square displacement is measured directly from time-domain observations and the oscillator spring constant can be found from

$$k = \frac{k_B T}{x_{\text{rms}}^2}. \quad (\text{A.2})$$

An alternative and more accurate way to determine x_{rms} is to calculate x_{rms} as the area under the position-fluctuation power spectral density. The area under the power spectral density, equal to $k_B T/k$, can be used to determine the cantilever spring constant if the cantilever's temperature is known [1]. The power spectral density at all frequencies for a harmonic oscillator at thermal equilibrium is [2]

$$P_z(f) = \left(\frac{2 k_B T}{\pi k Q f_0} \right) \frac{f_0^4}{(f_0^2 - f^2)^2 + f^2 f_0^2 / Q^2}, \quad (\text{A.3})$$

where Q is the quality factor and f_0 is the cantilever resonance frequency. The first term in parenthesis has units of [m 2 /Hz] and serves to fix the area under the power spectral density. The second term is unitless and traces out the response versus frequency of the oscillator to thermal-bath fluctuations.

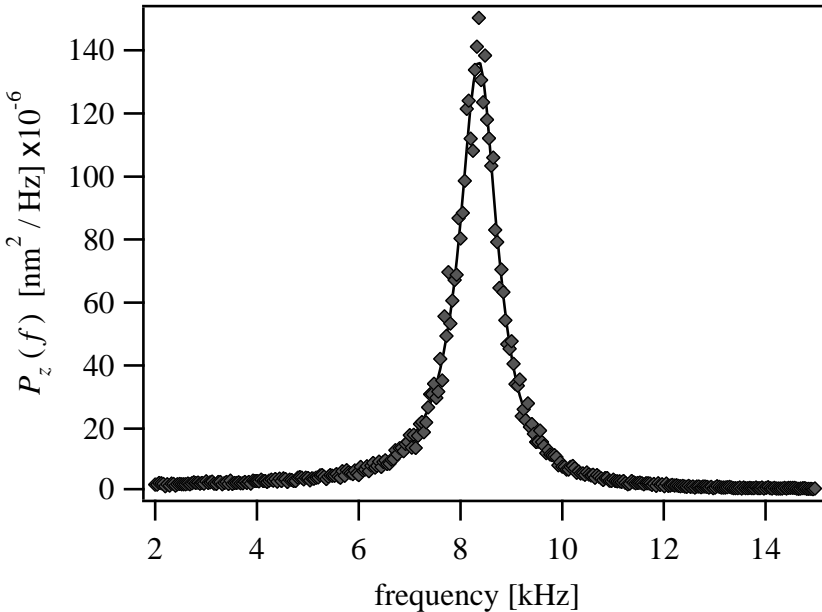


Figure A.1: Power spectral density of a commercial silicon nitride cantilever.

Figure A.1 shows the power spectral density of a cantilever at 298 K at ambient pressure. The manufacturer's specifications give a resonance frequency $f_0 = 8$ kHz and spring constant $k = 0.02$ N/m for the silicon nitride cantilever.

Using Equation A.3 to fit $P_z(f)$, we obtain the parameters listed in Table A.1. The spring constant, k , is calculated assuming a temperature of 298 K. The spring constant is very close to the manufacturer's specifications in this case.

The minimum detectable force, F_{\min} , is given by

$$F_{\min} = \sqrt{\frac{2k k_B T B}{\pi Q f_0}}, \quad (\text{A.4})$$

where F is the force between the cantilever and the surface and B is the measurement bandwidth [3].

| parameter | value | units |
|------------|-----------------------|-------------------------------------|
| $P_z(0)$ | 1.56×10^{-6} | $\frac{\text{nm}^2}{\text{Hz}}$ |
| Q | 9.3 | — |
| f_0 | 8383 | Hz |
| k | 0.022 | $\frac{\text{N}}{\text{m}}$ |
| F_{\min} | 2.7×10^{-14} | $\frac{\text{N}}{\sqrt{\text{Hz}}}$ |

Table A.1: Cantilever parameters calculated from the power spectral density in Figure A.1.

A.1.1 The discrete power spectral density

National Instruments, the software and hardware company that created LabView, has published a detailed technical report explaining the use of the discrete power spectral density [4].

A.1.2 Analysis of a force-distance curve

Figure A.2(a) shows a force-distance curve between a cantilever with a 8.8 kHz resonance frequency and a 0.02 N/m spring constant. The measurement was performed in high vacuum. The y -axis is the output signal of the interferometer. The x -axis is the distance traveled by the cantilever as it is approached to the surface. At $x = 0$ nm, the cantilever is approximately 940 nm away from the surface. The approach of the cantilever is shown in red. The retraction of the cantilever is shown in grey. Note the arrows give the direction of the red and grey curves.

Figure A.2(b) is an illustration to guide the force-distance curve. As the cantilever is approached to the surface (red curve and red cantilevers), the deflection

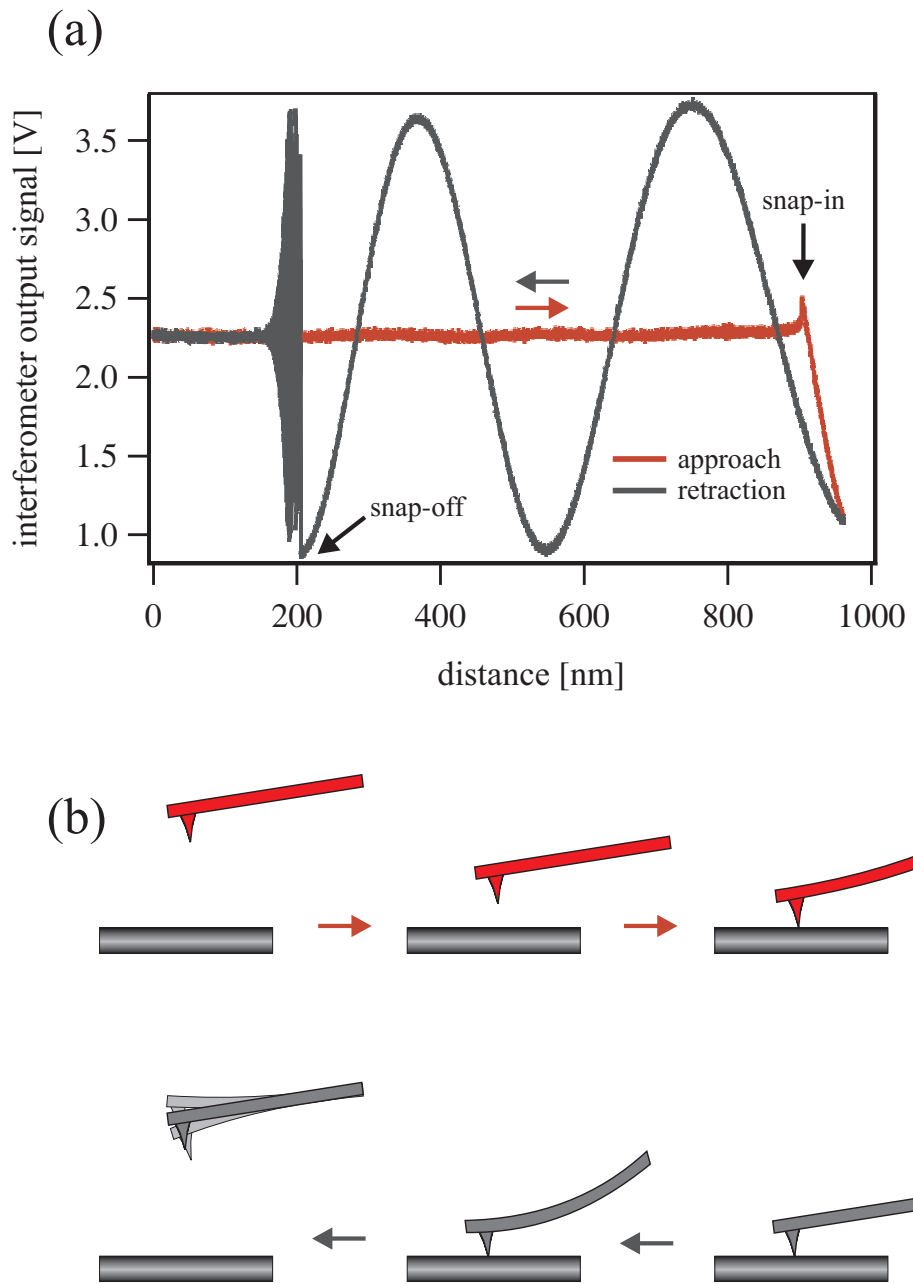


Figure A.2: Analysis of a force-distance curve. (a) Force-distance curve. The interferometer output signal is plotted versus the distance traveled by the cantilever from a point above the surface ($x = 0$). The wavelength of the interferometer is $\lambda_l = 780$ nm. (b) Illustration showing various stages of the cantilever during the force-distance measurement.

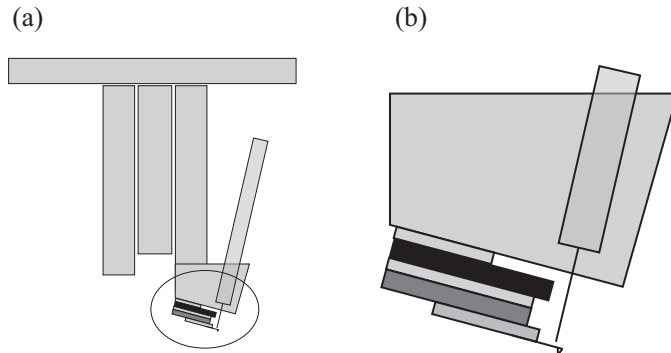


Figure A.3: Piezo stage for cantilever excitation. (a) Inertial slider. (b) Piezo stage.

remains constant until it snaps in to the surface at approximately 920 nm. At this point, the cantilever deflection is toward the surface. Because the interferometer signal is on a negative slope, snap-in to the surface appears as an increase in the interferometer output signal. As the cantilever is pushed closer to the surface, the sign of the deflection, and thus the force, eventually change direction. The cantilever is then retracted at 960 nm (grey curve and grey cantilevers). The force of adhesion is strong enough to keep the cantilever in contact with the surface, so that as it is retracted, the cantilever undergoes significant deflection. The deflection is so large, in fact, that it falls out of the sensitive range of the interferometer and crosses through the interference pattern, which is the sinusoid shape of the force-distance curve. Eventually, the cantilever snaps off the surface at 200 nm and rings down.

A.1.3 Induced cantilever excitation

The cantilever is driven at the base by a small bimorph piezo crystal (Piezo Systems, Inc.), shown in Figure A.3(b). The piezo is approximately 3 mm × 2 mm and 0.020" thick. If the piezo was too large, a mechanical resonance appeared

between 20-50 kHz. Electrodes were soldered to the edge of the piezo with minimal solder. The wires were 36-gauge or lighter. Electrical isolation from the piezo was achieved by gluing a thin piece of paper to the piezo (the piezo is black in Figure A.3(b)) and mounting a thin, 0.020" BeCu plate on the bottom of the piezo. The top of the piezo was also glued to a small, 1 mm × 1 mm piece of paper to allow for overhang of the bimorph piezo and electrically isolate it from the coarse approach plate on which it was mounted (Figure A.3(a)). Finally, the cantilever was glued to the BeCu plate with epoxy. The cantilever was electrically grounded by attaching a small lightweight wire to the base of the cantilever with Silver Paint. To remove the cantilever, small amounts of acetone and methanol were applied with a toothpick until the cantilever can be pried off the CuBe plate. A toothpick was used to remove residual epoxy.

Figure A.4 shows the amplitude response resulting from the driving force of the piezo. The amplitude responds linearly to the piezo voltage. The amplitude and phase response are shown in Figure 3.22.

A.2 Origin of the contact potential difference

This section describes the origin of the contact potential difference, $\Delta\Phi$. Figure A.5(a) shows energy level diagrams for two materials, A and B , with different work functions, Φ_A and Φ_B , sharing a common vacuum level, E_{vac} , but not in contact with each other. If the circuit is closed between the two materials, electrons will flow from the material with the smaller work function to the material with the higher work function ($B \rightarrow A$). The electrons flow until the Fermi levels become equal. The excess electrons reside on the surface of the material and just enough of them move so that the potentials inside the bulk material are equivalent. At

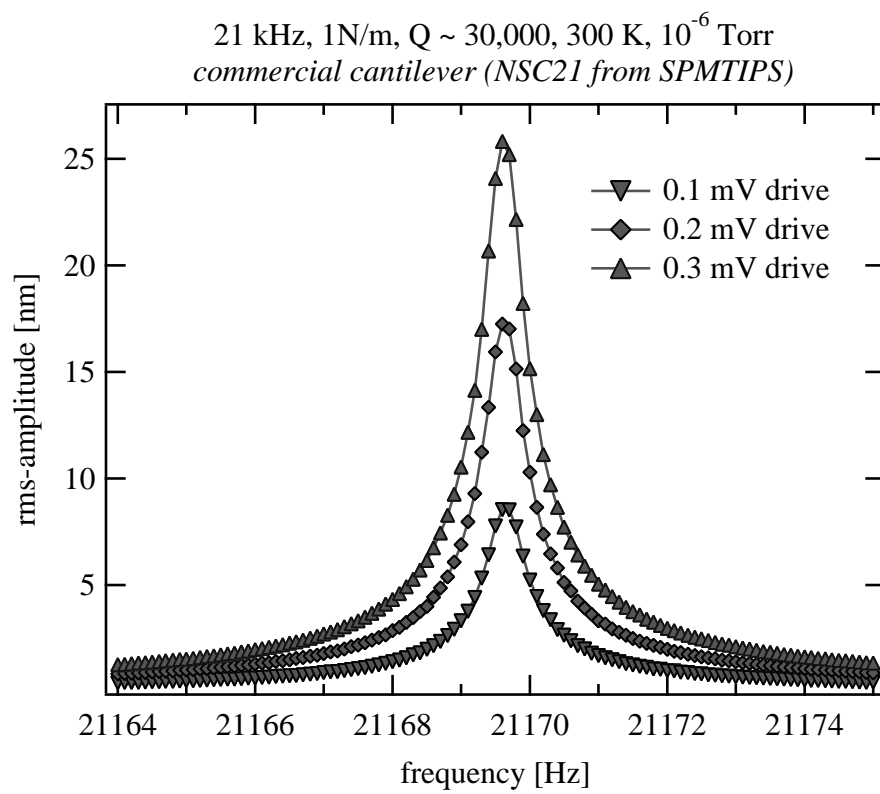


Figure A.4: Piezo excitation of a cantilever in high vacuum.

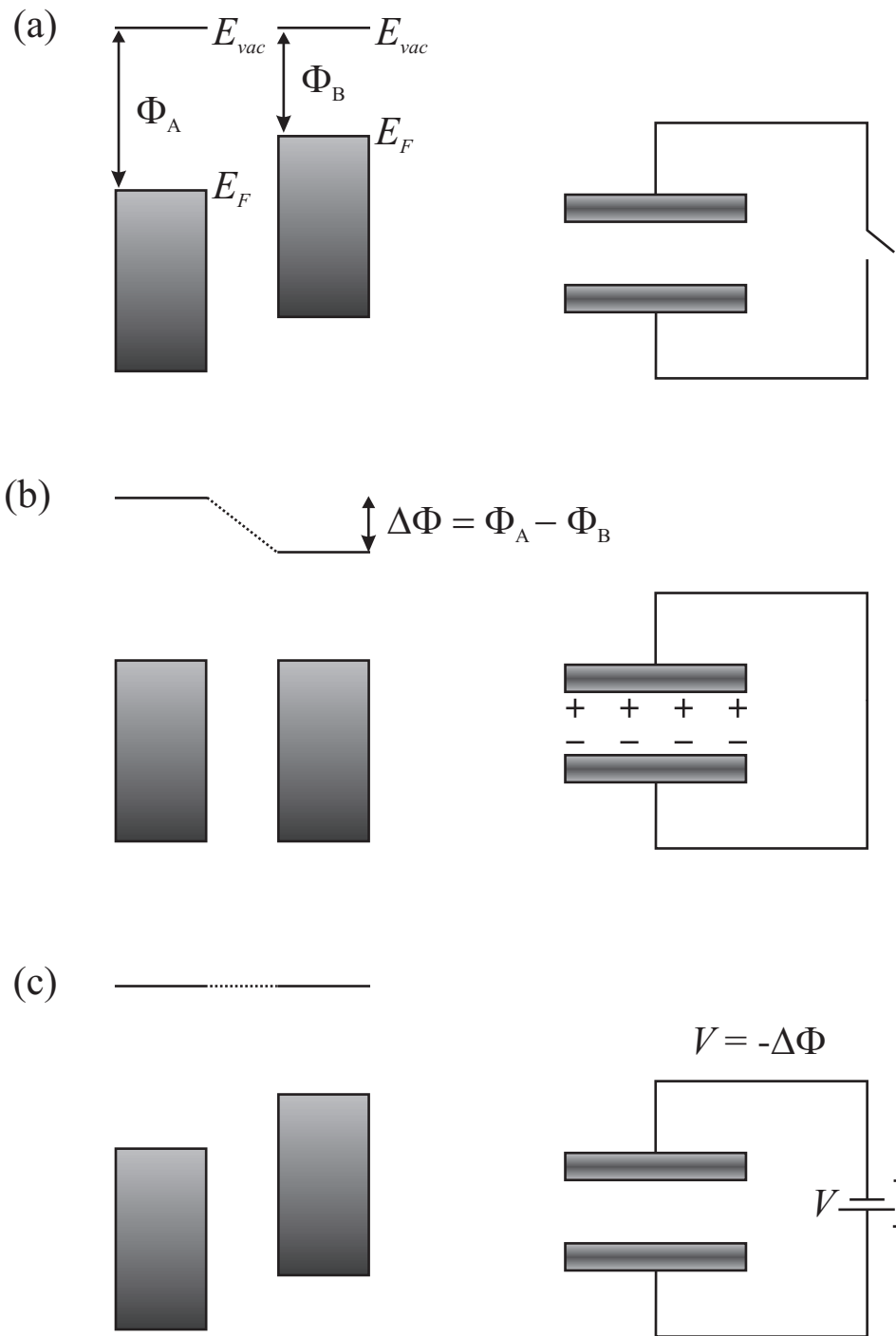


Figure A.5: (a) Materials A and B with different work functions. (b) Equilibrium is reached by the transfer of electrons from B to A . (c) The electric field is canceled by an applied potential, V .

this point, the vacuum level is no longer equivalent for the two materials because of the net charge transfer, shown in Figure A.5(b). The difference between the two vacuum levels is called the contact potential difference, $\Delta\Phi$, which is given by

$$\Delta\Phi = \Phi_A - \Phi_B. \quad (\text{A.5})$$

In Figure A.5(b), an electric field is present between the two plates. In order to determine the magnitude of $\Delta\Phi$, one can insert a battery into the circuit until the electric field is nulled, which is shown in Figure A.5(c). It is important to note that $\Delta\Phi$ is present even when there is no applied potential between plates *A* and *B*. We have found in electric force microscopy experiments on extremely low mobility materials, this built-in potential can assist unwanted triboelectric charge transfer when the cantilever tip contacts the surface.

In this discussion, the vacuum level we refer to is the vacuum level just outside the material. An excellent, intuitive discussion of the difference between the vacuum level just outside the material and the vacuum level at infinite distance is given in a review by Ishii *et al.* [5]. The vacuum level just outside a materials is slightly higher than the vacuum level at infinity because the electron density does not abruptly stop at the surface boundary, but tails off, creating a surface dipole. This is why different crystal faces of the same metal have different work functions. This is also why the work function of a metal can change dramatically in the presence of adsorbates, which alter the nature of the tailing electron cloud at the surface of a metal.

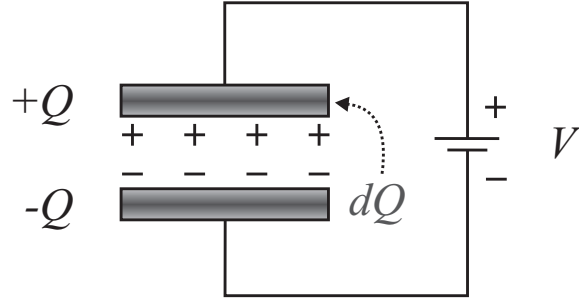


Figure A.6: Capacitor with an applied potential V between the plates.

A.3 Energy stored in a capacitor

We begin with a capacitor, the simplest approximation to the cantilever-sample interaction, with an applied potential V , capacitance C , and stored charge of Q , is illustrated in Figure A.6. The capacitance is related to the charge and applied potential by

$$C = \frac{Q}{V}. \quad (\text{A.6})$$

One plate has a total charge of Q and the other plate has a total charge of $-Q$. Moving a small amount of charge, dQ , from one plate to the other requires an energy,

$$dE = dQ V. \quad (\text{A.7})$$

Substituting $V = Q/C$ gives $dE = Q/C dQ$. Integrating both sides

$$\int_0^E dE = \frac{1}{C} \int_0^Q Q dQ, \quad (\text{A.8})$$

we find

$$E = \frac{Q^2}{2C} = \frac{1}{2} CV^2. \quad (\text{A.9})$$

The energy varies linearly with the capacitance and is quadratic with the potential between the two plates. This relation holds for a capacitor of any shape.

A.4 The capacitive force

The force, F , between the plates of a capacitor is given by the derivative of the energy with respect to distance, z , resulting in

$$F_z = -\frac{\partial E}{\partial z} = -\frac{1}{2} \frac{\partial C}{\partial z} V^2. \quad (\text{A.10})$$

If we include the contribution from the contact potential difference, $\Delta\Phi$, discussed in Section A.2, the force becomes

$$F_z = -\frac{1}{2} \frac{\partial C}{\partial z} (V + \Delta\Phi)^2. \quad (\text{A.11})$$

By setting $V = -\Delta\Phi$, the force between the plates vanishes. This is the idea behind most electric force microscopy measurements. The cantilever is one plate of the capacitor and the sample is the other plate. By recording the potential, V , required to null the force spatially, we map changes in the work function of the sample, assuming the work function of the cantilever remains constant.

In practice, this is often achieved by applying a voltage $V_{ac} \sin(\omega t) + V_{dc}$. V_{dc} is adjusted so that it nulls the modulated force at frequency ω [6]. The sensitivity is greatly increased by utilizing this modulation scheme.

Using this simple cantilever-sample model, we can extend this model by considering the force gradient, which we measure in high vacuum when the quality factor, Q , is large. The resonance frequency shift, Δf , of a cantilever with a natural resonance frequency, f_0 , is approximated by

$$\frac{\Delta f}{f_0} \approx -\frac{1}{2k} \frac{\partial F_z}{\partial z}, \quad (\text{A.12})$$

which is valid for small vibration amplitudes. Therefore, we can quantify the force gradient by monitoring the frequency of the cantilever. The force gradient is

$$\frac{\partial F_z}{\partial z} \approx -\frac{1}{2} \frac{\partial^2 C}{\partial z^2} (V + \Delta\Phi)^2, \quad (\text{A.13})$$

assuming that the $\Delta\Phi$ is not height dependent. The relative resonance frequency shift, $\Delta f/f_0$ becomes

$$\frac{\Delta f}{f_0} \approx \frac{1}{4k} \frac{\partial^2 C}{\partial z^2} (V + \Delta\Phi)^2. \quad (\text{A.14})$$

We can rewrite Equation A.14 as

$$f \approx f_0 - \frac{f_0}{4k} \frac{\partial^2 C}{\partial z^2} (V + \Delta\Phi)^2, \quad (\text{A.15})$$

where we have used $\Delta f = f_0 - f$. By measuring the resonance frequency as a function of V , we can obtain the capacitance derivative, $\partial^2 C/\partial z^2$, and the contact potential difference, $\Delta\Phi$, spatially.

Although this is a very simple capacitive model for the cantilever-sample interaction, it is extremely useful for extracting $\partial^2 C/\partial z^2$ and $\Delta\Phi$. If a working device is studied, there may be an additional spatial component, $\phi(x)$, to the sample potential, which gives

$$f \approx f_0 - \frac{f_0}{4k} \frac{\partial^2 C}{\partial z^2} (V + \phi(x) + \Delta\Phi)^2. \quad (\text{A.16})$$

In this case, nulling the force gradient means setting the applied potential, V , to $-(\phi(x) + \Delta\Phi)$. Care must be taken to make sure the sign of the potential is correct in a real experiment. Often this is lost in the theoretical description. The sign of the null voltage depends on the specific configuration of the voltages applied to the device electrodes and the cantilever. In order to clarify this matter, consider Figure A.7. The cantilever potential is V_t and the potential across the device is $\phi(x)$. Ignoring any contribution from $\Delta\Phi$, we have

$$f \approx f_0 - \frac{f_0}{4k} \frac{\partial^2 C}{\partial z^2} (V_t - \phi(x))^2. \quad (\text{A.17})$$

Therefore, the frequency reaches a maximum when $V_t = \phi(x)$. If $\Delta\Phi$ is quite large, it can be measured with the device off. In fact, Bürgi *et al.* subtract this quantity from V_t to obtain $\phi(x)$ [7].

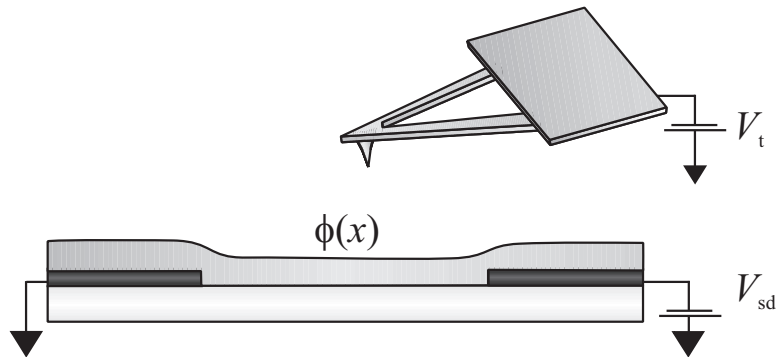


Figure A.7: Minimizing the force gradient between the device and the cantilever requires $V_t = \phi(x)$.

In some experiments, we found that $\Delta\Phi$ is height-dependent. In this case, it is appropriate to use this model only with very flat samples and image at constant cantilever tip-sample separation. This ensures that the force gradient arises only from variations in the capacitance and sample work function. The reason for the height dependence remains to be explained, although we suspect it is due to different work functions on the cantilever tip and lever arm.

Appendix A references

- [1] J. L. Hutter and J. Bechhoefer, Review of Scientific Instruments **64**, 1868 (1993).
- [2] J. A. Marohn, Marohn Group Report, *unpublished* (2001).
- [3] K. Y. Yasumura *et al.*, Journal of Microelectromechanical Systems **9**, 117 (2000).
- [4] K. Fahy and E. Pérez, Fast fourier transforms and power spectra in labview, Technical Report 040, National Instruments, 1993.
- [5] H. Ishii, K. Sugiyama, E. Ito, and K. Seki, Advanced Materials **11**, 605 (1999).
- [6] M. Nonnenmacher, M. P. O'Boyle, and H. K. Wickramasinghe, Applied Physics Letters **58**, 2921 (1991).
- [7] L. Bürgi, H. Sirringhaus, and R. H. Friend, Applied Physics Letters **80**, 2913 (2002).

APPENDIX B

SPACE-CHARGE LIMITED CONDUCTION

B.1 Space-charge limited conduction

In this section, the space-charge limited current density, J_{SCL} , in an insulating material is derived adapting the derivation of the Child-Langmuir problem in Chapter 10 of *Mathematical Physics* by Kusse and Westwig [1]. It is assumed that the injecting electrode can supply any current to the material and that diffusion does not contribute to the current density.

Figure B.1 illustrates the parallel plate device of length, L , used to obtain the unipolar current through an insulator of mobility, μ , with a dielectric constant of ϵ . A voltage, V , is applied to the electrode at $x = L$ and the electrode at $x = 0$ is grounded. The current density, J , is the measured current, i , divided by the area of the electrodes i/A . Ignoring diffusion, the current is the charge density $\rho(x)$ multiplied by the velocity $v(x)$. The velocity is given by $\mu E(x)$, which gives a current density,

$$J = \rho(x)\mu E(x). \quad (\text{B.1})$$

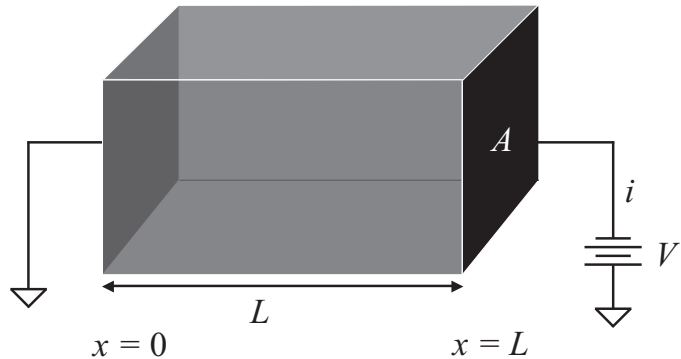


Figure B.1: Parallel plate device for space-charge limited conduction (SCLC).

Using Poisson's equation,

$$-\frac{d^2\phi}{dx^2} = \frac{\rho(x)}{\epsilon}, \quad (\text{B.2})$$

and the fact that $\rho(x) = J/\mu E(x)$ gives

$$-\frac{d^2\phi}{dx^2} = \frac{J}{\epsilon\mu E(x)}.$$

The electric field is the derivative of the potential, $E(x) = -d\phi/dx$. Using this relation and moving both derivatives to the lefthand side leads to

$$\frac{d\phi}{dx} \frac{d^2\phi}{dx^2} = \frac{J}{\epsilon\mu}. \quad (\text{B.3})$$

Now for a trick on the lefthand side of Equation B.3. It is equivalent to

$$\frac{1}{2} \frac{d}{dx} \left(\frac{d\phi}{dx} \right)^2 = \frac{J}{\epsilon\mu}. \quad (\text{B.4})$$

Reorganizing Equation B.4 and integrating from $x = 0$ to a distance x , we have

$$\int_0^x d \left(\frac{d\phi}{dx} \right)^2 = \frac{2J}{\epsilon\mu} \int_0^x dx,$$

which evaluates to

$$\left(\frac{d\phi}{dx} \right)_{x=x}^2 - \left(\frac{d\phi}{dx} \right)_{x=0}^2 = \frac{2Jx}{\epsilon\mu}.$$

Using a boundary condition, $E(0) = 0$, simplifies the expression to give form of the electric field, $E(x)$,

$$\left(\frac{d\phi}{dx} \right)^2 = \frac{2Jx}{\epsilon\mu} \rightarrow E(x) = -\frac{d\phi}{dx} = -\left(\frac{2J}{\epsilon\mu} \right)^{1/2} x^{1/2}, \quad (\text{B.5})$$

which we can rearrange to be

$$d\phi = \left(\frac{2J}{\epsilon\mu} \right)^{1/2} x^{1/2} dx.$$

Integrating the lefthand side from $\phi = 0$ to $\phi = \phi(x)$ and the righthand side from $x = 0$ to $x = x$, gives

$$\int_0^{\phi(x)} d\phi = \left(\frac{2J}{\epsilon\mu} \right)^{1/2} \int_0^x x^{1/2} dx.$$

This leads to the functional form of the potential,

$$\phi(x) = \left(\frac{2J}{\epsilon\mu} \right)^{1/2} \frac{2}{3} x^{3/2}. \quad (\text{B.6})$$

Applying a boundary condition, $\phi(L) = V$, and solving for J to obtain the space-charge limited current,

$$J_{\text{SCL}} = \frac{9}{8}\mu\epsilon \frac{V^2}{L^3}. \quad (\text{B.7})$$

From Poisson's equation (Equation B.2), we obtain the charge density

$$\rho(x) = - \left(\frac{\epsilon J}{2\mu} \right)^{1/2} x^{-1/2}. \quad (\text{B.8})$$

So, after all that what does Equation B.7 mean? The current goes as the square of the applied voltage, $J \propto V^2$. This is much different from Ohmic conduction with $J \propto V$. The insulator does not remain neutral, as does the material in an Ohmic conductor. Space-charge builds up and modifies the potential, electric field, charge density. A simple explanation for the V^2 dependence is given in Appendix B.2.

A summary of the key relationships (discussed in Section 4.5.1):

$$\begin{aligned} J_{\text{SCL}} &= \frac{9}{8}\mu\epsilon \frac{V^2}{L^3} \\ \phi(x) &= \left(\frac{8J}{9\epsilon\mu} \right)^{1/2} x^{3/2} \\ E(x) &= - \left(\frac{2J}{\epsilon\mu} \right)^{1/2} x^{1/2} \\ \rho(x) &= - \left(\frac{\epsilon J}{2\mu} \right)^{1/2} x^{-1/2} \end{aligned} \quad (\text{B.9})$$

B.2 Simplified argument for the current in the space-charge limit

The following simplified explanation is commonly used to explain the dependence of the current on the applied potential in an insulator.

The current density, J , for injecting charge from a metal into an insulator is given by

$$J = \frac{Q}{t}, \quad (\text{B.10})$$

where Q is the total charge injected per unit area and t is the time it takes for a charge to travel from the injecting electrode to the extracting electrode, which are separated by a distance, L . The time, t , required to travel from one electrode to the other is simply

$$t = L/v, \quad (\text{B.11})$$

where v is the average velocity of the charge. Much like a charging capacitor, the metal plate that injects charge can supply a charge density to the insulator that is proportional to the applied potential, V and the capacitance per unit area, C ,

$$Q \approx CV. \quad (\text{B.12})$$

The capacitance, C , per unit area is related to the separation between the metal plates, L , by

$$C = \frac{\varepsilon\varepsilon_0}{L}, \quad (\text{B.13})$$

with a dielectric constant, ε . Combining Equations B.13 and B.12 gives

$$Q \approx \frac{\varepsilon\varepsilon_0}{L}V. \quad (\text{B.14})$$

The average velocity, v , of the charges is given by the product of the mobility, μ , and the electric field, E , resulting in

$$v = \mu E. \quad (\text{B.15})$$

Now, substituting Equations B.15 and B.14 into Equation B.10 gives

$$J \approx \frac{\mu \epsilon_0 V^2}{L^3}, \quad (\text{B.16})$$

which differs only by a factor of 9/8 from the rigorously derived expression.

Appendix B references

- [1] B. Kusse and E. Westwig, *Mathematical Physics*, John Wiley and Sons, Inc., 1998.

APPENDIX C

PROBE DESIGN

C.1 Cryogenic vacuum space

The vacuum space is shown in Figure C.1. At the top of the vacuum tube, a NW-40 stainless steel flange is welded to a 1.750" stainless steel tube (Figure C.1(a)). A 6-way NW-40 vacuum component is placed on the NW-40 flange. Through this structure, we pass optical fiber, electrical connections, and maintain high vacuum throughout the microscope. The stainless steel tube (shown in blue) is 6 feet in length (Figure C.1(b)). Stainless steel has relatively poor thermal conductivity, which helps prevent heat leaks to the experiment, which occurs inside the copper chamber at the bottom of the tube. At the bottom of the stainless steel tube is a removable copper chamber (Figure C.1(c)). The removable chamber is constructed of three copper parts. A fourth copper part is fit to the stainless steel tube and mates to the removable copper section. The horizontal blue arrows indicate where a silver solder joint has been made. The red arrow indicates where the removable chamber is released. This connection is a 1° vacuum seal (see the cryogenic ideas presented by Richardson and Smith [1]). A small amount of vacuum grease ensures high vacuum is achieved and prevents the copper surfaces becoming scratched. It is not critical the angle is exactly 1.0° . However, it is critical the angle on the matching copper parts be the same. In order to achieve this, the parts must be machined on a lathe without readjusting the tool angle. Initially, experiments were performed in a similar 1.5" diameter tube. However, extra space was required for adequate heat sinking and vibration isolation. A 1.75" diameter tube will still fit in most of the Cornell University wide-neck transfer dewars for

cryogenic testing.

The individual copper parts shown in Figure C.1(c) are drawn in detail in Figures C.2, C.3, C.4, and C.5. Copper is used here for its excellent thermal conductivity.

The copper vacuum space component in Figure C.2 shows the male end of the 1.0° vacuum seal. This piece is silver soldered into the stainless steel tube of Figure C.1(b). The 2-56 tap holes are meant for additional heat sinking or may serve as a mounting plate. Figure C.3 shows the copper female end of the 1.0° vacuum seal, which is silver soldered into the 9.5" copper tube of Figure C.4. Finally, the copper part in Figure C.5 seals the end of the tube and provides additional heat sinking. This piece is silver soldered into the copper tube of Figure C.4.

C.1.1 Probe height adjustment

The stainless steel tube was anchored by an aluminum structure designed to allow for height adjustment. This is desirable for variable temperature experiments where the copper end of the vacuum chamber is held above the cryogen level, rather than immersed in it. Figure C.6 gives a simple schematic of the mechanism (viewed from the side). The tube was held by a tall aluminum clamp, which was halved and fit with bolts (not shown) to tighten against the stainless steel tube. This clamp was bolted, via 4-40 hex screws (upside down in Figure C.6) to an aluminum plate. This aluminum plate rested on an O-ring, which hugged the stainless steel tube. The plate was bolted, via 4-40 hex screws, through a second aluminum plate of the same diameter to a larger, thicker plate with a O-ring seat. This design sealed the cryogenic space below and allowed for continuous height adjustment.

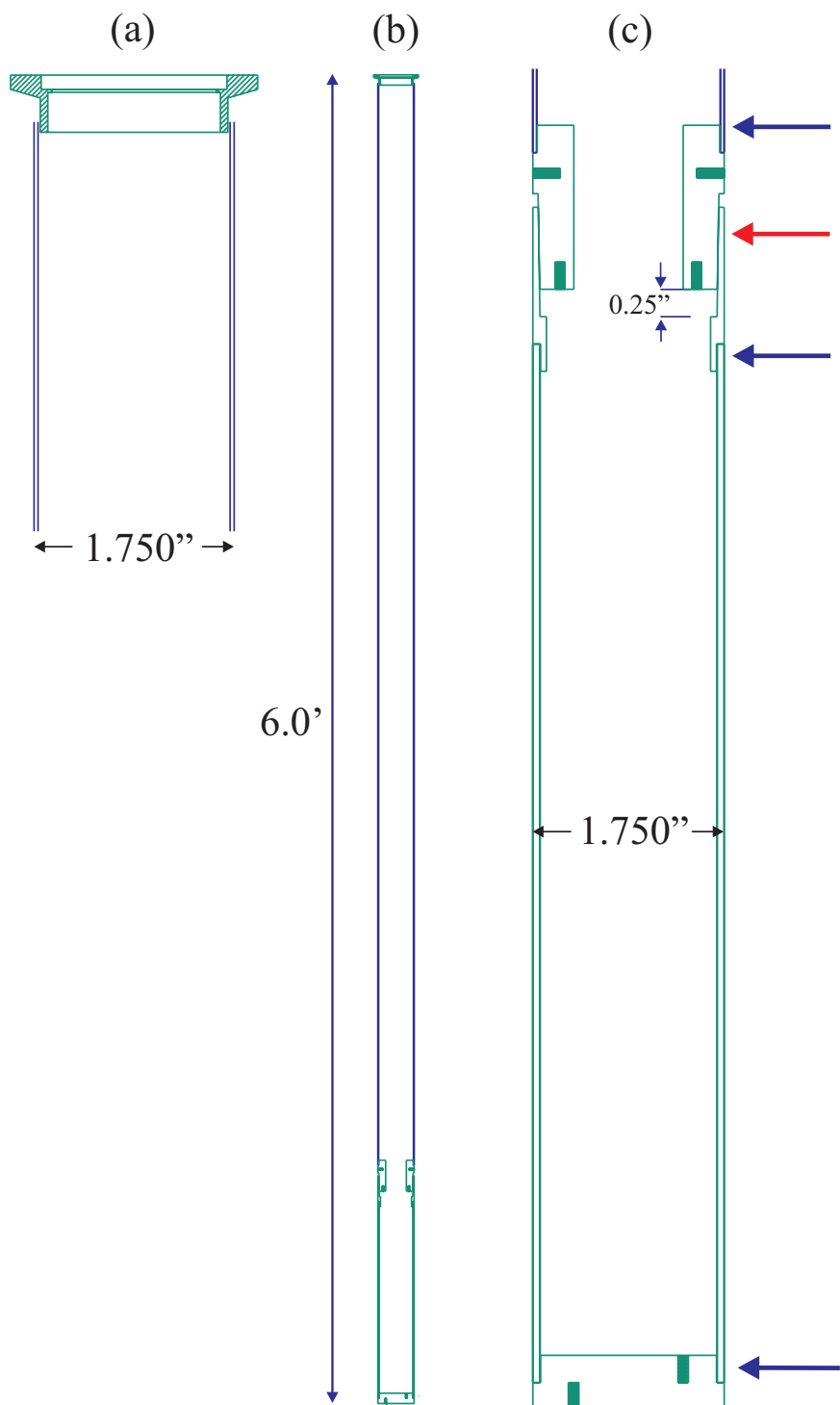


Figure C.1: High vacuum cryogenic vacuum space.

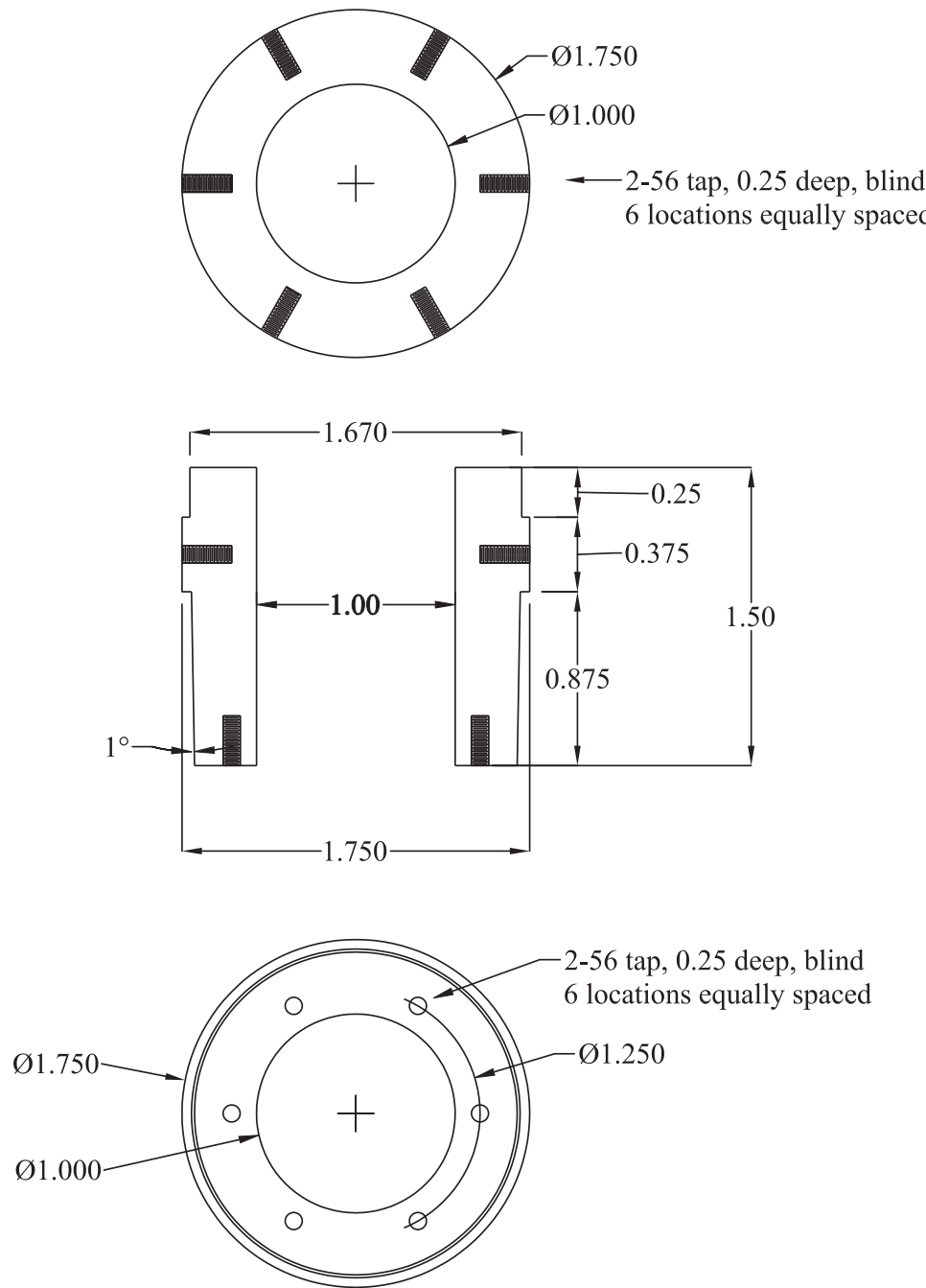


Figure C.2: Vacuum space component 1 (copper). Units are in inches.

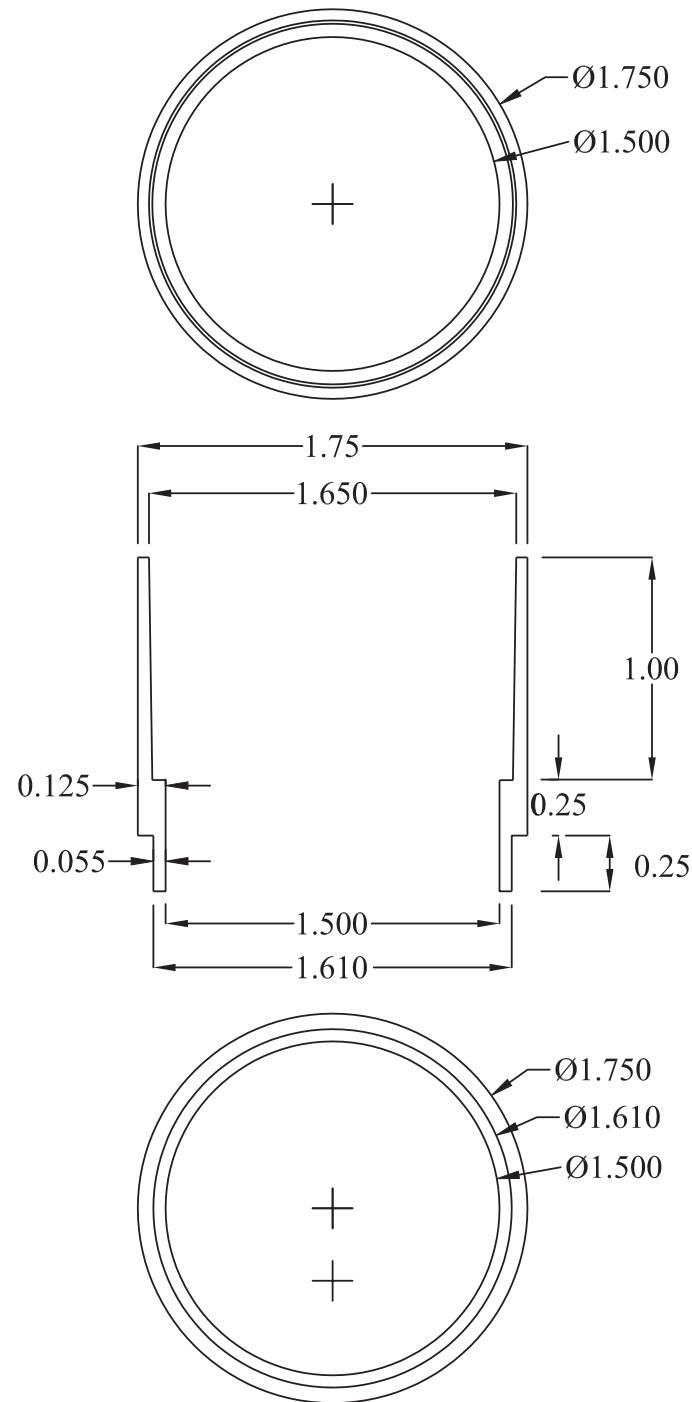


Figure C.3: Vacuum space component 2 (copper). Units are in inches.

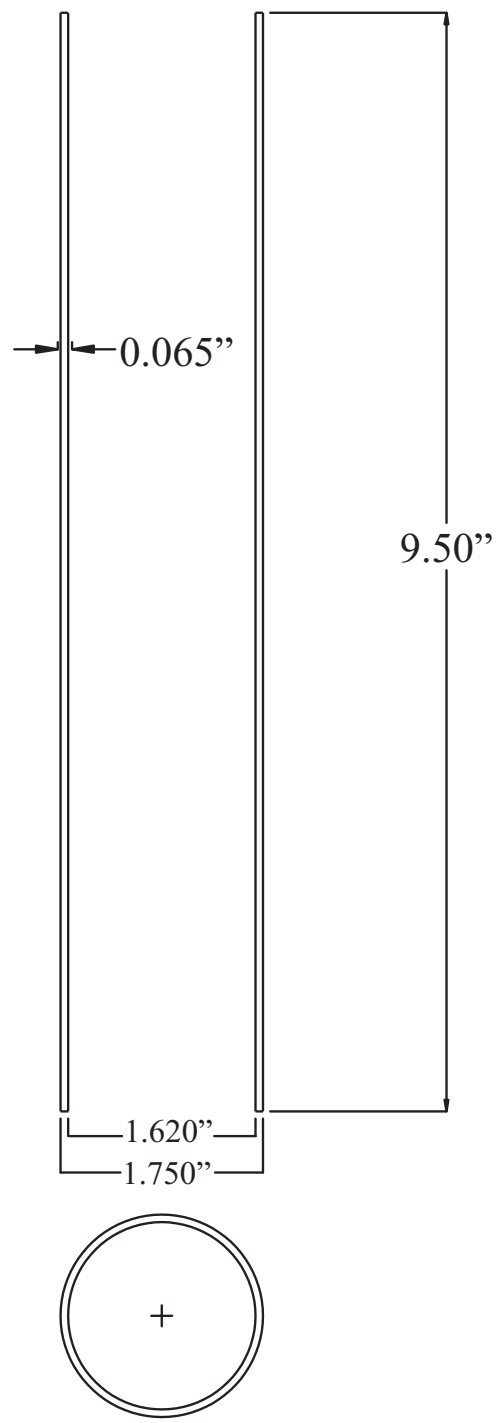


Figure C.4: Vacuum space component 3 (copper).

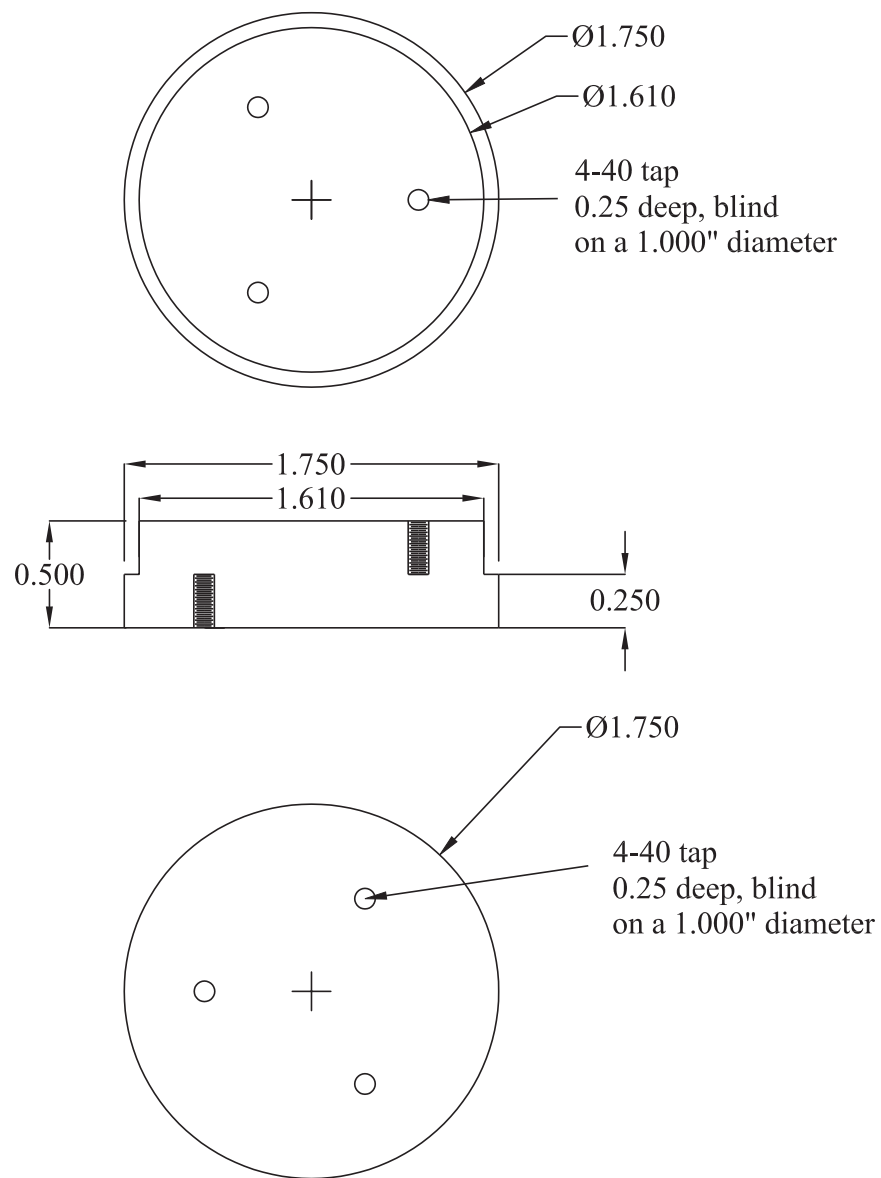


Figure C.5: Vacuum space component 4 (copper). Units are in inches.

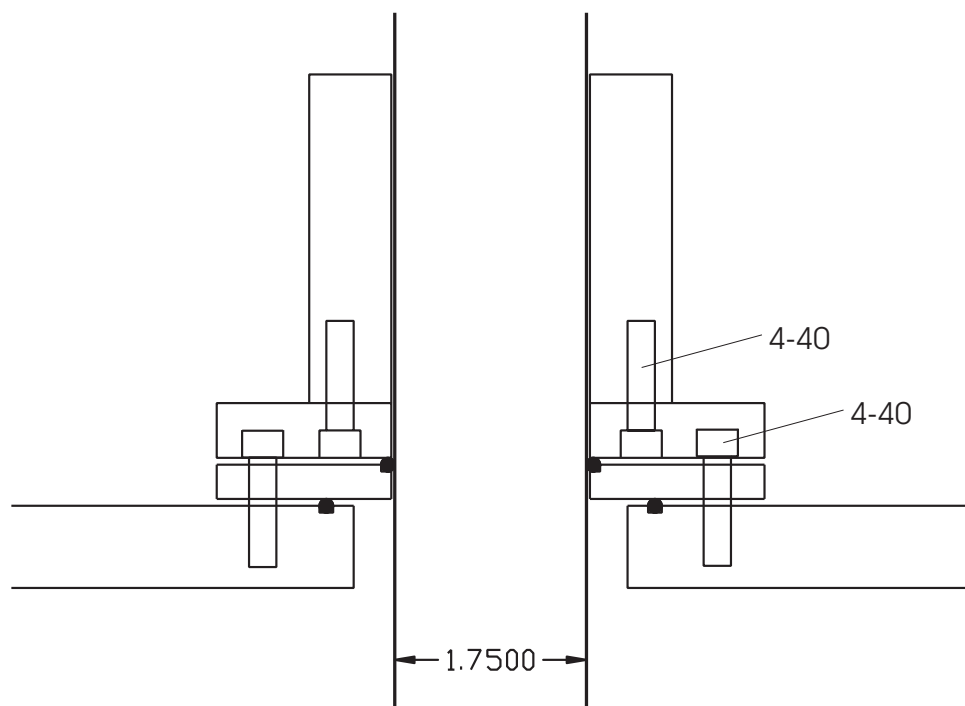


Figure C.6: Dewar seal and probe height adjustment mechanism (Aluminum). Units are in inches.

C.1.2 Fiber-optic and electrical feedthroughs

We used a fiber-optic feedthrough similar to the design by Abraham and Cornell [2]. However, in the published design, the optical fiber is stripped to the polymer coating, which works well for ultrahigh vacuum. For operation in high vacuum, it was only necessary to strip the fiber to the thicker plastic coating surrounding the polymer coating, assuming the plastic coating tightly surrounds the polymer. The Swagelok connector was welded to a stainless NW-40 steel flange.

A 19-pin vacuum Feedthrough, part No. VFT19-F from Lake Shore Cryotronics, Inc. was used to pass electrical connections into high vacuum. The connector was soldered to a NW-40 brass flange. Occasionally these connectors will leak. In this case, a small amount of Vacuum Seal has been found to stop the leak.

C.2 Modular design of the microscope head

The microscope head was designed to be as modular as possible to allow for simple modifications when new experiments should arise. Figure C.7 shows an early prototype of the microscope. Figure C.7(a) and C.7(b) show the bottom stainless steel and copper components of a smaller version (1.50" diameter) of the vacuum tube described in Appendix C.1. Figure C.7(c) shows the microscope head attached to a soft bellows. The bellows [3], shown in Figure C.7(d), were purchased from Palatine Precision, Inc. The bellows were attached to a system of baffles that fit inside the stainless steel vacuum tube of Figure C.7(a). The microscope head was inside the copper vacuum tube of Figure C.7(b). Unfortunately, this design suffered because the microscope head often came into contact with the copper sidewall, causing unwanted vibrations. This was the primary reason for switching

to a 1.75" diameter vacuum tube. We also required more vertical space for heat sinking the wiring.

The microscope head in Figure C.7(c) demonstrates the basic design used to achieve a simple, modular assembly. Mounting plates were connected to each other through three 1/8" diameter rods. The plates were held in place by 2-56 set screws through the plates into the sides of the 1/8" diameter rods. Importantly, the *xy*-scanner mounting plate was the bottommost plate, which made it very convenient for sample removal and access to the cantilever mounted on the inertial translation device.

The general design of the mounting plates used in the microscope is illustrated in Figure C.8. The plates were made of brass and are 1.188" in diameter and 1/8" thick. The 1/8" holes for the rods to pass were placed on a 1.000" diameter. 2-56 set screws held the plate to the 1/8" rod. The necessary features were machined into the remaining area of the plate.

How to make a new plate

In order to create a new mounting plate, begin with a piece of 1.5" diameter brass stock and turn it down to 1.188" in diameter on the lathe. Mount the piece in a 6-jaw chuck on the milling machine and center the piece using an indicator. Machine the three 1/8" holes with a 1/8" drill or with a 1/8" end mill (lock the milling machine head and bring the bed to the end mill slowly). Do this by using coordinates, not by rotating the chuck – the chuck introduces error greater than 0.010". The rods fit nicely into the holes in the plate without clearing them. At this time, machine the required features into the center area of the plate. Next, slot the side of the part for placement of the set screws: (a) turn the 6-jaw chuck over

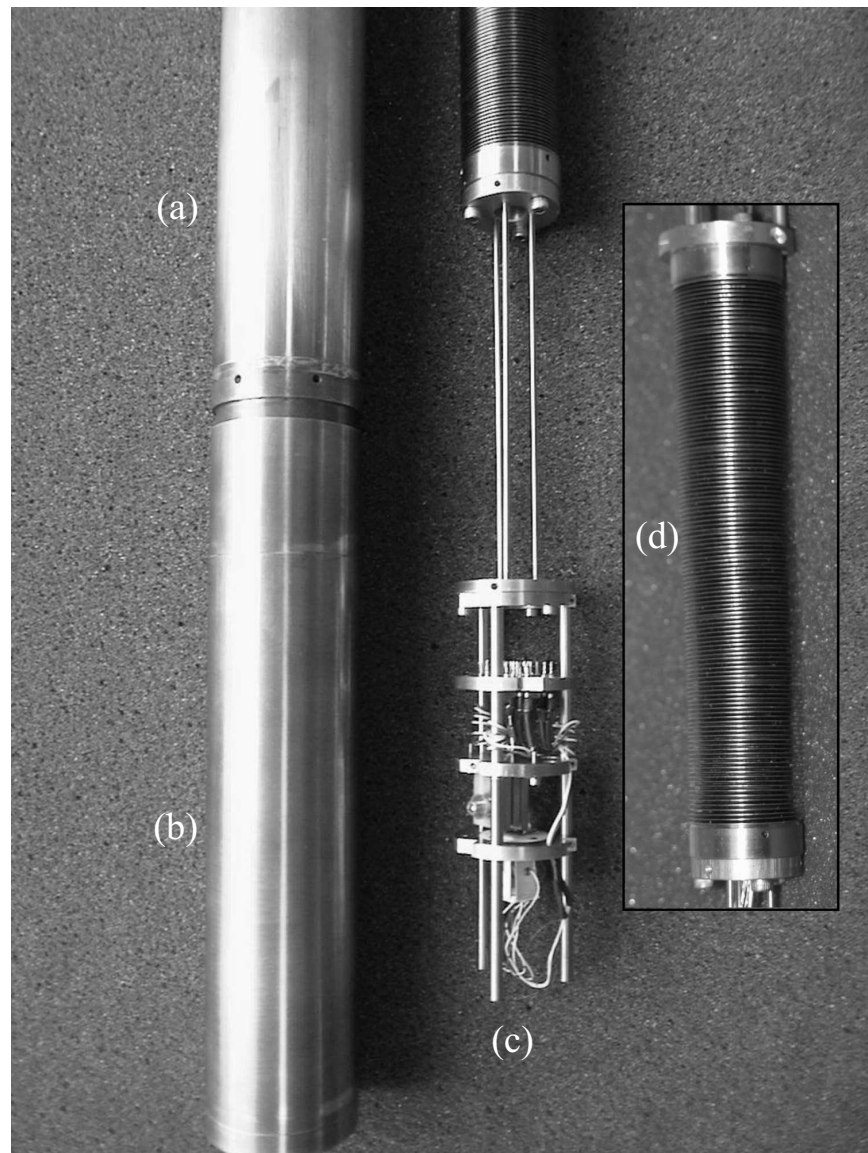


Figure C.7: Early prototype of the electric force microscope. (a) 1.5" diameter stainless vacuum tube. (b) 1.50" diameter copper vacuum space. (c) Microscope head. (d) Soft bellows for vibration isolation.

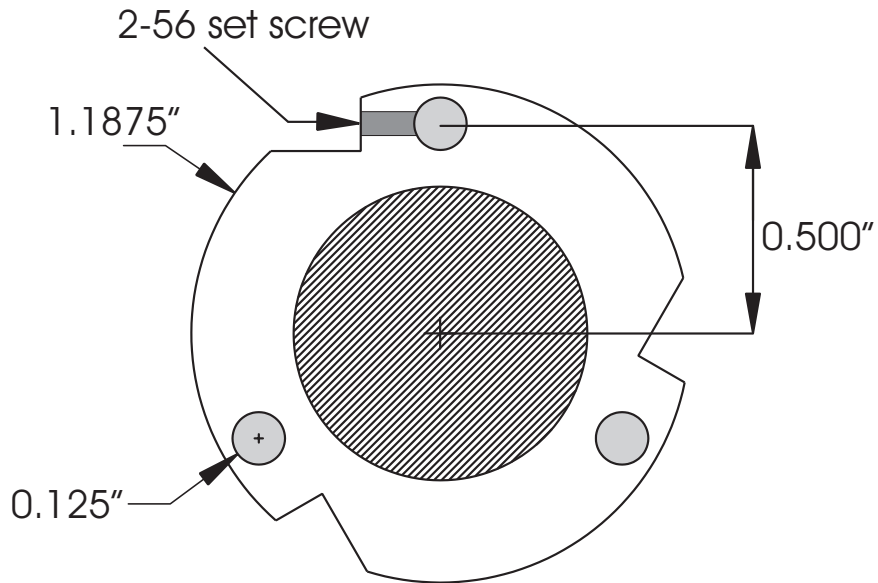


Figure C.8: General design of the mounting plates used in the microscope head.

90° so that the piece is now parallel with the table, and (b) rotate the piece in the 6-jaw chuck until the desired slot can be made parallel to the 1/8" hole and machine a horizontal slot into the piece (make several small passes), leaving approximately 1/8" for the 2-56 set screw, and (c) rotate the part 120° and complete the other two slots. Now drill a pilot hole into the face of the slot and drill the proper size hole (2-56 tap) through to the 1/8" rod holes. Tap the set screw hole for 2-56. Finally, take the piece to the lathe and 'part' the disk off to the desired thickness with a parting tool. If the resulting part is not too thin, it can be carefully faced off on the lathe. Be careful not to smash the thin disk in the chuck.

Figure C.9 shows the final version of the microscope head, which hangs from a soft bellows and fits inside the 1.75" diameter vacuum space described in Appendix C.1. The wiring (phosphor bronze, 36 gauge, Lake Shore Cryotronics, Inc.) enters the probe head through a 3/16" stainless steel tube and enters a plate with an electrical connector mount (connectors are from Samtec, Inc.). The wire that

exits the connector is 36 gauge copper (insulated), which enters a copper heat sink, where it wound 3-4 times around a copper spool and held in place by GE varnish. The wire exits the heat sink, where it is connected to a second plate fit with an electrical connector. Components of the microscope head, such as the piezos for the scanner and the inertial translation devices to the organic device structure, are plugged into the underside of this electrical connector. The stage below the connector is the inertial slider mounting plate, on which an optical fiber is used to monitor the motion of one of the plates on the inertial slider. A second optical fiber is mounted to one plate of the inertial slider, monitoring the motion of the cantilever (see Figure A.3). The last stage is the scanner mounting plate, which is placed below the inertial slider.

C.3 Cryogenic sample scanner

This section gives details about the sample scanner, which was introduced in Section 3.3.1. The sample scanner shown in Figure C.10(a) was described by Siegel *et al.* [4]. The motion of the bimorph piezos is shown in Figure C.10(b). The piezos used were $0.500'' \times 0.250'' \times 0.020''$ (Length \times Width \times Thickness), purchased from Piezo Systems, Inc.

We specified that the custom 2-layer piezoelectric transducer use silver electrodes, which are nonmagnetic. Otherwise, nickel is the standard electrode, which is fine for experiments which do not involve high magnetic fields. The wires were centered on the electrodes to minimize image distortion. Occasionally, a wire will break off. In this case, it is critical to solder very quickly with minimal solder and flux. Heating the piezo for extended periods of will degrade the piezo response. After soldering, the motion of the scanner should be recalibrated.

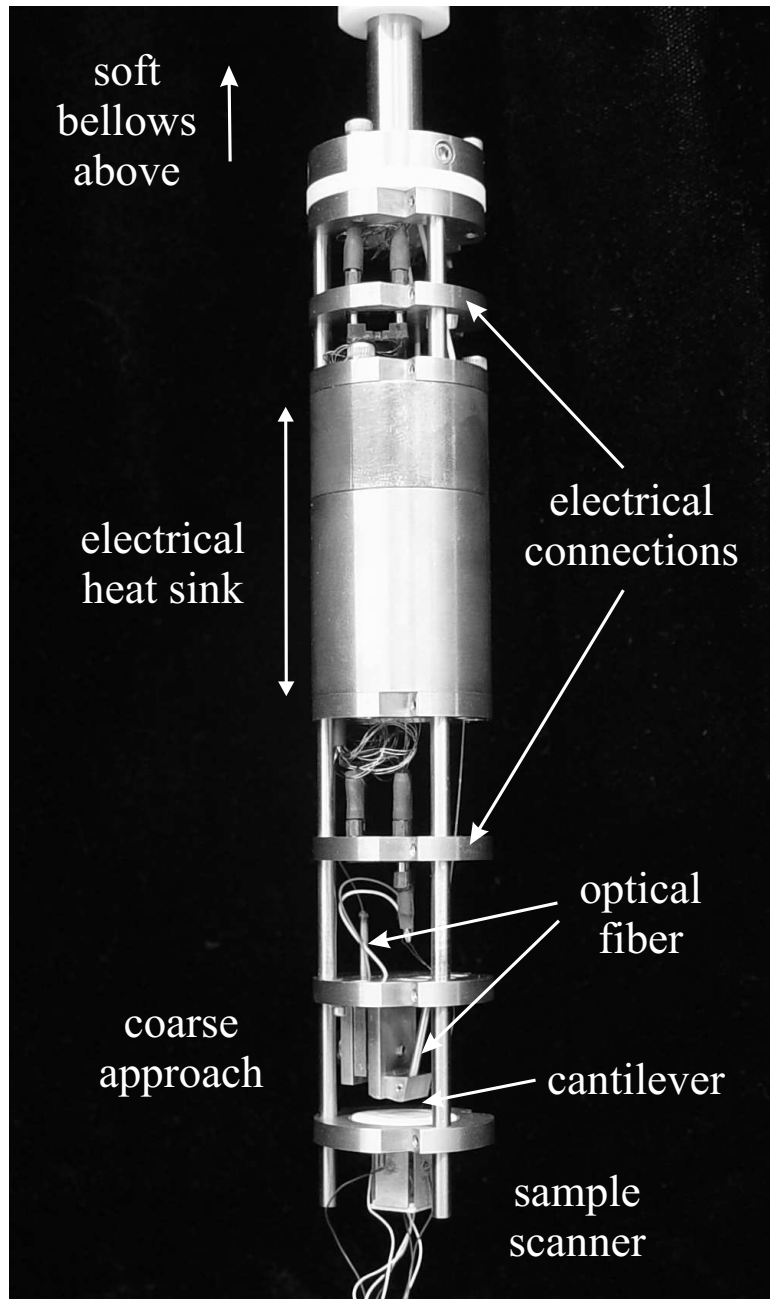


Figure C.9: Entire microscope head.

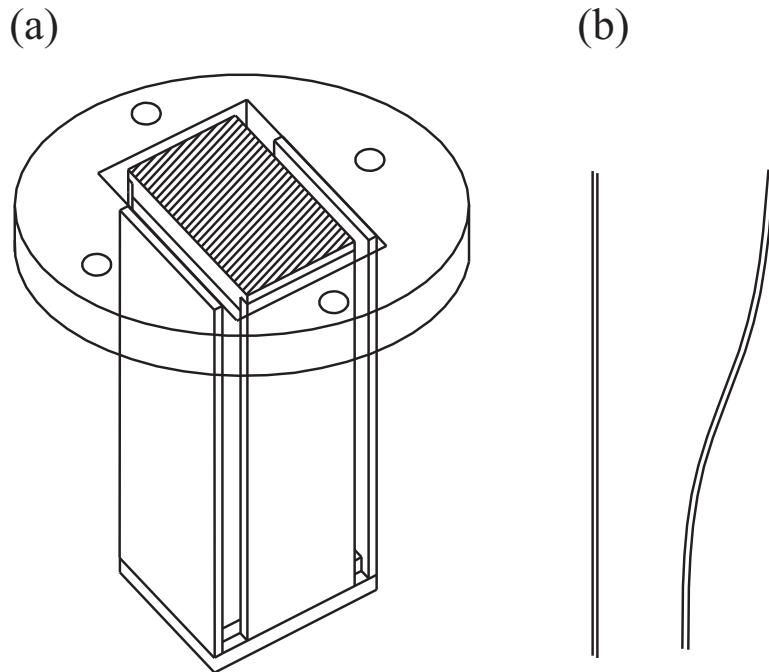


Figure C.10: (a) Cryogenic sample scanner. (b) Bending of the bimorph piezo.

Figure C.14 demonstrates how the components in Figures C.11, C.12, and C.13 fit together. Assembling the scanner is quite difficult and requires patience. First, glue two of the bimorph piezos to the center scan stage (Figure C.12). Then glue the remaining piezos to the outer stage (Figure C.11). Next, glue the free ends of the two piezos attached to the outer stage to the small square base (Figure C.13). Finally, place the two piezos glued to the center scan stage through the outer stage and glue the free ends of these piezos to the small square base. To unglue a piezo from Macor, apply acetone to the joint for 15 minutes. Do not pry, as this will break the edge of the piezo.

To drive the bimorph piezo, we use a National Instruments 6052-E board to digitize up to 330 kHz and create an output signal with a voltage range of ± 10 V. The output signal from the board is then amplified $\times 15$ with a piezoelectric ampli-

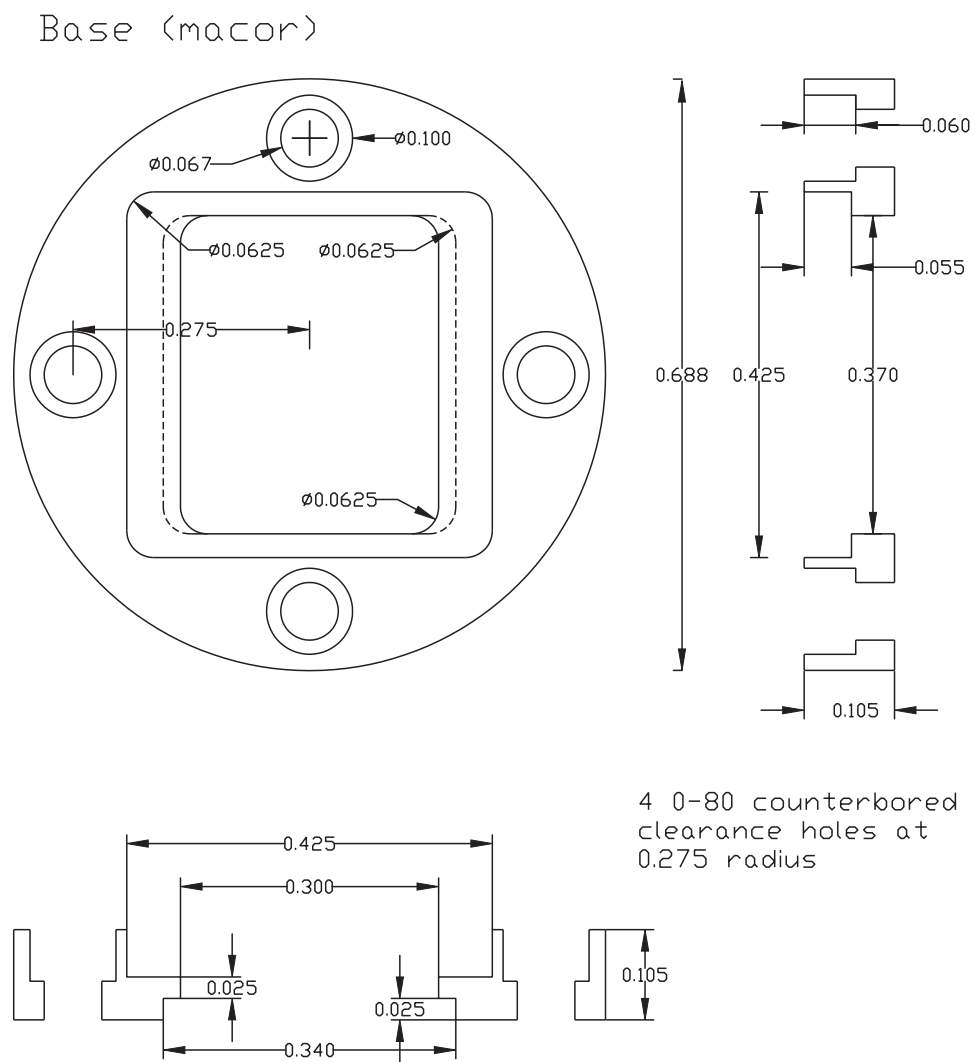


Figure C.11: Design of the cryogenic sample scanner: top outer scan base/stage (Macor). Units are in inches.

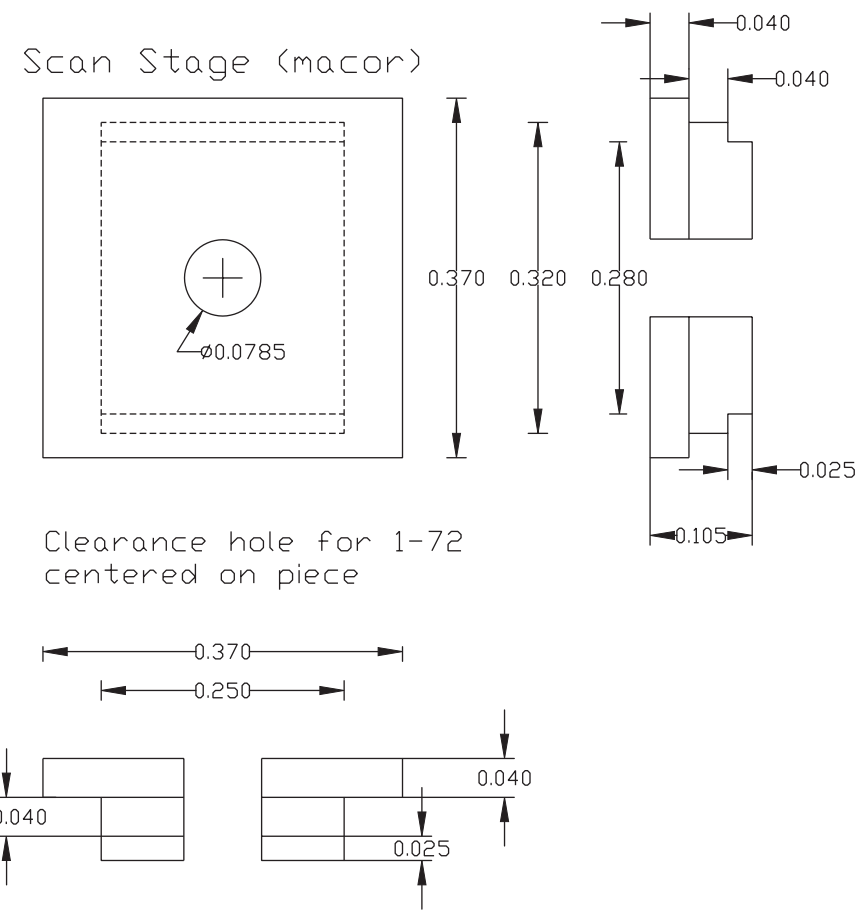


Figure C.12: Design of the cryogenic sample scanner: center scan stage (Macor). Units are in inches.

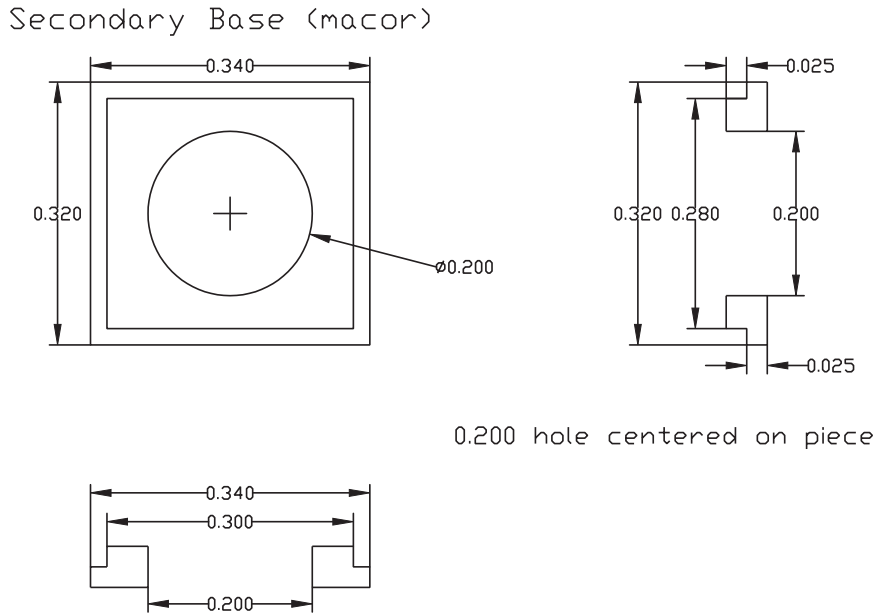


Figure C.13: Design of the cryogenic sample scanner: bottom base (Macor).

Units are in inches.

fier built by Piezo Systems, Inc. (part number EPA-102-115). This amplifier has offset adjustments and is bipolar up to ± 200 V. The gain may be set from $\times 1$ – 20 . Care must be taken not to accidentally bump the gain setting on the face of the amplifier. The gain should be checked periodically. The bimorph piezos should not be run higher than ± 180 V, at which point they will depole. We used a simple passive RC filter to bring the bandwidth down to 0–200 Hz while scanning. This reduced the noise levels considerably.

C.4 Vibration Isolation

The vibration isolation structure was constructed by Technical Manufacturing Corporation (TMC) in Peabody, MA. The design is very simple. A 2000 pound laminated steel plate rides on 4 air legs mounted on the top of a large steel frame. This allows for the isolation of the entire dewar/microscope. Figure C.15 is a

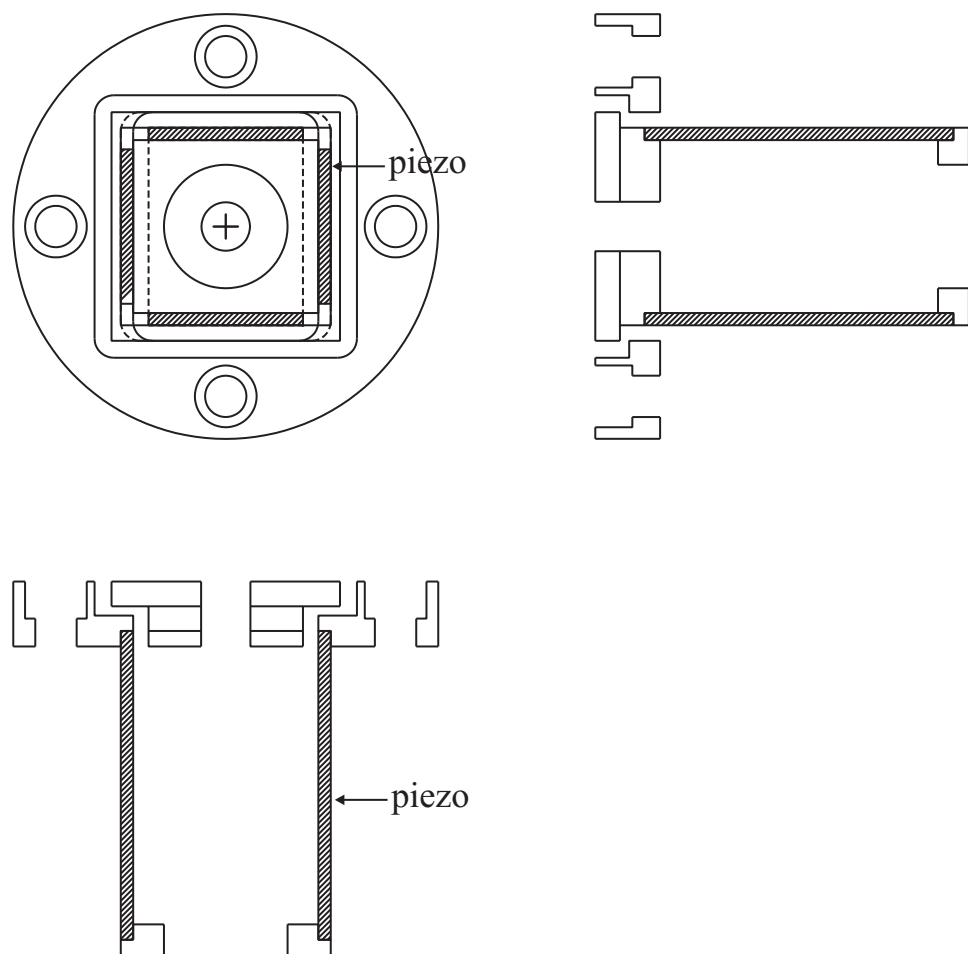


Figure C.14: Top and side views of the cryogenic sample scanner assembly.

Bimorph piezos are hatched. For scale, the bimorph piezo is 0.500" in length.

diagram of the steel frame as viewed from the above. It is important to note that each leg of the frame rests on a 12" × 12" plate so that the pressure on the floor in Baker 146 is minimized. The building engineer and the building manager checked the floor rating and approved the design. Figure C.16 shows a schematic of the vibration isolation structure viewed from the side.

A diagram of the 2000 pound plate is shown in Figure C.17 (viewed from above). The 3/8-24 clearance holes in the 2000 pound plate in Figure C.17 were used to mount the flexible vacuum pump line and components of a winch/pulley mechanism. The 28" diameter clearance hole of the 2000 pound plate is large enough to allow the dewar to pass through. On the top of the 2000 pound plate, the 8-bolt pattern on a 30" diameter is tapped 3/8-24. This is used to mount a 32" diameter circular aluminum plate. The large, 32" diameter, 1" thick, aluminum plate is shown in Figure C.18. The dewar is O-ring sealed to the 32" diameter aluminum plate through a sixteen-bolt (clearance) pattern of 3/8-24 hex bolts on a 12" diameter. This plate has a large 8" diameter clearance hole (hatched area). An eight-bolt pattern on a 9.5" diameter is used to mount a smaller probe interface plate (aluminum), shown in the photograph in Figure C.18. The probe interface plate rests on a O-ring, 8.5" in diameter. This plate contains pressure release valves and mates with cryogen fill lines and the vacuum tube through the probe height adjustment anchor discussed in Appendix C.1.1 and illustrated in Figure C.6.

A winch mechanism was designed to raise the dewar. The winch lines and pulleys are shown in the photograph of Figure C.18. In order to raise the dewar evenly, the winch line must be monitored so that it does not cross on the winch spool. Once the dewar is raised high enough so that the 3/8-24 bolts can be threaded into the dewar, a few bolts should be threaded in by hand, and the

dewar should be pulled tightly against the 32" plate of Figure C.18. However, it should not be pulled too tight as the winch may break the lines. The bolts are then tightened using a star pattern, which gives a uniform seal against the O-ring on the dewar.

The turbomolecular vacuum pump sits on the floor. Through a stainless steel flexible hose (NW-40), the line passes through a vibration isolation box, which rests on a small table. The flexible line connects to a U-shaped tube which is encased in a 1 foot \times 1 foot block of cement. The block rests in sand, which is inside the black box. The vacuum line exits the box and is anchored to the 2000 pound plate, where it then enters the vertical vacuum tube through a valve. At the top of the vertical vacuum tube, near the valve, the fiber optic and electrical feedthroughs (Appendix C.1.2) enter the six-way NW-40 vacuum component.

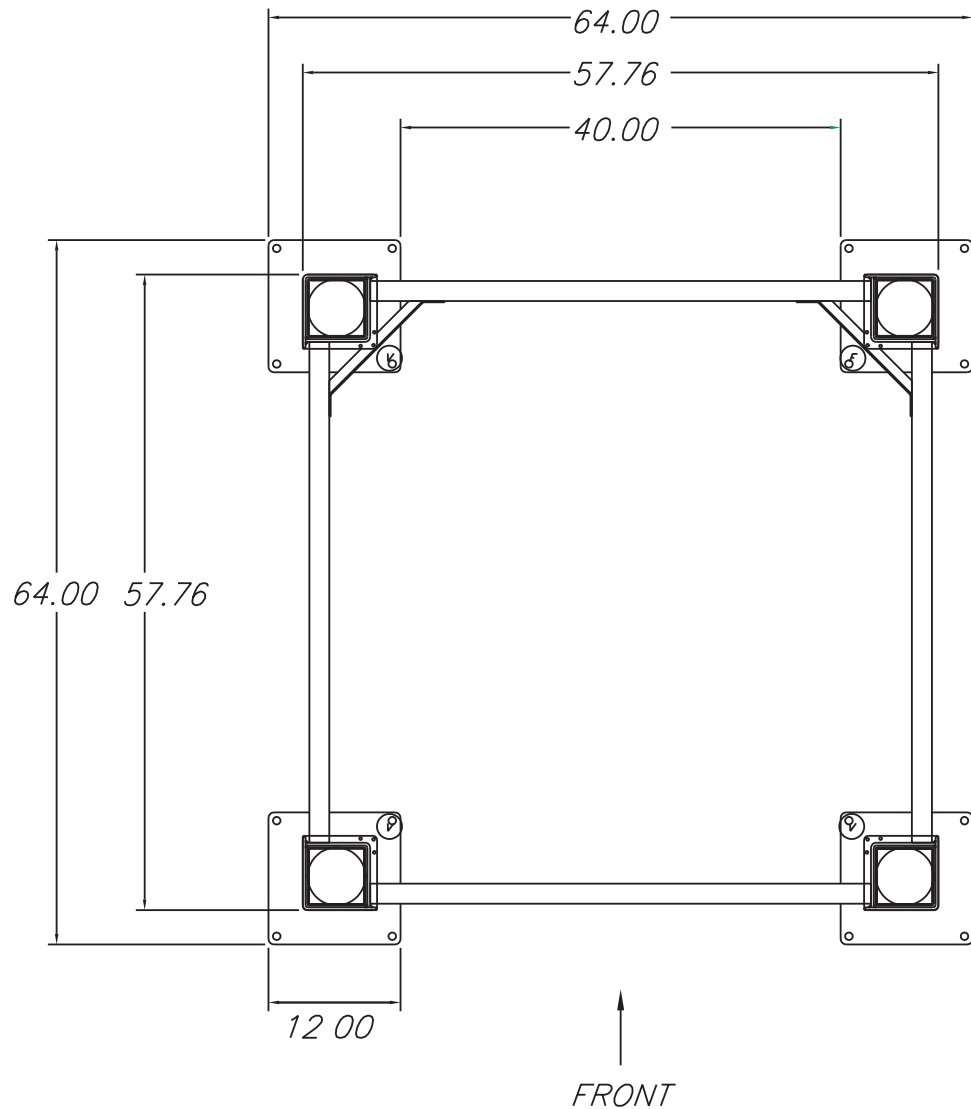


Figure C.15: Vibration isolation frame - top view. Units are in inches.

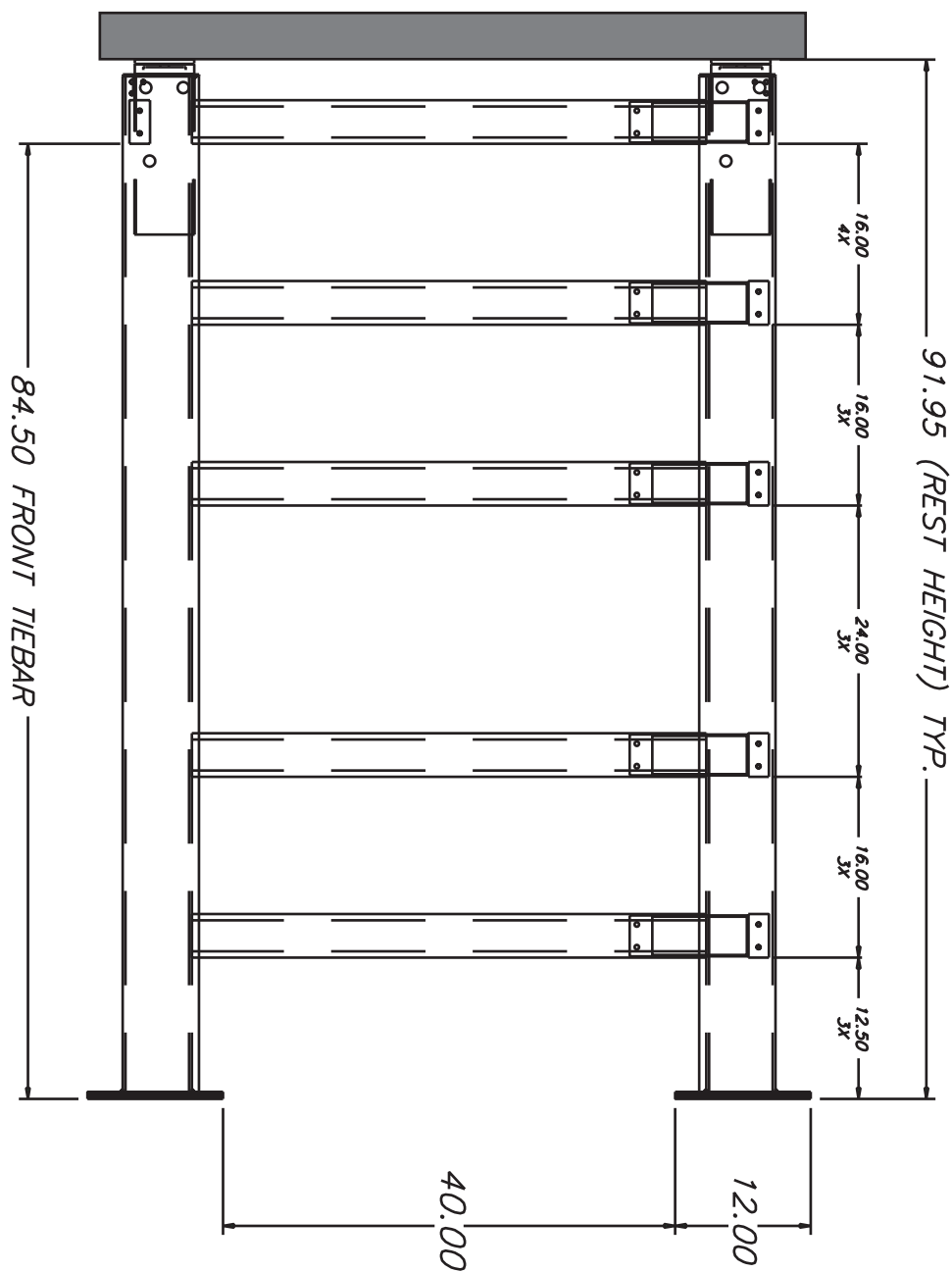


Figure C.16: Vibration isolation frame and top plate - side view. Units: Inches

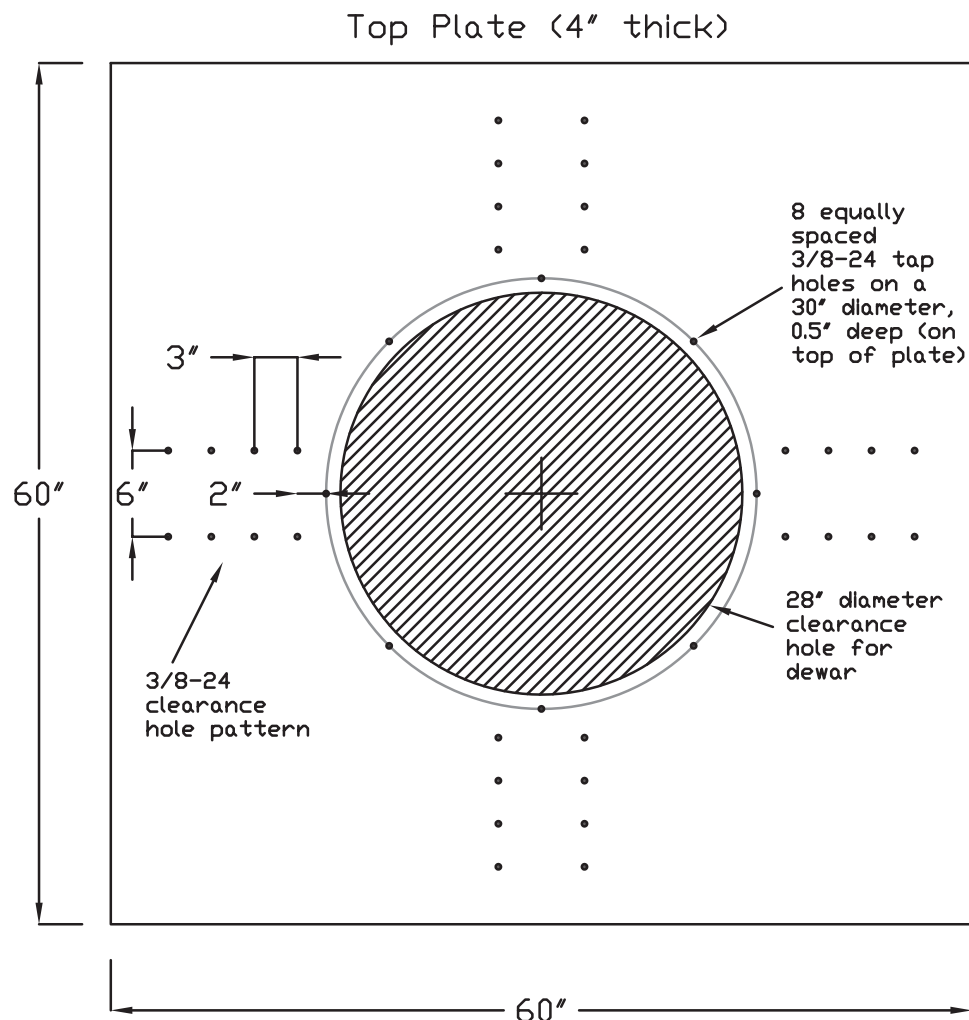


Figure C.17: Vibration isolation - top view of 2000 pound plate (laminated steel).

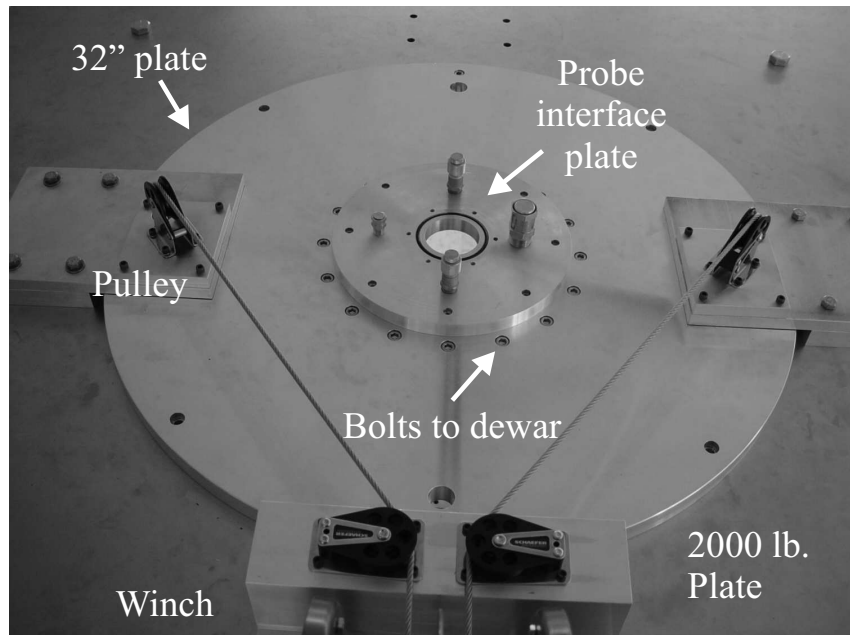
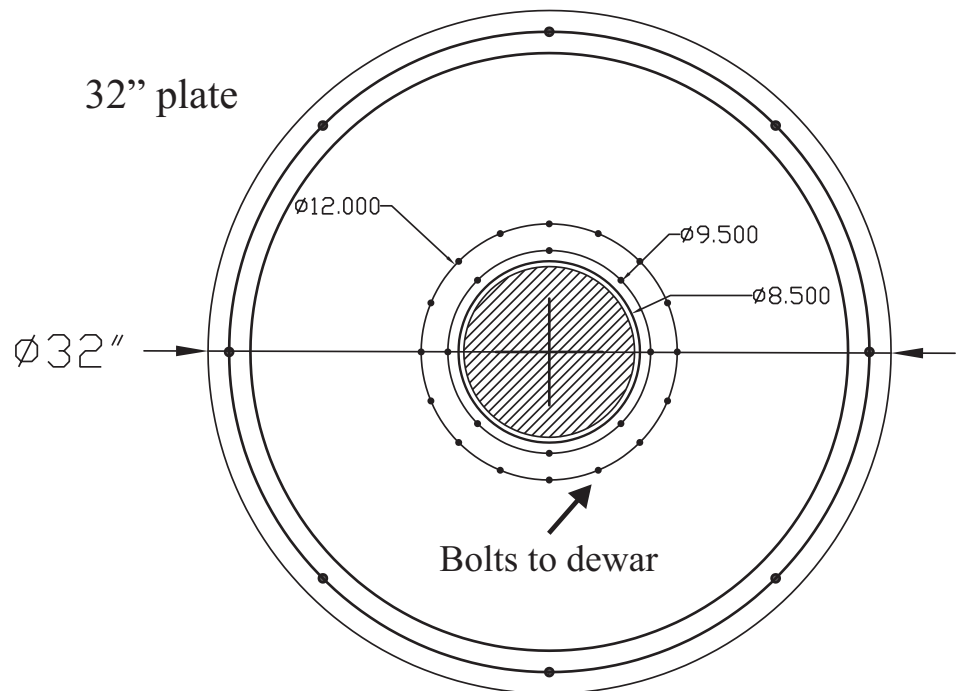


Figure C.18: Mounting plate (32" diameter) for dewar (Aluminum). This plate rests on the top of the 2000 pound plate in Figure C.17. Units are in inches.

Appendix C references

- [1] R. C. Richardson and E. N. Smith, *Experimental Techniques in Condensed Matter Physics at Low Temperatures*, Addison-Wesley, 1988.
- [2] E. R. I. Abraham and E. A. Cornell, Applied Optics **37**, 1762 (1998).
- [3] M. Roseman and P. Grütter, Review of Scientific Instruments **71**, 3782 (2000).
- [4] J. Siegel, J. Witt, N. Venturi, and S. Field, Review of Scientific Instruments **66**, 2520 (1995).

APPENDIX D

CIRCUIT DIAGRAMS

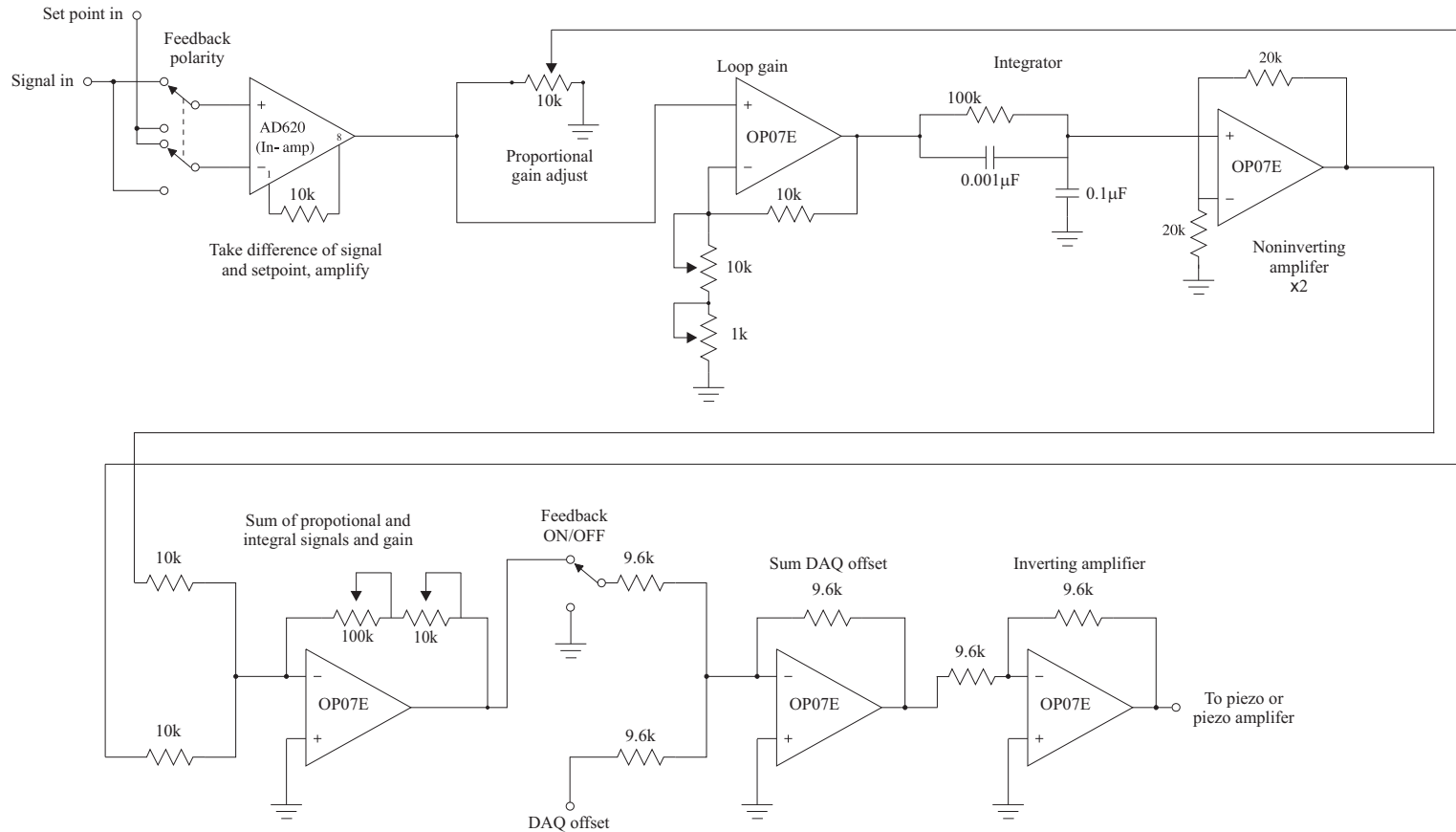
D.1 Feedback circuitry for tip-height control

Figure D.1 shows the proportional-integral feedback circuitry used to keep the cantilever tip-surface height constant during contact mode and intermittent contact mode imaging. The feedback circuit presented in David Peale's Ph.D. thesis [1] was used as the basis for this circuit. The variable resistors are all 10-turn potentiometers. Figure D.2 is a diagram of the proportional-integral feedback circuit.

For contact mode imaging, the input signal was the interferometer signal. The feedback polarity was set depending on which slope of the interference pattern is used. For intermittent contact mode imaging, the input signal was the fast output from the EG&G lock-in amplifier. The output was set to MAG (magnitude). Also, a time constant $\tau = 640 \mu\text{s}$ worked well.

Figure D.3(a) represents a simple test stage when working with the feedback circuitry. It was much more convenient than an actual experiment for testing purposes and does not involve a fragile cantilever. Piezo 1 was sent a square wave pulse, causing it to move (bottom graph of Figure D.3(b)). The feedback circuitry was connected to Piezo 2, which caused Piezo 2 to move in response to Piezo 1, keeping the distance, d , constant (top graph of Figure D.3(b)). The step in the voltage was 0.01 seconds wide.

Figure D.1: Circuit diagram of the proportional-integral feedback controller.



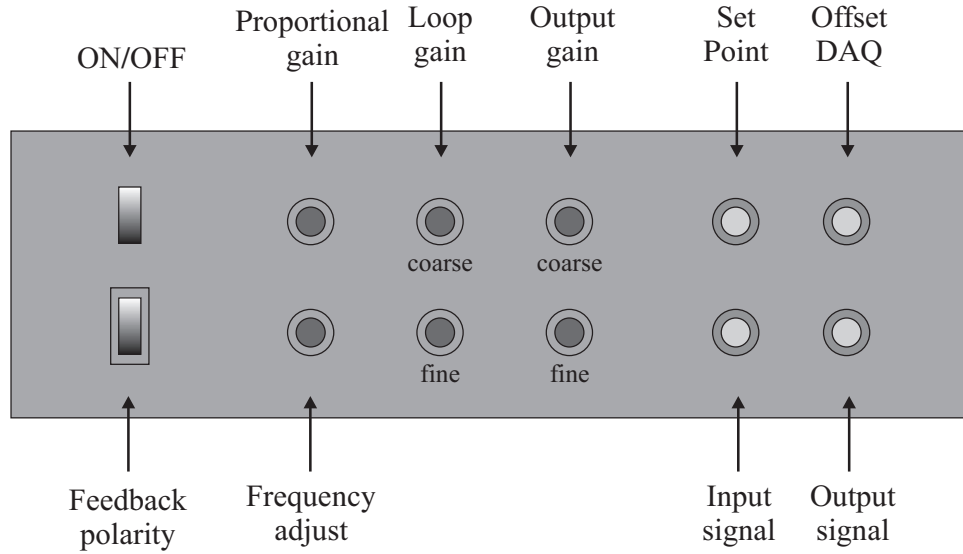


Figure D.2: Front panel of feedback circuit box.

D.2 Positive feedback circuitry

The resonance frequency response was measured to obtain the force gradient. In order to measure the resonance frequency, the cantilever was made the resonant element in a positive feedback loop [2]. Figure D.4 illustrates the basic principle of the circuitry involved. First, the output signal of the fiber-optic interferometer is band pass filtered around the resonance frequency of the cantilever. Next, the phase of the signal is adjusted by $\pi/2$ and the output signal is limited by a multiplier voltage. This output signal is routed into a frequency counter and the bimorph piezo at the base of the cantilever, which creates the self-oscillation.

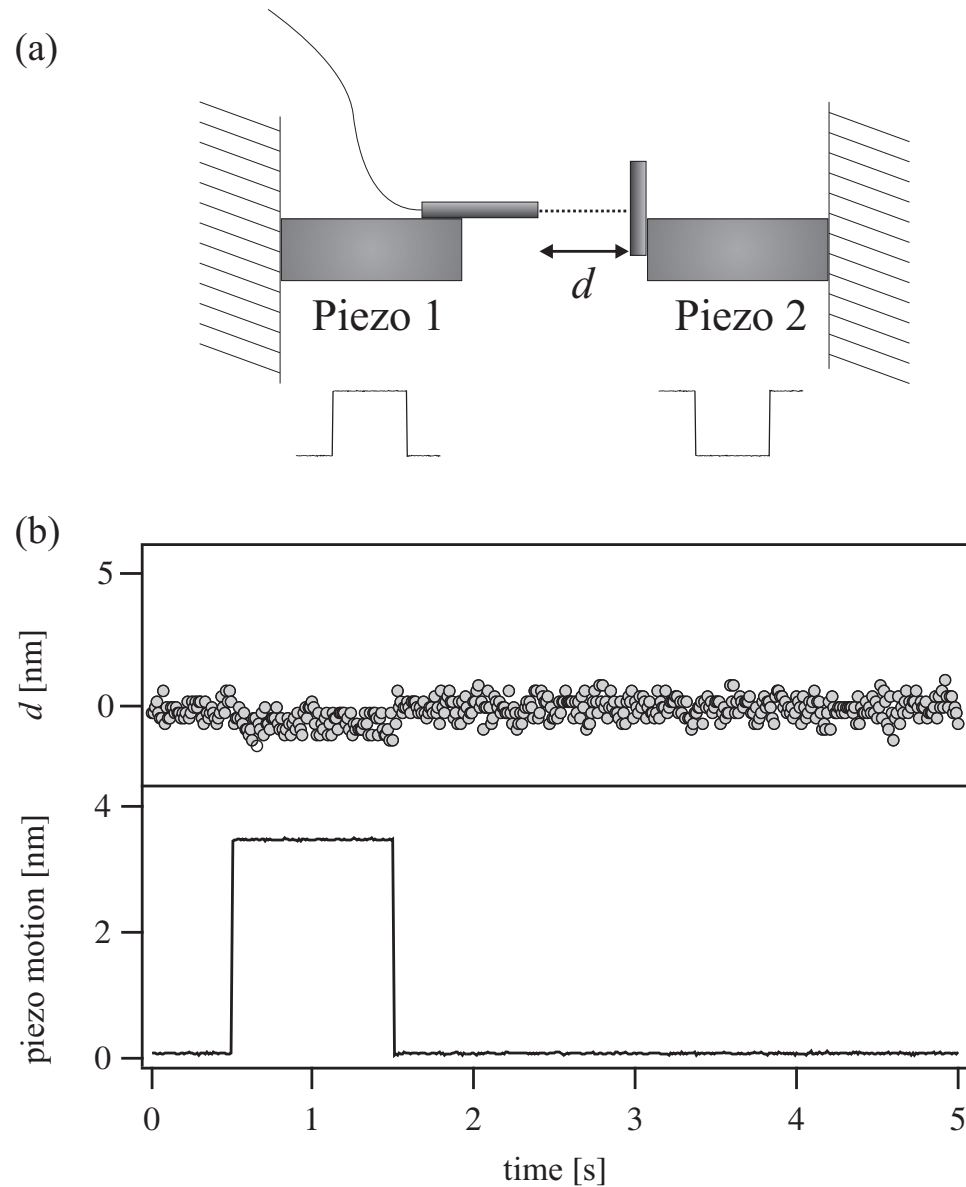


Figure D.3: (a) Simple stage for testing feedback circuitry. (b) Top graph: displacement, d , between the optical fiber on Piezo 1 and the mirror on Piezo 2. Bottom graph: displacement of Piezo 1.

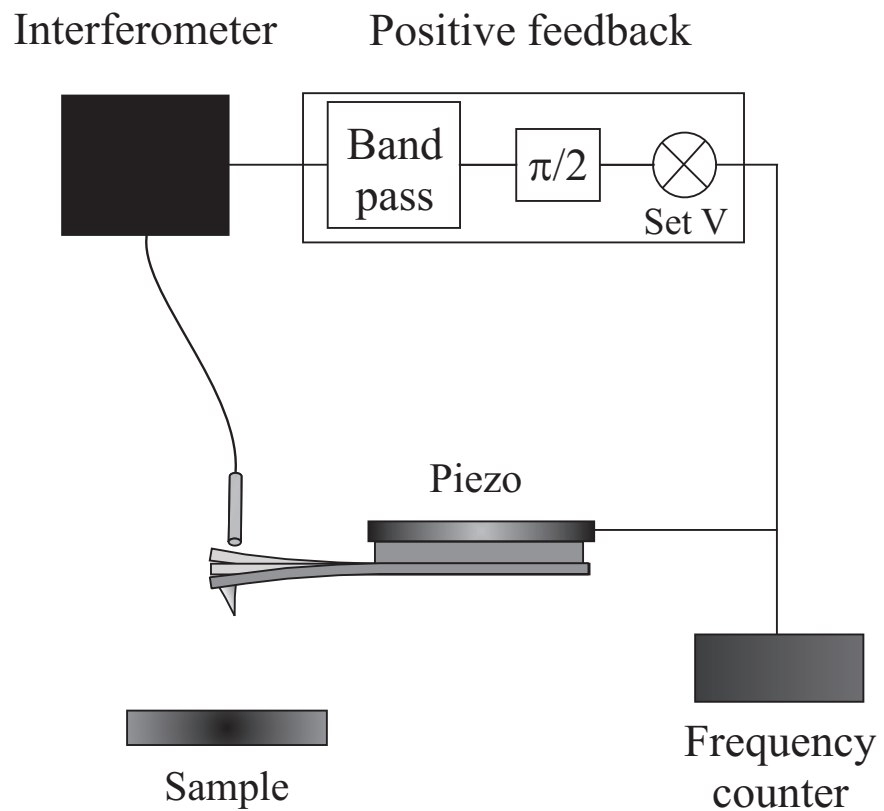


Figure D.4: Basic principle of the positive feedback circuitry for measuring the force gradient.

Appendix D references

- [1] D. R. Peale, *Diffusion and mass flow dynamics on the gold (111) surface observed by scanning tunneling microscopies*, PhD thesis, Cornell University, Ithaca, NY, 1992.
- [2] T. R. Albrecht, P. Grütter, D. Horne, and D. Rugar, Journal of Applied Physics **69**, 668 (1991).